National Technical University of Athens (NTUA)

School of Electrical and Computer Engineering

Development of New Photovoltaic Devices Based on Perovskite Cells and Application in Electric Power Systems

DOCTORAL THESIS

in
Electrical Engineering
Electrical Power Systems Engineering
by

Eng. Alaa Ahmed Zaky Hussein
M.Sc in Engineering (Electrical Power and Machines)

under the Supervision of

Prof. Antonios Kladas	National Technical University of Athens School of Electrical and Computer Engineering
Prof. Evangelos Heristoforou	National Technical University of Athens School of Electrical and Computer Engineering
Prof. Polycarpos Falaras	Institute of Nanoscience and Nanotechnology, National Center for Scientific Research "Demokritos"

Athens

2021

Development of New Photovoltaic Devices Based on Perovskite Cells and Application in Electric Power Systems

DOCTORAL THESIS

in

Electrical Engineering

Electrical Power Systems Engineering

by

Eng. Alaa Ahmed Zaky Hussein

M.Sc in Engineering (Electrical Power and Machines)

Supervisoin Committee

Prof. Antonios Kladas	National Technical University of Athens School of Electrical and Computer Engineering
Prof. Evangelos Heristoforou	National Technical University of Athens School of Electrical and Computer Engineering
Prof. Polycarpos Falaras	Institute of Nanoscience and Nanotechnology, National Center for Scientific Research "Demokritos"

Seven Member Examination Committee

…… **Antonios Kladas** Professor NTUA	…… **Evangelos Heristoforou** Professor NTUA	…… **Polycarpos Falaras** Professor NCSR Demokritos
…… **Athanasios Kontos** Associate Professor NTUA	…… **Thomas Stergiopoulos** Associate Professor Aristotle University of Thessaloniki	…… **Stavros Papathanasiou** Professor NTUA

……..
Georgios Stavrakakis
Professor at Technical University of Crete

Athens

2021

Acknowledgment

All gratitude goes in the first place to ALLAH almighty who has guided and helped me in this work from beginning to end. Egyptian Ministry of Higher Education in cooperation with the Hellenic Ministry of Foreign Affairs are greatly appreciated for this PhD studies financial supporting. I would like to take this opportunity to thank all those people who helped me in the preparation of this thesis. First of all, I owe my deepest gratitude to **Prof. Falaras** to whom I deeply indebted for his guidance, encouragement, support and boundless patience during the period of doing this thesis at National Technical University of Athens (NTUA) and National Center for Scientific Research NCSR Demokritos in Athens. My immense appreciations also go to my supervisors **Prof. Kladas and Prof. Hirstoforou** for their help, support and discussions**.** Great thanks for the seven member examination committee for their effort and discusions. Finally, I would like to acknowledge immeasurable sacrifices and abundant support made by both of my parents, my wife, my son and the rest of my family. I, therefore, dedicate this work to all of them.

Alaa Zaky

Table of Contents

Table of Figures

List of Tables

Abstract

In recent times, the use of solar energy has grown, especially as a source to generate electricity from light in a direct way as an alternative to fossil fuels due to its being an environmentally friendly and inexpensive source over the range of operation, as its operating cost is almost zero. The problem lies in the cost of manufacturing and the efficiency of converting light energy into electricity from this point of view researchers are interested in manufacturing solar cells that overcome this problem, so the trend was towards third generation solar cells that rely on nanotechnology techniques to overcome the aforementioned problem.

It is worth noting that solar energy and other renewable energy sources have become widely used in the electric power system, and thus have affected the operating conditions, as is evident in the unit commitment problem in electric power system, where the problem differs in the case of incorporating solar units from their counterparts in the case of the absence of solar units.

Also, when connecting solar energy units to the electrical grid, operating conditions differ due to this connection, and therefore control systems must be developed to control the operating conditions. Recently third generation solar cells especially perovskite solar cells (PSCs) gained research interest due to their remarkable photovoltaic (PV) performance reaching up to 25.2% power conversion efficiency in 2020 few years since their first solid-state high performing device reported in 2009.

For the first time, we proposed the concept of interface engineering for obtaining high efficient and stable third generation solar cells based on nanotechnology techniques and test

this cells in real electrical applications like unit commitment, grid connected PV units and water pumping system based on solar energy.

Doping technique was also used in order to obtain efficient third generation solar cells. As a result, PSCs with PCE higher than 18% owing to high open circuit voltage (V_{oc}) of 1.1 V, high current density (J_{sc}) of 23.15 $mA \cdot cm^{-2}$, and a high fill factor (FF) of 73% were obtained.

Three electrical models of PSCs called single, double and triple diode models has been proposed for two PSCs devices. Estimation and extracting the PSC models parameters are carried out using the elephant herd optimization algorithm (EHO). To prove the capability of the proposed estimation procedure, a comparison study between the proposed EHO with crow search optimization and differential evolution algorithms has been employed.

Finally an efficient and low cost photovoltaic pumping system based on perovskite solar cells (PSCs) is proposed. The fabrication process of PSCs and its application as a power source for powering a synchronous reluctance motor (SynRM) to drive a water pump for irrigation purpose are presented. The total area used for installing the perovskite solar array was 3.42 m^2, which is very small in comparison with the area of silicon solar array that exceeds 36 m^2 for the same case. This will help to avoid the partial shading condition that reduces the efficiency of PV system.

In addition, a simple control algorithm is based on perturbation and observation (P&O) proposed to derive both the PV array and SynRM to work at the maximum output power resulting in a low cost and efficient system. A proposed control system applied to the conventional voltage source inverter to drive the system in an efficient way.

1 Chapter 1

1 Introduction

1.1 Introduction

A lot of studies have been made in order to enhance the grid-connected photovoltaic (PV) system quality for meeting the electrical energy rising request. Due to the fact that PV array output depends on the environmental conditions resulting in a big challenge for PV array output power utilizing. PV array consist of modules which are connected in series and parallel combinations. High output power from a PV systems requires improvement in the fabrication materials and methods used to control this source of power. The materials used in PV manufacturing play a vital role in the efficiency of the all PV system. In order to increase the PV system efficiency there are to methods the first one is through materials properties enhancement and the other method is via increasing the radiation intensity received from the sun. Sun tracking technique, maximum power point (MPP) tracking method or both of them are efficient methods for PV system efficiency improvement. Many studies introduced controllers such as Perturb & Observe method, Incremental Conductance and fuzzy based methods.

Renewable energy such as sunlight, wind, tides, geothermal heat etc. gained a lot of attention as alternative of conventional power sources as it has a lot of advantages for instance environmentally friend and low running cost. Solar energy is the most promise renewable energy as it is pollutant free, no noise and almost zero running cost.

There is no doubt that the global demand for energy is being increased and accelerating significantly in parallel with the depletion of the global reserves of fossil fuels. Therefore, there is a strong need to develop and use renewable energy technologies. It is well known that

solar energy being one of the most promising renewable energy sources. Indeed, the power striking from the sun into earth's surface is near to 1.8×10^{11} MW which is much more than all the present power demands. Moreover it is a clean and environmentally friendly energy source, it has low running cost and occupies the highest rankings in terms of use and reliability, promising to expand its utilization more and more. The demand for solar energy and especially PV technologies has increased due to many advantages such as safety, security and reliability, lack of maintenance needs, effectiveness, direct conversion of sunlight directly to electricity economically feasibility into illumination of remote areas, flexibility and tunability of the size of the solar cell systems. PVs can be used for the lighting of isolated areas, for the power providing of remote communication stations, for water pumping to irrigate crops, for the lighting of residential houses, for space vehicles, while they can be integrated alongside diesel engines (hybrid systems) and street lights. Due to high installation cost for this technology and according to the fact that the ouput power from the solar cells depends on the environment conditions, mainly solar irradiation and temperature. Solar cell photo voltage increases with the decrease of temperature, while the photo current also increases with the increase of solar irradiation and vice versa [1-5]. According to this it is very necessary to make the solar cells work at MPP.

Photovoltaics (PVs) are systems that directly convert sunlight into electricity, covering approximately a quarter of the renewable energy production worldwide with important applications in portable electronics, buildings and solar farms [6]. During the previous decades intensive research was focused on first-generation PVs, which are single-crystal devices that have high efficiencies but use energy consuming and time intensive fabrication methods. These are also the main issues of second-generation PVs employing high–vacuum and expensive Si-based thin-film technologies. On the contrary, third-generation approaches to photovoltaics aim to develop highly performing devices, using abundant nontoxic materials

and low-cost deposition methods [7-10]. Third generation solar cells present high power conversion efficiencies, especially for some laboratory-scale, multi-junction devices [11]. Very recently, the scientific research has shifted towards novel photovoltaic materials and cell architectures. Thus, apart from the evolution of conventional single-junction solar cells into multi junction and/or thin-film devices, emerging technologies such as organic solar cells (OSCs), dye-sensitized solar cells (DSSCs), quantum-dot solar cells (QDSCs), and perovskite solar cells (PSCs) are studied. Currently emphasis is given to PSCs that were considered as one of the ten main breakthroughs in science for 2013 and have received tremendous attention from the research community during the last years [12].

PSCs are based on hybrid organic-inorganic halide perovskites [13] which have the inherent ability to strongly absorb light, are solution processable and combine quality and properties typical of inorganic materials [14-16]. Furthermore, they have a suitable and tunable direct band gap and long diffusion lengths for electrons and holes, they are obtained from cheap and abundant elements, all of which makes them ideal materials for use in PVs [17-22]. The major advantage of these new solar cells is related to their potential as an economically and environmentally viable option to traditional silicon-based technology and the main outcomes show that PSCs offer more environmentally friendly and sustainable option, with the least energy payback period, as compared to other PV technologies. Their efficiency depends largely on the specific cell arrangement, the chemical composition, structure, morphology and size of the incorporated materials as well as the efficient charge collection at the corresponding nanostructured interfaces. Recent advances focus on our ultimate goals to provide additional data on the devices lifetime and to ensure their enhanced stability for real-world applications [23-48].

1.2 Objectives

The main objective of this thesis is to fabricate new efficient and stable solar cells (perovskite solar cells) that belong to third generation solar cells and examine its application in electrical power system performance.

1.3 Outline of the thesis

The thesis consists of ten chapters, chapter one is general introduction. While, chapter 2 introduces solar energy overview and investigating the effect of incorporating PV generation units on the unit commitment problem in power system and the PV grid connected system performance under constant and variable irradiation profiles, chapter 3 presents the experimental setup, chapters 4 talking about interface engineering role in perovskite solar cells power conversion efficiency and stability under both thermal stress and light exposure, chapter 5 presents solar cells with both high power conversion efficiency and stability based on Cu doping in electron transporting layer, also presents the role of Reduced Graphene Oxide in enhancing the perovskite solar cells performance, chapters 6 presents the optimal performance emulation of perovskite solar cells using the Elephant Herd Algorithm associated with experimental validation, chapter 7 presents energy efficiency improvement of water pumping system operated with Synchronous Reluctance Motor using perovskite solar cells and chapter 8 gives the general conclusions and future work.

References

[1] Roberto Faranda, S.L., *Energy Comparison of MPPT Techniques for PVSystems.* WSEAS Trans. on POWER SYSTEMS, vol. 3, No.6.

[2] V. Salas, E.O., A. Barrado, A. Lazaro, *Review of the Maximum Power Point Tracking Algorithms for Stand-alone Photovoltaic Systems,* Solar Energy Materials and Solar Cells, 2006, p.p 1555–1578.

[3] Hohm, D.P. and M.E. Ropp, *Comparative Study of Maximum powerpoint tracking algorithms,* Progress in Photovoltaics: Research andApplications, 2003, Vol.11, No.1, pp. 47-62.

[4] Nicola Femia, Giovanni Petrone, Giovanni Spagnuolo, and MassimoVitelli, *Optimization of Perturb and Observe Maximum Power PointTracking Method,* IEEE Trans. on Power Electronics, 2005, Vol. 20,NO. 4, p.p. 963-973.

[5] Youngseok, J., et al., *Improved Perturbation and Observation Method (IP&O) of MPPT Control for Photovoltaic Power Systems,* PhotovoltaicSpecialists Conference, IEEE 31st, 2005.

[6] Balamurugan M, Sahoo SK, Sukchai S.Application of soft computing methods for grid connected PV system: A technological and status review. Renewable and Sustainable Energy Reviews. 2017;75:1493-1508.

[7] Jean J, Brown PR, Jaffe RL, Buonassisi T, Bulović V. Pathways for solar photovoltaics. Energy Environ. Sci., 2015,8(4), 1200-1219.

[8] Zhou Y. Eco-and renewable energyMaterials. Springer; 2015.

[9] Kilner JA, Skinner SJ, Irvine SJC, Edwards PP. Functional materials for sustainable energy applications. Elsevier; 2012.

[10] Energy Initiative Massachusetts Institute of Technology. The Future of Solar Energy- an interdisciplinary MIT study. 2015.

[11] Polman A, Knight M, Garnett EC, Ehrler B, Sinke WC. Photovoltaic materials: Present efficiencies and future challenges. Science. 2016;352(6283):aad4424.

[12] http://www.sciencemag.org/news/2013/12/sciences-top-10-breakthroughs-2013.

[13] O'regan B, Grätzel M. A low-cost, high-efficiency solar cell based on dye-sensitized colloidal TiO2 films. Nature 1991;353:737-740.

[14] Docampo P, Ball JM, Darwich M, Eperon GE, Snaith HJ. Efficient organometal trihalide perovskite planar-heterojunction solar cells on flexible polymer substrates. Nat Commun. 2013;4:2761

[15] Lee MM, Teuscher J, Miyasaka T, Murakami TN, Snaith HJ. Efficient Hybrid Solar Cells Based on Meso-Superstructured Organometal Halide Perovskites. Science.2012;338(6107):643-647.

[16] Kim HS, Lee CR, Im, JH, et al. Lead Iodide Perovskite Sensitized All-Solid-State Submicron Thin Film Mesoscopic Solar Cell with Efficiency Exceeding 9%. Sci Rep. 2012;2(591).

[17] Kirchartz T, Bisquert J, Mora-Sero I , Garcia-Belmonte G. Classification of solar cells according to mechanisms of charge separation and charge collection, Phys. Chem. Chem. Phys. 17 (6) (2015) 4007-4014.

[18] Li F, Ma C, Wang H, Hu W, Yu W, Sheikh AD, Wu T. Ambipolar solution-processed hybrid perovskite phototransistors. Nat Commun. (2015).6, 8238

[19] Kulkarni SA, Baikie T, Boix PP, Yantara N, Mathews N, Mhaisalkar S. Band-gap tuning of lead halide perovskites using a sequential deposition process. J. Mater. Chem. A.2014;2(24):9221-9225.

[20] Lu H, Zhang H, Yuan S, Wang J, Zhan Y, Zheng L. An optical dynamic study of MAPbBr3single crystals passivated with MAPbCl3/I3-MAPbBr3 heterojunctions. Phys. Chem. Chem. Phys.2017;19:4516-4521.

[21] Yang XD, Lu C, Wang XX, Wang BL, Ge GX, Wang GH, Wan JG. Tuning spontaneous polarization and optical absorption by intercalating Sr–Cl-layers in organic–inorganic halide perovskite $CH_3NH_3PbI_3$ thin films. J. Mater. Chem. A. 2018;6.

[22] National Renewable Energy Laboratory (NREL), https://www.nrel.gov/pv/cell efficiency.html.

[23] Kaltzoglou A, Elsenety MM, Koutselas I, Kontos AG, Papadopoulos K, Psycharis V, Raptopoulou CP, Perganti D, Stergiopoulos T, Falaras P. Synthesis, characterization and optoelectronic properties of chemically stable $(CH_3)_3SPbI_3$-xBrx and $(CH_3)_3SPbI_3$-xClx (x = 0, 1, 2, 3) perovskite, Polyhedron, 2018; 140: 67-73.

[24] Kontos AG, Manolis GK, Kaltzoglou A, Palles D, Kamitsos EI, Kanatzidis MG, Falaras P. Halogen-NH2+ Interaction, Temperature Induced Phase Transitions and Ordering in $(NH_2CHNH_2)PbX_3$ (X = Cl, Br, I) Hybrid Perovskites. J. Phys. Chem. C., 2020; 124: 8479–8487.

[25] Ralf G. Niemann, Kontos AG, Palles D, Kamitsos EI, Kaltzoglou A, Brivio F,Falaras P, Cameron PJ. Halogen Effects on Ordering and Bonding of CH_3NH^{3+} in $CH_3NH_3PbX_3$ (X = Cl, Br, I) Hybrid Perovskites: A vibrational spectroscopic study. J. Phys. Chem. C. 2016;120: 2509–2519.

[26] Antoniadou M, Siranidi E, Vaenas N, Kontos AG, Stathatos E, Falaras P. Photovoltaic performance and stability of $CH_3NH_3PbI_3$-xClx perovskites. J. Surf. Interfac. Mater. 2014; 2: 323-327.

[27] Fabini DH, Stoumpos CC, Laurita G, Kaltzoglou A, Kontos AG, Falaras P, Kanatzidis MG, Angew RS. Reentrant Structural and Optical Properties and Large Positive Thermal Expansion in Perovskite Formamidinium Lead Iodide. Chem. Int. Ed. 2016; 55:15392-15396.

[28] Konstantakou M, Perganti D, Falaras P, Stergiopoulo T. Anti-Solvent Crystallization Strategies for Highly Efficient Perovskite Solar Cells. Crystals 2017 ;7(10):291.

[29] Balis N, Zaky AA, Perganti D, Kaltzoglou A, Sygellou L, Katsaros F, Kontos AG, Falaras P. Dye Sensitization of Titania Compact Layer for Efficient and Stable Perovskite Solar Cells. ACS Appl. Energy Mater. 2018; 1(11):6161-1671.

[30] Kontos AG, Kaltzoglou A, Arfanis M, McCall KM, Stoumpos CC,Wessels BW, Falarasa P, Kanatzidis MG. Dynamic disorder, band gap widening and persistent near-IR photoluminescence up to at least 523 Kelvin in $ASnI_3$ perovskites (A= Cs+, CH_3NH^{3+} and $NH^{2-}CH=NH^{2+}$)", J. Phys. Chem. C, 2018;122: 26353-26361.

[31] Elsenety M, Maria A, Nikolaos B, Kaltzoglou A, Sygellou L,Stergiou A, Tagmatarchis N, Falaras P,Stability Improvement and Performance Reproducibility Enhancement of Perovskite Solar Cells Following (FA/MA/Cs) PbI_3-xBrx/$(CH_3)_3SPbI_3$ Dimensionality Engineering ACS Applied Energy Materials, 2020;3(3): 2465-2477.

[32] Kontos AG, Manolis GK, Kaltzoglou A, Palles D, Kamitsos EI, Kanatzidis MG, Falaras P.Halogen-NH^{2+} Interaction, Temperature Induced Phase Transitions and Ordering in $(NH_2CHNH_2)PbX_3$ (X = Cl, Br, I) Hybrid Perovskites. J. Phys. Chem. C 2020, 124, 8479-8487.

[33] Vasilopoulou M, Fakharuddin A, Coutsolelos AG, Falaras P, Argitis P,Yusoff ARM, Nazeeruddin MK. Molecular Materials as Interfacial Layers and Additives in Perovskite Solar Cells. Chem. Soc. Rev., 2020.

[34] Balis N, Zaky AA, Athanasekou C, Silva AMT, Sakellis E, Vasilopoulou M, Stergiopoulos T, Kontos AG, Falaras P. Investigating the role of reduced graphene oxide

as a universal additive in planar perovskite solar cells. J. Photochem. Photobio. A. 2020;386.

[35] Zaky AA, El Sehiemy RA, Rashwan YI, Elhossieni MA, Gkini K, Kladas A, Falaras P. Optimal Performance Emulation of PSCs using the Elephant Herd Algorithm Associated with Experimental Validation.The Electrochemical Society.2019;8(12):249-255.

[36] Zaky AA, Balis N, Gkini K, Athanasekou C, Kaltzoglou A, Stergiopoulos T, Falaras P. Dye Engineered Perovskite Solar Cells under Accelerated Thermal Stress and Prolonged Light Exposure. Chemistry Select. 2020;5(1), 4454-4462.

[37] Patil JV, Mali SS, Patil AP, Patil PS, Hong CK. Highly efficient mixed-halide mixed-cation perovskite solar cells based on rGO-TiO_2 composite nanofibers. Energy. 2019;189,116396.

[38] Liao T, He Q, Xu Q, Dai Y, Cheng C, Ni M. Performance evaluation and optimization of a perovskite solar cell-thermoelectric generator hybrid system. Energy; 2020;201, 117665.

[39] Billen P, Leccisi E, Dastidar S, Li S, Lobaton L, Spatari S, Fafarman AT, Fthenakis VM, Baxter JB. Comparative evaluation of lead emissions and toxicity potential in the life cycle of lead halide perovskite photovoltaics. Energy, 2019;166:1089-1096.

[40] Nkele AC, Nwanya AC, Shinde NM, Ezugwu S, Maaza M, Shaikh JS, Ezema FI. The use of nickel oxide as a hole transport material in perovskite solar cell configuration: Achieving a high performance and stable device. Int J Energy Res. 2020;1– 25.

[41] Zheng H, Li C, Wei A, Liu J, Zhao Yu, Xiao Z. Study of carbon-based hole-conductor-free perovskite solar cells, International Journal of Hydrogen Energy. 2018;43(24): 11403-11410.

[42] Wang M, Yang J, Chi B, Pu J, Li J. High performance Ni exsolved and Cu added La0.8 $Ce_{0.2}Mn_{0.6}Ni_{0.4}O_3$-based perovskites for ethanol steam reforming. International Journal of Hydrogen Energy. 2020;45(33):16458-16468.

[43] Rahul, Bhattacharya B, Singh PK, Singh R, Khan ZH. Perovskite sensitized solar cell using solid polymer electrolyte. International Journal of Hydrogen Energy. 2016;41(4):2847-2852.

[44] Ansón-Casaos A, Hernández-Ferrer J, Vallan L, Xie H, Lira-Cantú M, Benito AM, Maser WK. Functionalized carbon dots on TiO_2 for perovskite photovoltaics and stable photoanodes for water splitting. International Journal of Hydrogen Energy.2020.

[45] Yang CJ, Chen PT, Huang KD. The optimization of electrolyte flow management to increase the performance of Zn–air fuel cells. Int.J.Energy.Res. 2020; 44: 4224-4234.

[46] Qi Y, Li X, Li S, Li T, Espinoza-Andaluz M, Tunestål P, Andersson M. Temperature control strategy for polymer electrolyte fuel cells. Int .J .Energy .Res. 2020; 44: 4352-4365.

[47] Sangeetha T, Yang CJ, Chen PT, Yan WM, Huang KD. Discharge performance of Zn-air fuel cells under the influence of Carbopol 940 thickener. Int.J.Energy Res. 2020; 44: 4543-4555.

[48] Vijaykumar V, Nirala G, Yadav D, Kumar U, Upadhyay S. Sucrose-nitrate auto combustion synthesis of $Ce_{0.85}Ln_{0.10}Sr_{0.05}O_{2-\delta}$ (Ln = La and Gd) electrolytes for solid oxide fuel cells. Int.J.Energy Res. 2020; 44: 4652–4663.

2 Chapter 2

2 Solar Energy Application in Electric Power System

2.1 Solar energy

Now renewable energy sources become a very important source of electric power generation. There are many types of renewable energy sources that can be used for electric power generation, for instance solar energy, wind energy, Tidal Energy etc. Solar PV energy is used in a wide range as a source of electrical energy. PV arrays which consist of series and parallel modules are used for direct transformation of solar irradiation to electric energy. Figure 2.1 shows the solar PV global capacity where, it is clear that the solar energy increased every year and recently the rate of increasing is high. Figure 2.2 presents the annual solar PV installed capacity and revenue by region world markets.

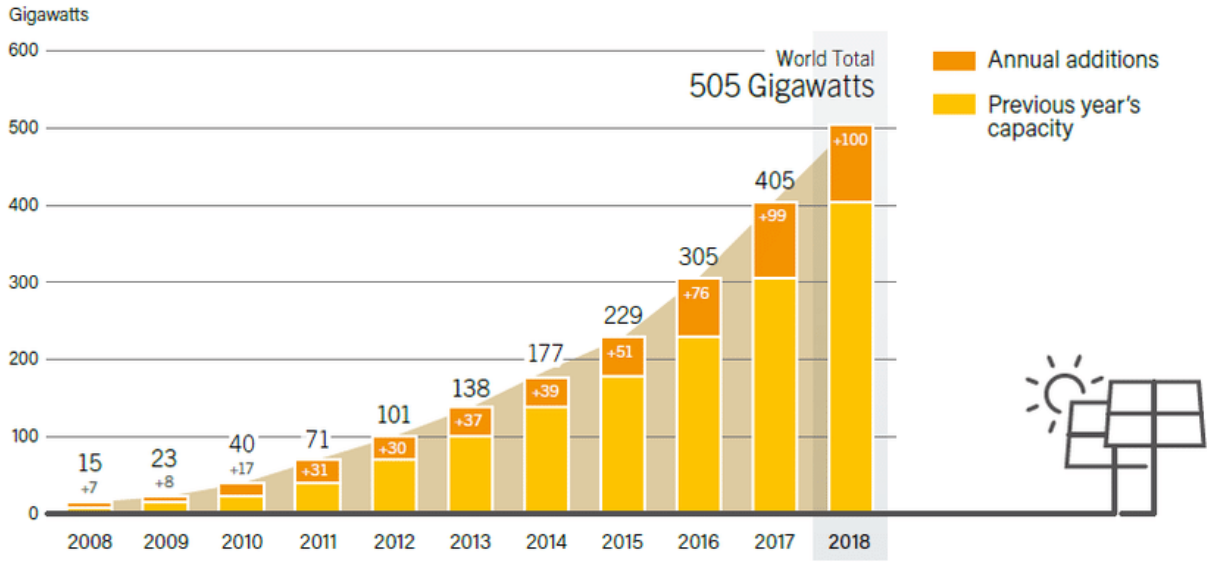

Figure 2.1 Solar PV global capacity (2008-2018)

During the last decades, PV systems have gained a lot of interest because they constitute available free fuel cost and not polluting sources of energy, contrary to fossil fuels.

Moreover, PV technology is growing more and more, making great progress towards meeting the continuously increasing world energy demands. Furthermore, they can used as in off line (isolated) mode to supply remote area loads (houses...etc.), desert irrigation applications or in on line grid connected mode. The PV systems are used as energy generation plants, called distributed generations both in small or large power scale. Due to the high initial installation cost of PV systems, solar irradiation intensity changes due to weather conditions, namely temperature and shading conditions. Thus, a Maximum Power Point Tracker (MPPT) integrated within PV systems is essential to make sure that PV systems work in the optimum operating condition.

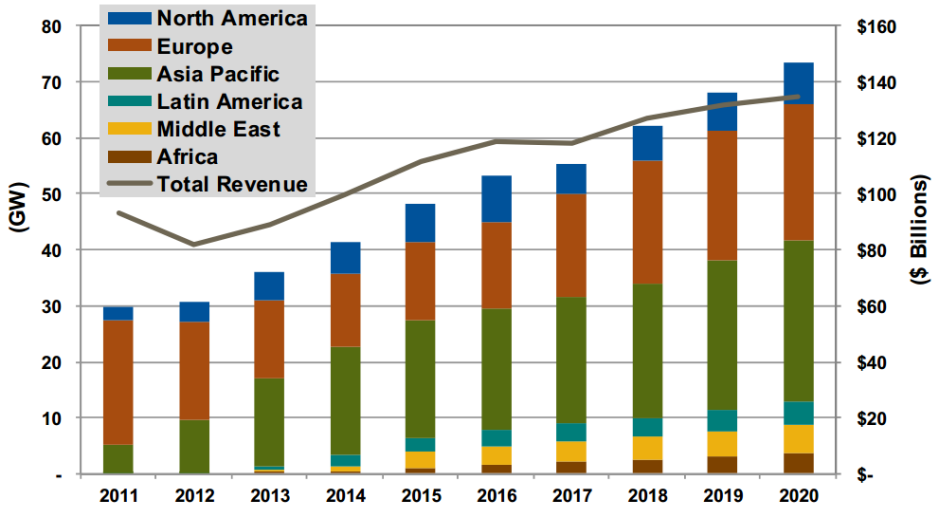

Figure 2.2 Annual solar PV installed capacity and revenue by region world markets: 2011-2020

2.2 Types of PV cells

There are three generations of solar energy and different types of solar cells which differ in their material, price, and efficiency till the moment. These generations are shown in Figure 2.3.

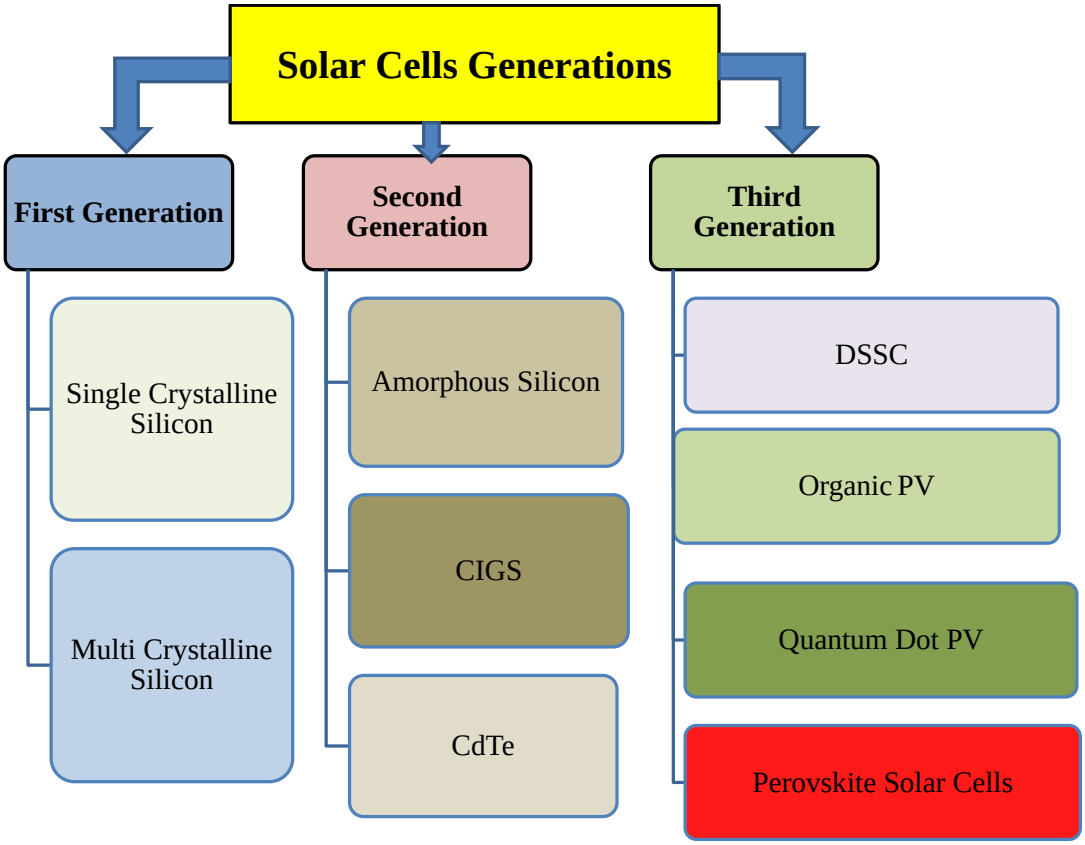

Figure 2.3 The solar cells generations

2.2.1 First generation

2.2.1.1 Silicon solar cells principle of operation

Semiconductors have four electrons in the outer shell called valence electrons [1]. Sunlight hits the photovoltaic cells; the absorbed energy into the semiconductor allows the valence electrons to flow freely. The electrons flow is a current as shown in Figure 2.4.

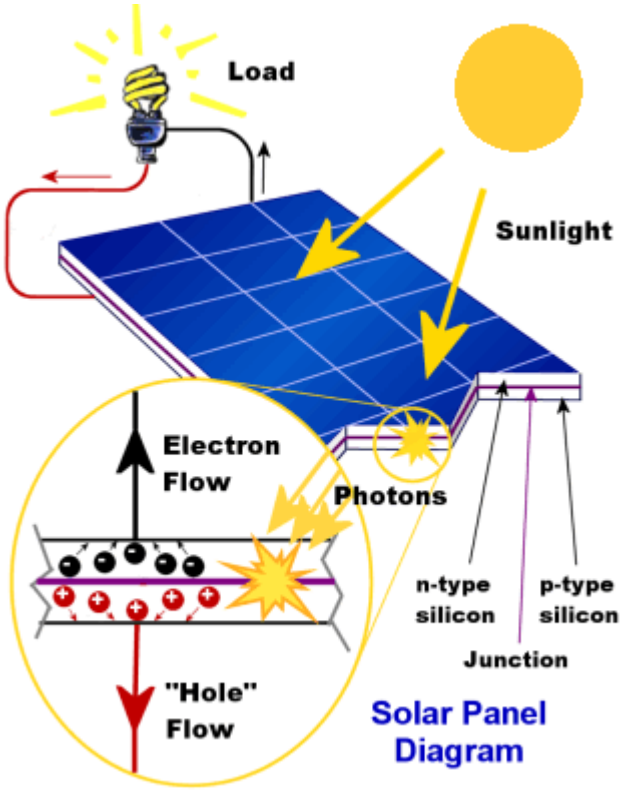

Figure 2.4 Photovoltaic cells principle of operation

2.2.1.2 Mono-crystalline Solar cells:

This type has the highest efficiency in absorbing sunlight and converting it into electricity among the first generation types. This type is made from a large silicon crystal; its form is shown in Figure 2.5. It performs in a good way better in lower light conditions than the other types of solar cells but, it is the most expensive type in the first generation. Its efficiency is around 15% - 18% with 25% as maximum efficiency.

Figure 2.5 Mono-crystalline Solar Panels

2.2.1.3 Polycrystalline Solar cells

This type of solar cell is different from the Mono-crystalline type as it consists of multiple amounts of smaller silicon crystals as shown in Figure 2.6. This type has efficiency approximately equal to 15% with 20% as maximum efficiency.

Figure 2.6 Polycrystalline Solar Panels

2.2.2 Second generation (Thin Films):

2.2.2.1 Amorphous Solar cells

This type is as shown in Figure 2.7 it consisting of a thin-like film which fabricated from molten silicon spread directly across large plates of stainless steel or similar materials. This type has an advantage over the other two types of this generation is that it is shadow protected.[2, 3]

As a result when a part of the panel made from this type is in a shadow the solar panel continues to give output. However, this type of solar panel has lower efficiency than the other two types in this generation; it is the cheapest to produce. The efficiency of this type is around 8-10% with 13% as maximum efficiency.

2.2.2.2 CdTe (Cadmium Telluride)

CdTe has a high light absorptivity level, only about a micrometer thick can absorb 90% of the solar spectrum. While, the instability of CdTe cell performance is the major drawback of using CdTe for solar cell and it is a toxic substance. The energy conversion efficiency for CdTe solar cell is about 18%.

2.2.2.3 CIGS (Copper Indium Gallium Selenium)

This type of thin film technology gained attention because CIGS has the highest research energy conversion efficiency of 17.7% in 1996.

Figure 2.7 Amorphous solar panels

2.2.3 Third generation

This generation is low cost and high efficient generation of solar cells it contains some types like DSSC (Dye-sensitized solar cells), QDSSC (Quantum Dot-sensitized solar cells), OPV (Organic photovoltaics), QDs-Polymer Hybrid solar cells and perovskite solar cells. The most efficient and economic type of them is the perovskite solar cells which is the main topic of this thesis.

2.2.3.1 Perovskite solar cells:

The crystal structure of perovskites (AMX_3), typically consists of a unit cell with five atoms in a cubic structure (α phase), in which the cation *A* has twelve nearest neighboring anions *X* and the cation M has six as shown in Figure 2.8. Under ideal conditions, in order to maintain high –symmetry cubic structure, the tolerance factor t should be close to 1. The tolerance factor *t* is expressed as a function of ionic radii of *A, M* and *X* site ions, which is written as

$$t = \frac{RA+RX}{sqrt\,(2(RM+RX))}$$

where, *R*A, *R*M, and *R*X are the ionic radii of the corresponding ions. Larger the deviation from the ideal value t, the crystal structure will be distorted and the symmetry would be lowered. Therefore, in order to satisfy the ideal tolerance factor (t ≈ 1), the A-site ion must be much larger than the M-site ion.

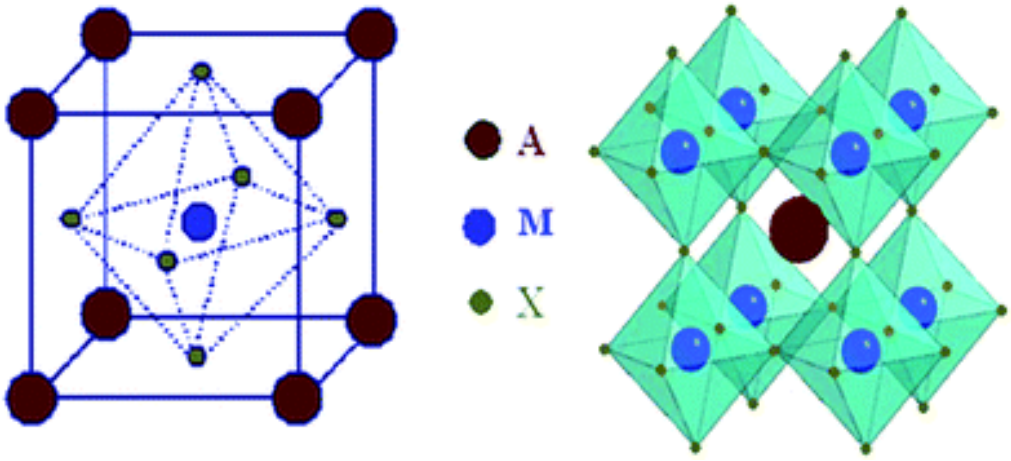

Figure 2.8 Perovskite crystal structure

The device structure, related materials, and interfacial modification are key factors in the performance of perovskite solar cells (PSCs).

PSCs have two typical structures can be constructed: a) mesoscopic nanostructure and b) planar structure as shown in Figure 2.9.

Mesoporous TiO_2 layer usually is used to collect the electrons while, organic Hole transporting material (HTM) collects the holes. Planar structure has simpler structure and higher efficiency. Another type of PSCs appeared recently called inverted perovskite solar cells this type is shown in Figure 2.10. PSCs appeared in 2009 with 3% efficiency and reached to 25.2% efficiency in 2019 as shown in Figure 2.11.

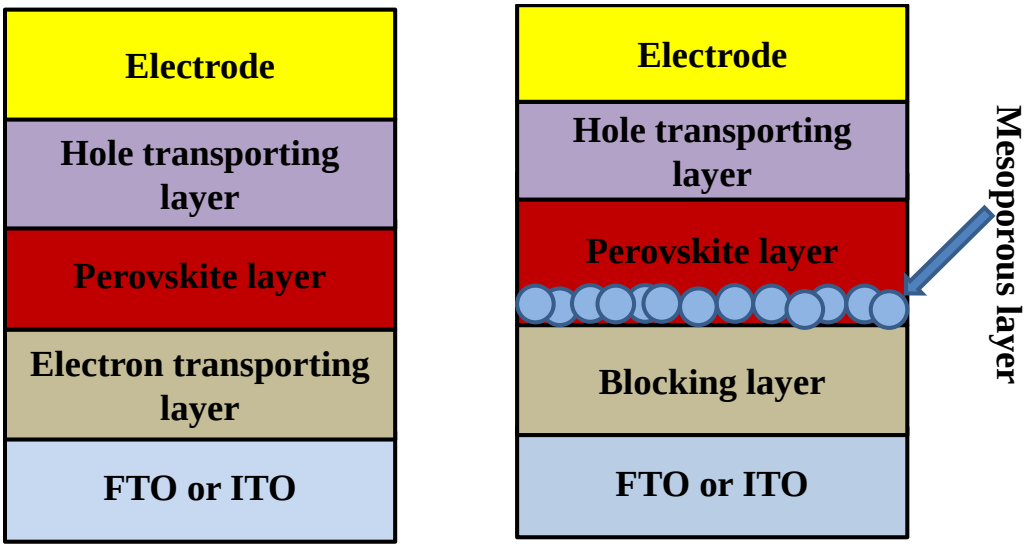

Figure 2.9 Perovskite solar cells structure, planar (left) and mesoporous (right)

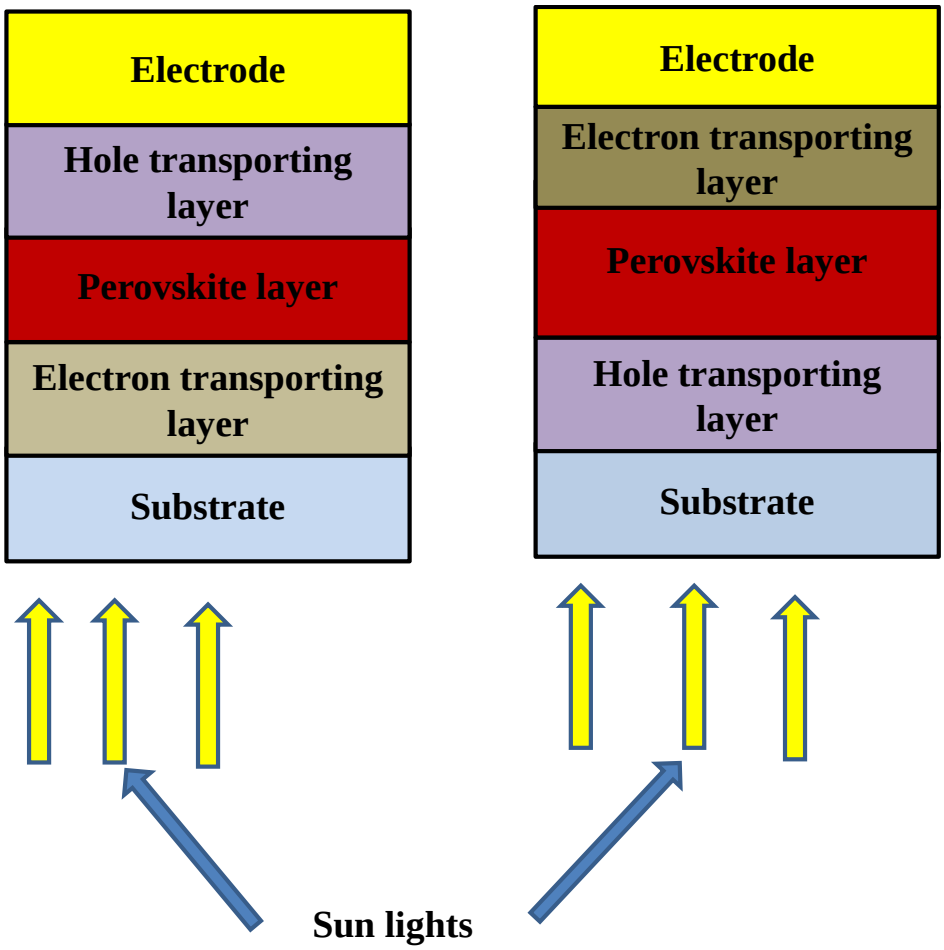

Figure 2.10 Perovskite solar cells structure, planar (left) and inverted (right)

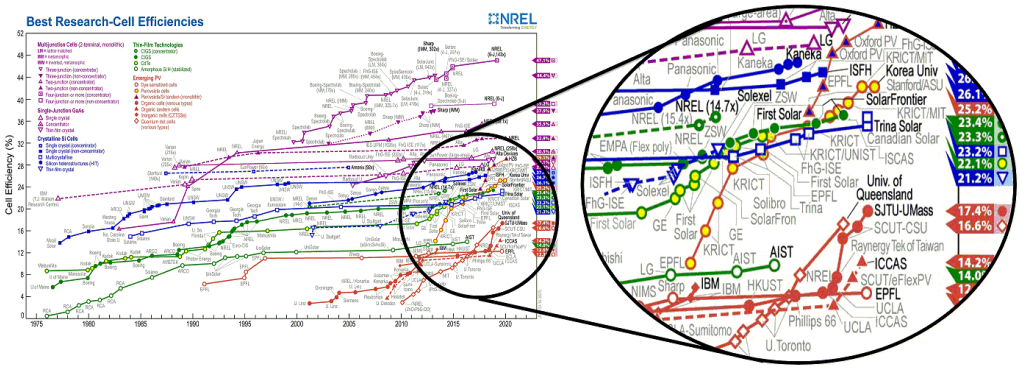

Figure 2.11 Best research cell efficiencies till 2020

2.3 Equivalent circuit and mathematical model

The performance of PV was evaluated using the electrical models (single, double and three diode models). Generally, the rectification of characteristics of solar cells including heterojunctions and perovskites can be described by the Shockley diode equation [4], [5] as:

$$j_d = j_{d0}\left[\exp\left(\frac{qV}{(m \cdot k \cdot T}\right) - 1\right] \tag{1}$$

where, j_d is the dark current, V is the applied voltage, j_{d0} the reverse saturation current density, q is the elementary charge, m is the ideal factor of the cell, K is the Boltzmann constant, T is the absolute temperature.

The ideal model is considered as a single PN junction (diode) in parallel with photo current j_{ph} . Eq. 2 presents the mathematical expression for the ideal model [6] as:

$$j = j_{ph} - j_{d0}\left[\exp\left(\frac{qV}{(m \cdot k \cdot T}\right) - 1\right] \tag{2}$$

where, j_{ph} is the photocurrent and j is the output current.

In practice, there are different electrical models were presented in the literature to model PV cells as shown in Figure 2.12. In Figure 2.12.a the solar cell can be modelled by using single PN junction (diode model). In this model, the solar cell is represented by a current source, two resistances and a diode. The current source represents the I_{ph} which is sensitive to solar radiation change and ambient temperature. The series resistance represents all resistances in the current path, electrode resistance, material bulk resistance and contact resistance. The shunt resistance represents the leakage current across the p-n junction.

Applying Kirchhoff's current law (KCL), it is obvious that the output current j can be represented by Eq.3 [7] as:

$$j = j_{ph} - j_{d0}\left[\exp\left(\frac{q(V + R_s.j)}{m \cdot k \cdot T}\right) - 1\right] - \frac{V_t + R_s.j}{R_{sh}} \quad (3)$$

where, R_s and R_{sh} are the series and shunt resistance, respectively.

It can be generalized the single diode model for solar cell to the two diode model as Eq.4 to consider the effect of recombination losses in the space charge region (SCR) and expresses it an additional diode beside the first diode which represents the recombination and diffusion in the quasi neutral regions(QNRs) was added [8] as:

$$j = j_{ph} - j_{d1}\left[\exp\left(\frac{q(V + R_s.j)}{(m_1) \cdot k \cdot T}\right) - 1\right] - j_{d2}\left[\exp\left(\frac{q(V + R_s.j)}{(m_2) \cdot k \cdot T}\right) - 1\right] - \frac{V + R_s.j}{R_{sh}} \quad (4)$$

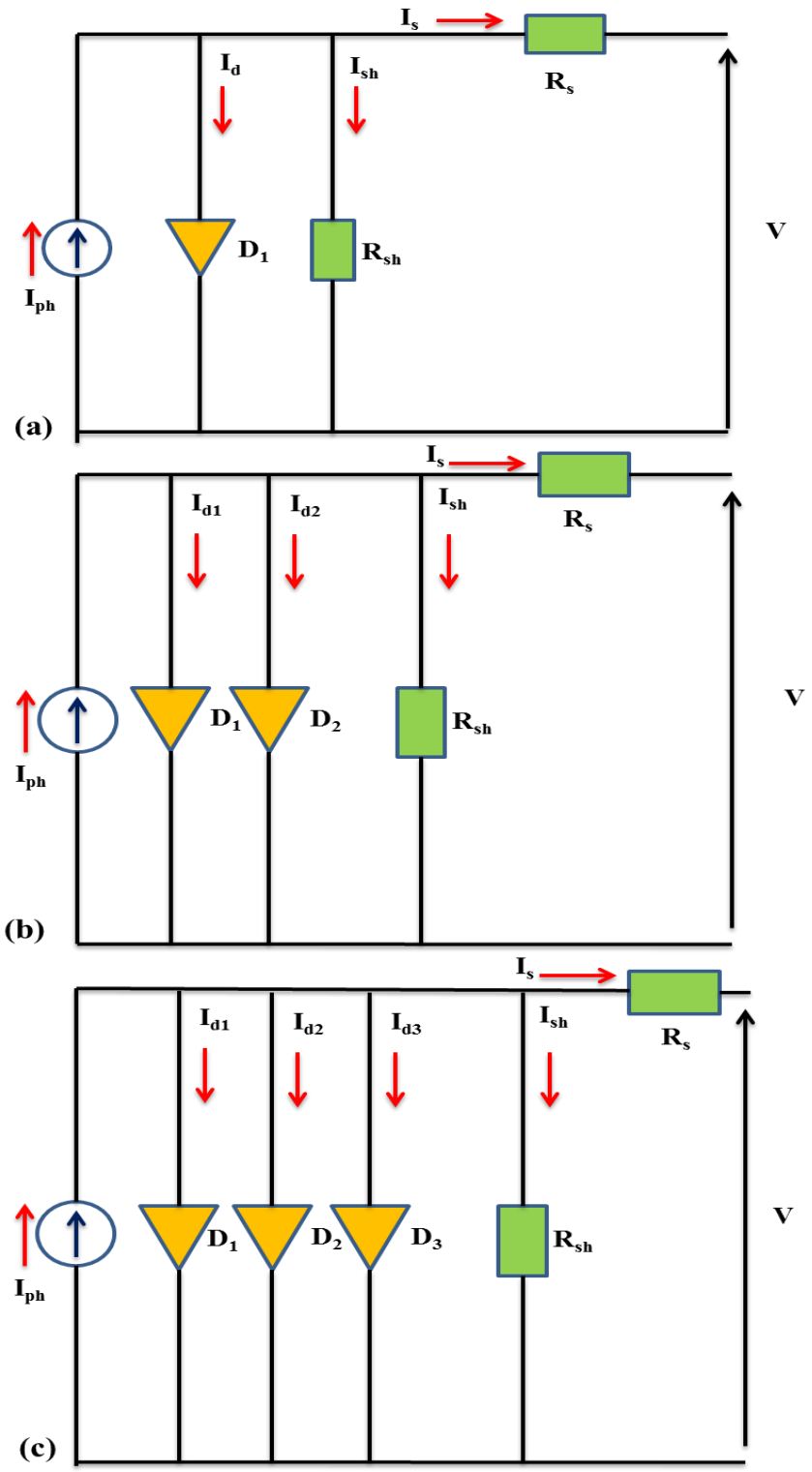

Figure 2.12 Solar cell model a) single diode model b) double diode model c) triple diode model

Also, the solar cell can be extended to triple diode model as in Figure 2.12.c and Eq.5 to include the effect of grain boundaries and leakage current which is considered by adding a third diode to the double diode PV model with the same physical meaning like the two diode model [9] as:

$$j = j_{ph} - j_{d1}\left[\exp\left(\frac{q(V + R_s.j)}{(m_1)\cdot k\cdot T}\right) - 1\right] - j_{d2}\left[\exp\left(\frac{q(V + R_s.j)}{(m_2)\cdot k\cdot T}\right) - 1\right] - j_{d3}\left[\exp\left(\frac{q(V + R_s.j)}{(m_3)\cdot k\cdot T}\right) - 1\right] - \frac{V + R_s.j}{R_{sh}} \quad (5)$$

2.4 PV characteristics

Figure 2.13 shows the I-V and P-V characteristics of the PV module at constant irradiation and constant temperature while Figure 2.14 shows the I-V and P-V characteristics of the PV module at different irradiances and constant temperature (25°C) and Figure 2.15 shows the I-V and P-V characteristics of the PV module under constant irradiance and different temperature. Figure 2.16 shows the effect of series and shunt resistances on the PV characteristics.

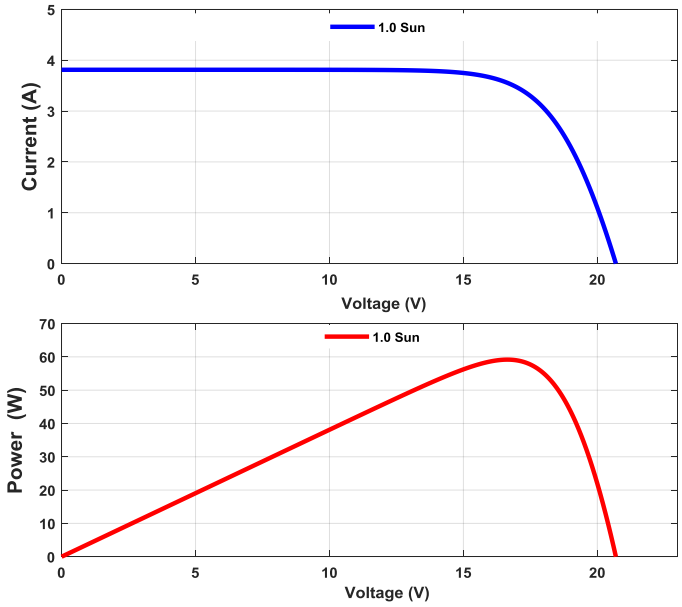

Figure 2.13 The I-V (up) and P-V (down) characteristics of the PV module at constant irradiation and constant temperature

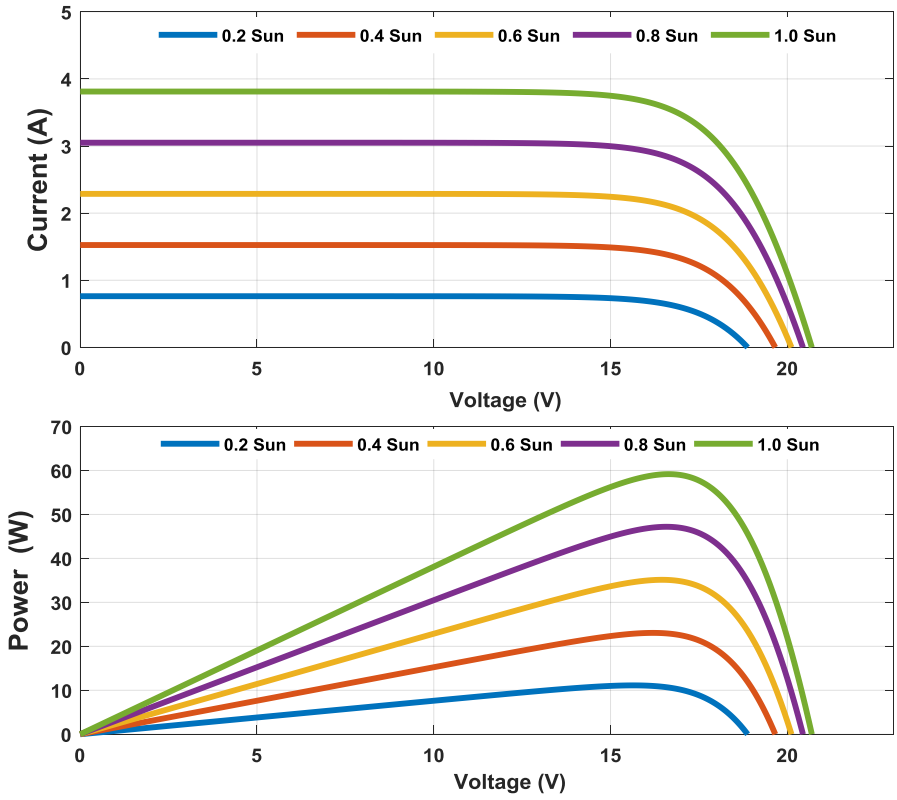

Figure 2.14 The I-V and P-V characteristics of the PV module at different irradiances and constant temperature (25°C)

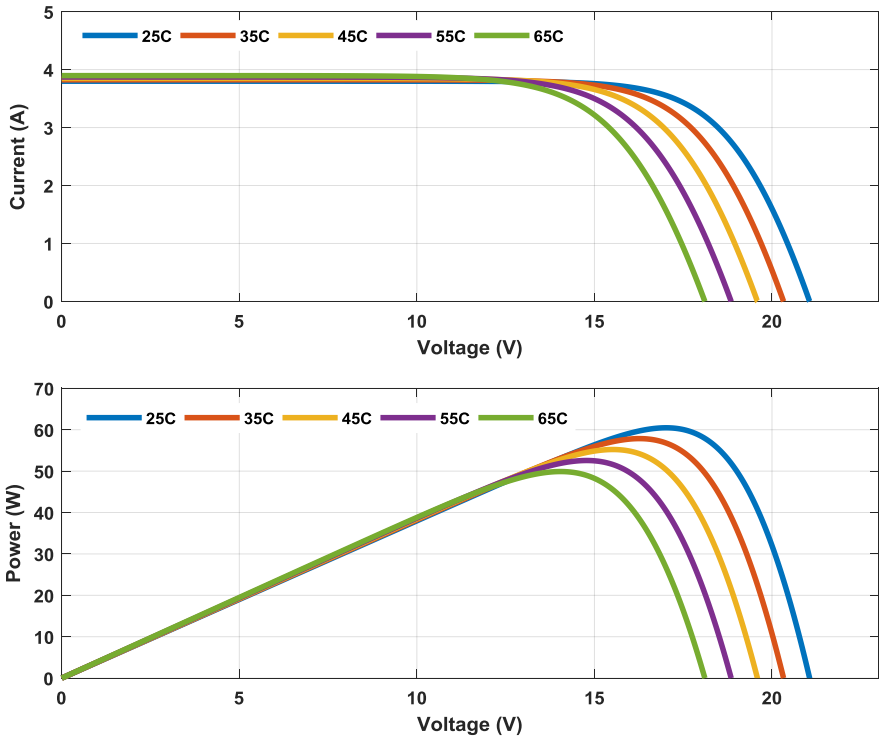

Figure 2.15 The I-V and P-V characteristics of the PV module under constant irradiance and different temperature

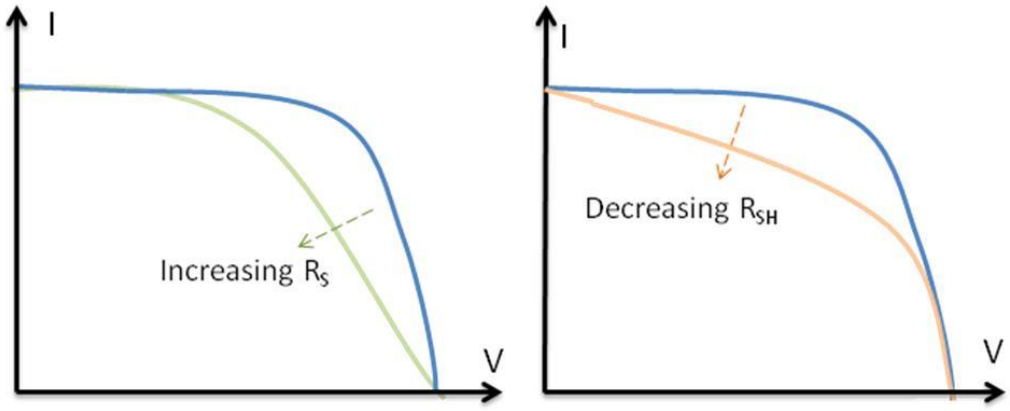

Figure 2.16 The effect of series and shunt resistances on the PV characteristics

2.5 PV applications in power system

A photovoltaic system can be used as solar farms generating hundreds of megawatts [10] or small residential rooftop systems generating a few kilowatts. This variation in the PV output is due to its modules are scalable.

2.5.1 Effect of Incorporating Photovoltaics as a Generation Units on Unit Commitment Problem

This section deals with the unit commitment (UC) problem in case of incorporating photovoltaic (PV) units in the unit commitment problem of power system. The unit commitment problem in case of considering the contribution of PV units, aims to determine the start-up/shut-down status as well as the amount of generating power for all thermal units at minimum operating cost during the scheduling horizon, subject to the system and unit operational constraints.

2.5.1.1 Formulation of unit commitment problem (Conventional Unit Commitment problem)

Unit commitment is an optimization problem of determining the schedule of generating units within a power system with a number of constraints.The objective of the UC problem is to minimize the total operating costs subjected to a set of system and unit constraints over the scheduling horizon.

$$F = \sum_{i=1}^{ng} \sum_{t=1}^{t=T} F(P_{it}) U_{it} + SUC_{it} U_{it} (1 - U_{it-1}) + SDC_{it} U_{it-1} (1 - U_{it}) \qquad (2\text{-}1)$$

where, F, Total cost of generation ($), ng Number of generator units, T Number of hours U_{it} On/off status of generator i at hour, $F(P_{it})$ Production cost of unit i in time period t ($), SUC_{it} Start-up cost for unit i in time period t ($) and SDC_{it} Shut-down cost of unit i at time period t, ($) .

The generator fuel-cost function can be expressed as:

$$F(P_{it}) = a_i + b_i.P_{it} + c_i.P_{it}^2 \qquad (2\text{-}2)$$

where, a_i, b_i and c_i are the unit cost coefficients.

Subject to:

Demand Constraint:

Sum of Power generated from thermal units = Load demand

System spinning reserve requirements

An appropriate spinning reserve is required for the stable and reliable operation

Sum of maximum power generated by thermal units ≥ Load demand+ spinning reserve

Power generation and reserve limits:

$$P_{i\min} \le P_{(i,t)} \le P_{i\max} \qquad \text{i=1,…,N} \qquad (2\text{-}3)$$

$$0 \le R_{(i,t)} \le P_{i\max} - P_{i\min} \quad \text{i=1,…,N} \qquad (2\text{-}4)$$

Minimum Up and Down time Constraints:

$$[X^{on}_{(i,\,t-1)} - T_i^{on}][\,U_{(i,\,t-1)} - U_{it}\,] \ge 0 \qquad (2\text{-}5)$$

$$[X^{off}_{(i,\,t-1)} - T_i^{off}][U_{it} - U_{(i,\,t-1)}] \ge 0 \qquad (2\text{-}6)$$

Start-up cost is calculated from (7)

$$SUC_{it} = \begin{cases} HSC_i, & X^{off}_{(i,\,t-1)} \le T_i^{off} + CH_i \\ CSC_i, & X^{off}_{(i,\,t-1)} > T_i^{off} + CH_i \end{cases} \qquad (2\text{-}7)$$

where, Pi_{min} Minimum limit of generator i, MW, P_{it} Power generation of unit i at hour t, MW, Pi_{max} Maximum limit of generator i ,MW, R_{it} Reserve generation of unit i at hour, t MW, $X^{on}_{(i,t-1)}$ Time duration for which unit i has been on-time at hour t, T_i^{on} Minimum-on time of unit i (hr), $X^{off}_{(i,t-1)}$ Time duration for which unit i has been off-time at hour t, T_i^{off} Minimum off-time of unit i (hr), HSC_i Hot start-up cost for unit i, ($), CH_i Cold start hour (hr) at unit i and CSC_i Cold start-up cost for unit i, ($).

The system power balance

$$PG_{i\,t} - PD_{it} = V_{it}\, V_{jt} \sum (G_{ij}\, CosB_{ij} + B_{ij}\, SinB_{ij}) \qquad (2\text{-}8)$$

$$QG_{it} - QD_{it} = V_{it}\, V_{jt} \sum (G_{ij}\, SinB_{ij} - B_{ij}\, CosB_{ij}) \qquad (2\text{-}9)$$

where, PG_{it}, QG_{it} are the active and reactive power generation at bus (i) at time (t) respectively. PD_{it}, QD_{it} are the active and reactive power demand at bus (i) at time (t) respectively. G_{ij}, B_{ij} - Conductance and susceptance between bus (i) and bus (j) respectively. V_{it} - Voltage magnitude of bus (i) at time (t) pu.

To guarantee secure operation of units and network, terms like voltage constraints and power flow constraints are used.

$$V_{min} < V < V_{max} \qquad (2\text{-}10)$$

$$PF_{it} \leq PF_{imax} \qquad (2\text{-}11)$$

where, V_{min} and V_{max} - minimum and maximum voltage magnitude limit at bus i (pu), respectively. PF_{it} - Power flow through branch i at time t (MVA), PF_{imax} - Maximum flow limits for branch i (MVA).

2.5.1.2 Unit Commitment problem with PV Generation Units

$$F = \sum_{i=1}^{ng}\sum_{t=1}^{t=T}[F(P_{it})U_{i,t} + SUC_{it}\{U_{i,t}(1-U_{i,t-1})\} + SDC_{it}\{U_{i,t-1}(1-U_{i,t})\} + \sum_{t=1}^{t=T} C_{PVj}] \quad (2\text{-}12)$$

C_{PVj} Includes the capital cost, the replacement cost of operation and the maintenance cost, which is expressed as

$$C_{PV} = P_{PV} * (C_{cap}^{PV} + C_{\mathrm{Re}\,p}^{PV} + C_{om}^{PV}) \quad (2\text{-}13)$$

All the above equations in conventional unit commitment problem are valied in the case of incorporating PV units in the unit commitment problem but the demand constraint changed to be sum of power generated from thermal units + Sum of power from solar units = Load demand in order to take into account the PV units output. Also the spinning reserve constraint is changed to be the sum of maximum power generated by thermal units + Sum of power from solar units ≥ Load demand+ spinning reserve.

2.5.1.3 Case studies

2.5.1.3.1 Case of 10-unit 24-hour test system

Tables 2-1, 2-2 and Figure 2-17 illustrate the data of this system. This system has a total capacity of 1662 MW and peak and minimum load of 1500 and 700 MW, respectively. The PV generation unit (unit 11) capacity is assumed to be 45 MW. Figure 2-18 shows the generation units status without PV units while, Figures 2-19 and 2-20 give the power in MW from each unit at each hour to fed the load. Figure 2-21 presents the generation units status with PV unit. Figures 2-22 and 2-23 show the power in MW from each unit at each hour to feed the load in the presence of PV unit. The total production costs equal 445285.2$ with a 21.04% reduction from the case without PV unit.

Table 2-1 Cost Coefficients, Unit Characteristics of 10- unit system

Gen No	Max MW	Min MW	a ($/hr)	b ($/MW.hr)	C ($/MW^2.hr)	Min uptime(hr)	Min down time (hr)	Cold start (hr)	Initial unit status	Hot startup cost($)	Cold starup cost($)
1	455	150	0.00048	16.19	1000	8	8	5	8	4500	9000
2	455	150	0.00031	17.26	970	8	8	5	8	5000	10,000
3	130	20	0.002	16.6	700	5	5	4	-5	550	1100
4	130	20	0.00211	16.5	680	5	5	4	-5	560	1120
5	162	25	0.00398	19.7	450	6	6	4	-6	900	1800
6	80	20	0.00712	22.26	370	3	3	2	-3	170	340
7	85	25	0.00079	27.74	480	3	3	2	-3	260	520
8	55	10	0.00413	25.92	660	1	1	0	-1	30	60
9	55	10	0.00222	27.27	665	1	1	0	-1	30	60
10	55	10	0.00173	27.79	670	1	1	0	-1	30	60

Table 2-2 10-Units load pattern

Hour(hr)	**1**	**2**	**3**	**4**	**5**	**6**	**7**	**8**
Load(MW)	700	750	850	950	1000	1100	1150	1200
Hour(hr)	**9**	**10**	**11**	**12**	**13**	**14**	**15**	**16**
Load(MW)	1300	1400	1450	1500	1400	1300	1200	1050
Hour(hr)	**17**	**18**	**19**	**20**	**21**	**22**	**23**	**24**
Load(MW)	1000	1100	1200	1400	1300	1100	900	850

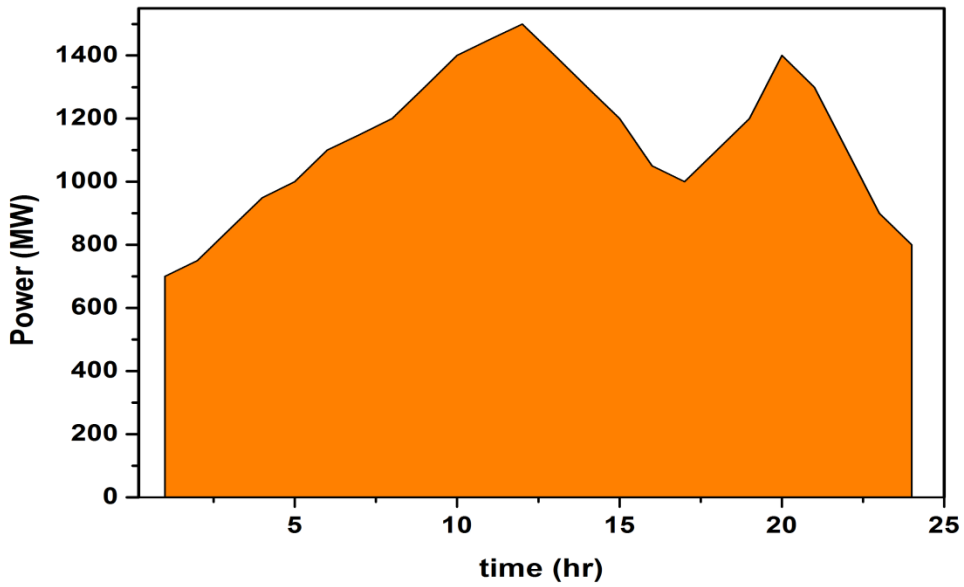

Figure 2.17 10 units load profile

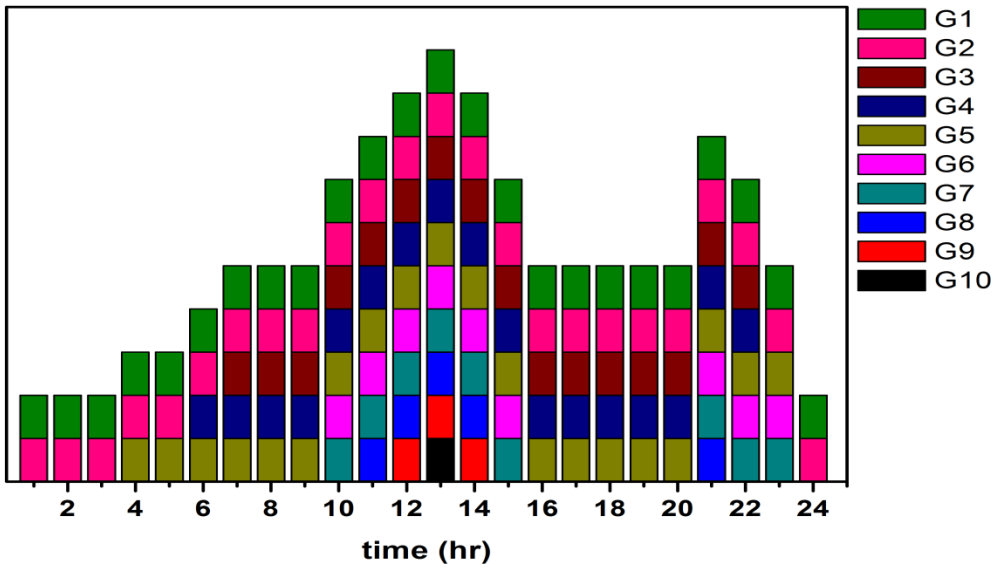

Figure 2.18 10 units on off status

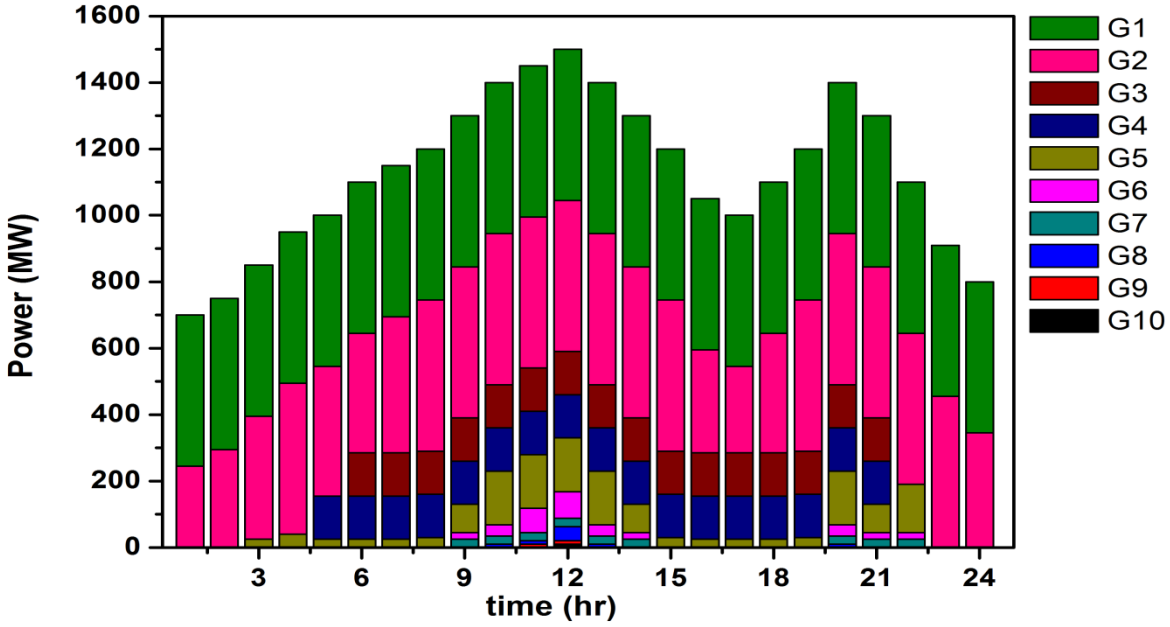

Figure 2.19 10 units output power

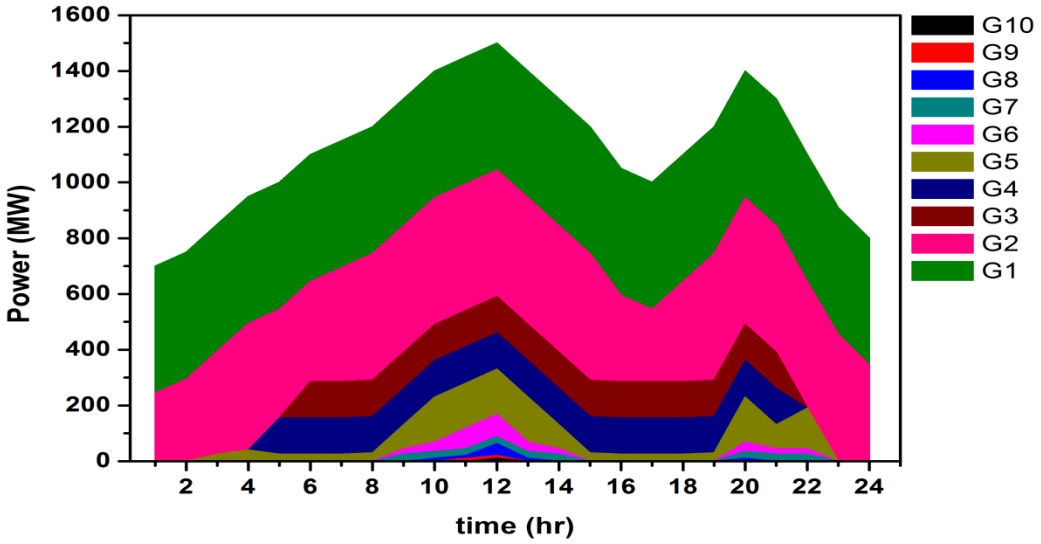

Figure 2.20 10 units out put power profile

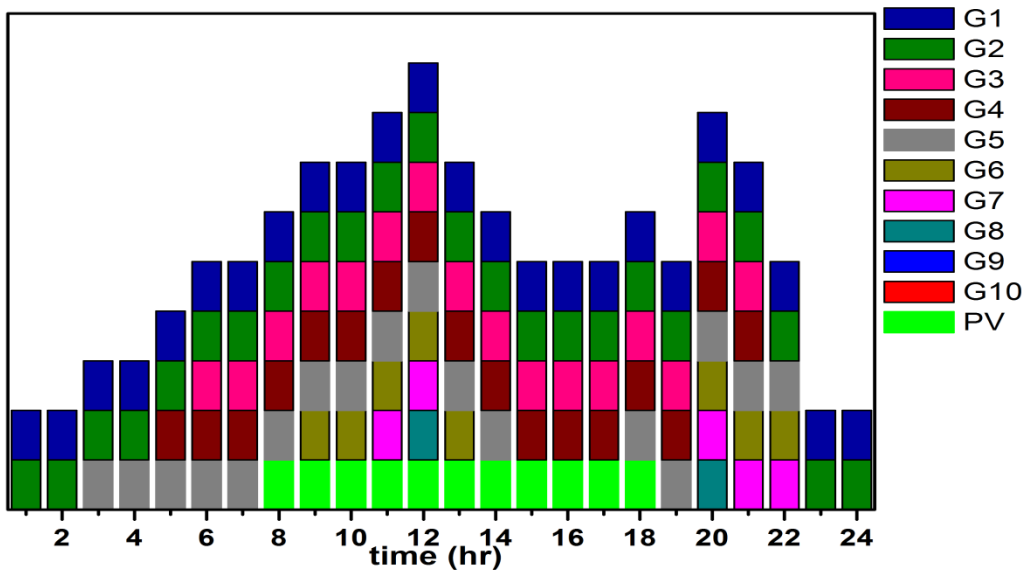

Figure 2.21 10 units on off status in the presence of PV unit

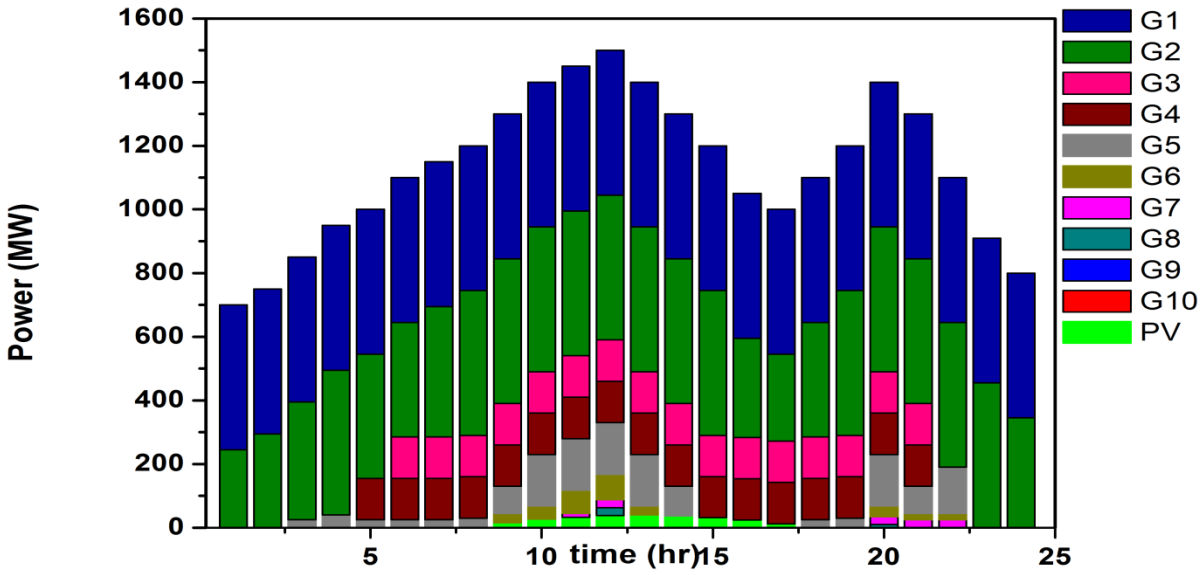

Figure 2.22 10 units output power in the presence of PV unit

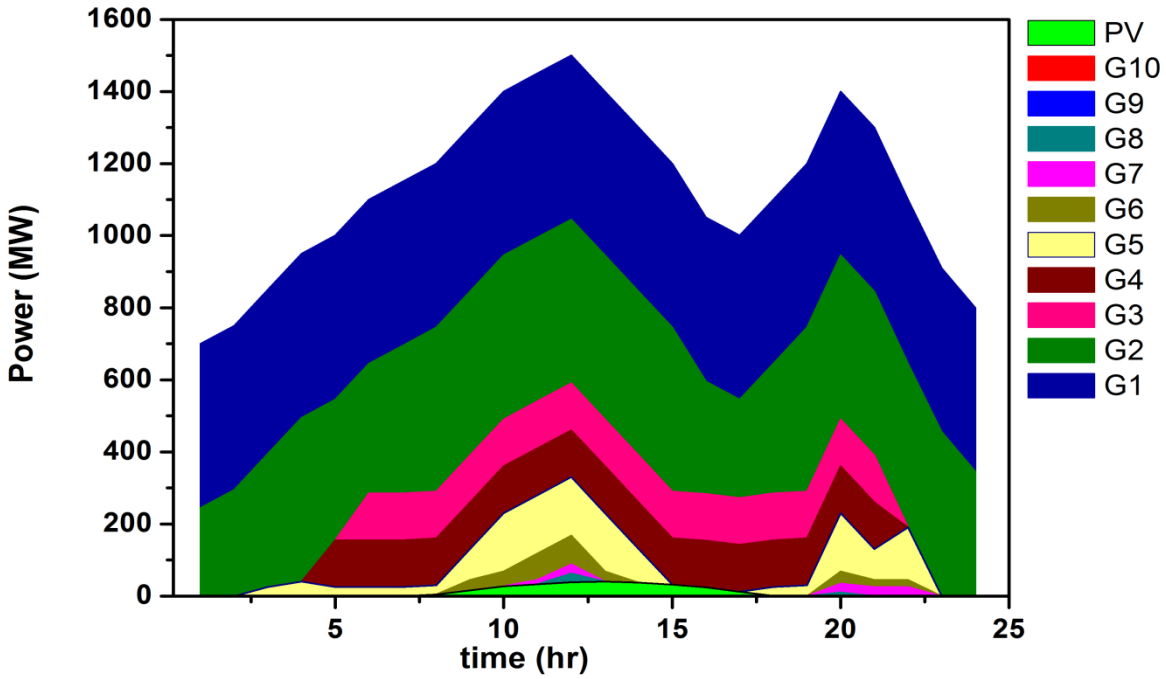

Figure 2.23 10 units output power profile in the presence of PV unit

2.5.1.3.2 IEEE 30 bus test system

The single line diagram of the system is shown in Figure 2-24 while, Tables 2-3 and 2-4 and Figure 2-25 show the data for standard IEEE 30 bus test system. The single line diagram of this system is shown in Figure 2-26. The PV generation unit (unit 7) capacity is assumed to be 30 MW. Figure 2-27 shows the generation units status without PV units while, Figures 2-28 and 2-29 give the power in MW from each unit at each hour to feed the load. Figure 2-30 shows the IEEE 30 bus test system maximum and minimum voltage with time where it is clear that the voltage is within limit. Figure 2-31 presents the generation units status with PV unit. Figures 2-32 and 2-33 show the power in MW from each unit at each hour to fed the load in the presence of PV unit. Figure 2-34 shows the IEEE 30 bus test system in the presence of PV unit maximum and minimum voltage with time where it is clear that the voltage is within limits which is betwwen 1.05 and 0.95 PU. The total production costs equal 10797$ with reduction 18.12 % from the case without PV unit which is 13187$.

Table 2-3 Cost, Emission Coefficients, Unit Characteristics of IEEE 30 Bus system

Gen No	Max MW	Min MW	Ramp level MW/hr	a ($/hr)	b ($/MW.hr)	C ($/MW^2.hr)	Min uptime (hr)	Min down time (hr)	Shut down cost($)	Cold start (hr)	Initial unit status	Hot startup cost($)	Cold starup cost($)
1	200	50	50	0.00375	2.0	0	1	1	50	2	-1	70	176
2	80	20	20	0.01750	1.7	0	2	2	60	2	-3	74	187
3	50	15	13	0.06250	1.0	0	1	1	30	1	2	50	113
4	35	10	9	0.00834	3.25	0	1	2	85	1	3	110	267
5	30	10	8	0.02500	3.0	0	2	1	52	1	-2	72	180
6	40	12	10	0.02500	3.0	0	1	1	30	1	2	40	113

Table 2-4 IEEE 30 Bus system load pattern

Hour(hr)	**1**	**2**	**3**	**4**	**5**	**6**	**7**	**8**
Load(MW)	166	196	229	267	283.4	272	246	213
Hour(hr)	**9**	**10**	**11**	**12**	**13**	**14**	**15**	**16**
Load(MW)	192	161	147	160	170	185	208	232
Hour(hr)	**17**	**18**	**19**	**20**	**21**	**22**	**23**	**24**
Load(MW)	246	241	236	225	204	182	161	131

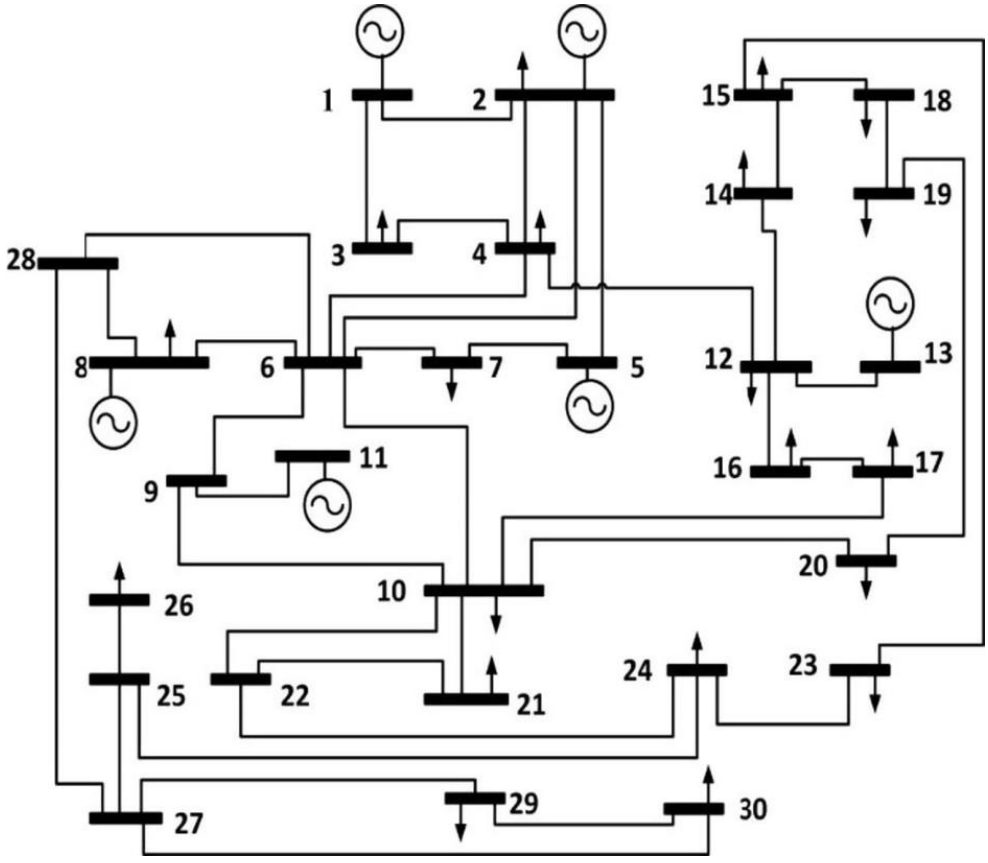

Figure 2.24 Single line diagram for IEEE 30-bus test system

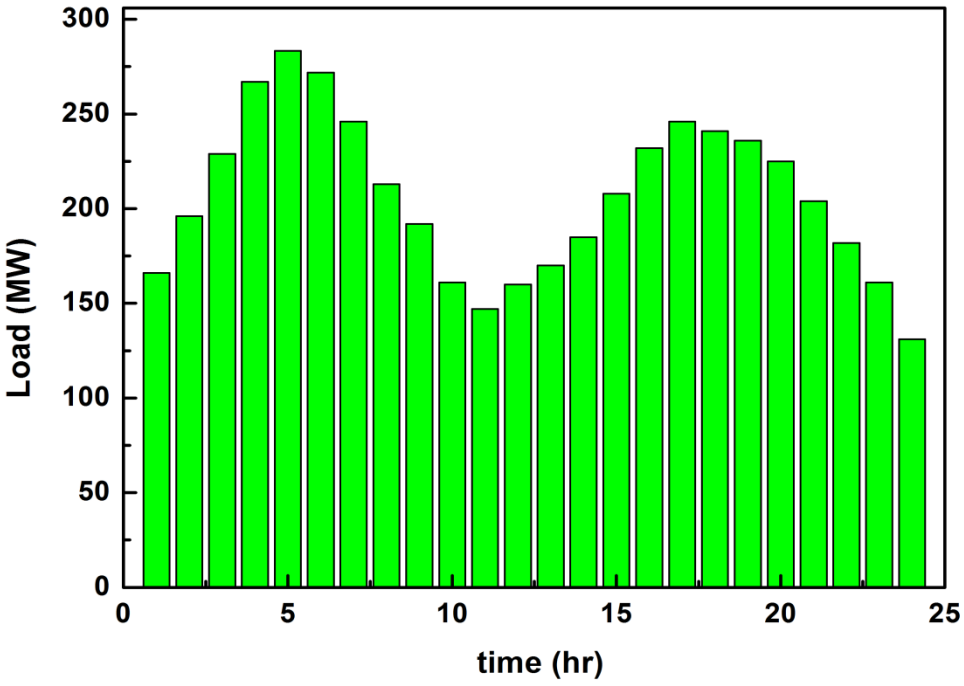

Figure 2.25 IEEE 30 bus system load curve

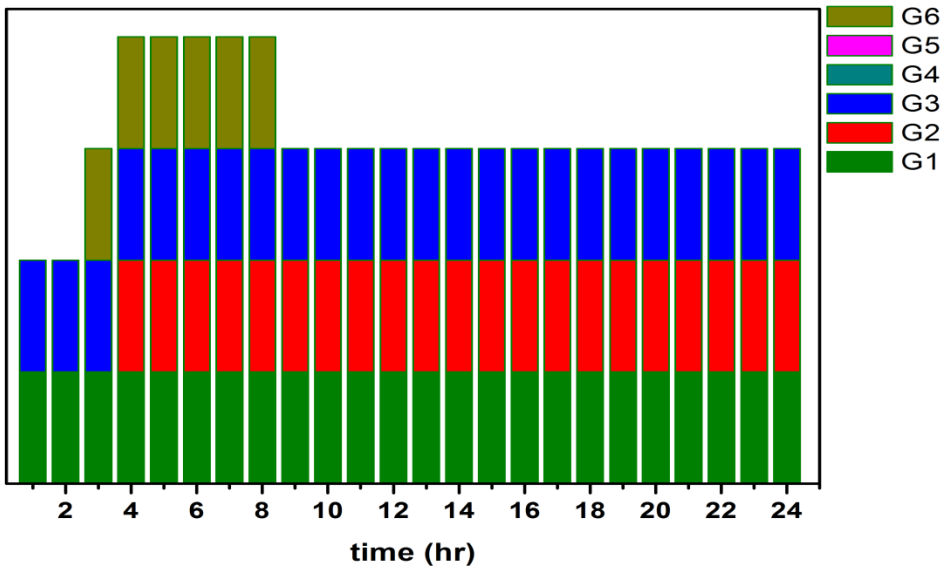

Figure 2.26 IEEE 30 bus test system units on off status

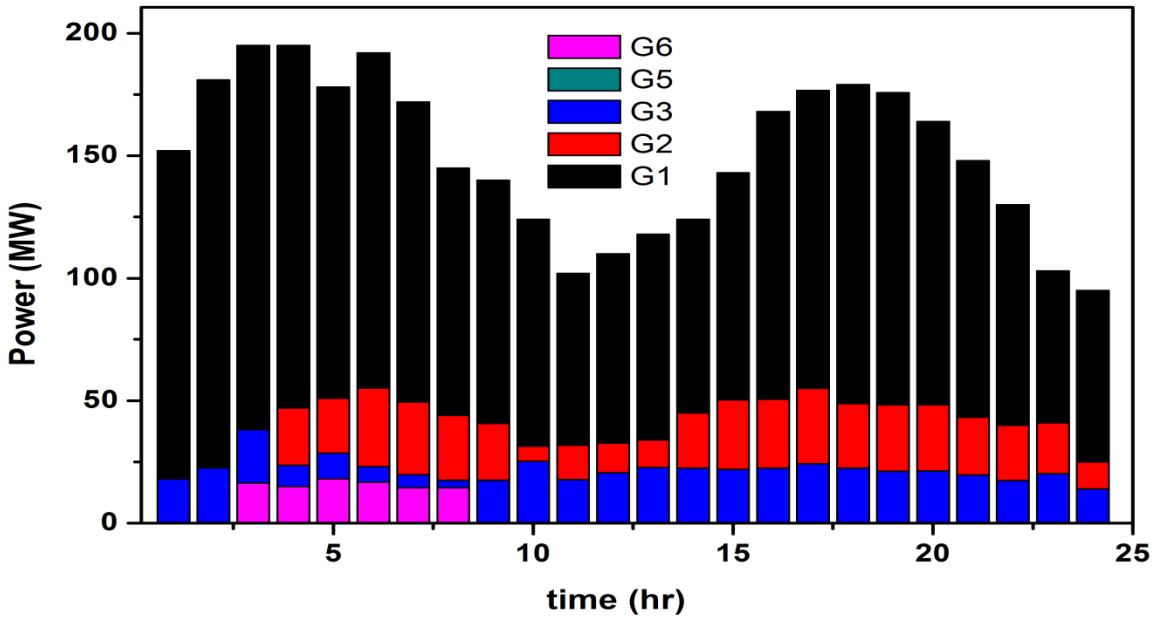

Figure 2.27 IEEE 30 bus test system units output power

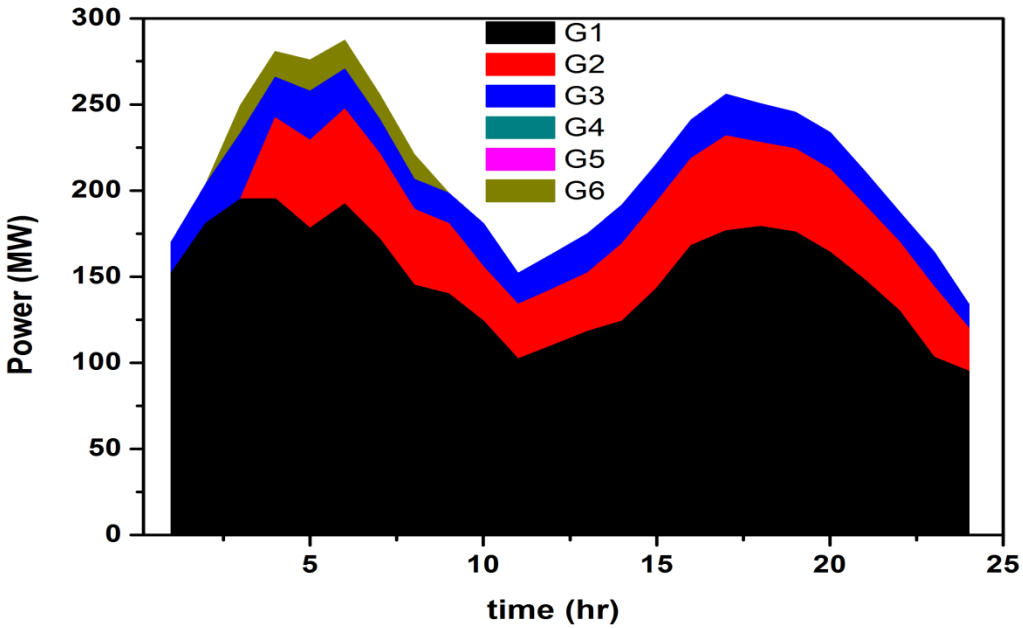

Figure 2.28 IEEE 30 bus test system units output power profile

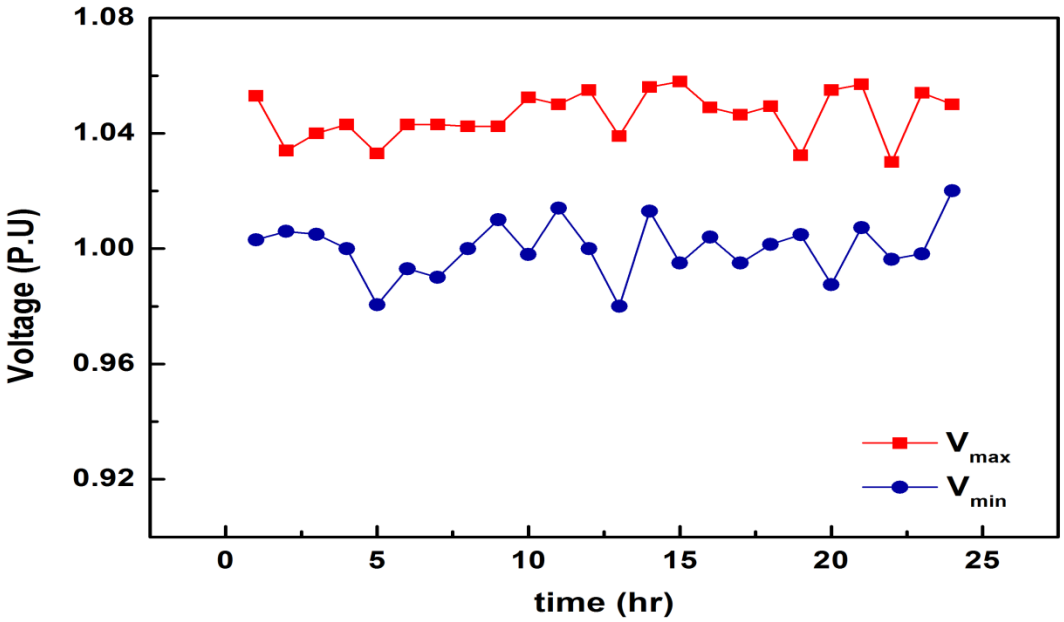

Figure 2.29 IEEE 30 bus test system maximum and minimum voltage with time

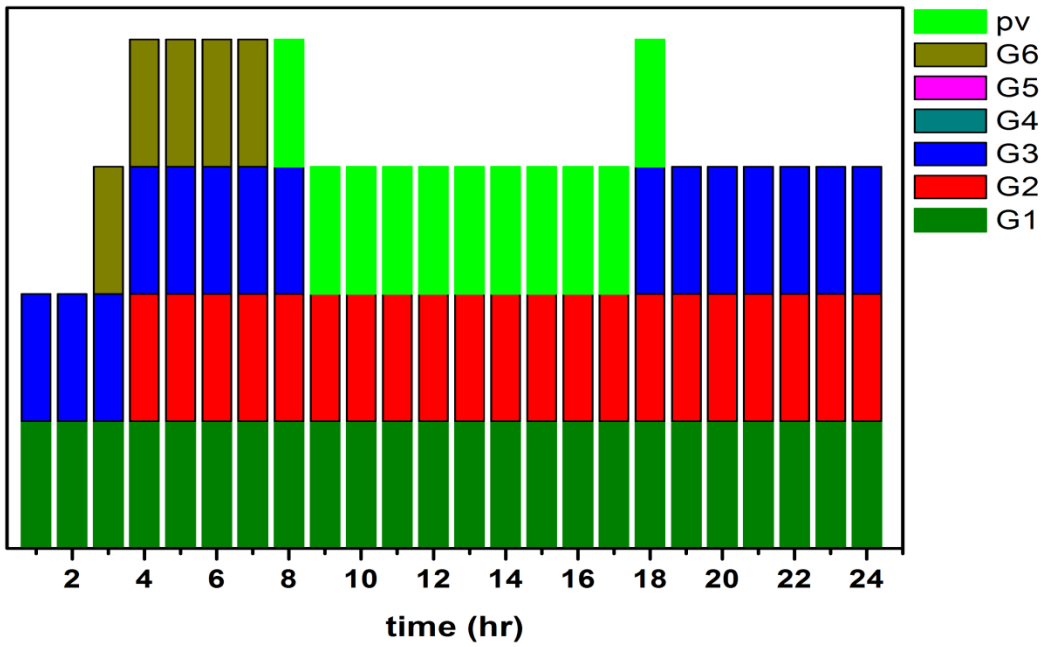

Figure 2.30 IEEE 30 bus test system units on off status with PV unit

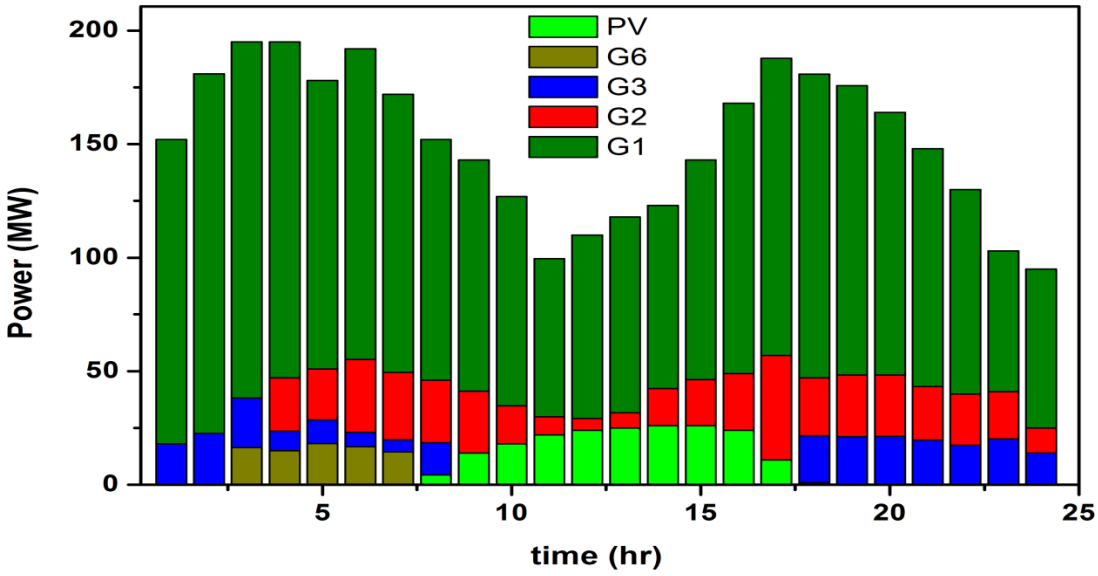

Figure 2.31 IEEE 30 bus test system units output power with PV unit

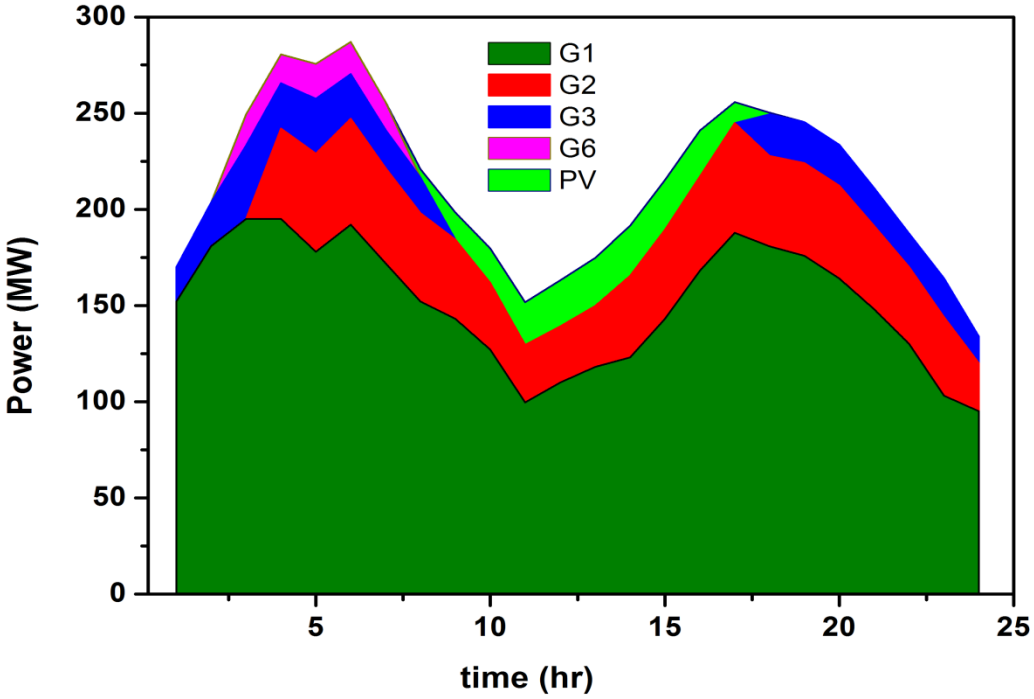

Figure 2.32 IEEE 30 bus test system units output power profile in presence of PV unit

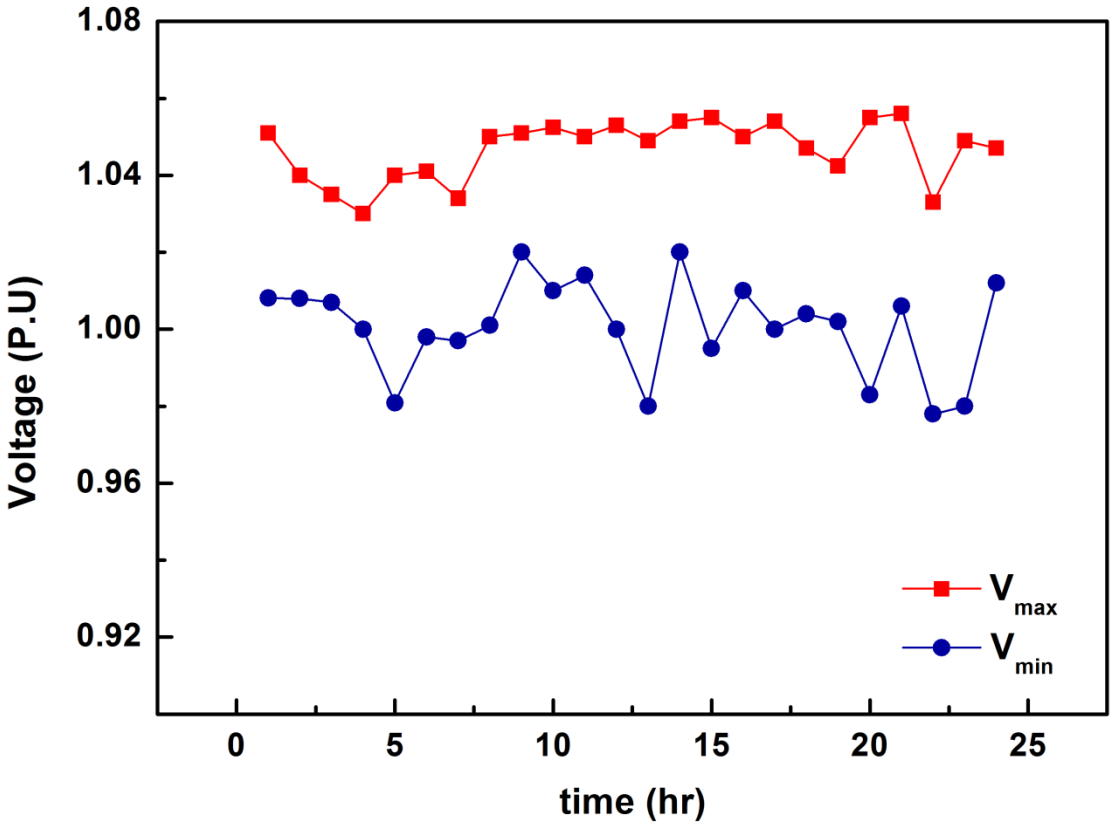

Figure 2.33 IEEE 30 bus test system maximum and minimum voltage with time in presence of PV unit

2.5.2 Grid Connected PV System

2.5.2.1 Steady state analysis

PV system can be used in either grid connected mode or off grid mode. In the grid connected mode the PV system is connected to the utility grid and feed the exceeded power from the load feeding to the grid as shown in Figure 2.34. A PV array a 100-kW connected to a 25-kV grid via a boost converter and a three-phase inverter and a maximum power point tracking is to control the boost converter based Incremental Conductance + Integral Regulator technique implemented via a MATLAB simulation model in order to investigate the effect of PV units on the utility grid the full and the detailed models are shown in Figures 2.35, 2-36, 2-37, 2-38, 2-39 and 2-40. The simulation model contains 100 kW PV array, 5-kHz boost converter

increasing voltage from PV output voltage (272 V DC at maximum power) to 500 V DC, maximum power point tracker controller that generates the switching duty cycle of the boost converter, 3-level 3-phase inverter that converts the 500 V DC to 260 V AC and keeps the power factor equal unity, 10-kvar capacitor bank for harmonics filtering produced by the inverter, 100-kVA 260V/25kV three-phase coupling transformer and utility grid model (25-kV distribution feeder + 120 kV equivalent transmission system). The PV array consists of N_{par} strings of modules (Module type Sunpower SPR -305 –WHT (Appendix A)) connected in parallel, each string consisting of N_{ser} modules connected in series with the following specifications.

Number of cells per module 96, Number of series-connected modules per string 5, Number of parallel strings 66, Module specifications under STC [V_{oc}=64.2 V, I_{sc}=5.96 A , V_{mp}= 54.7V and Imp=5.58 A], Model parameters for 1 module [R_s= 0.0379987 Ω, R_p= 993.51 Ω , I_o=1.1753e-08 A, Iph= 5.9602 A, Diode ideality factor =1.3]

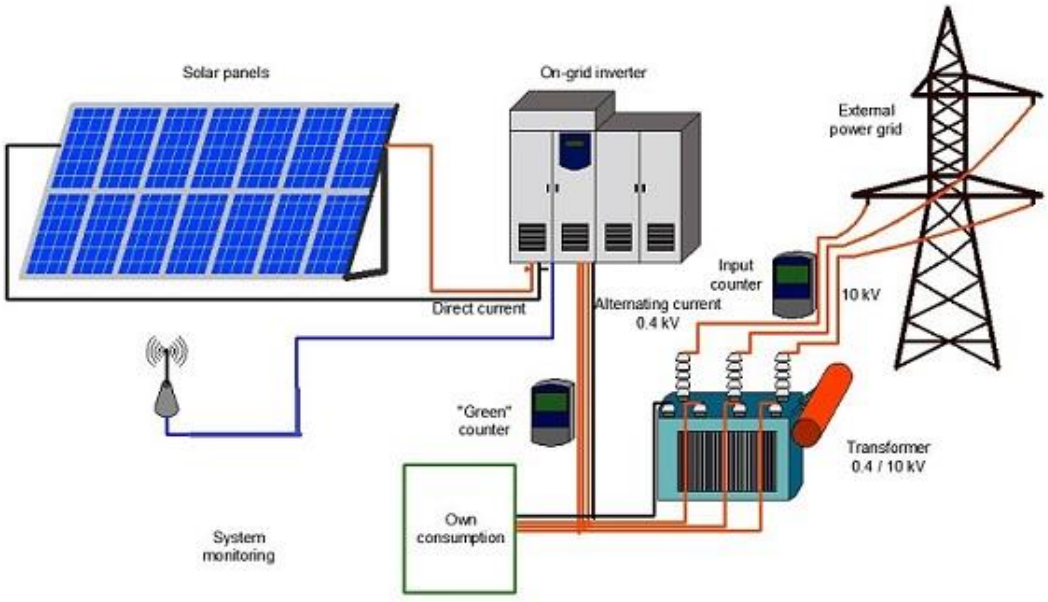

Figure 2.34 PV grid connected application

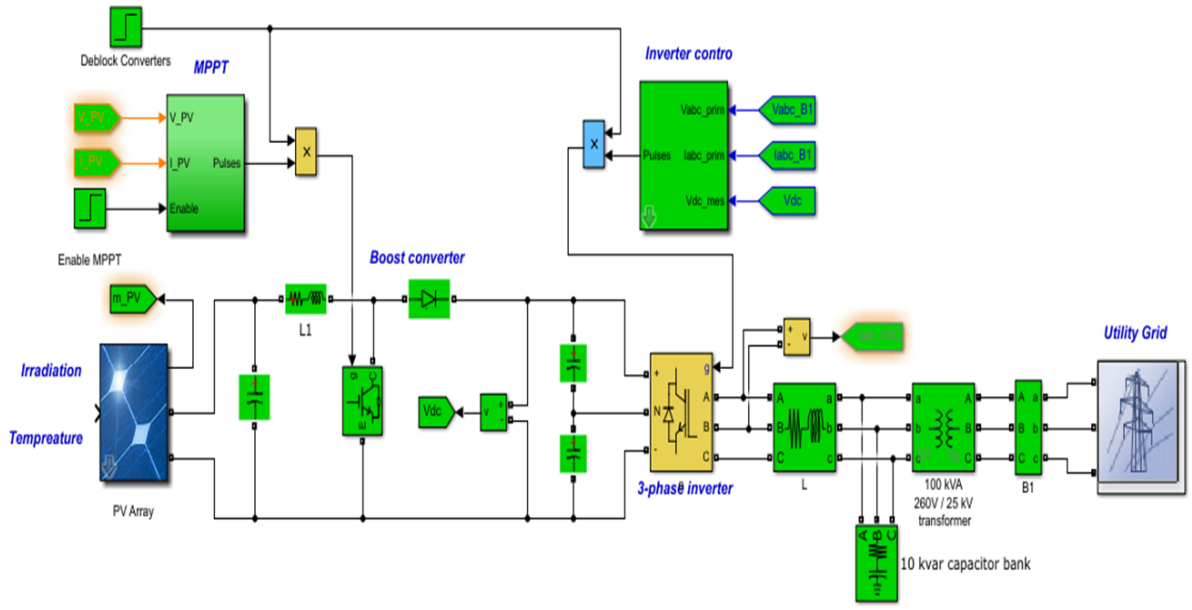

Figure 2.35 PV grid connected full model matlab simulation

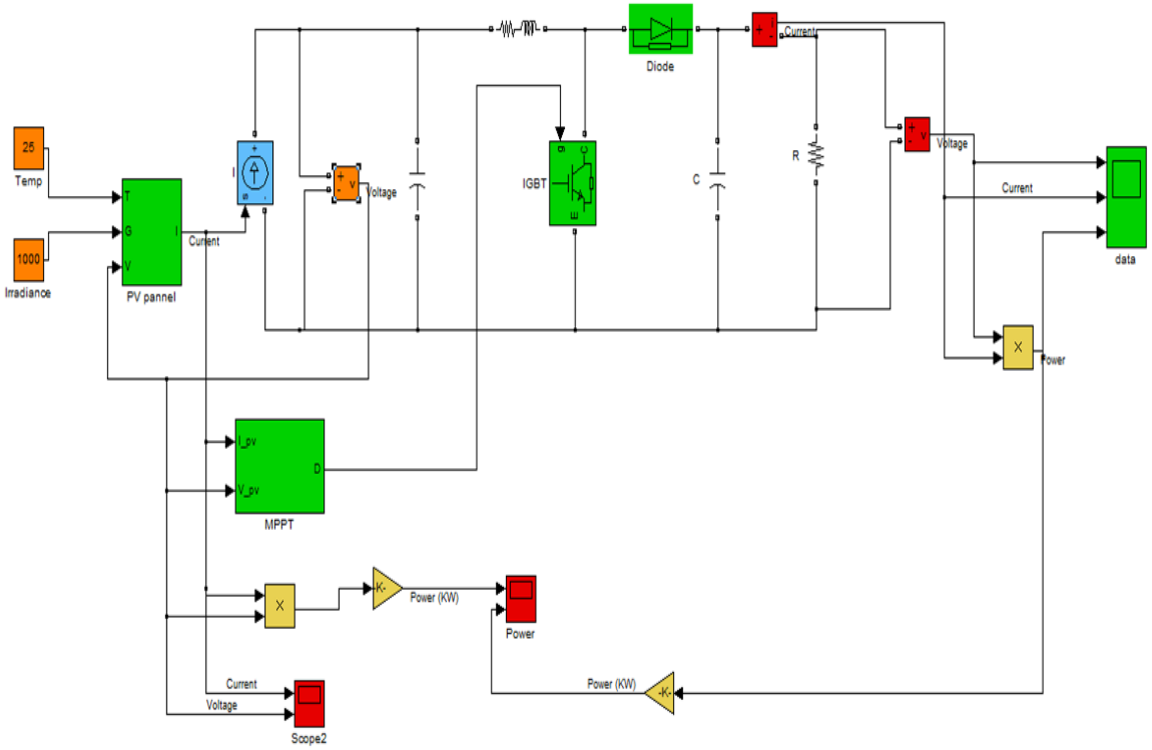

Figure 2.36 Configuration of PV with MPPT algorithms in matlab simulink

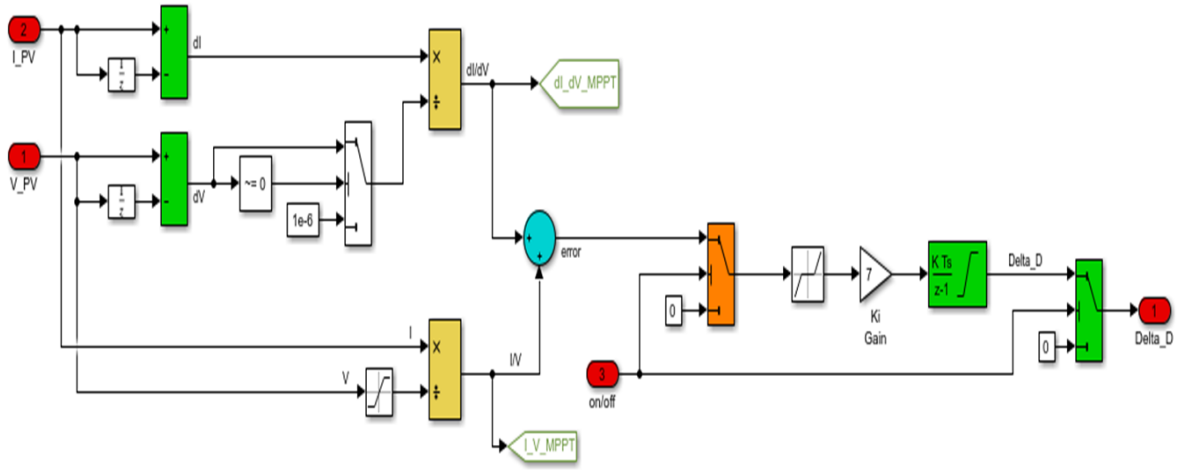

Figure 2.37 Configuration MPPT (incremental conductance) algorithm in matlab Simulink

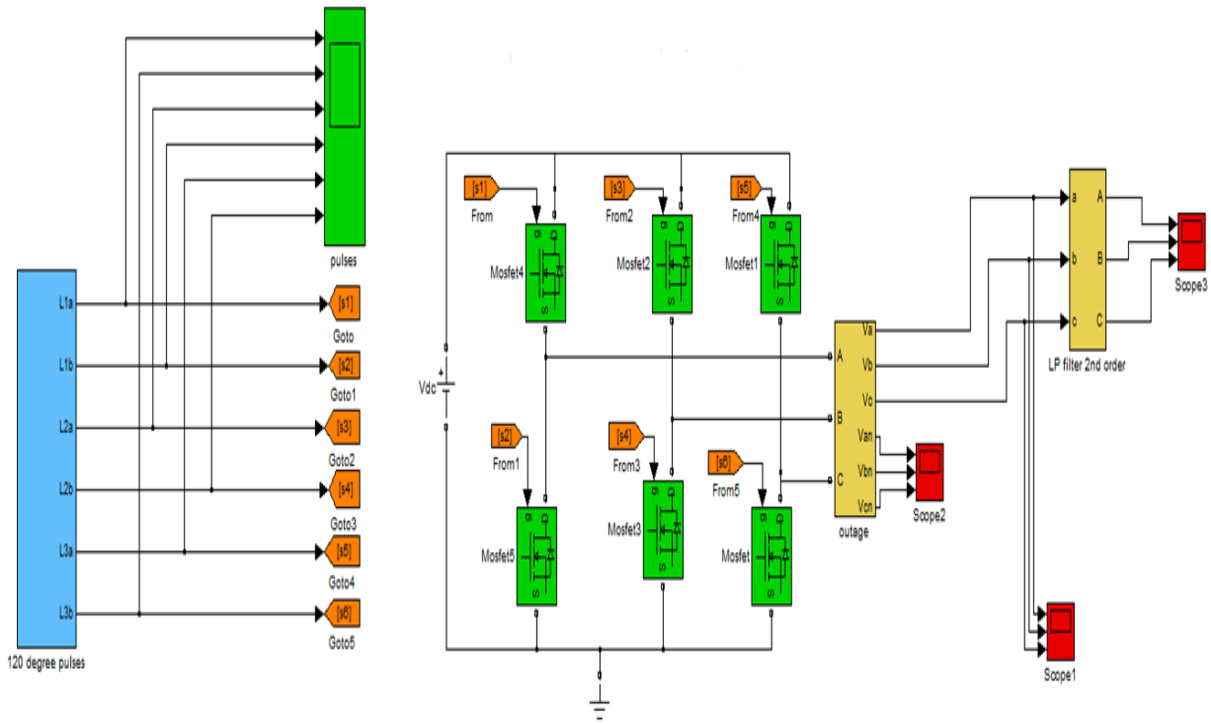

Figure 2.38 Inverter model in matlab Simulink

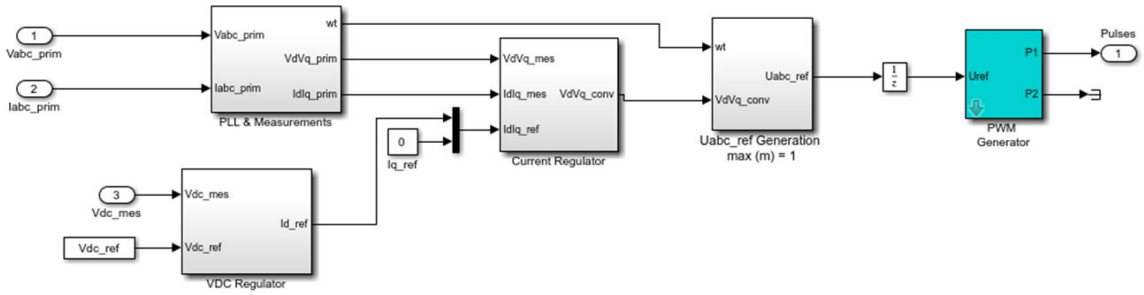

Figure 2.39 3- phase inverter control model

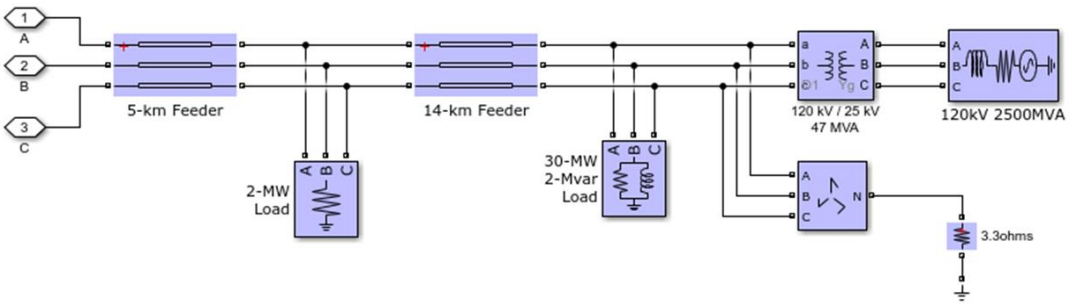

Figure 2.40 Utility grid simulation model

Figure 2-41 shows the sunpower 305 PV module charachteristics while, Figures 2-42 and 2-43 show the constant irradiation (1000W/m^2) case performance.

Figures 2-44 and 2-45 show the irradiation changing case performance where, from t=0 till t= 0.05 sec, there is no pulses to the boost converter and the three phase inverter (the pulses are blocked). PV output voltage is the open-circuit voltage (N_{ser}*V_{oc}=5*64.2=321 V) and the DC link capacitors are charged above 500 V. At t=0.05 sec, the Boost converter and the three phase inverter pulses are de-blocked. The voltage at the DC link is regulated at 500V. The Duty cycle of boost converter is fixed (D= 0.5 and sun irradiance is set to 1000 W/m^2). Steady state is reached at t=0.25 sec. the PV voltage is therefore V_{PV} = (1-D)*V_{dc}= (1-0.5)*500=250 V. The maximum power point tracker starts adjusting the voltage of the PV unit at t=0.4 sec based on changing the duty cycle of the boost converter in order to obtain the

maximum output power (100 kW) which is obtained at duty cycle equal 0.453. When the sun irradiance changed from 1000 W/m^2 to 250 W/m^2 the maximum power point tracker keeps tracking maximum power point showing the high efficient performance of the maximum power point tracker controller. Figures 2-46 and 2-47 show the inveter output phase voltage and the phase voltage and current at the point of coneecting.

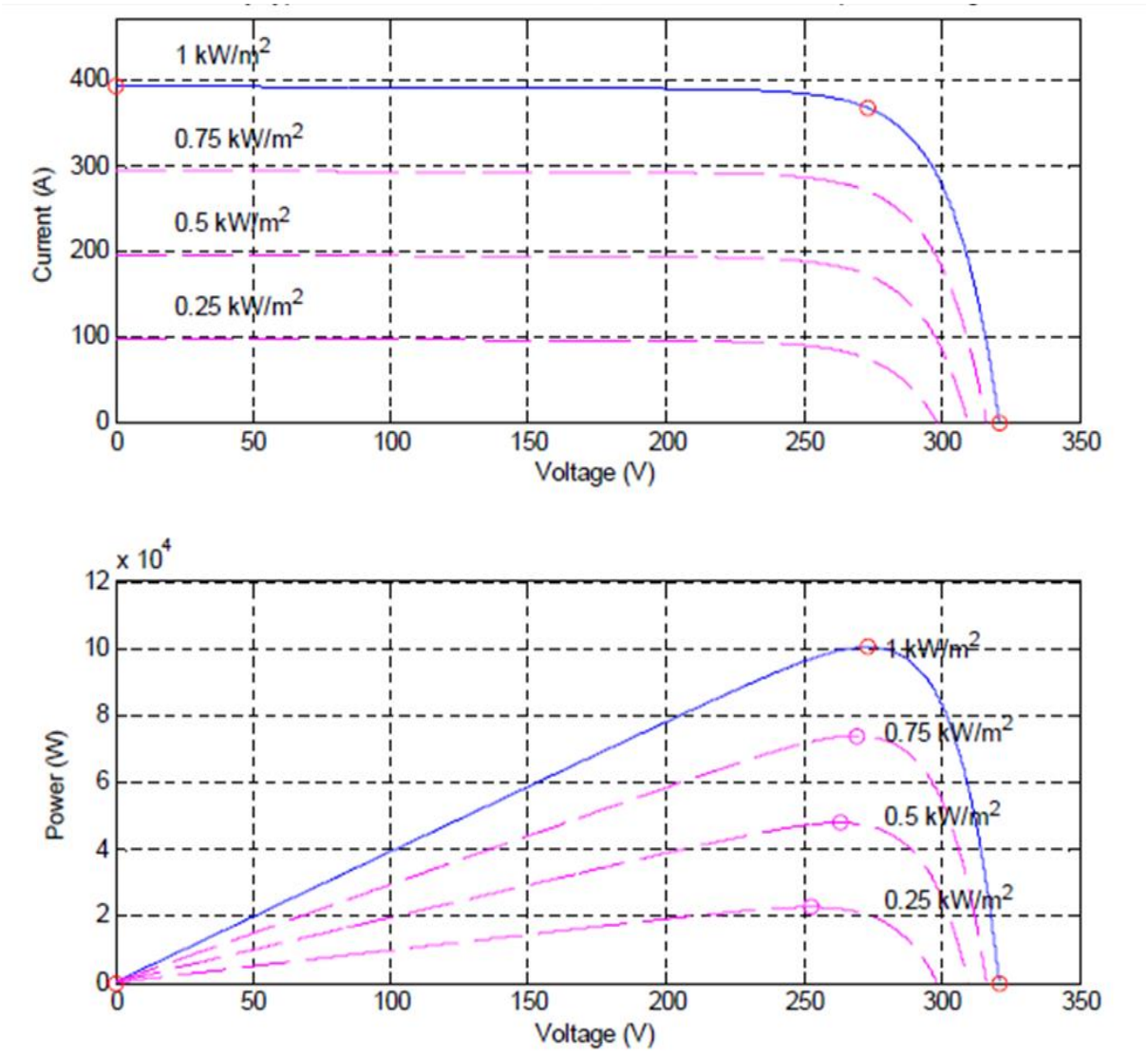

Figure 2.41 Sun power 305, PV module charachteristics

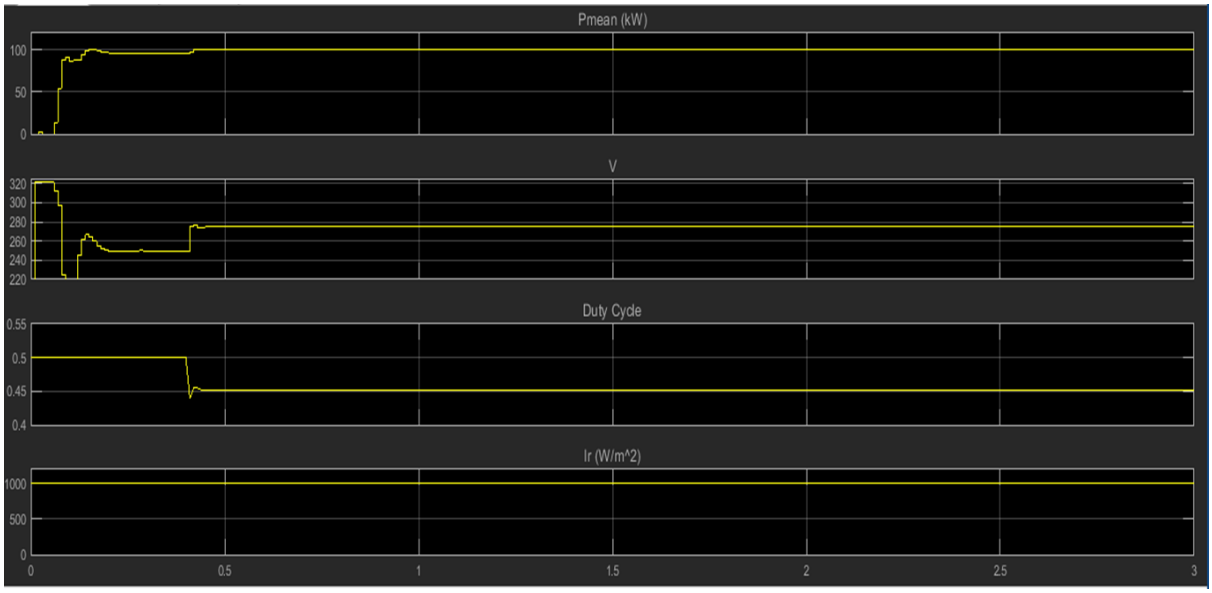

Figure 2.42 PV out put power, PV voltage, Duty cycle and irradiation profile respectively at constant irradiation case

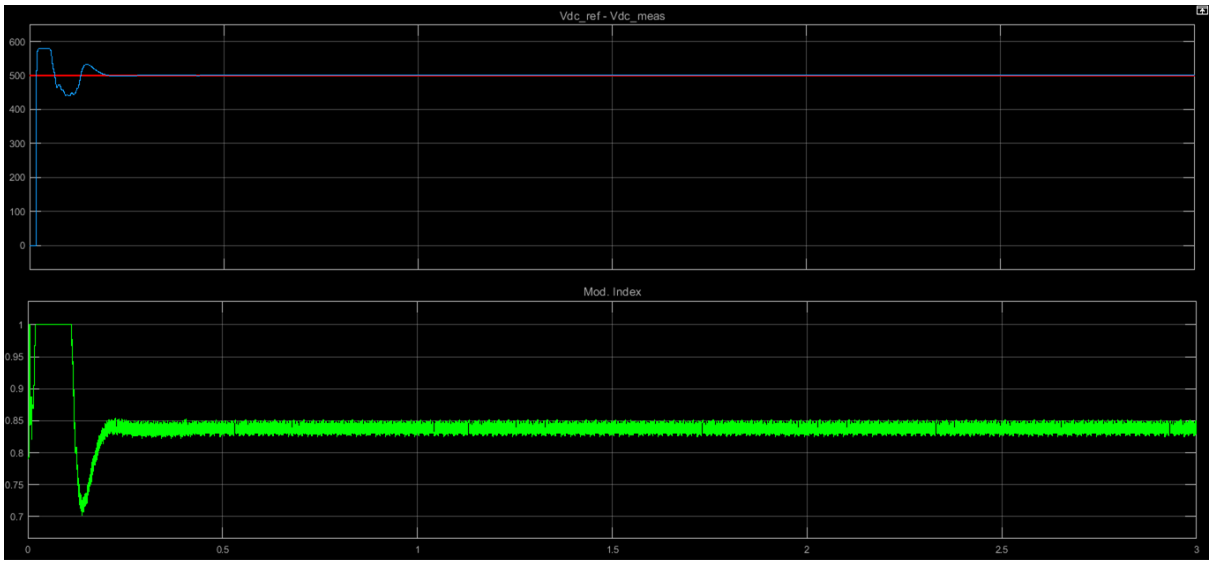

Figure 2.43 The DC Voltage, reference votage and the modulation index respectively at constant irradiation case

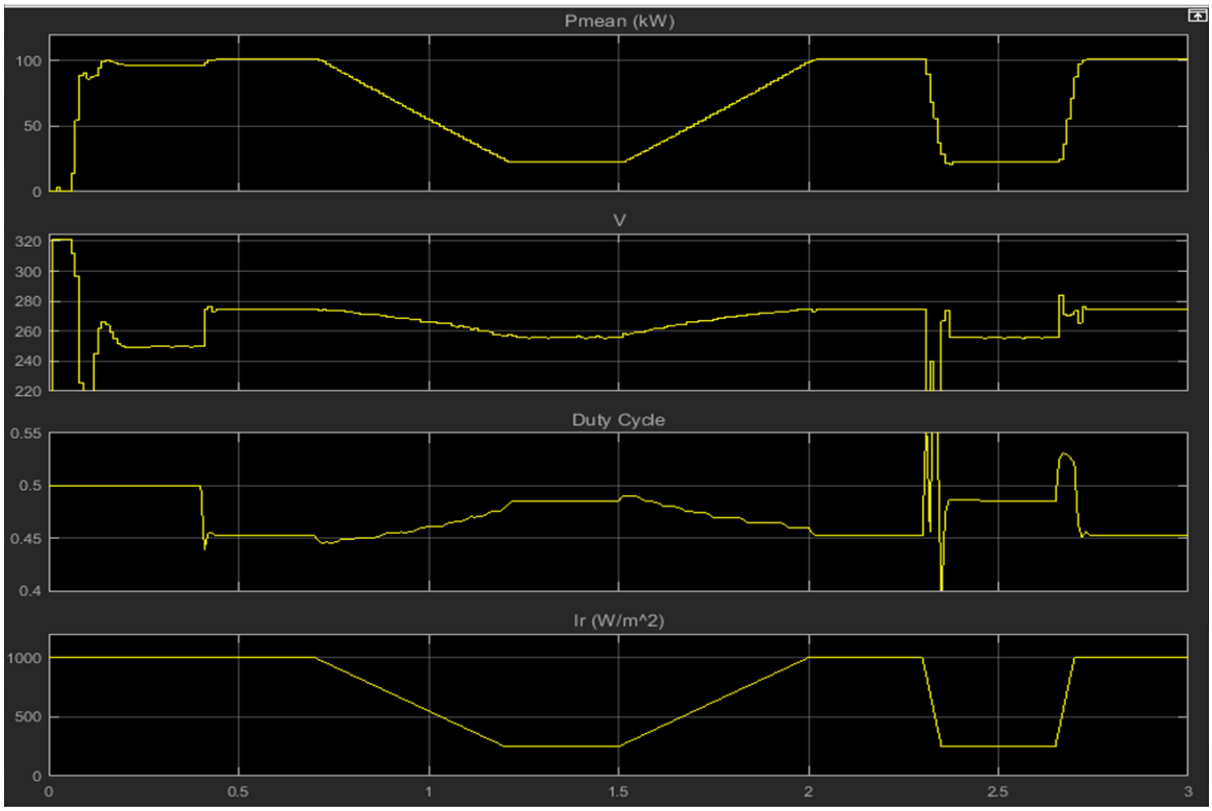

Figure 2.44 PV out put power, PV voltage, Duty cycle and irradiation profile respectively at variable irradiation case

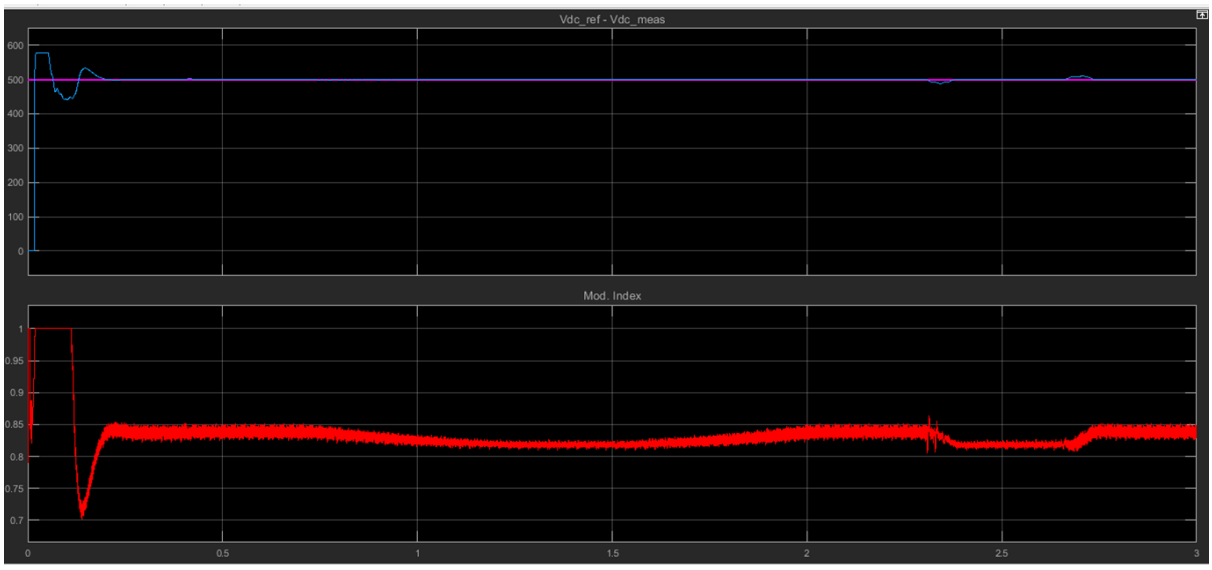

Figure 2.45 The DC Voltage, reference votage and the modulation index respectively at variable irradiation case

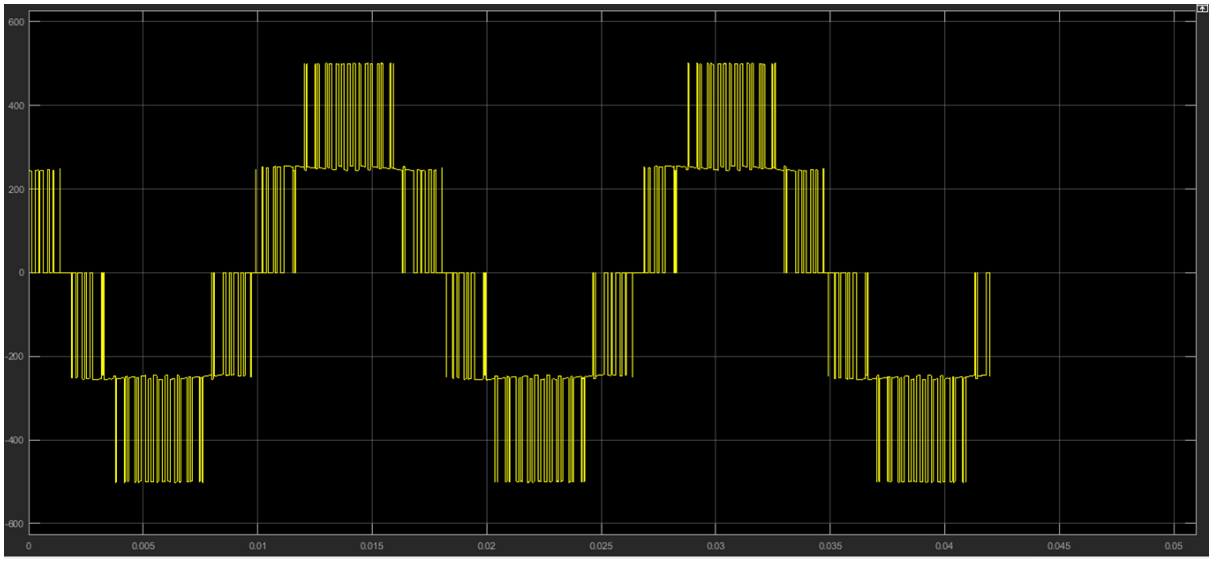

Figure 2.46 Inveter out put phase voltage

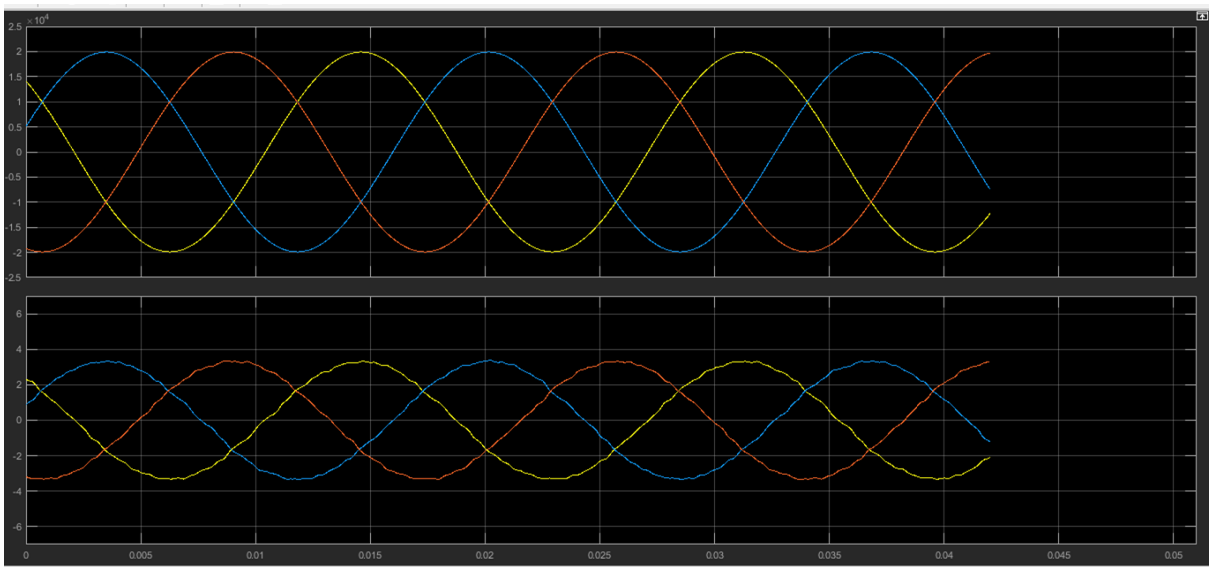

Figure 2.47 3-phase voltage and 3- phase current respectively at point of connecting

2.5.2.2 Transient analysis (Fault analysis)

The irradiation is seted to 1000 W/m^2 and temperature to 25^{0}C while; the fault is applied on the grid side for a duration of 100 m seconds. Three lines to ground fault as symmetrical fault and the unsymmetrical fault cases (Appendix B) both investigated as follows.

2.5.2.2.1 Three lines to ground fault

The voltage and the current at point of connecting in this case are shown in Figure 2-48 while the PV output power is shown Figure 2-49 showing the ability of the maximum power point tracking kontroller to successfully follow point of maximum power during the fault condtion.

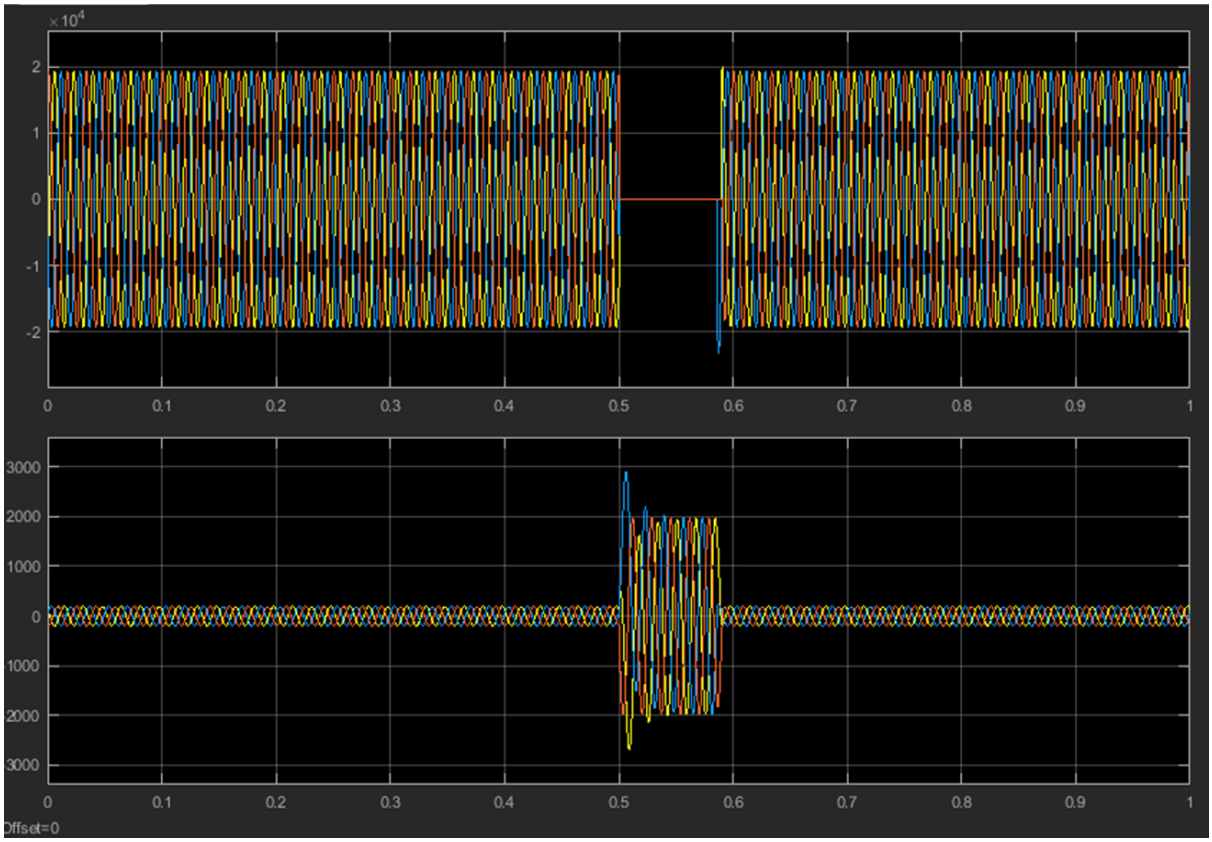

Figure 2.48 Voltages and current at point of connecting in the case of three lines to ground fault

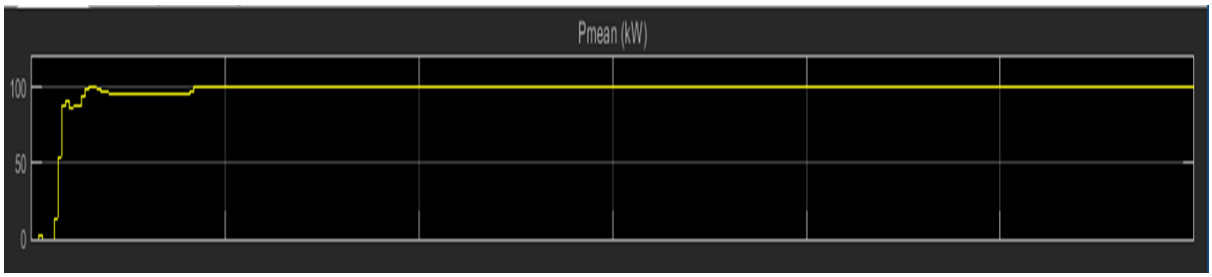

Figure 2.49 PV array output power in the case of three lines to ground fault

2.5.2.2.2 Single line to ground fault

The voltage and the current at point of connecting in this case are shown in Figure 2-50 while the PV output power is shown Figure 2-51 showing the ability of the maximum power point tracking kontroller to successfully follow point of maximum power during the fault condtion.

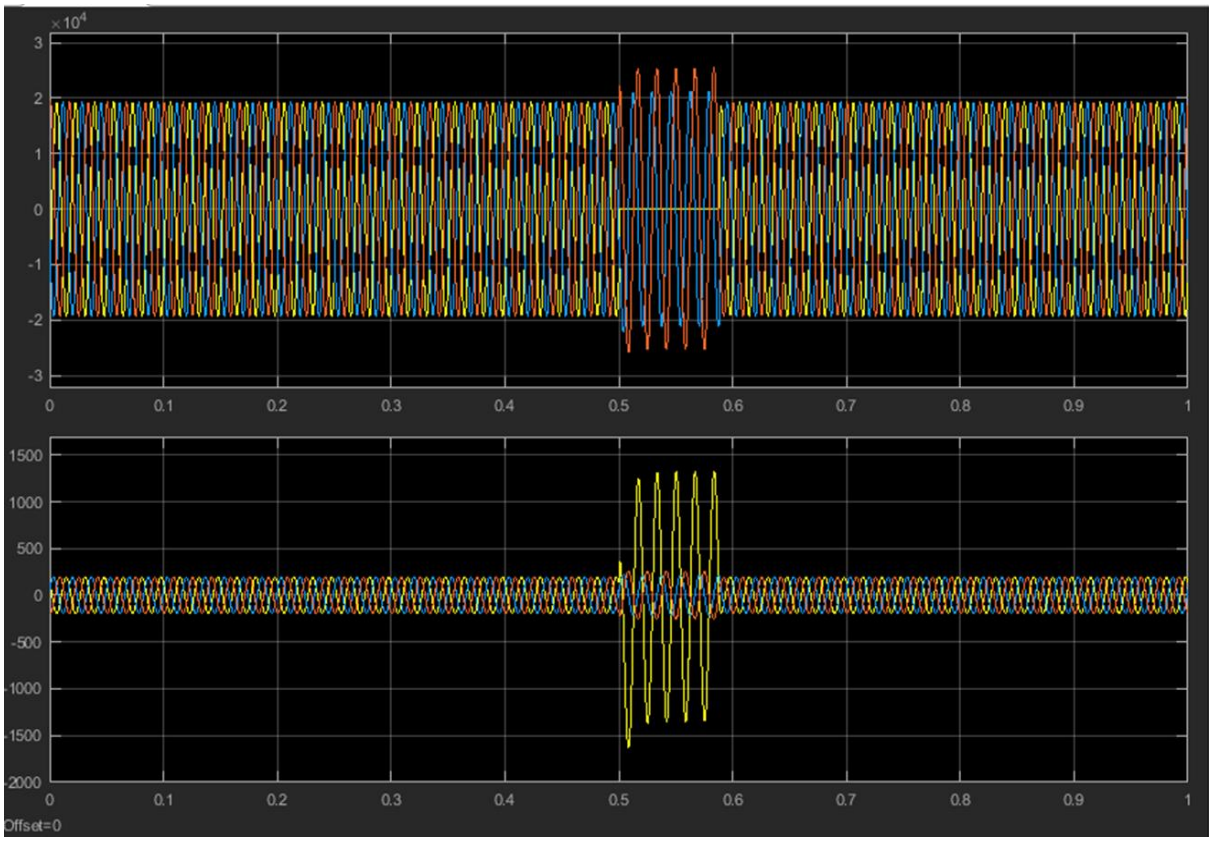

Figure 2.50 Voltages and current at point of connecting in the case of single line to ground fault

Figure 2.51 PV array output power in the case of single line to ground fault

2.5.2.2.3 Line to line fault

The voltage and the current at point of connecting in this case are shown in Figure 2-52 while the PV output power is shown Figure 2-53 showing the ability of the maximum power point tracking kontroller to successfully follow point of maximum power during the fault condtion.

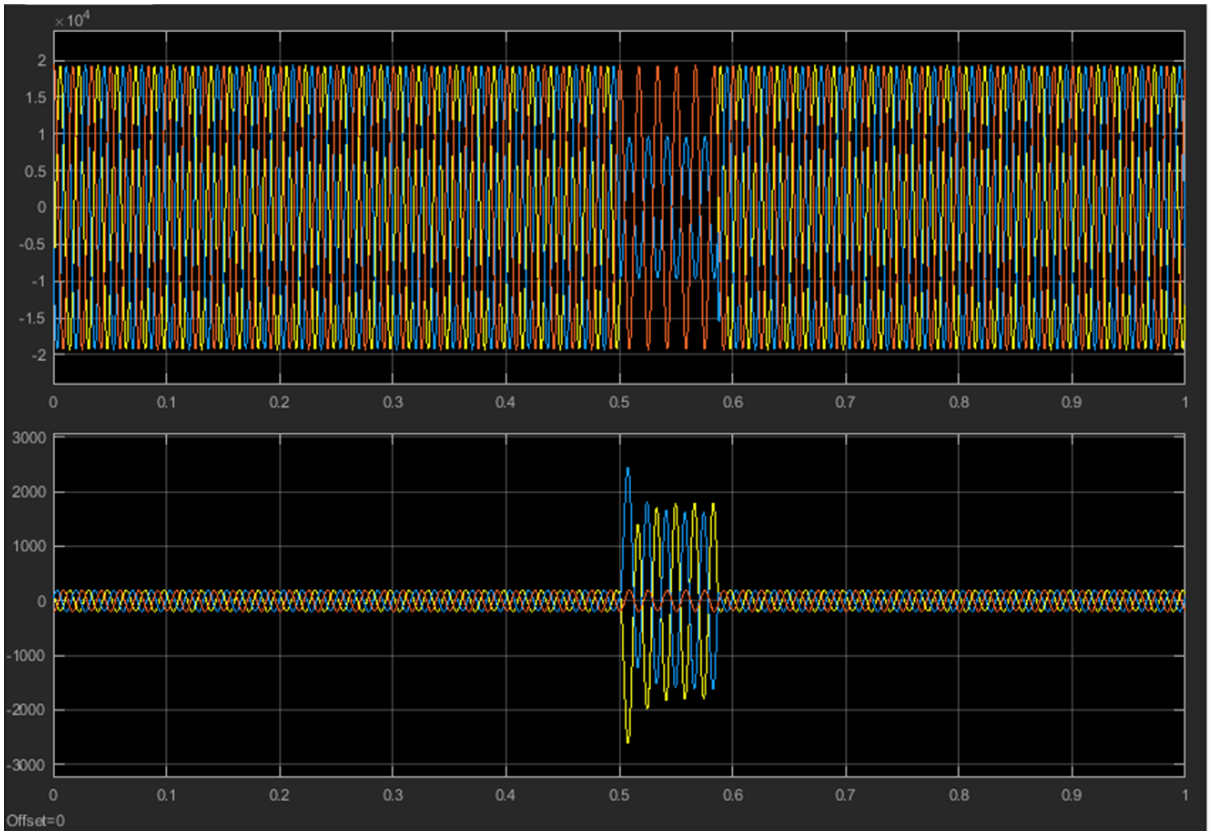

Figure 2.52 Voltages and current at point of connecting in the case of line to line fault

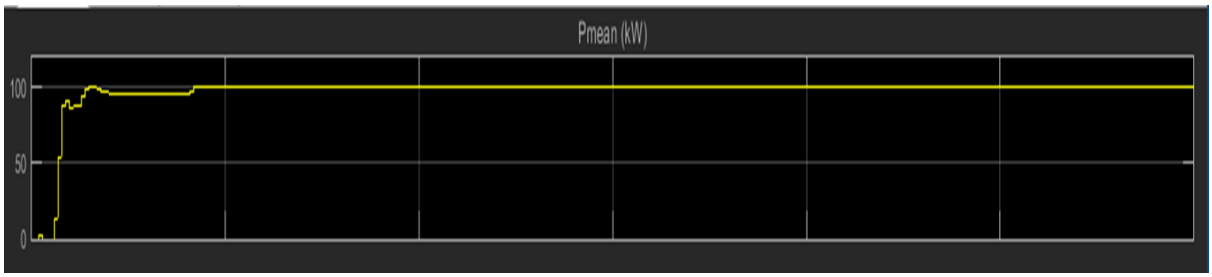

Figure 2.53 PV array output power in the case of line to line fault

2.5.2.2.4 Line to line to ground fault

The voltage and the current at point of connecting in this case are shown in Figure 2-54 while the PV output power is shown Figure 2-55 showing the ability of the maximum power point tracking kontroller to successfully follow point of maximum power during the fault condtion.

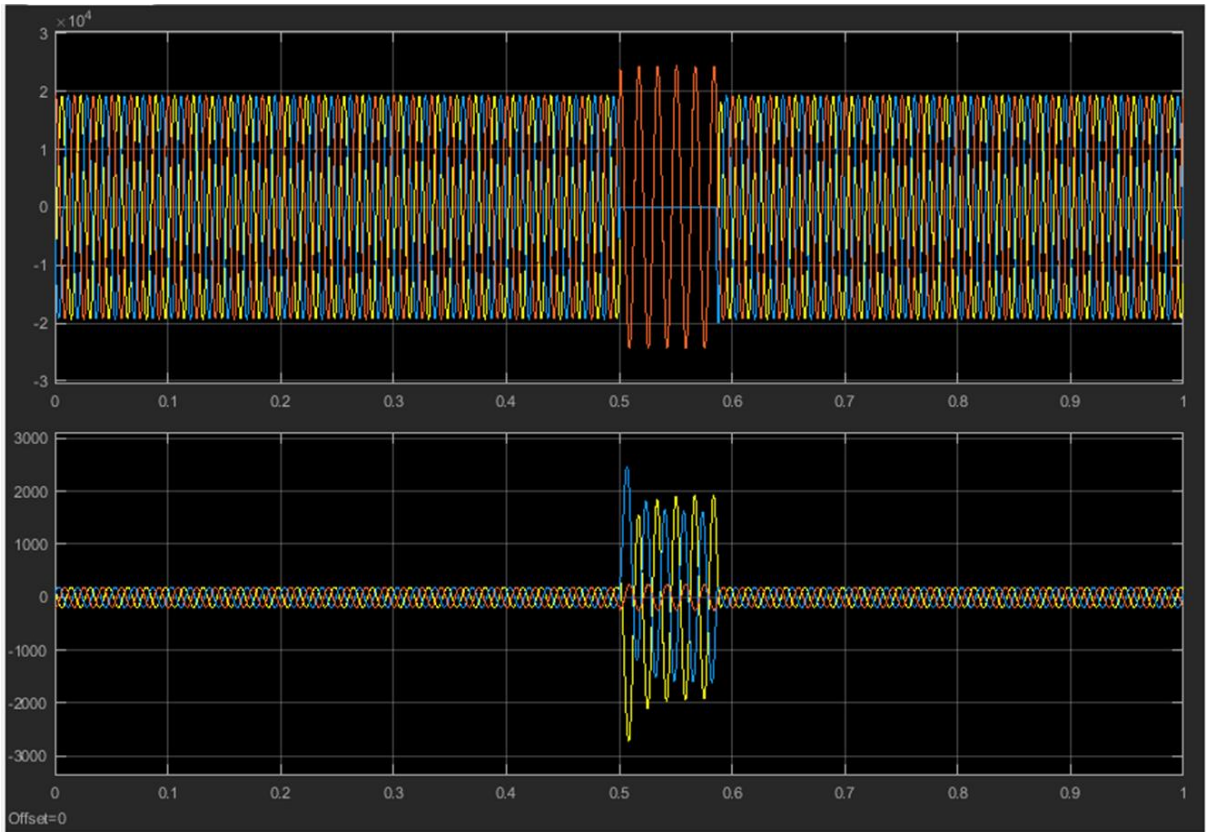

Figure 2.54 Voltages and current at point of connecting in the case of line to line to ground fault

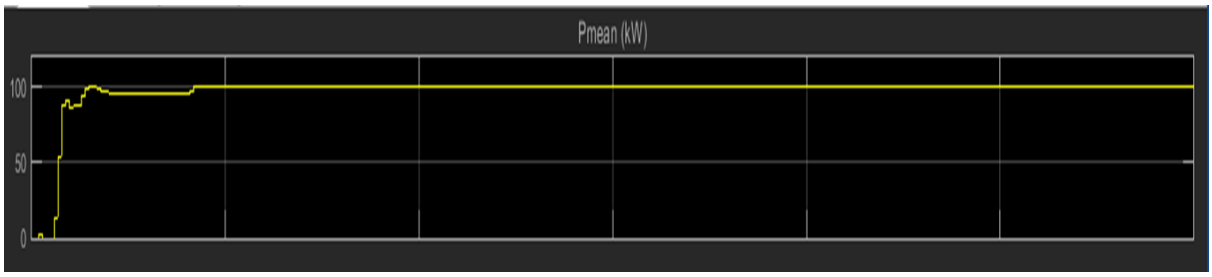

Figure 2.55 PV array output power in the case of line to line to ground fault

From the above results in different fault cases it is clear that the PV array output power injected to the grid almost constant because of the incremental conductance based maximum power point tracker.

2.5.3 PV Off Grid System

The off grid system supplies a local load and stores the exceeded power in a battery system as shown in Figures 2.56 and 2.57. This system is used when the grid is fare or in the disert for irrigation purposes also it is used in the street lightining.

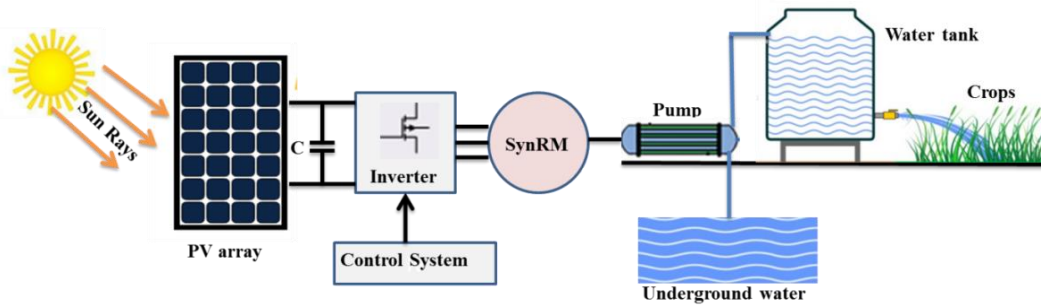

Figure 2.56 Off grid application (irrigation system)

Figure 2.57 PV off grid application (home application)

2.6 PV systems advantages and disadvantages

The advantages of photovoltaic system can be summarized as [11]:

- They are static source for electricity
- Direct transformation of sunlight to electricity
- No moving parts
- PV systems is sizable system making it to be suitable for different applications
- PV system can be expanded in easy way to produce high voltage and current by adding more modules either in series to expand the system's voltage or in parallel to enlarge the current
- PV systems have not carbon emissions or any pollution

The disadvantages of photovoltaic system can be summarized as [11]:

- High manufacturing cost
- Maximum power point needs controller in order to follow it
- Requires regular cleaning from dust, sand and bird droppings
- The PV system efficiency is still low

References

[1] V. Quaschning, Understanding Renewable Energy Systems, London, Carl Hanser Verlag GmbH & Co KG, 2005

[2] M.G.Villalva, J.R.Gazoli and E. Ruppert F, Comprehensive Approach to Modeling and Simulation of Photovoltaic Arrays, IEEE Transactions, vol. 25, no. 5, pp. 1198-- 1208, ISSN 0885-8993, 2009

[3] T.Burton, D.Sharpe, N.Jenkins and E.Bossanyi, Wind Energy Handbook. England, 2001.

[4] G. J. A. H. Wetzelaer, M. Scheepers, A. M. Sempere, C. Momblona, J. Avila, and H. J. Bolink, Adv. Mater, 27, 1837 (2015).

[5] P. Liao, X. Zhao, G. Li, Y. Shen, and M. Wang1, Nano-Micro Lett. 10, (2018).

[6] D. Allam, D. A. Yousri, and M. B. Eteiba, Energy Convers. Manage, 123,535 (2016).

[7] Fathy, and H. Rezk, Renew. Energy, 111, 307 (2017).

[8] M. Shaheen, S. M. Farrag, and R. A. El-Sehiemy. IET. Gen. Trans. Distrib., 11, 570 (2017).

[9] M. H. Qais, H. M. Hasanien, and S. Alghuwainem, *Appl. Energy*, 250, 109 (2019).

[10] U.S. Department of Energy, 2010 Solar Technologies Market Report, First Solar. [Online]. http://www.firstsolar.com/Projects/Topaz-Solar-Farm.

[11] Goetzberger, Photovoltaic Solar Energy Generation. Springer, 2005.

3 Chapter 3

3 Experimental setup

3.1 Fabrication of third generation (perovskite) solar cells

The solar cells were fabricated by using 20mm x 15mm FTO conductive glasses (Aldrich, 7 $Ohm \cdot sq^{-1}$) as the anode substrates. The FTO were etched with a 2 mol L^{-1} HCl aqueous solution in combination with Zn powder. They were thoroughly cleaned with Hellmanex, acetone, 2-propanol and treated with UV ozone in 15 min cycles.

The titania compact layer was spin coated at 2000 r.p.m. for 60 s from an ethanolic solution of titanium (IV) isopropoxide (Aldrich, 97%) containing a tiny quantity of HCl solution. The films were calcinated for 45 min at 500^{o}C (5^{o}C$\cdot min^{-1}$ temperature ramp rate). Then, the films were dried under Ar flux and transferred into an Ar-filled glove box for the perovskite deposition.

The $MAPbI_3$ layer was deposited by spin coating in a one-step procedure using a perovskite solution in anhydrous DMF, containing a 40 wt% Methylammonium iodide (Dyesol) along with Lead acetate trihydrate ($PbAc_2.3H_2O$, 99.999% trace metals basis, Aldrich) in a 3:1 molar ratio. An aliquot of hypophosphorous acid (50% w/w, aquatic solution, Alfa Aesar) was also added to the perovskite solution so as the final molar ratio of HPA:$PbAc_2$ to be 1:4. The deposition was realized at 2000 r.p.m. for 45 s. The films were left to dry at room temperature for 10 min and were annealed at 100^{o}C for different times.

Finally, a 7 wt% Spiro-MeOTAD (Solaronix) solution in chlorobenzene was deposited as the hole transport layer, containing additives of lithium bis(trifluoromethanesulfonyl)imide lithium salt (≥99%, Aldrich) in acetonitrile and 4-tert-butylpyridine (96%, Aldrich). The deposition was realized at 3000 r.p.m for 30s. Finally, the devices were transferred outside

the glovebox and six 100 nm silver electrodes were thermally evaporated under vacuum of 10^{-6} Torr, at a rate of ~1Å·s^{-1}. Figure 3.1 shows the schematic diagram of the fabrication process.

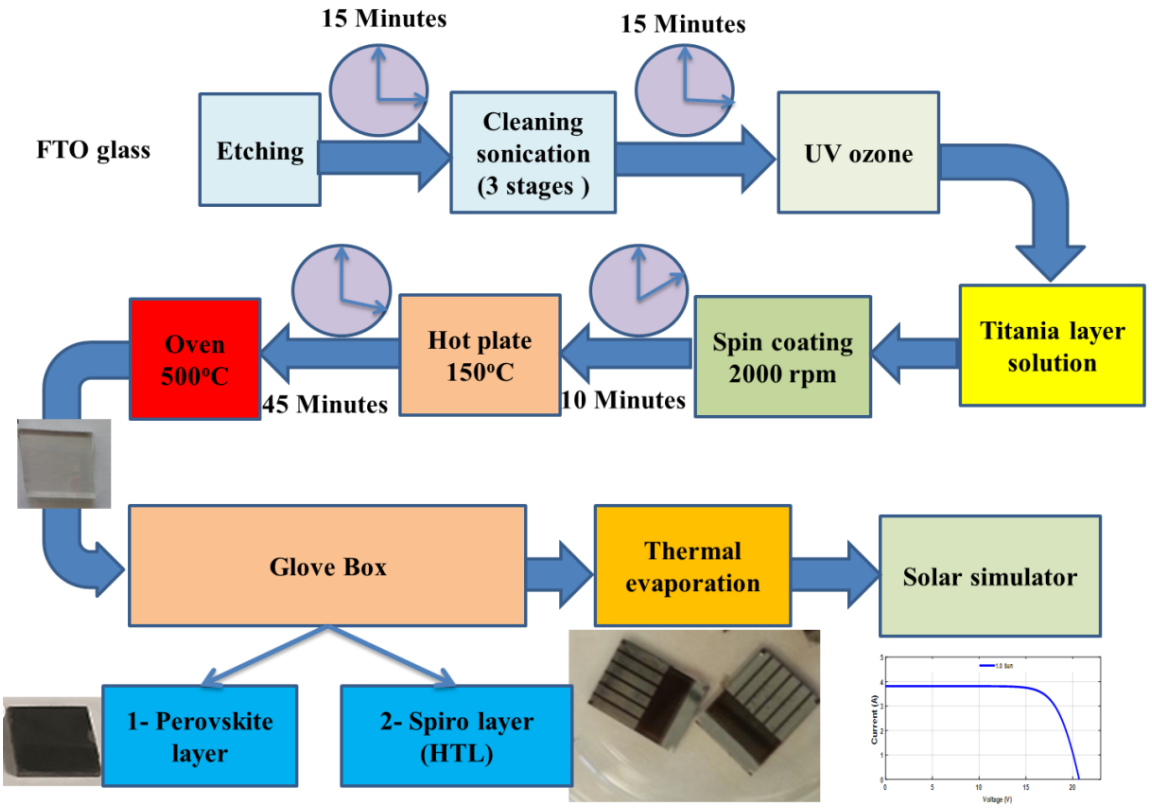

Figure 3.1 Schematic diagram of the fabrication process

3.2 Evaluation Apparatus

Raman spectroscopy (Figure 3.2) is concerned with the phenomenon of the change in frequency when the light is scattered by molecules. The magnitude of this change is referred to as Raman frequency and total frequency characteristics of a species are the scattered Raman spectrum of this species. It is a spectroscopic technique based on inelastic scattering of monochromatic radiation, usually from a laser source of visible or near infrared. During irradiation, the spectrum of the scattered radiation is measured at some angle (often 90^0) with a suitable spectrometer. Raman spectroscopy is a powerful technique with different options

such as area mapping, depth profile for beyond the standard spectra analysis. Mapping analysis is important in order to see the homogeneity of the sample and to compare the different Raman features in the select area. The depth profile is useful beyond the standard spectra, to select how the Raman signal changes in respect of the depth of the sample. It is used for analysis of solid, liquid & vapor, it is not a destructive technique and no vacuum is required.

Raman Spectroscopy was performed using a Renishaw in Via Reflex microscope with solid state laser (λ = 514.4 nm) excitation source see Figure 3.2. The laser light was focused on the samples using an x50 objective lens of a Leica DMLM microscope at power density equal to 0.035mW·μm^{-2}, in order to avoid sample heating.

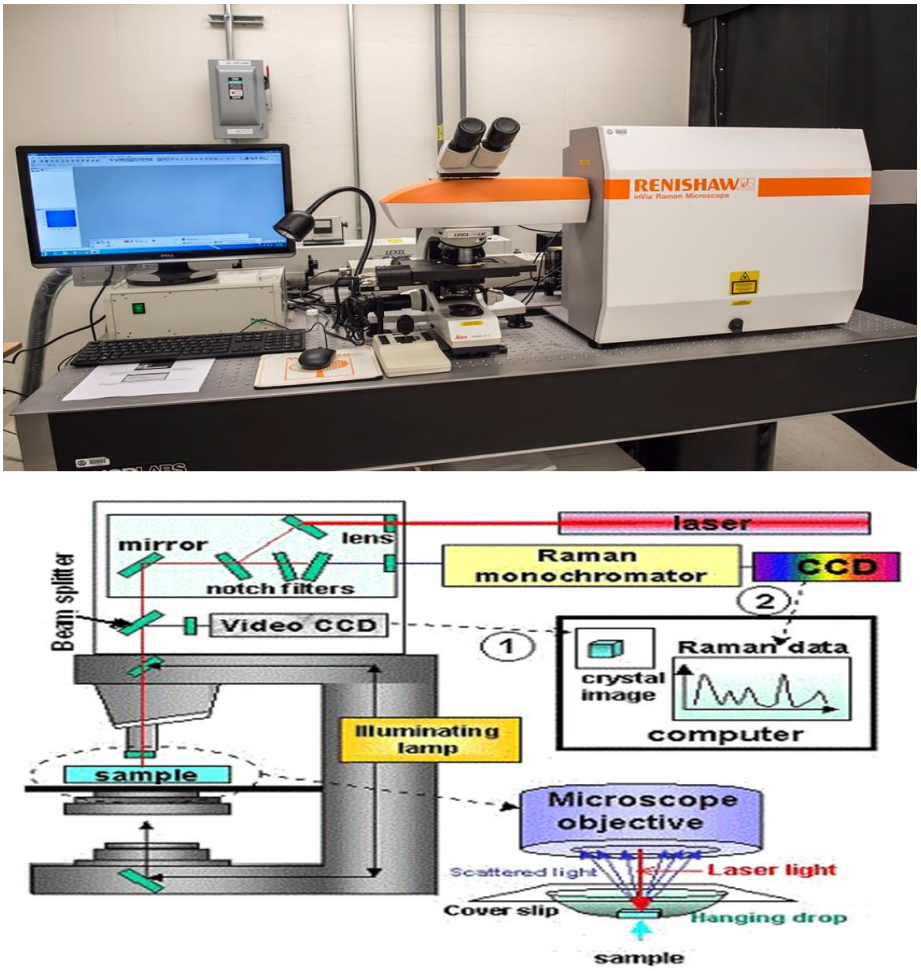

Figure 3.2 Raman microscopy (up) and schematic drawing of a Raman microscope (down).

J-V curves were obtained by illuminating the solar cells under a Solar Light Co. 300 W Air Mass Solar Simulator Model 16S-300 (1sun, 1000 $W \cdot m^{-2}$) calibrated using an Optopolymer Si reference cell as shown in figure 3.3. The curves were recorded with an Autolab PG-STAT-30 potentiostat under a 150 mV·s-1 scan rate see Figure 3.4. Figure 3.5 shows the complete system of J-V curves measurement.

Figure 3.3 Solar Simulator Model 16S-300

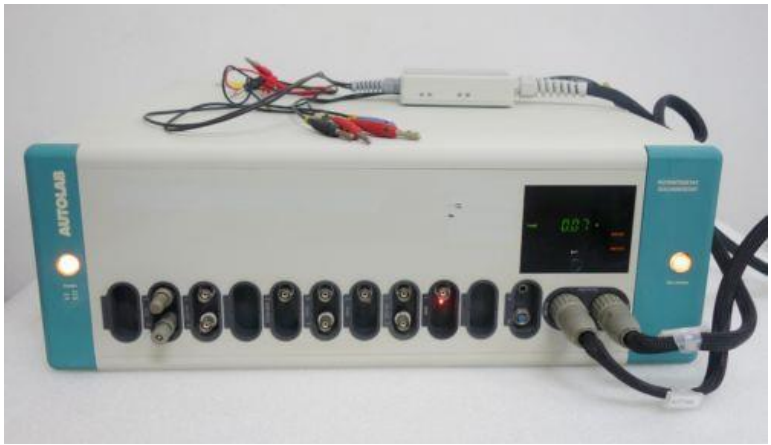

Figure 3.4 Autolab PG-STAT-30 potentiostat

Figure 3.5 Complete system of J-V curves measurement.

The measurements were carried out using Ossila's Push-Fit Test Board for Photovoltaic Substrates with a 0.12 cm^2 aperture mask.

Ultra Violet Photoelectron Spectroscopy. The UPS studies were performed in a UHV chamber with a SPECS LHS-10 hemispherical electron analyzer. The UPS spectra were obtained using HeI irradiation with hν=21.22eV produced by a UV source (model UVS 10/35). During UPS measurements the analyzer was working at the Constant Retarding Ratio (CRR) mode, with CRR=10. A bias of −12.29 V was applied to the sample in order to avoid interference of the spectrometer threshold in the UPS spectra. The high and low binding energy cutoff positions were assigned by fitting straight lines on the high and low energy cutoffs of the spectra and determining their intersections with the binding energy axis. Regarding measurement errors it should be noted that an error of ±0.1 eV is assigned to the absolute values for ionization energies, work function and other UP-spectra cutoff features where the error margin is significant, due to the process of fitting straight lines.

X-Ray Diffraction characterization was realized on a Siemens D-500 powder diffractometer see Figure 3.6, that operates with Cu Kα1 (λ = 1.5406 Å) and Cu Kα2 (λ = 1.5444 Å) radiation. Data were collected in Bragg-Brentano mode over the angular range 5° ≤ 2θ ≤ 80° counting for 3 s at each step of 0.03° in detector position.

Absorbance measurements were carried on a UV-Vis Hitachi 3010 spectrophotometer as shown in Figure 3.7 equipped with a 60 mm diameter integrating sphere, ($BaSO_4$) was used as a reference. The reflectance data were transformed in Kubelka–Munk absorbance units.

Figure 3.6 Siemens X-Ray Diffraction D-500 powder diffractometer

Figure 3.7 UV-Vis Hitachi 3010

Scanning Electron Microscopy analysis was conducted with a field emission scanning electron microscope (JSM 7401F, JEOL Ltd.,Tokyo, Japan), equipped with Gentle Beam mode as shown in Figure 3.8.

Figure 3.8 scanning electron microscope (JSM 7401F, JEOL Ltd.,Tokyo, Japan)

Sunlight saturation experiments was done in the ATLAS SUNTEST CPS+ solar simulator, equipped with a xenon lamp covering the 300 nm-800 nm spectral range with of 765 $W \cdot m^{-2}$ incident irradiance see Figure 3.9.

Figure 3.9 ATLAS SUNTEST CPS+ solar simulator

Sonication process was performed by pro-sonic sonicator see Figure 3.10.

Spin coating process was performed by Ossila spin coater as shown in Figure 3.11.

Figure 3.10 Sonication device

Figure 3.11 Spin coating device

The perovskite absorber layer and hole transporting layer were fabricated inside a Glove box shown in Figure 3.12

Thermal evaporation process was performed by thermal evaporator shown in Figure 3.13.

Figure 3.12 Glove box

Figure 3.13 Thermal evaporator

Laboratory system used for experimental verification

A 5.5 kW Synchronous reluctance motoer (SynRM) is connected with a 9.3 kW induction motor via a torque sensor unit. The SynRM is driven through a three-phase voltage source inverter. A DS1103 unit used for driving the SynRM. The motor speed is measured via an incremental encoder of 1024 sample/revolution. The SynRM currents are measured through three identical current sensors (LA25-P). A power analyzer is used for measuring the electrical components of the system i.e. voltage, current, power factor etc.

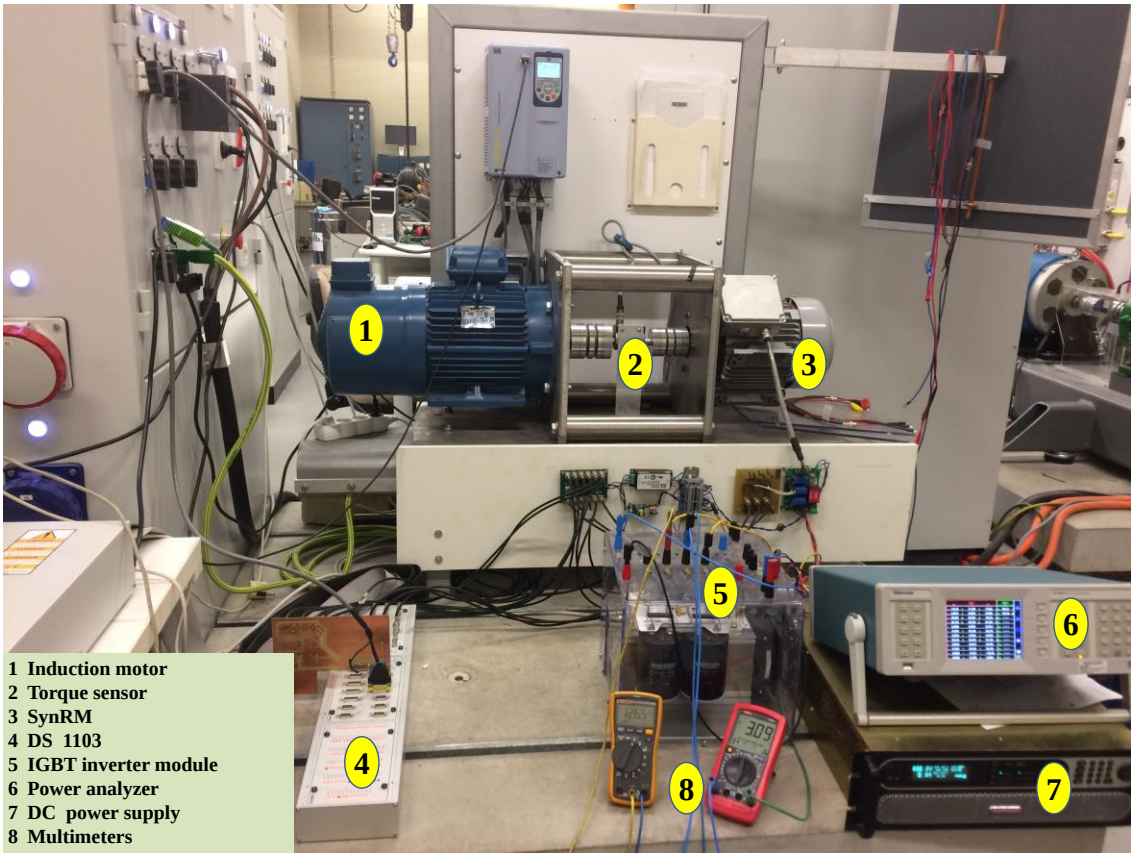

Figure3.14 Laboratory system used for experimental verification

4 Chapter 4

4 High Effeicient Perovskite Solar cells Based on Interface Engineering

4.1 Preface:

Perovskite solar cells have been undoubtedly leading the efficiency race among other, solution processed, 3rd generation photovoltaics (PV). Emerging from the solid state DSSCs by completely substituting a solution processed perovskite absorber for the chemisorbed molecular dye monolayer[1-4] they have been remarkably improved, exceeding a 22% PCE within only a few years[5,6] showing also improved stability[7] and fabrication versatility.[8,9,10] However, various phenomena such as the origin of hysteresis [11,12,13] and the nature of perovskites' degradation [14,15] are under intense study. A vast number of reports are being published towards optimizing the performance of the PSCs, since they constitute the most promising 3rd generation PV technology, towards replacing silicon solar cells with a low cost, eco-friendly and readily implemented alternative. In this context, many studies for the optimization of the PSCs focus on modification of the interfaces between the absorber and the electron and hole transport layers, ETL and HTL, correspondingly.[16-18] As concerns the ETL, titanium dioxide is the most commonly employed material, since it is low cost, it presents suitable energy bands position against the most popular absorbers, it can be readily synthesized by several solution-processed routes and it forms highly transparent and homogenous films. However, it has a rather low conductivity and electron mobility, which are unfavorable for the electron transport and collection. Besides, it has many defects such as oxygen vacancies, Ti^{+3} ions and grain boundaries, which act as charge traps and result in high recombination rates of photogenerated carriers. Moreover, it presents an

outstanding UV-photocatalytic behavior, thus contributing significantly to the degradation of the PSCs by decomposing the organic groups employed.[19] Therefore, various modifications of the TiO_2 ETL have been proposed, such as element doping [20-22] interface passivation [23-25] heterojunction structures [26,27] while various organic compounds, e.g HOCO-R-$NH^{3+}I^-$, 3-aminopropanoic acid, silane self-assembled monolayer (SAM) etc., have been also introduced towards modifying the ETL/perovskite interface [28-31] in order to facilitate electron transfer, reduce charges recombination, passivate the titania layer and improve perovskite crystallization.

4.2 Experimental Methods

Fabrication of perovskite solar cells. The PSCs were fabricated by depositing the successive layers upon 20mmx15mm FTO conductive substrates (Aldrich, 7 Ohm/□). The FTO were patterned with a 2M aqueous HCl solution in combination with zinc powder and were carefully cleaned and sonicated into a bath with Triton-X, acetone, 2-propanol and UV ozone in 15 min cycles. The TiO2 ETL was spin coated at 2000 r.p.m. for 60s from a mildly acidic solution of titanium (IV) isopropoxide (Aldrich, 97%) in ethanol. The films obtained, were annealed for 45 min at 500oC under a 5oCmin-1 temperature ramp rate. To modify the films with the metal-free organic (E)-3-(5-(4-(bis(2',4'-dibutoxy-[1,1'-biphenyl]-4-yl)amino)phenyl)thiophen-2-yl)-2-cyanoacrylic acid (D35) dye, we immersed them overnight into a 4mol L-1 ethanolic solution. Subsequently, we sonicated them for 10min into ethanol in order to discard the dye molecules not chemically bonded with the titania substrate. Then, the films were dried under Ar flux and transferred into an Ar-filled glove box for the further experimental procedures. The $CH_3NH_3PbI_3$ layer was deposited by spin coating in an one-step procedure a perovskite solution in anhydrous N,N-dimethylformamide, containing a 40wt% Methylammonium iodide (Dyesol) along with Lead acetate trihydrate ($PbAc_2.3H_2O$, 99.999% trace metals basis, Aldrich) in a 3:1molar ratio. A small amount of

hypophosphorous acid (50% w/w, aquatic solution, Alfa Aesar) was also added to the perovskite solution so as the final molar ratio of HPA:$PbAc_2$ to be 1:4. The procedure was carried out at 2000rpm for 45s. The films were left to dry at room temperature for 10 min and were annealed at 100oC for 5 min. Finally, a 7wt% Spiro-MeOTAD (Solaronix) solution in chlorobenzene was deposited as the hole transport layer, containing additives of lithium bis(trifluoromethanesulfonyl)imide lithium salt (≥99%, Aldrich) in acetonitrile and 4-tert-butylpyridine (96%, Aldrich). The deposition was realized at 3000 r.p.m for 30s. Finally, the devices were transferred outside the glove-box and six 100nm silver electrodes were thermally evaporated under vacuum of 10^{-6} Torr, at a rate of ~1Å s^{-1}.

4.3 Results and discussions

In this chapter, we report on a planar PSC of improved efficiency and stability, based on dye-modified titanium dioxide electron transport layer. We thus propose an innovative engineering approach, introducing the concept of organic dye-sensitization for optimizing the compact layer/perovskite interface, stemming from our recent publication of utilizing a triazine-substituted zinc porphyrin as an ETL layer [32] and the effective passivation of NiO_x HTL surface by the N719 organometallic dye. [33] More specifically, we chemisorbed D35, a triphenylamine (TPA)-based D-π-A dye [consisting of an electron donor (D, TPA unit), a conjugated linker (π, thiophene group), and an electron acceptor (A, cyanoacrylic acid group), Figure 4.1a (right, large inset)] from an ethanol solution on the compact titania layer in order to both improve electron transfer and affect the crystallization process of the perovskite layer. The D35 is a widely known metal-free organic dye, mainly used as a sensitizer in liquid or solid-state DSSCs and is characterized by a high molar extinction coefficient, thus can work effectively in cooperation with a thin titania ETL. [34-37] Moreover, D35 is an efficient sensitizer (with and without chenodeoxycholic acid-CDCA coadsorbent), since its butoxyl chains effectively protect the semiconductor by providing self-

assembly and permitting the formation of an aggregate-free dye layer on the TiO2 surface, acting also as an insulating hydrophobic shield that keeps oxidized species at a distance from the TiO2 surface, suppressing the electron recombination.[38] These properties render it a suitable material regarding to TiO_2 dye modification and employment in the PSC field, as the dye interface engineering approach apart from creating a smooth ETL, is expected to facilitate the charge electron transfer, favor the growth of homogeneous and smooth perovskite layers consisting of robust and homogenously distributed crystals, while it's hydrophobic nature may act as a moisture shield promoting the device stability.

Therefore, we fabricated planar PSC devices employing D35 in the ETL. The structure we followed is depicted in Figure 1a (left), while the perovskite absorber was deposited by a single step-procedure using lead-acetate as the lead-containing precursor.[39] The deposition of the perovskite was performed inside an Ar-filled glove box (H_2O and O_2 contents < 1 ppm) while the cathode electrodes deposition and the photovoltaic measurements were realized in ambient conditions. The fabricated planar perovskite solar cells with the D35 modified titania ETL, presented a stabilized ~13 % PCE for the champion device, along with an improved air-stability after prolonged storage inside a desiccator. The dye chemisorption via a covalent bond, since the bidentate bridge binding (Figure 1a, small inset) is the most likely adsorption mode for D35 on the TiO_2 surface,[40] eliminates the adsorbed water molecules from the titania surface (that can promote the degradation of the top perovskite absorber), offering additional stability in the PSC devices retaining at least 50% of its initial PCE, after 80 days.

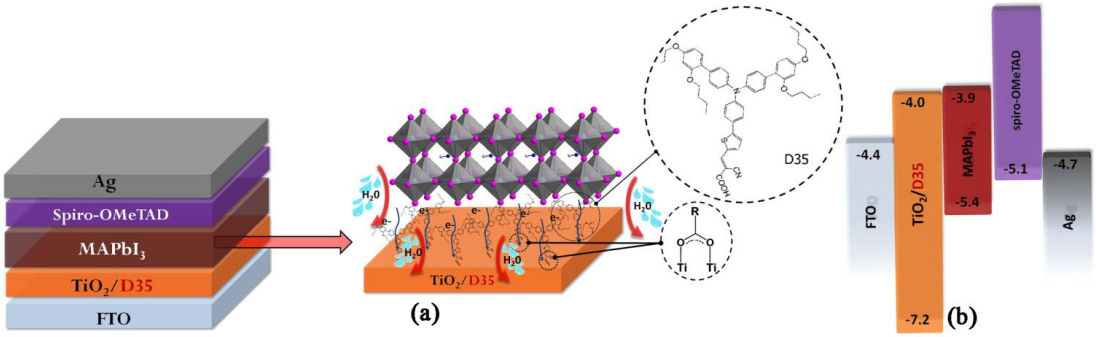

Figure 4.1 (a) The planar PSC architecture (left) using a D35/TiO_2 underlayer beneath the $MAPbI_3$ absorber (right). (b) The corresponding energy bands diagram. The values of the TiO_2, D35 and spiro-OMeTAD were determined using UPS and UV-vis data.

At first, experiments confirming the presence of the dye molecules on TiO_2 were conducted. In this context, FTO/TiO_2 compact layers with and without chemisorbed D35 dye were examined. The dye is obvious macroscopically by the naked eye (light orange color in Figure 4.2) and results in a slight decrease of the electrode transmittance in the UV-Vis region (Figure 4.3), as well as a small red shift of the main absorption maximum around 470nm which is attributed to a single strong HOMO→LUMO excitation, Figure 4-8d. However, its contribution in the total light absorbance of the photoelectrode is negligible, in agreement with the monolayer dye coverage onto a very thin (around 50 nm) compact layer. On the contrary, UV-vis reflectance measurements carried out on 4μm mesoporous titania layers (Figure 4.4), show strong visible absorption along with a bathochromic shift (at 490nm), due to the electron coupling derived from the strongest interaction among the dye molecules and the titania. Therefore, the presence of the dye is not expected to affect significantly the corresponding device performance.

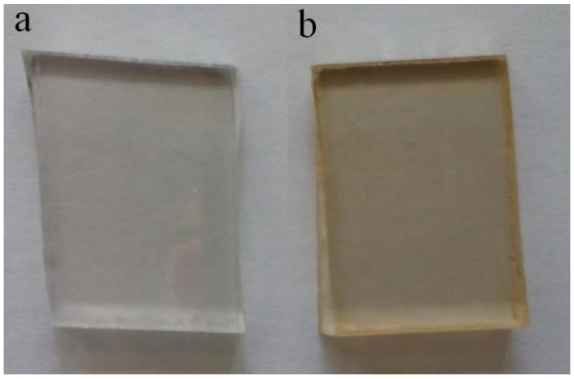

Figure 4.2 Optical images of (a) TiO_2 and (b)TiO_2/D35 films upon FTO glasses. The slightly orange colored film in the latter case reveals the presence of the D35, chemisorbed upon the titania substrate.

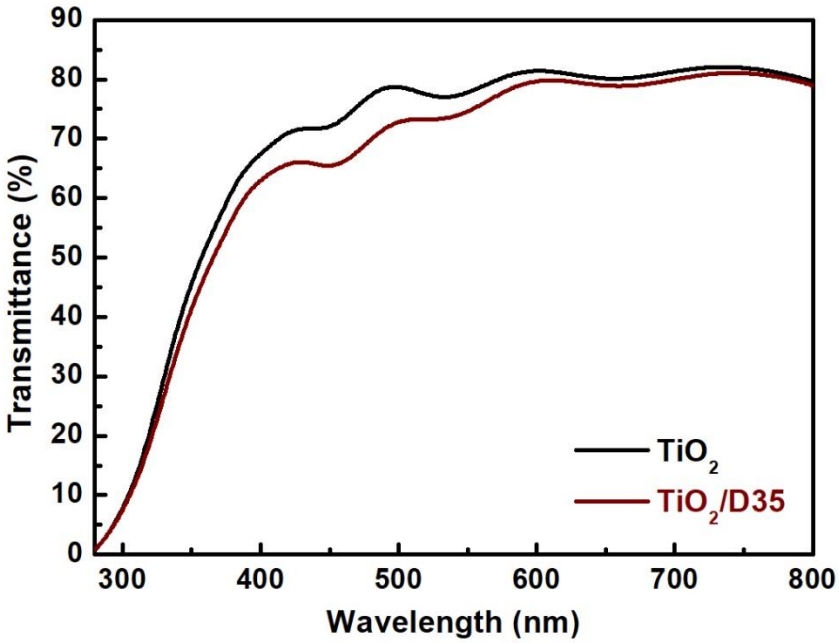

Figure 4.3 Transmission spectra of TiO_2 films, modified with and without D35over FTO glasses

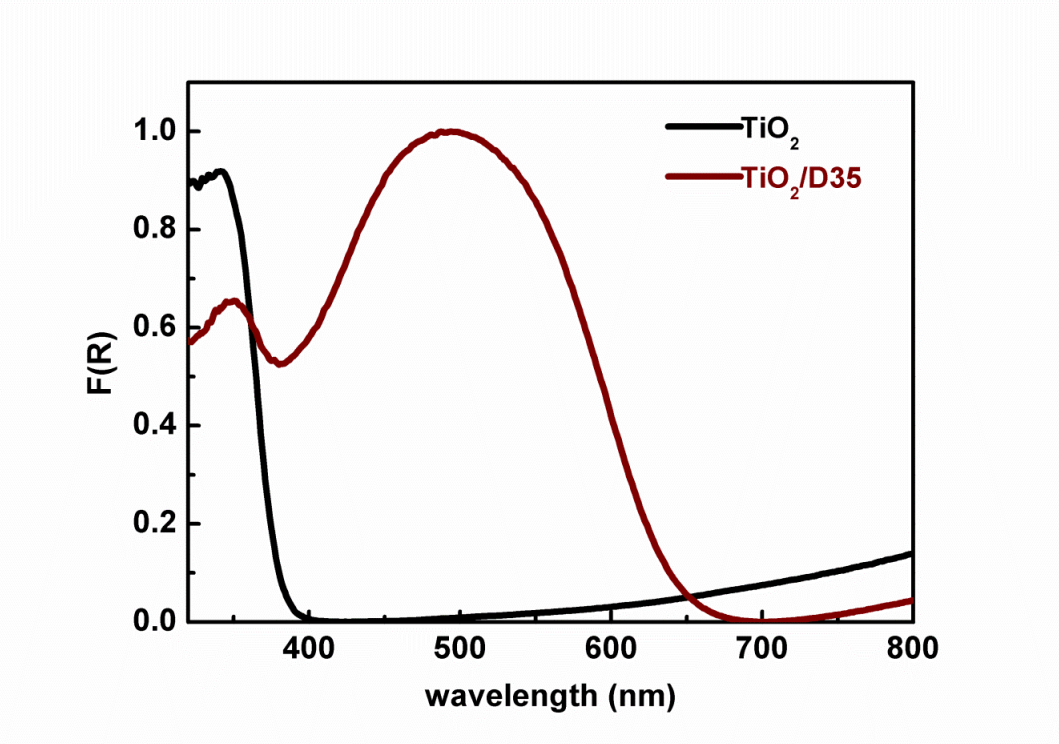

Figure 4.4 UV-vis diffuse reflectance spectra F(R) curves of TiO_2 and TiO_2-D35 films.

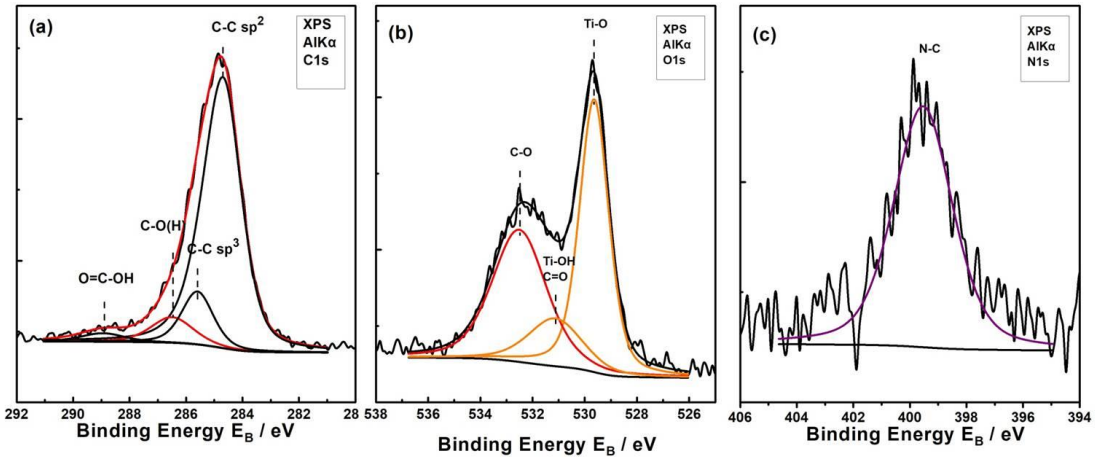

Figure 4.5 a) XP spectra of C1s, (b) O1s and (c) N1s of the TiO_2/D35 sample.

The chemisorption of the dye was also confirmed by X-ray photoelectron spectroscopy (XPS). More specifically, XPS analysis was performed on a FTO/TiO_2/D35 samples. Detailed spectra of C1s, O1s and N1s are shown in Figure 4.5. The C1s peak is deconvoluted into four components assigned to carbon-carbon bonds in sp^2 and sp^3 configuration at

284.5eV and 285.3eV respectively, and carbon-oxygen bond in epoxides at 286.8eV and carboxyls at 291.0eV.[41] 291.0eV. The O1s peak is deconvoluted into three components assigned to Ti-O bonds at 529.6eV, to C=O and Ti-OH bonds at 531.1eV and to C-O at 532.5eV.[42] The N1s peak is centered at 399.5eV assigned to carbon-nitrogen bonds (amide groups).[43] From the intensity (peak area) of the C1s and N1s photoelectron peaks, divided by the experimental sensitivity factors corrected for the transmission characteristics of the EA10 energy analyzer, the C:N atomic ratio is about 40, close to the nominal value of 30. In addition, Figure 4.8 (a,b,c) shows the ultraviolet photoelectron spectroscopy (UPS) measurements performed over FTO/TiO_2 and FTO/TiO_2/D35 samples. The high (Fig.4.8a) and low (Fig.4.8c) binding energy cutoffs are depicted, from which the work function and the ionization potential were determined.[44] As emerged from the UPS data, the work function (Wf) of the D35 modified ETL is lowered by 0.1 eV compared to the bare TiO_2 one, while the valence band maximum is located at 3.3 eV for both samples. The Wf shift, expected to slightly affect the open-circuit voltage value,[45,46] is well attributed to the presence of the D35 dipole moment pointing away from the TiO_2 layer, a fact also confirmed by density functional theory (DFT) calculations (Fig. 4.6).[47,48]

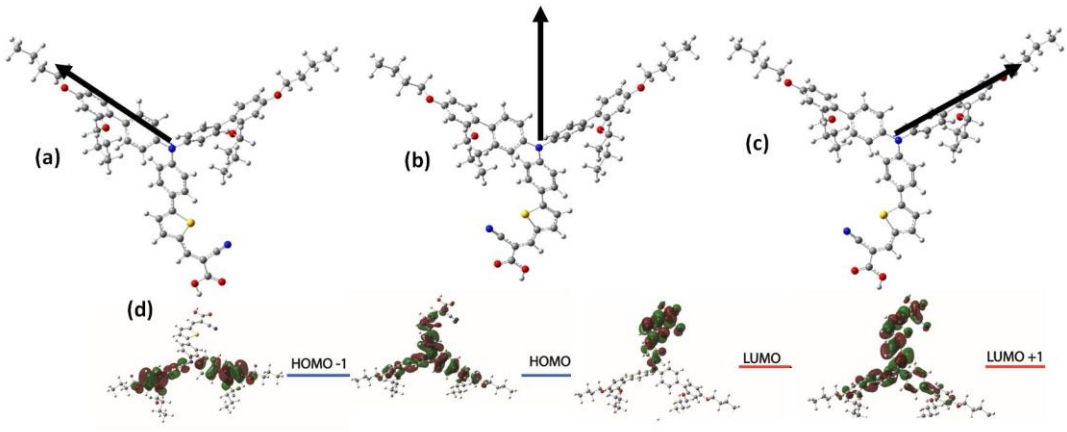

Figure 4.6 Geometry optimization and the corresponding dipole moment vectors of D35 dye (top) in (a) conformation 1, (c) conformation 2, and (b) simulated average between both conformations. (d) Visualization of the HOMO-1, HOMO, LUMO and LUMO+1 atomic orbitals of the investigated compound at the CAM-B3LYP/ 6-31G(d,p) level.

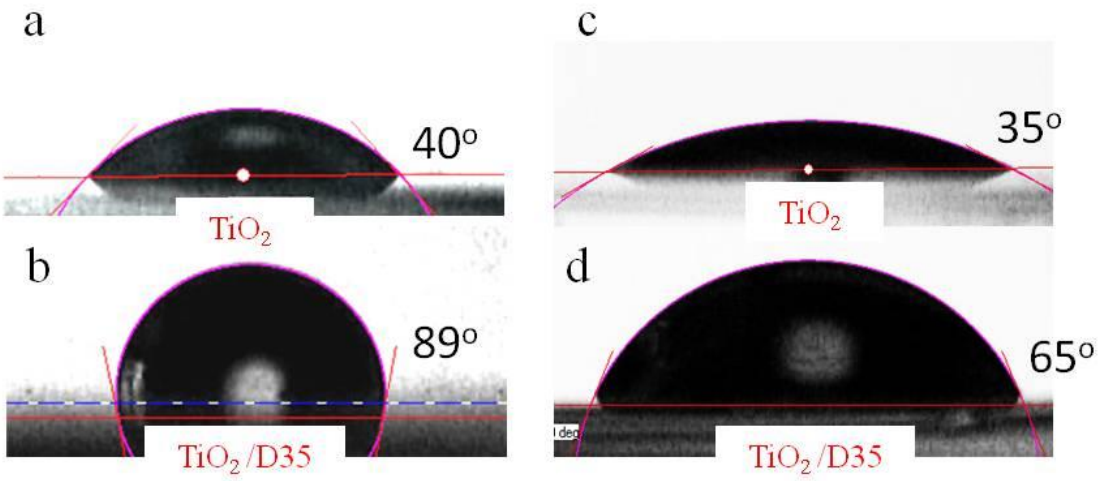

Figure 4.7 Contact angle measurements of (a,b) water and (c,d) DMF upon TiO_2 surfaces with and without D35 modification.

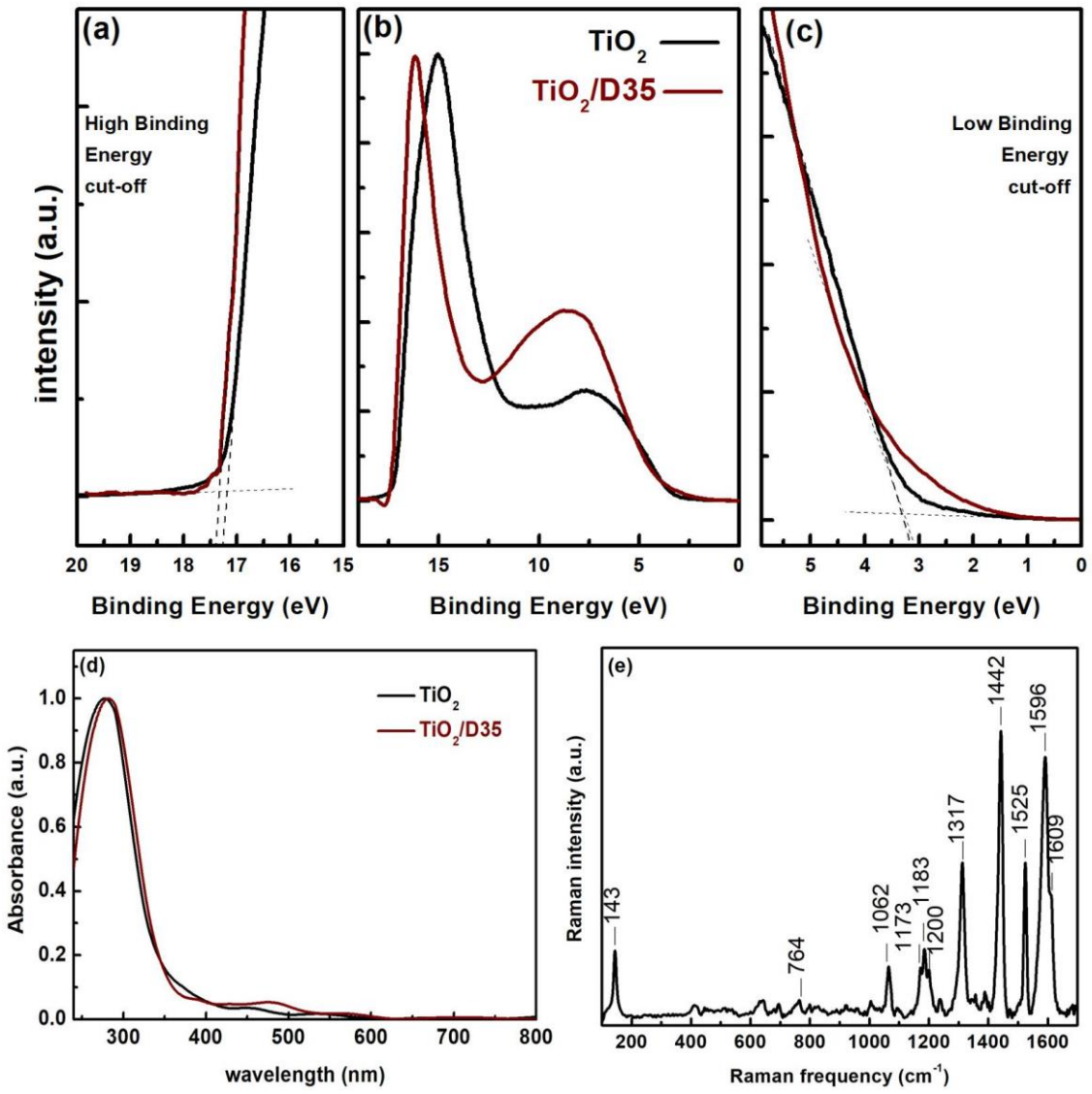

Figure 4.8 (a,b,c) UP spectra of the TiO_2 and TiO_2/D35 samples. The high (a) and low (c) binding energy cutoffs are magnified for clarity. (d) Absorption spectra of compact TiO_2 films, modified with and without D35 over FTO glasses. (e) Raman spectrum (from 100 up to 1700 cm^{-1}) of a D35 sensitized compact TiO_2 film.

Moreover, the extended Raman spectrum was obtained by focusing the laser beam onto the D35 sensitized film. The Raman vibrations are masked by the strong photoluminescence (PL) signal of the dye. PL background subtraction in the 100-1700 cm^{-1} frequency range yields the Raman spectrum of Fig. 4.8e. Below 650 cm^{-1}, the vibrational modes of titania anatase are observed, the strongest being the E1g mode, at 143 cm^{-1}.[49] The characteristic fingerprint

bands of the D35 dye are present in the 1000 – 1600 cm^{-1} range: Phenyl ring deformation at 1062 cm^{-1}, C-C stretching vibrations at 1173, 1183 and 1200 cm^{-1}, C–N vibration at 1317 cm^{-1}, a strong band at 1442 cm^{-1} in the CH bending range and the high energy bands at 1525, 1593 and 1609 cm^{-1} which are assigned to C=C stretching vibrations of the phenyl rings, the strongest of them, at 1596 cm^{-1}, is due to the triphenylamine unit.[50] Above this frequency range only two weak Raman peaks are resolved, at 2216 (ν(C≡C)) and 2964 cm^{-1} (ν (C−H)).

The light absorption of the $MAPbI_3$ on pristine and D35-modified TiO_2 substrates is shown in Fig. 4.11a. Upon dye-sensitization the shape of the spectrum doesn't change, which indicates that there is no additional absorption from the D35 dye (see Figure 4.4). On the contrary, it is clear that absorbance from perovskite itself is enhanced in all spectral range and this is attributed to better crystallization of the perovskite due to the dye underlayer. Perovskite polycrystals grown on TiO_2 and D35/TiO_2 substrates were investigated by X-ray diffraction (XRD) measurements. Figure 4.11b shows the XRD patterns of the two films as well as the theoretical peaks of tetragonal $MAPbI_3$ in the form of histograms. Both samples contain crystalline $MAPbI_3$ and only a slight but clear difference in the full-width at half maximum (FWHM) values for the perovskite is observed between them [e.g. for the reflection at $2\theta = 28°$ FHWM(TiO_2/D35) = 0.106(2)° and FHWM(TiO_2) = 0.134(2)°], confirming higher crystallinity for the perovskite film grown on the dye-sensitized titania substrate. This is in agreement with SEM analysis depicting higher size of crystallites. Thus, higher crystal quality can be expected as a result of a lower number of strains ensuing from structural defects.

The presence of the chemisorbed D35 dye strongly influences the properties of the compact layer substrate and therefore it is expected to affect the perovskite crystallization. In fact, in the one-step solution process the perovskite precursors are evenly mixed and coated upon the substrates. Crystallization is controlled by the nucleation of the perovskite films on the titania

underlayer, and subsequently the procedure can be affected by modifying the compact layer properties, e.g. hydrophilicity. Thus, in order to examine the wettability of the TiO_2 layer, contact angle measurements were carried out on both a bare TiO_2/FTO and a TiO_2/D35/FTO samples. As we can see in Figure 4.7, the mean contact angle (of water drops) increased significantly (from 40^o to 89^o) after sensitizing the titania substrate with D35, indicating a major decrease in surface hydrophilicity. This is in agreement with atomic force microscopy (AFM) image analysis (not shown) confirming a slight decrease in surface roughness. Moreover, the hydrophobic treatment of the compact ETL seems to affect significantly the formation of the perovskite, since, as depicted in SEM and AFM images (Figures 4.11c and 4.11d respectively), large and well distributed $MAPbI_3$ grains are formed over the TiO_2/D35 layer (AFM and SEM images of $MAPbI_3$ films grown on pristine TiO_2 substrate are presented in Fig. 4.9), creating a smooth and robust perovskite film.

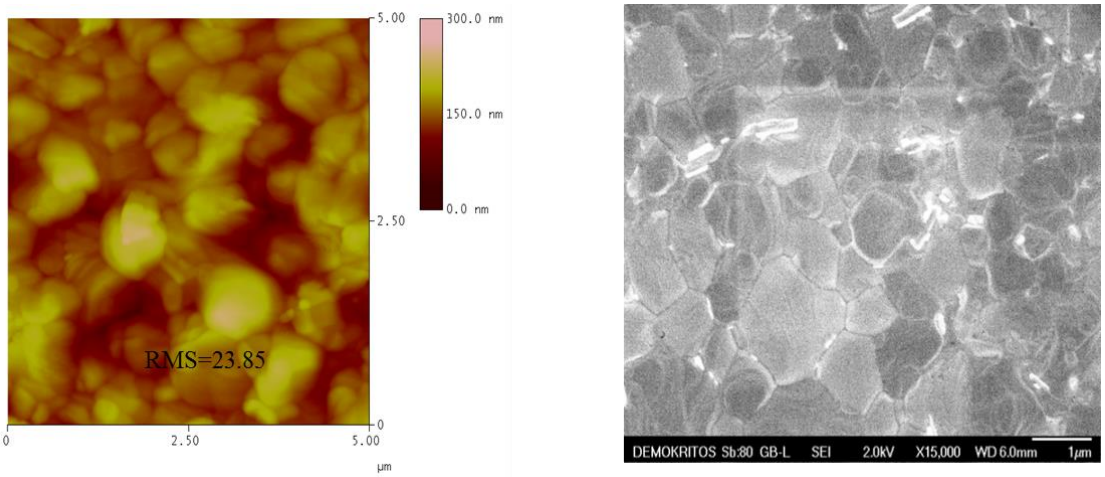

Figure 4.9 AFM (5x5 μm2) surface topography (left) and SEM (right) images of $MAPbI_3$ films grown on a TiO_2 substrate.

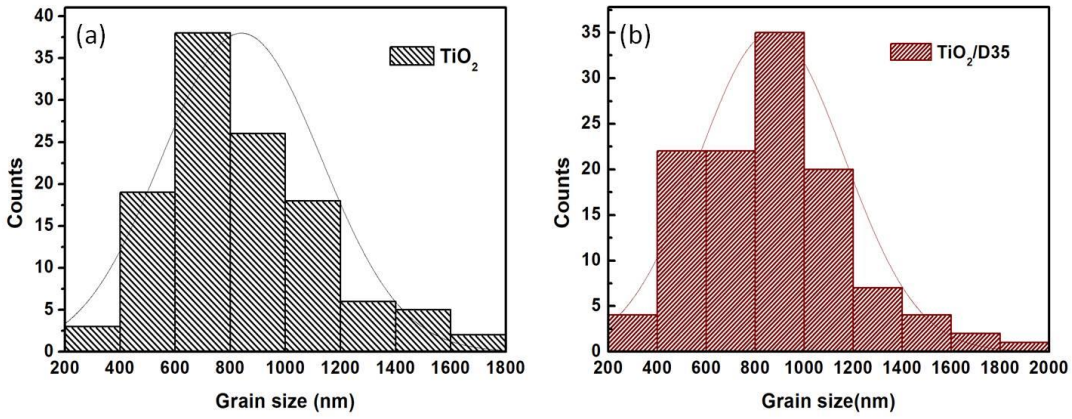

Figure 4.10 Size distribution of $MAPbI_3$ grains grown upon (a) TiO_2 and (b) TiO_2/D35 substrates.

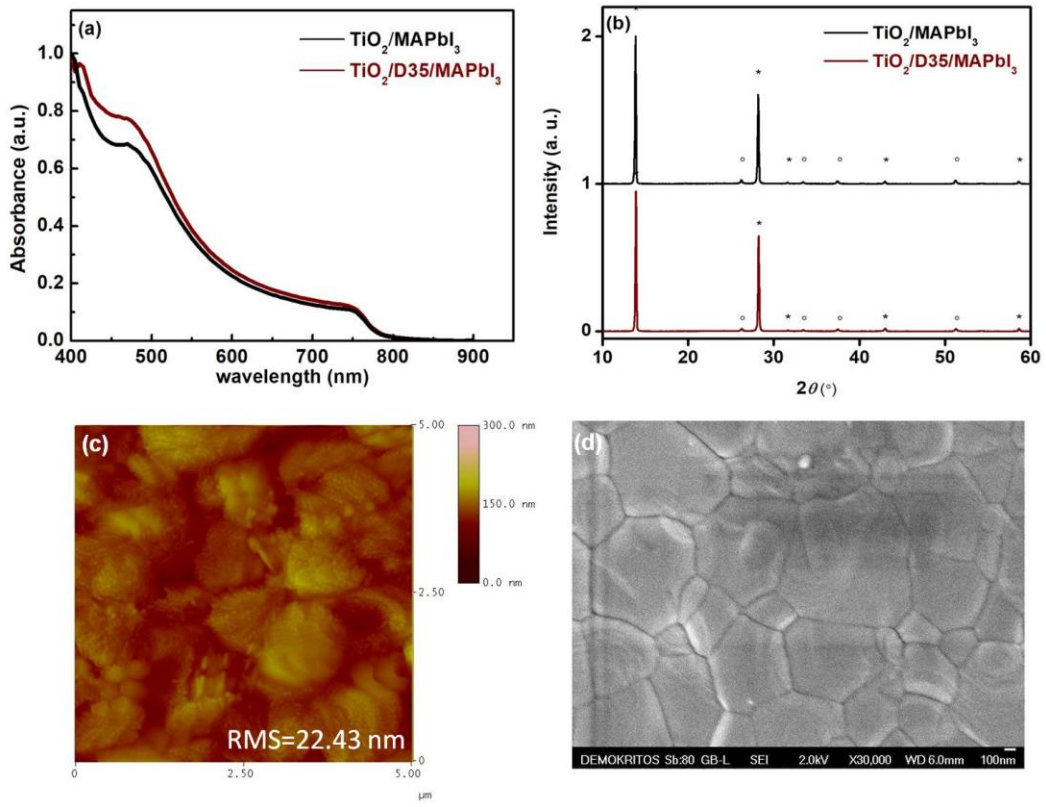

Figure 4.11 (a) Absorption spectra of $MAPbI_3$ perovskite films grown on pristine and D35-modified TiO_2 substrates. (b) Corresponding XRD patterns (stars and open circles denote

$MAPbI_3$ and SnO_2 peaks, respectively). (c) AFM (5x5 μm^2) surface topography and (d) SEM image of $MAPbI_3$ absorber on the TiO_2 /D35 substrate.

Smoothness and hydrophobicity characterizing the dye-modified TiO_2, apart from shielding perovskite and titania layers from moisture penetration, also lead to perovskite films with larger grains. In fact, lower surface tension is related to the existence of a lower number of nucleation sites on the non-wetting surfaces (compared to the unmodified hydrophilic ones).[51] As derived from Fig. 4.10, in the case of the neat TiO_2 the perovskite average grain size is 840nm in contrast with the D35-modified one, where the average size is 865nm. This small difference proves that that the more hydrophobic substrate favors the growth of perovskite films with larger grains.

The developed perovskite photoelectrodes (FTO/TiO_2/D35/$MAPbI_3$) were incorporated in solar cells (PSCs) employing Spiro-OMeTAD as hole transporting material (HTM) and thermally evaporated silver (Ag) as counter electrode. The photovoltaic performance of the corresponding planar devices was evaluated via current-voltage (J-V) measurements under 1 sun (A.M. 1.5G) illumination conditions (Figure 4.12a) and the obtained parameters upon reverse scans are summarized on Table 4.1. The short circuit photocurrent density measured for the D35-sensitized device reached a value of 22.53 mA cm^{-2}, outperforming that of the corresponding solar cell based on the pristine TiO_2 (20.94 mA cm^{-2}). This 8% enhancement confirms the beneficial role of the chemisorbed D35 dye molecules at the compact layer/perovskite interface for photocurrent improvement. Moreover, the open-circuit voltage (Voc) values were also slightly increased (by about 30 mV), and this can be attributed to the lowering of the Wf, as observed in the UPS measurements. Finally, the fill factor (FF) showed also a slight increase, probably due to improved surface quality (lower roughness) of the perovskite layer. Thus, a power conversion efficiency of 17.04 % was determined for the champion device. The observed significant performance increase (13%) with respect to the

non-sensitized cell was further confirmed by statistical analysis of the results corresponding to 30 solar cells with and 30 cells without dye sensitization of titania. As depicted in Fig. 12c, the statistical analysis of the photovoltaic parameters, including maximum, minimum and mean and median values along with the dispersion of the interquartile range, clearly demonstrates that the chemisorbed D35 dye molecules at the compact layer/perovskite interface have remarkable contribution in the cell performance improvement. This enhancement might be attributed to a series of different reasons including charge electron transfer facilitation (via energy states), roughness reduction, dipole moment effects, improved perovskite crystallinity, defect passivation and humidity/UV protection.

Table 4-1 Mean values and standard deviation of photovoltaic parameters for solar cells prepared with bare TiO_2 and D35-modified TiO_2 electron transport layers. Values inside brackets refer to the champion devices. VOC: open-circuit voltage, JSC: short-circuit current density, FF: fill factor, PCE: power conversion efficiency. All values are derived from reverse scans.

Device	Jsc(mA cm-2)	Voc (V)	FF	PCE (%)
TiO_2	19.21±1.86 (20.54)	0.97±0.05 (1.02)	0.65±0.05 (0.71)	12.20±1.57 (15.04)
TiO_2/D35	21.19±1.17 (22.53)	0.99±0.04 (1.05)	0.69±0.04 (0.72)	14.43±1.96 (17.04)

According to the literature,[52] the improvement in PSCs' performance may be attributed to the chemical reactions/interactions between the perovskite and terminal/functional groups of surface modifiers. This is a very intriguing approach; however such a mechanism remains unclear in the literature. On the contrary, the existence of dipole moment perpendicular to the interface may be the reason for the larger crystallites and/or reduction of strain effects. This hypothesis is further corroborated by the relative low roughness of the titania modified

surface permitting easier deposition of the perovskite absorber as well as by the hydrophobic character of the chemisorbed D35 dye, repelling unwanted water molecules that would deteriorate the morphology of the perovskite layer. In addition, the presence of such a significant dipole moment makes the vectorial electron transfer across the modified titania-perovskite interface possible.[53,54] Such a dye mediated vectorial transfer is facilitated by possible defect annihilation/neutralization at dye binding sites.

In order to get further insight into the operation of the novel devices, we conducted Incident Photon-to-Current efficiency (IPCE) measurements. As depicted in Figure 4.4b, the action spectrum of the D35 based device presents higher quantum efficiency reaching 95% at 450 nm and exceeding 80% almost in the whole 750nm-420nm region.

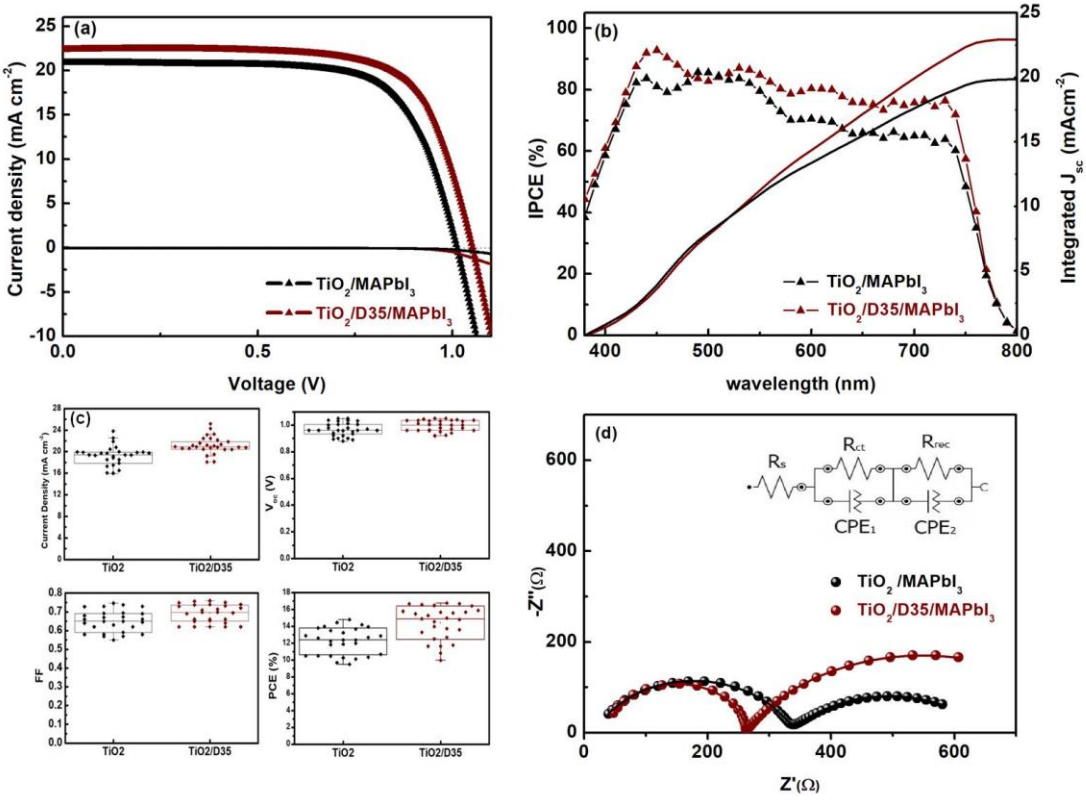

Figure 4.12 (a) Reverse scan J-V plots obtained for planar PSCs using the MAPbI3 absorber grown on pristine and D35-modified compact TiO2 substrates. (b) Corresponding

IPCE spectra and integration currents. (c) Box chart comparison of PSC parameters. (d) Nyquist plots registered under 1 sun illumination conditions.

The IPCE enhancement can be attributed to the improved electron extraction capability of the TiO_2/D35 ETL, leading to a better injection of electrons generated by the long-wavelength part of the excitation spectrum. As reported elsewhere, if the extraction ability of ETL is poor, these low energy photogenerated electrons can be easily trapped into the perovskite layer prior to be injected into the ETL.[55] Moreover, in Fig. 4-12b, the integration of the action spectra on the entire wavelength region, considering one sun irradiation intensity (100mW cm-2, A.M. 1.5G), results in photocurrent density consistent with the Jsc values (deviation smaller than 2%), obtained by the J-V curves, thus confirming the accuracy of the J-V measurements. Furthermore, the stabilized output current corresponding to the maximum power point (MPP) of the J-V plots was determined for devices with TiO_2 and TiO_2/D35 as the electron transport layer. The results as presented in Figure 4.13, depict a similar exponential trend for the two devices with a final PCE loss of 25% for both, attributed to the accumulated capacitive current.[56] Moreover, reverse and forward scans show that the cells are characterized by significant hysteresis. This is a well-known effect in $MAPbI_3$ perovskite especially accompanying planar PSCs, attributed to the low conductivity of compact TiO_2 provoking a significant imbalance between electron and hole flux through the device,[57] and to the existence of electrode polarization from increased capacitance currents.[54] In order to avoid the errors introduced in the PCE determination by the hysteresis effects, we report stabilized output efficiencies of the champions cells equal to 11.21% for those based on pristine TiO_2 relative to 12.92% for those based on sensitized TiO_2, which also makes a 13% improvement. However, PSC devices employing the TiO_2/D35 ETL present a slight decrease in the hysteresis, attributed to the increased

conductivity of titania and the reduction of reactive sites in the interface with the $MAPbI_3$ resulting from the presence of the D35.

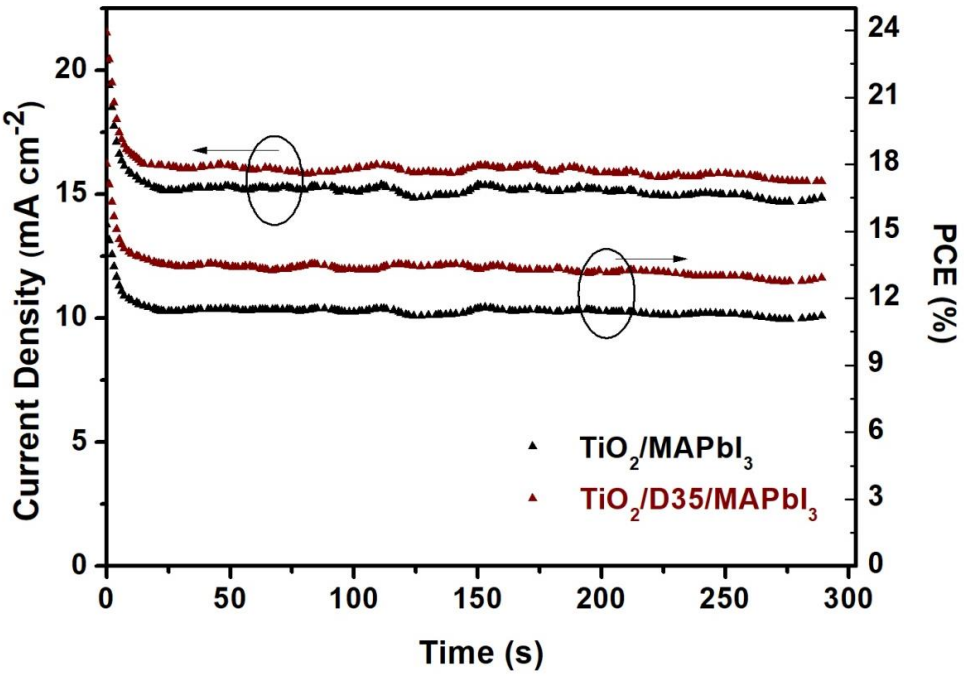

Figure 4.13 The current density and the PCE at the MPP of the TiO_2 and the TiO_2/D35 samples.

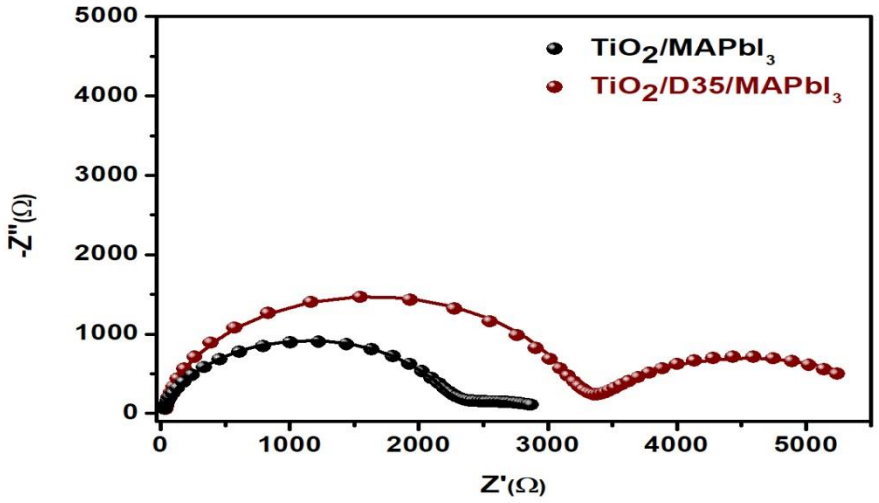

Figure 4.14 Nyquist plots under dark conditions of $MAPbI_3$-based solar cells with compact TiO_2 and TiO_2/D35 as the ETL.

Table 4-2 Resistance parameters as derived from the simulation of the Nyquist plots.

		Rs (ohm)	R_{ct} (ohm)	R_{rec} (ohm)
Light conditions (100 $mWcm^{-2}$)	TiO_2/D35	47.89	224	573
	TiO_2	39.4	316	321
Dark conditions	TiO_2/D35	39.86	2690	3170
	TiO_2	30.54	753	2190

The improved performance of the D35-modified solar cells was also confirmed by Electrochemical Impedance Spectroscopy (EIS) measurements, conducted under open-circuit conditions in dark and under 100mW cm^{-2} illumination conditions. Figure 4.12d shows the Nyquist plots taken while illuminating the solar cells in the 1MHz-0.1Hz range under a 10mV AC perturbation. Even though EIS is a cumulative technique (measuring the device), this is its clear advantage over other spectroscopic methods, like transient photoluminescence spectroscopy: it can clearly distinguish the interfaces within a device when an appropriate and reliable equivalent circuit is being used. The high frequency arc is attributed to charge transfer resistance (R_{ct}) in the perovskite/TiO_2 interface. [12, 58] This resistance is significantly smaller in the case of the D35-modified cell, confirming easier electron transfer in the corresponding device. This can be attributed to the chemical bonding of the D35 dye to TiO_2, strengthening their electronic coupling and inducing a faster electron injection rate. Such a mechanism was recently proposed by Tountas et al.[59] to explain the beneficial role of covalently bonded porphyrin molecules as effective cathode interfacial modifiers in inverted organic solar cells (OSCs). In addition, the mid frequency arc related to the recombination resistance (R_{rec}) depicts a net increase in the case of the D35-modified device. This implies that the recombination between electrons in the TiO_2 compact layer and holes in

the perovskite is severely inhibited by the addition of the D35 dye. A possible explanation is that the chemisorbed dye monolayer keeps holes in the perovskite at a distance from the TiO_2 surface, suppressing the electron recombination. In fact, the D35 sensitizer contains four bulky long butoxyl chains in ortho and para positions of the TPA phenyl rings by single bonds, allowing free rotation.[60] These rotatable bulky groups may induce surface blocking through steric hindrance, preventing the access of electrons back to the perovskite, which will be in favor of higher V_{oc}, as observed in the J-V characteristics.[61]

In conclusion, the behavior of the D35-modified solar cell is improved due to the dye sensitization of the titania ETL/perovskite interface.[62] The above results were further supported by the EIS measurements carried out in dark conditions (Figure 4.14), where the charge transfer resistance is significantly larger in the case of the dye-modified device. Since, the photoexcited dye acts as an electron transfer mediator, it doesn't contribute to the charge transfer under dark conditions yet dominating its insulating nature the EIS date is registered in Table 4.2.

Finally, stability tests were performed, certifying the significant influence of the dye on curing degradation phenomena that commonly accompany the PSCs operation. Those issues are mainly attributed to perovskites' intrinsic structural instability, their high sensitivity against water molecules and their instability against UV radiation.[63] The devices were stored in the dark, inside a silica dried desiccator (relative humidity-RH=10%) and their performance parameters were systematically evaluated as to estimate their evolution over time. As presented in Figure 15 V_{oc} values show quite similar time dependence for both dye-sensitized and non-sensitized devices. In fact, the open circuit voltage values showed a total 30% loss of the initial V_{oc} after 80 days. However, significant differences were observed for both FF and J_{sc} values, where the D35–based PSCs present a clearly slower decline in cell parameters, resulting in improved stability and higher final power conversion efficiency,

retaining 50% of their initial performance and largely outperforming the corresponding values of the reference device.

The observed higher stability is probably related to the hydrophobic character of the D35 dye shielding the TiO_2/perovskite interface against humidity. In fact, the insulating effect of the butoxyl chains protecting the TiO_2 surface was well established in dye-sensitized solar cells.[60] This is corroborated by the contact angle measurements, indicating enhanced hydrophobicity of the titania compact layer following dye chemisorption. Lower surface wetting of the underneath compact layer increases its compatibility with the top hybrid perovskite absorber and is also at the origin of the observed higher resistance of the FTO/TiO_2/D35/$MAPbI_3$ photoelectrodes to UV stress.[19] In fact, it is well known that TiO_2 is one of the best performing photocatalysts provoking the direct decomposition of a numerous organic molecules under UV irradiation. The photocatalysis mechanism involves the participation of highly reactive hydroxyl radicals (.OH) resulting of the reaction between the photogenerated holes and adsorbed water.[64] Thus, the introduction of the water repealing dye interlayer not only protects the top perovskite layer from self-decomposition (the instability in humid environments is the main drawback of the perovskite technology) but also inhibits the formation of potent hydroxyl radical "killers" at the corresponding interface, thus justifying an indirect UV shield function.

The relative stability of the $MAPbI_3$ films upon dye sensitization is easily corroborated by the optical images (Fig. 4.16) taken from perovskite films grown over TiO_2 and TiO_2/D35 substrates, after storage for 80 days. The $MAPbI_3$ film grown on the D35-sensitized substrate is far less affected comparing it with the film on the pristine TiO_2, that has turned yellow due to the presence of PbI_2. The above results were further confirmed by Raman spectroscopy. It is important to mention that no Raman signal of the pristine perovskite can be obtained under on-resonance Raman excitation due to laser induced degradation and phase

transformations.[65] Thus, in principle, only the degradation PbI_2 products formed on the samples by ageing can be detected by Raman. Indeed, the Raman spectra recorded (Fig. 4.17a) on pristine titania present a no well resolved peak at ≈110 cm-1 which is partially masked by the rejection filter and a vibration peak at 215 cm-1 both indicating formation of PbI_2 degradation product across the sample.[66,67] On the contrary, the perovskite samples developed on the dye-modified titania substrate did not present any Raman vibration peaks at all, verifying the robustness of these samples against moisture induced degradation.

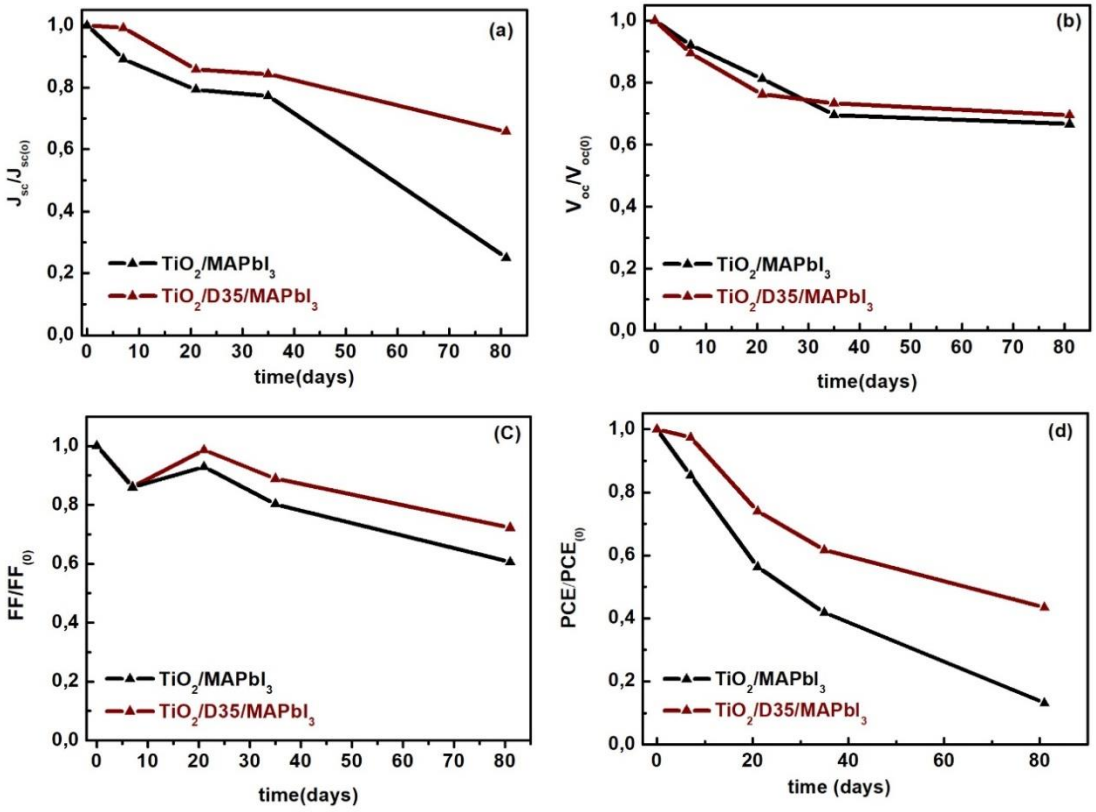

Figure 4.15 Stability test over the development of (a) current density, (b) open circuit voltage, (c) fill factor, and (d) efficiency of $MAPbI_3$-based solar cells with TIO_2 and $D35/TiO_2$ as the compact ETL.

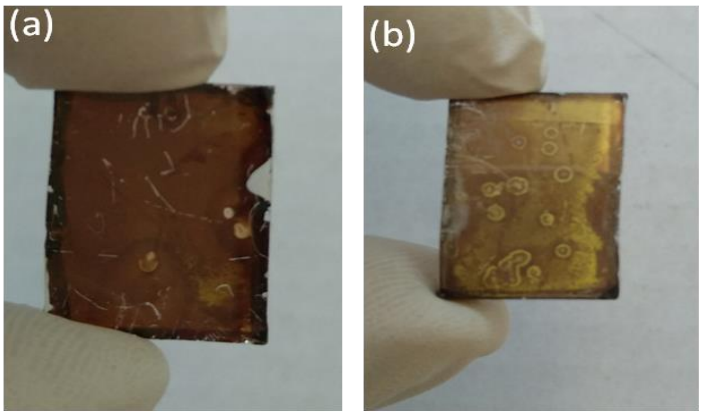

Figure 4.16 Optical images of $MAPbI_3$ films grown on (a) TiO_2/D35, and (b) TiO_2 substrates after storage for 80 days in the dark.

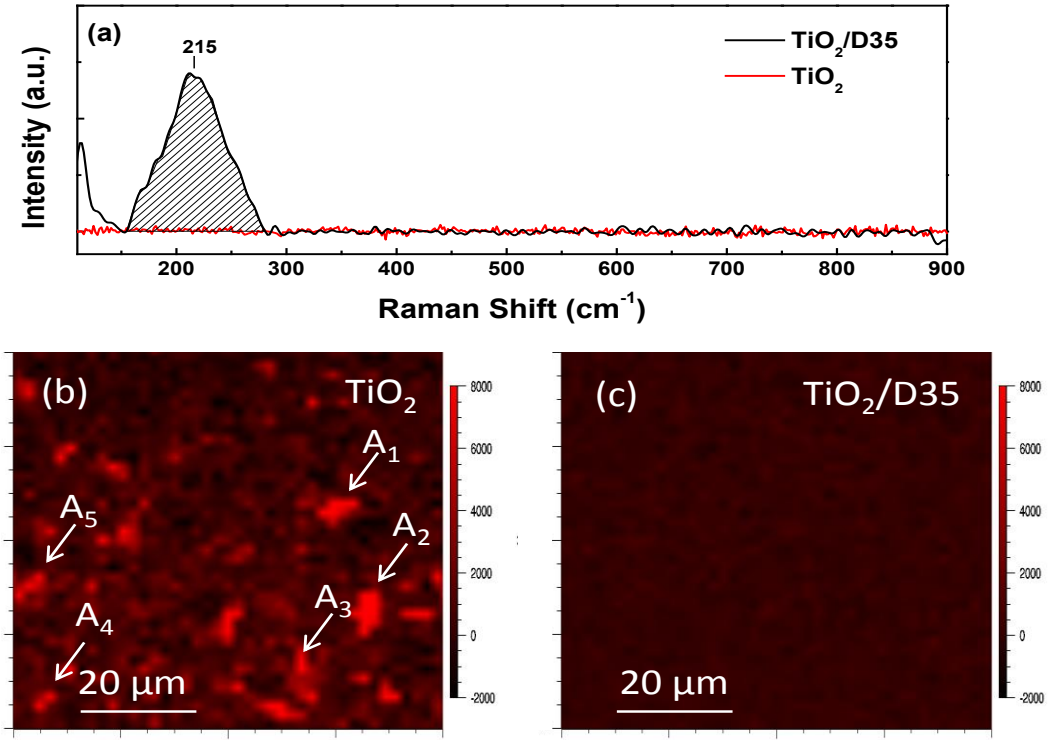

Figure 4.17 (a) Raman spectra (shaded graph corresponds to PbI_2 vibration peak) of 80-days aged $MAPbI_3$ films inside a desiccator. Integrated PbI_2 Raman signal mapping from 40x40 µm areas of perovskite films deposited on pristine TiO_2 (b) and D35 sensitized TiO_2 (c) substrates, after aging. A1-A5 are characteristic intensively degraded areas corresponding to the formation of PbI_2 islands.

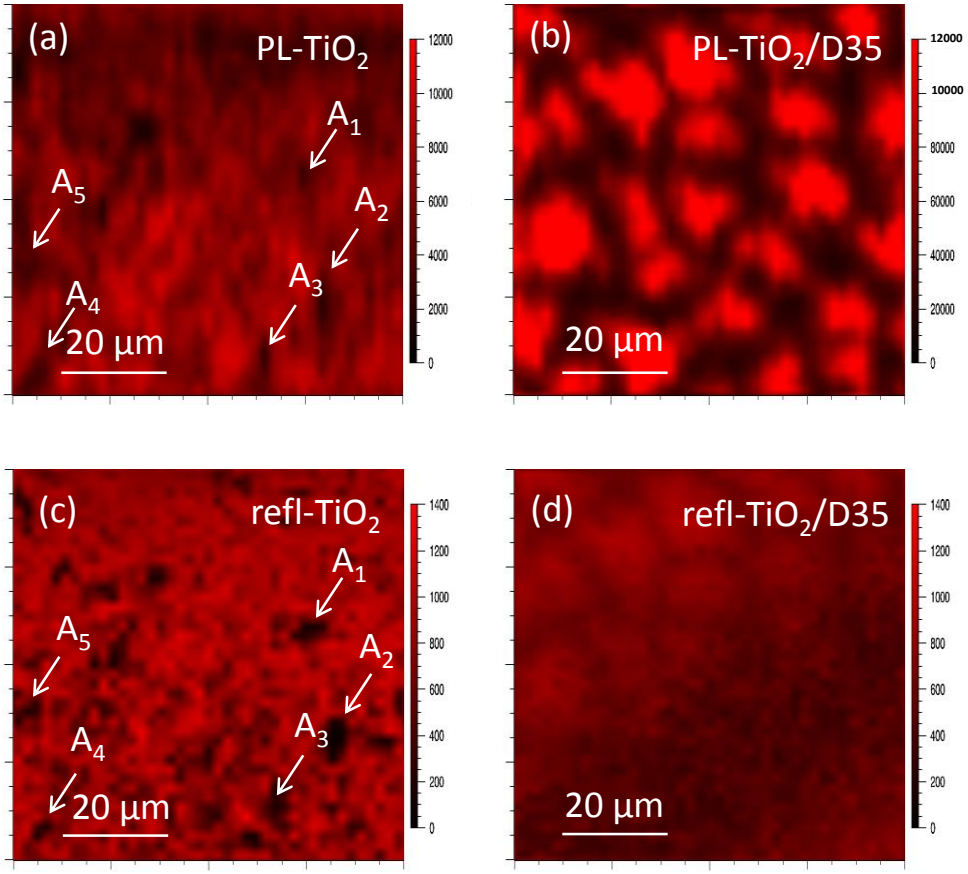

Figure 4.18 Integrated PL (788-820 nm) and laser reflectance at 514. 4 nm from the40x40 µm areas of perovskite films deposited on pristine TiO_2 (left) and D35 sensitized TiO_2 (right) substrates, after degradation for 80 days (stored in the dark and 10% humidity). The same areas under the same lateral resolution were examined later by Raman (see Fig 4.17). Marked areas A1-A5 are characteristic regions corresponding to the formation of PbI_2 islands (strong degradation) (see also Fig. 4.17).

Moreover, Raman mapping in 40x40 µm2 areas of the samples were carried out and the integrated signal of the PbI_2 215 cm^{-1} band is shown in chromatic scale, in Fig. 4.17(b,c). Fig. 4.17(b) shows that the reference perovskite developed on pristine TiO_2 films is fully covered (across all its area) with a significant amount of PbI_2 formed as degradation product. Moreover, in some areas (A1-A5) the PbI_2 Raman signal becomes very strong and defines extensive PbI_2 islands. These regions also present reduced photoluminescence (PL) signal

(Fig. 4.18a) and reflectivity (Fig.4.18c). On the contrary, the D35 sensitized films remain completely intact by PbI_2 formation and the reflectance images do not show dark patches. Overall, the mean PL signal on the D35 films is one order of magnitude higher than that of the reference sample. In the later, the extensive degradation product (PbI_2) does not permit the observation of the PL from the perovskite.[68] Furthermore, the PL signal mapping across the D35 modified film has a lateral profile typical of perovskite films.[69]

4.1 PSCs Performance under Accelerated Thermal Stress and Prolonged Light Exposure

At first we realized accelerated heat lifetime experiments in samples with the following structure: FTO/TiO_2/D35/$MAPbI_3$ as the dye-sensitized and FTO/TiO_2/$MAPbI_3$ as the reference one. The perovskite crystals were prepared using lead acetate as the metal - containing precursor. This material follows a fast crystallization path that leads to robust perovskite absorber layers due to the facile removal of the CH_3NH_3Ac by-product during the film formation. It is important to point out that in our experiments we did not insist on the influence of the hole transporter (2,2′,7,7′-tetrakis (N, N-di-p-methoxyphenylamine) - 9,9′-spirobifluorene, spiro-MeOTAD) and the silver cathode (Ag). In fact, the Spiro-MeOTAD HTM, despite resulting in highly efficient PSCs, suffers from low glass transition temperature that affects the thermal stability of the devices. Moreover, metal cathode electrodes like silver can migrate to the perovskite layer through Spiro-MeOTAD, a deterioration path further enhanced at high temperatures. In every case the behavior of the interfaces (such as ETL/perovskite and perovskite/HTL) plays a distinct and crucial role in the overall stability of the devices, thus we have focused on the influence of high temperatures exclusively in the interplay between titania and $MAPbI_3$ absorber. The samples were thermally treated inside a glove box (Ar-filled, O_2<0.5ppm, H_2O<0.5ppm) and special care was taken in order to exclude the presence of residual DMF. $MAPbI_3$ based on lead acetate only needs a few

minutes under 100^{o}C in order to crystallize in the tetragonal black phase. Taking this into account, we prepared the samples by heating them from 10min (which is the optimum crystallization time) up to 24 hours. In Figure 4.19, the SEM images of the films after 10min and 60min of thermal stress are shown. Independently of dye modification, the samples heated for 10 min present a similar appearance in the form of a smooth pinhole-free film with large and homogenous crystals, while after 60 min of heating at 100^{o}C the homogeneity of the films was deteriorated with the appearance of extended altered areas mostly located at the perovskite grain boundaries, a fact possibly associated with the formation of PbI_2. On the contrary the films developed on the titania substrates sensitized with D35 are slightly affected by heat denoting a far more stable perovskite layer.

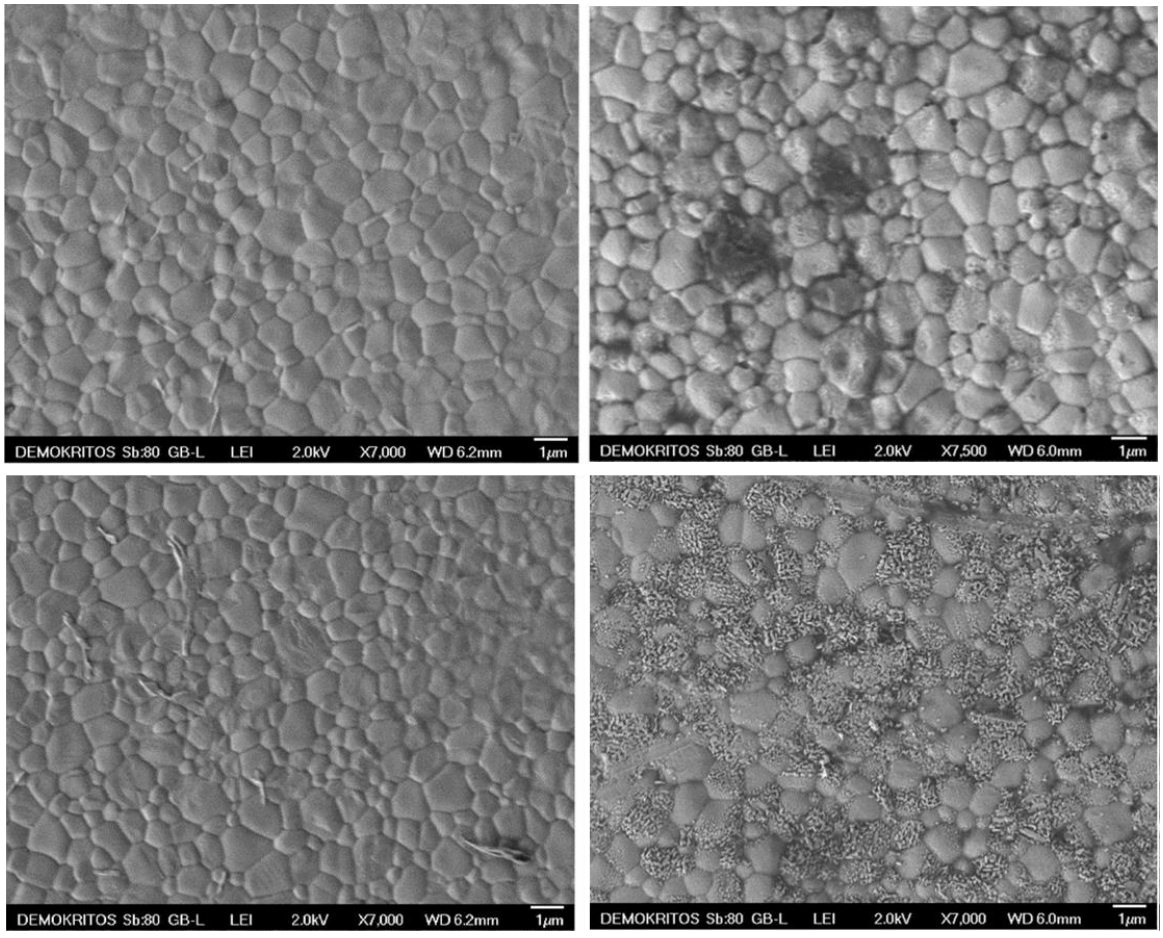

Figure 4.19 SEM images of perovskite layers upon TiO_2/D35 (up) and TiO_2 (down) substrates after 10min (left) and 60min (right) of thermal stress.

In order to confirm the nature of the spoils we conducted XRD measurements in the thermally treated samples along with the not stressed ones. As shown in Figure 4.20a, the XRD patterns of samples heated for 10min (not stressed) contain characteristic diffraction peaks of crystalline $MAPbI_3$, in agreement with the theoretically expected peaks at 2θ=13.65°, 28.01°, and 31.42°, denoting a well crystallized perovskite. Moreover, a slight difference in the full width at half maximum (FWHM) values for the perovskite is observed between the two patterns. This difference is in favor of the TiO_2/D35 sample confirming higher crystallinity for the perovskite films grown on the dye-sensitized titania substrate. This fact has been corroborated by the SEM analysis depicting higher size of crystallites and is expected to play a crucial role in the suppression of ion migration during heating. In fact, previous studies have revealed that ion migration stimulated by heat can be largely suppressed when perovskite crystals get larger, due to smaller grain boundaries and lower structural disorder and defects.

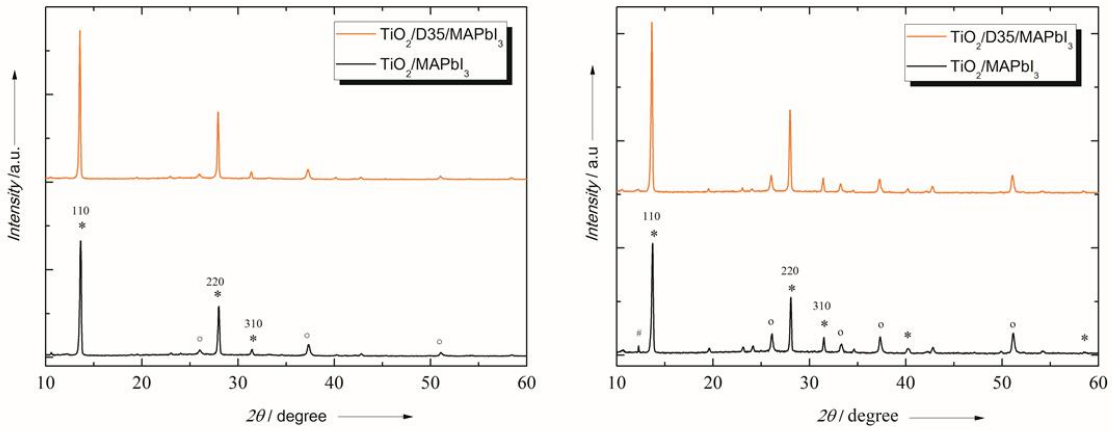

Figure 4.20 XRD patterns of 10min (left) and 30min heated perovskite films (right) on titania-based substrates

The structural analysis after 30min of thermal stress (Figure 4.20b) for both samples, reveals the appearance of the PbI_2-related peak (θ=12.5o) in the case of the neat TiO_2 substrate. When the samples were heated for 60min (Figure 4.21a), the diffraction peak

corresponding to the presence of PbI_2 is obviously more intense in the case of the unmodified sample corroborating the extent presence of lead iodide on the surface of the perovskite film.

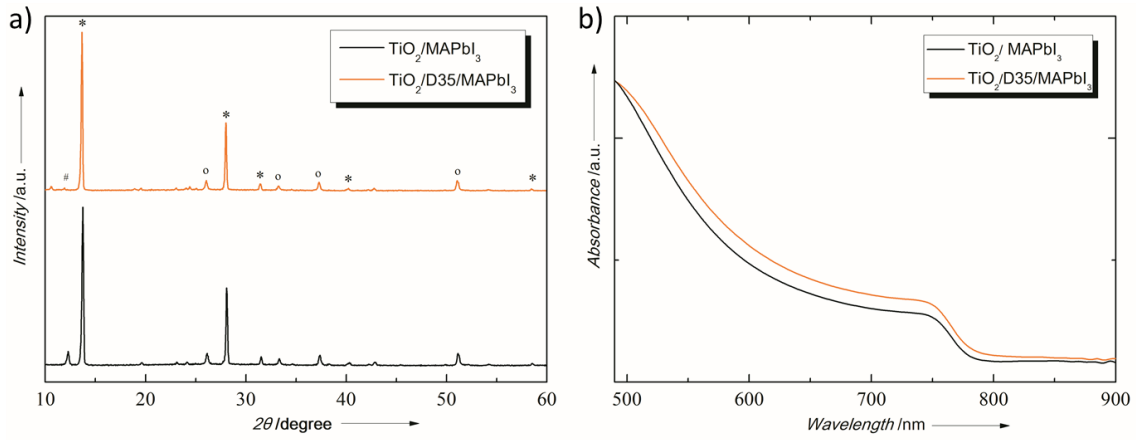

Figure 4.21 a) XRD patterns and b) Uv-vis absorption spectra of 60min heated perovskite films on titania-based substrates.

The formation of lead iodide is attributed to the existence and unhampered migration of under-coordinated ions out of the perovskite layer, and the interference with the ETL, after exposure to thermal energy. On the other side the samples developed on the dye-sensitized titania compact layer do not present any PbI_2 peak.

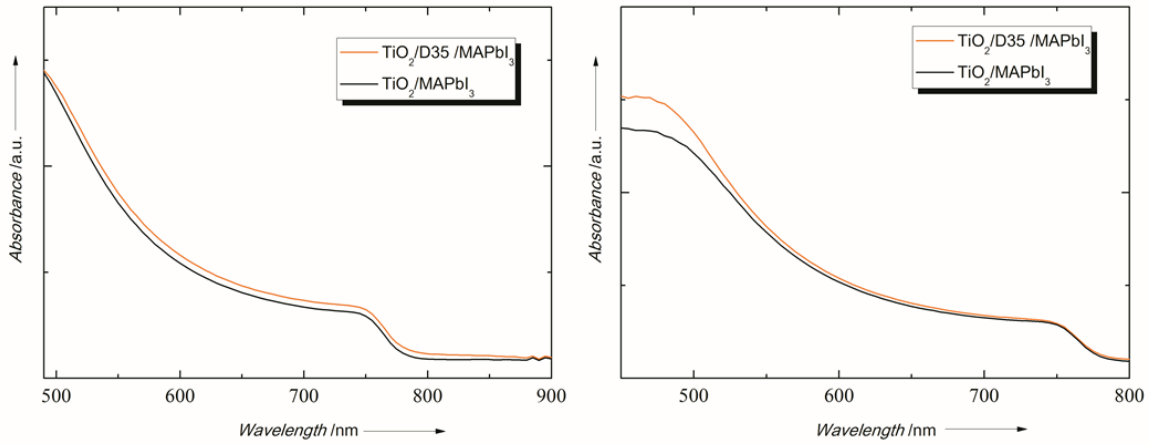

Figure 4.22 Uv-vis absorption spectra of 10min (left) and 30min heated perovskite films (right) on titania-based substrates

In order to evaluate the influence of thermal stress upon the optoelectronic properties, UV-Vis spectroscopy measurements were carried out.

In Figure 4.22a we can see the absorption spectra of the $MAPbI_3$ on pristine and D35-modified TiO_2 substrates. After dye-sensitization, the shape of the absorbance spectrum doesn't change, indicating no significant contribution from the D35. The same trend goes on after both 30min (Figure 4.22b) and 60min of thermal stress (Figure 4.21b). In all cases, and especially after one hour of heat treatment at 100^{o}C, the perovskite layer coated upon D35/TiO_2 presents improved absorbance in the whole spectrum when compared to the one grown upon TiO_2. It is obvious that D35 protects $MAPbI_3$ from heat, in terms of crystallinity and morphology, a fact that reflects in the improved absorption spectra. In order to evaluate the behavior of D35 against thermal treatment, we used Raman spectroscopy (Figure 4.23) on net D35 powder (Figure 4.23a) and TiO_2/D35 films coated upon FTO glasses (Figure 4.23b-f) and annealed at 100^{o}C as a function of the treatment duration.

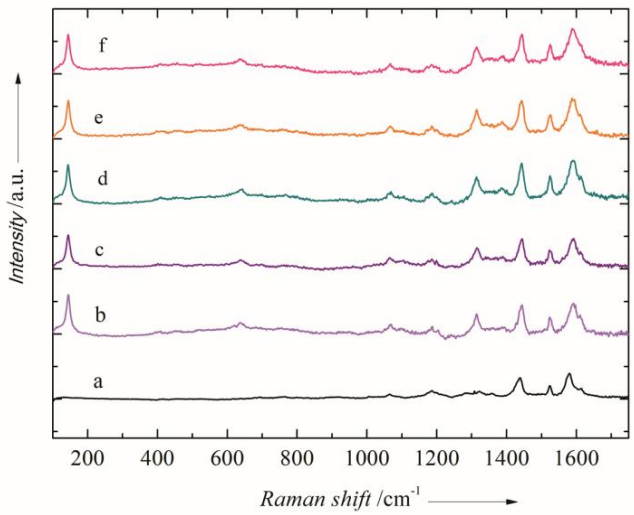

Figure 4.23 Raman spectra for (a) D35 powder and TiO_2/D35 films stressed for (b) 0min, (c) 10min, (d) 30min, (e) 60min, (f) 120min.

At low frequencies the vibrational modes of titania anatase are observed, the strongest being the E1g mode, at 143cm-1. As concerns the characteristic bands of the D35 dye [the phenyl ring deformation at 1066 cm-1; the C-C stretching vibrations at 1173, 1183, and 1200 cm-1; the C-N vibration at 1317 cm-1; a strong CH bending range band at 1442 cm-1; and the C=C stretching vibrations of the phenyl rings at 1525, 1593 (triphenylamine unit), and 1609 cm-1], they do not alter even after 1h of thermal treatment of the sample at 100oC indicating its good stability against thermal stress, a fact in agreement with literature.

4.1.1 Thermal Stability and Characterization of PSCs

As to further investigate the influence of thermal stress in $MAPbI_3$, we fabricated PSCs employing the thermally stressed samples. The configuration of the devices is the following: FTO/TiO_2/D35/$MAPbI_3$/SpiroMeOTAD/Ag for the sensitized and FTO/TiO_2/$MAPbI_3$/ SpiroMeOTAD/Ag for the reference ones.

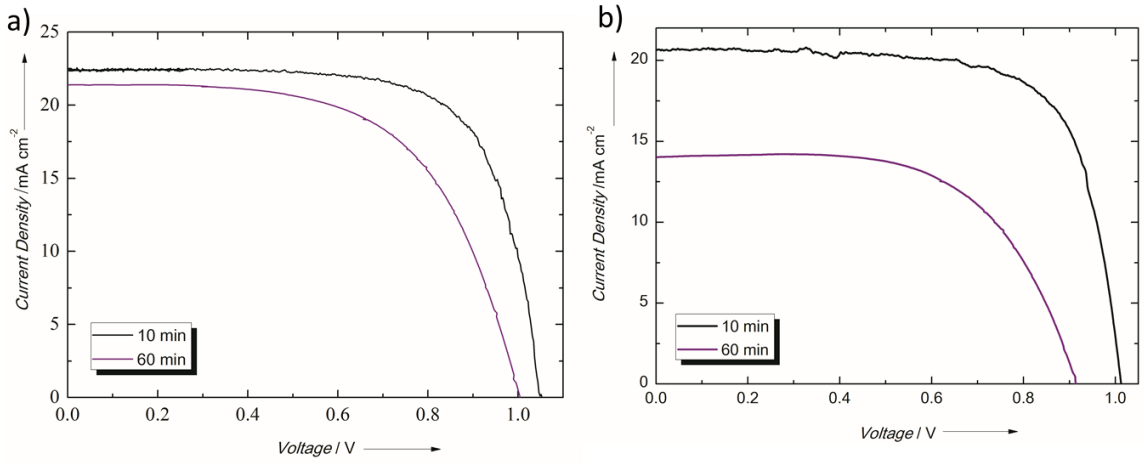

Figure 4.24 J-V characteristics of a) D35-containing and b) reference PSCs after 60min of thermal stress.

Table 4-3 Photovoltaic parameters for the best performing devices with and without D35 after various times of thermal stress at 100°C.V_{oc}: open-circuit voltage, J_{sc}: short-circuit current density, FF: fill factor, PCE: power conversion efficiency.

Device	**J_{sc} (mA·cm^{-2})**	**V_{oc}(V)**	**FF**	**PCE (%)**
TiO_2 (0 min)	20.62	1.01	0.72	15.05
TiO_2 (60 min)	14.00	0.92	0.60	7.74
TiO_2/D35 (0 min)	22.50	1.04	0.72	16.79
TiO_2/D35 (60 min)	21.42	1.00	0.65	13.92

From the presented results (Figure 4.23 and Table 4.3) it is obvious that after 60min of stress the reference devices decline substantially losing almost 50% of the initial efficiency. In contrast, the D35-sensitized one preserves 85% of the starting PCE. The performance decrease of the devices is mainly associated with the decrease of J_{sc}, since in the case of the V_{oc} the loss is smaller. Nevertheless, even in this case, the D35 sample has a far more stable behavior since the final value of V_{oc} is only 4% lower than the initial, contrary the reference one in which V_{oc} decrease by 9%. In the case of FF, the reference sample after thermal treatment loses almost 17% of the initial value while the sensitized device presents a more stable FF, declining only by 9%. The obtained results for the behavior of the PSCs upon thermal stress were highly reproducible as shown in Figure 4.25 and Figure 4.26 that present the statistical data for J_{sc}, V_{oc}, FF and PCE for 15 solar cells of each configuration.

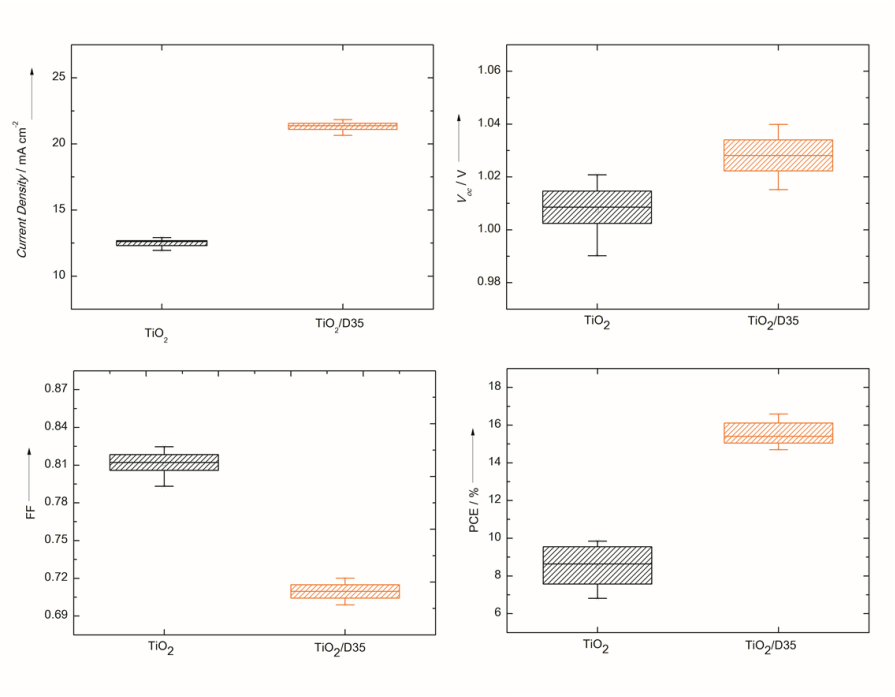

Figure 4.25 Statistical analysis of the main photovoltaic parameters for PSCs with and without D35 before and after 30min of heat treatment at 100^{o}C.

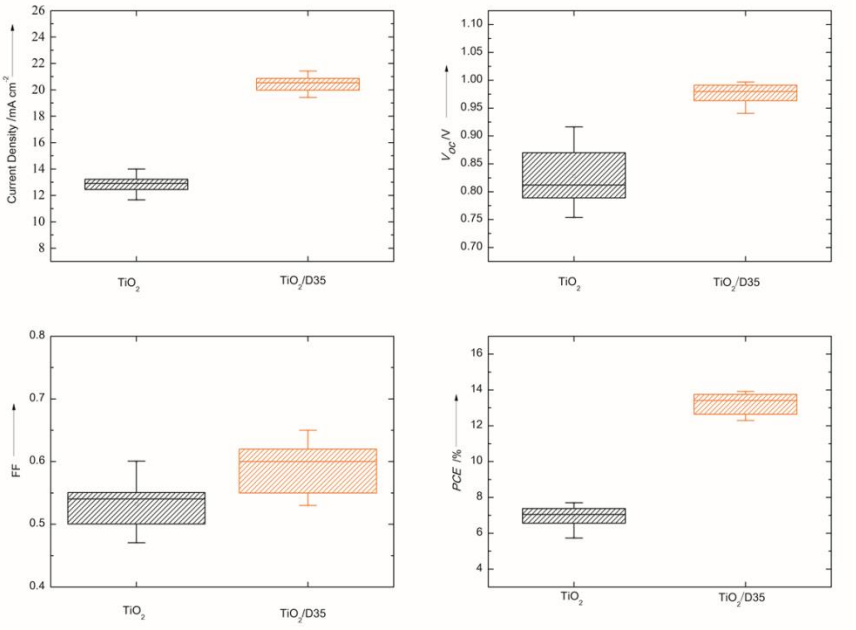

Figure 4.26 Statistical analysis of the main photovoltaic parameters for PSCs with and without D35 after 60min of thermal stress at 100^{o}C.

In order to have a more long-term insight into the performance of the PSC we conducted accelerated thermal stress tests on the sensitized and the reference samples for more than 60 min. The results, reported on Table 4.4 and Figure 4.27 show that in the case of the reference PSCs, their efficiency power conversion efficiency (PCE) considerably declined after 120min of thermal treatment reaching 4.85%, a value 70% lower than the initial PCE. Moreover, every attempt we made to register J-V curves after heating the sample for longer time periods failed since the performance of the PSCs collapsed. On the contrary, the sensitized devices present a far more stable behavior. After 120 min of thermal treatment in 100^{o}C under an inert atmosphere, the PSCs retain 75% of their initial PCE value, while the devices still work after 24h of continuous (accelerated) thermal stress. The evolution of the main photovoltaic parameters is shown in Figure 4.28. Both V_{oc} and FF present a small decay while the decrease in the PCE can be exclusively attributed to the decrease of J_{sc}.

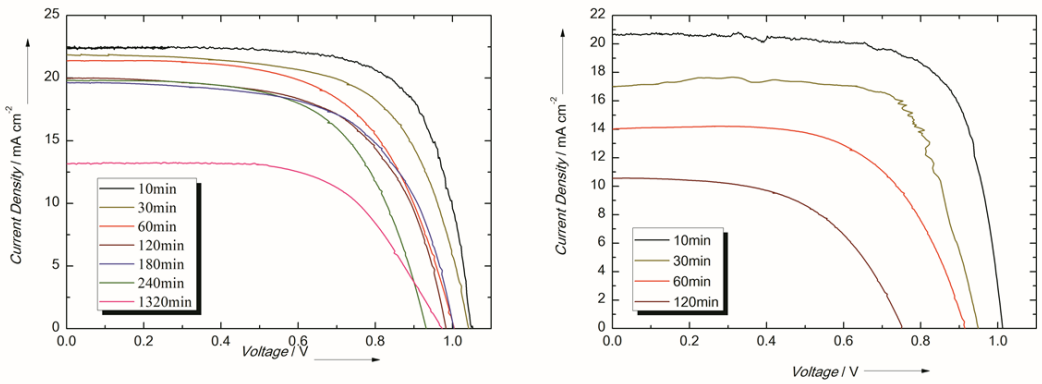

Figure 4.27 J-V characteristics of D35-containing (left) and reference PSCs (right) after various times of thermal stress.

Table 4-4 Photovoltaic parameters for the best performing devices with and without D35 after various times of thermal stress at 100°C. V_{oc}: open-circuit voltage, J_{sc}: short-circuit current density, FF: fill factor, PCE: power conversion efficiency

Device	**J_{sc} (mA·cm^{-2})**	**V_{oc}(V)**	**FF**	**PCE (%)**
TiO_2/D35 (0 min)	22.55	1.04	0.72	16.79
TiO_2/D35 (30 min)	21.81	1.04	0.71	16.10
TiO_2/D35 (60 min)	21.42	1.00	0.65	13.92
TiO_2/D35 (120 min)	19.89	0.98	0.65	12.66
TiO_2/D35 (180 min)	19.65	0.99	0.64	12.45
TiO_2/D35 (240 min)	19.79	0.93	0.63	11.59
TiO_2/D35 (1320 min)	13.11	0.98	0.67	8.60
TiO_2 (0 min)	20.62	1.01	0.72	15.05
TiO_2 (30 min)	17.00	0.95	0.71	11.46
TiO_2 (60 min)	14.00	0.92	0.60	7.74
TiO_2 (120 min)	10.69	0.74	0.61	4.85

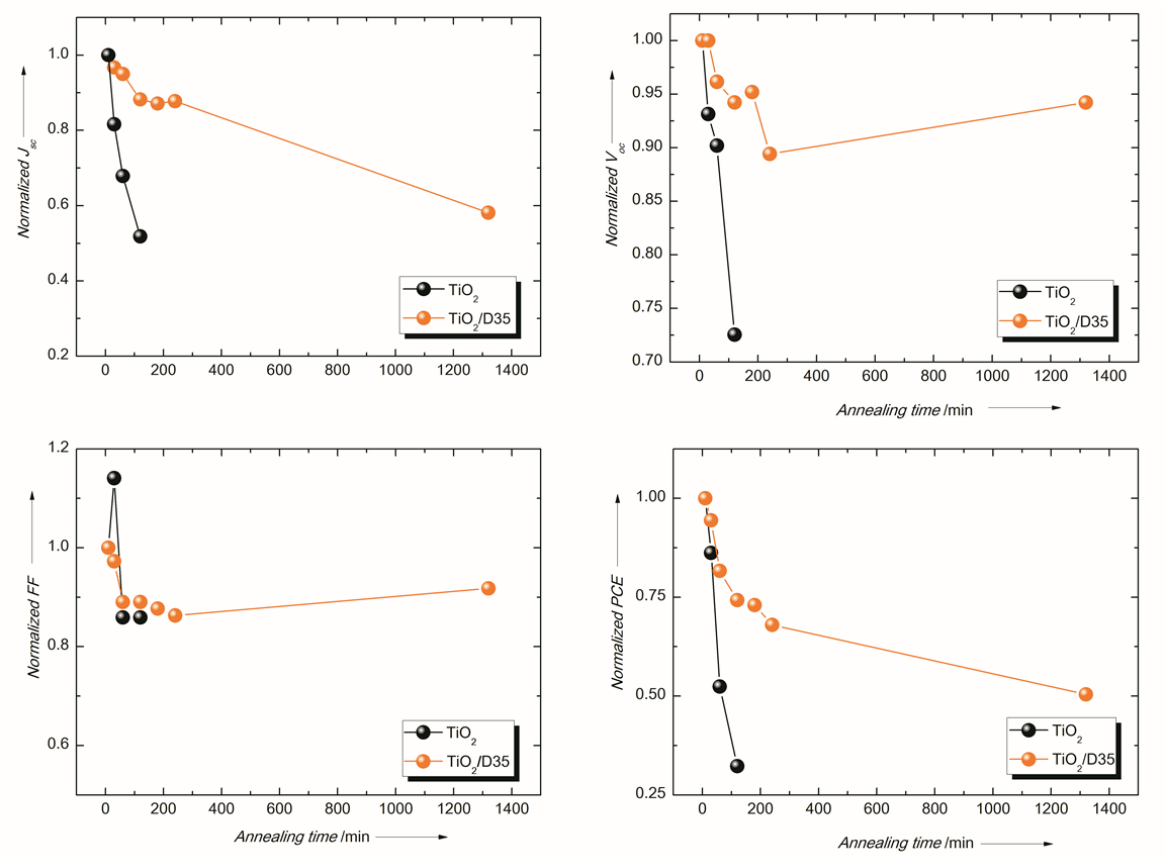

Figure 4.28 Evolution over time for the main photovoltaic parameters of thermally stressed PSCs with and without D35.

Moreover, in Figure 4.29 we present images of perovskite films developed on TiO_2/D35 and TiO_2 substrates, thermally stressed at 100°C on air as a function of the treatment duration. It is obvious that in the presence of moisture, the degradation of the reference films is rapid already after 60min of thermal treatment, while after 2 h almost the entire surface of the perovskite has turned to yellow, a clear macroscopic sign of surface coverage by PbI_2. On the contrary, the stressed sensitized films did not present any alteration in comparison with the fresh ones and no obvious change in color was observed following thermal treatment in inert atmosphere.

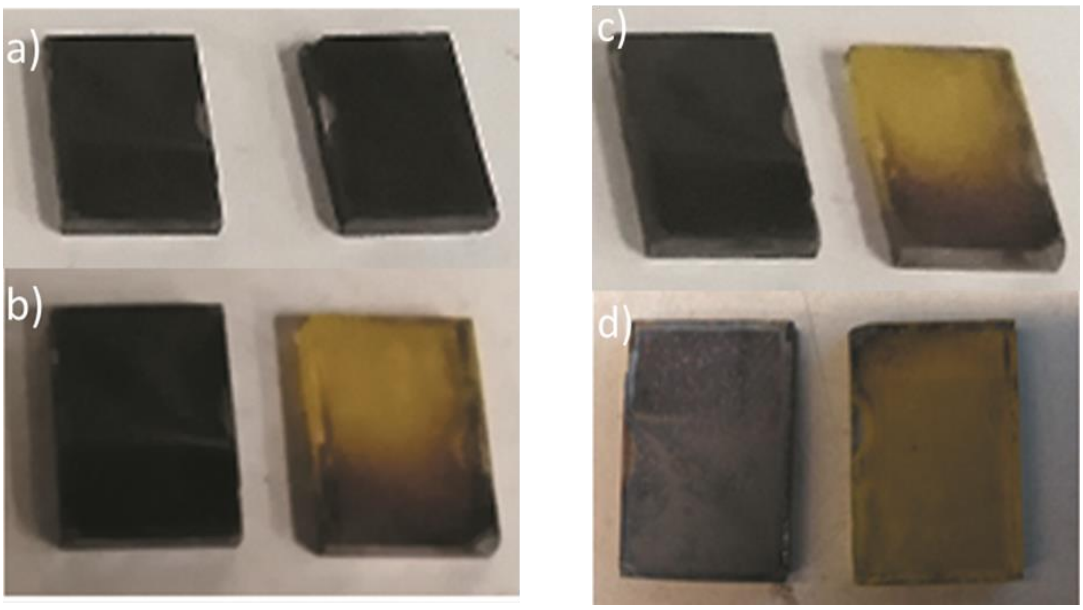

Figure 4.29 Images of perovskite films upon TiO_2/D35(left)and TiO_2 (right), thermally stressed at 100^{o}C on air for (a) 10 minutes, (b) 60 minutes, (c) 120 minutes and (d)180 minutes.

From the above results, it is obvious that D35, except for its beneficial effects in the performance of PSCs, also plays some significant role in protecting the devices against thermal stress. From the present data and in agreement with the literature, the contribution of D35 may be attributed to its hydrophobic characteristics, acidic nature and ability to induce high perovskite crystallinity. In this context Azpiroz et al. have found that MAI-terminated surfaces are easily subject to solvation, due to the nucleophilic substitution of dangling I^- ions on the surface by water (H_2O) molecules. Therefore, inserting a hydrophobic monolayer is very important as to stabilize the perovskite crystals, especially in the case of heat stress. Additionally, the D35 protective layer may hinder the diffusion of decomposition products (e.g. MAI and HI) and regenerate the perovskite phase by reacting with PbI_2 in the film. Furthermore it is reported that the thermal decomposition of the perovskite film is hindered by the acidic chemistry at ETL/Perovskite interface. In this context, the protective role of D35 may be due to its acidic character since it can create a more acidic environment in

comparison with neat titania. Thus, the dye hinders the deprotonation of the attributed methylammonium cation and facilitates the formation of methylamine and PbI_2.

4.1.2 Light Stability and Characterization of PSCs

In order to further investigate the stabilizing effect of D35, we conducted additional light saturation experiments under continuous illumination (300nm-800nm spectral range) of 76.5 mW/cm^2 incident irradiance. At first, we evaluated the endurance of perovskite films coated upon FTO/TiO_2 and FTO/TiO_2/D35 photoanodes irradiated under ambient conditions. As shown in the XRD pattern (Figure 4.30a), when the samples were irradiated for 60min, the lead iodide-related peak was increased intensively claiming the extent presence of lead iodide on the surface of the perovskite films. This is obvious in the corresponding images presented in Figure 4.31 where yellow areas corresponding to lead iodide are clear in the case of the reference sample. These results were also reflected in absorbance measurements (Figure 4.30b) where we can see the light absorption of the $MAPbI_3$ on pristine and D35-modified TiO_2 substrates. It is evident that after one-hour light exposure, the perovskite layer developed upon D35/TiO_2 presents improved absorbance in the whole spectrum when compared to the neat TiO_2 one.

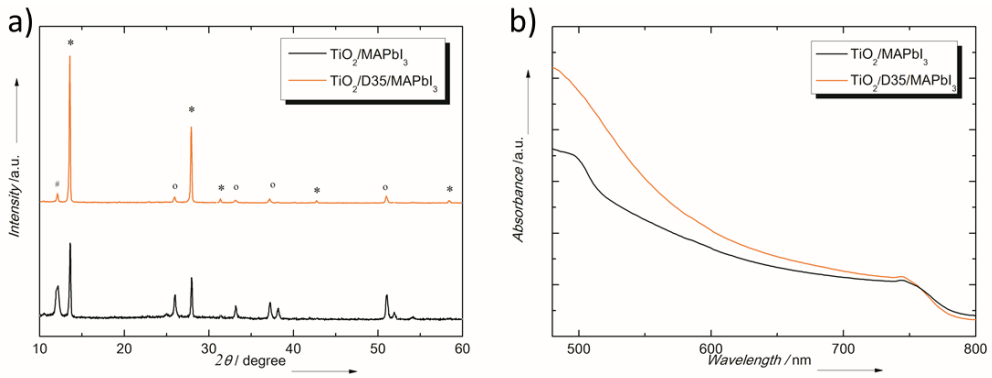

Figure 4.30 a) XRD patterns and b) Uv-vis absorption spectra of 60min light stressed perovskite films on titania-based substrates.

Figure 4.31 Photographs of TiO_2 (left) and TiO_2/D35 films (right) upon the perovskite layer after prolonged light exposure for 1hr.

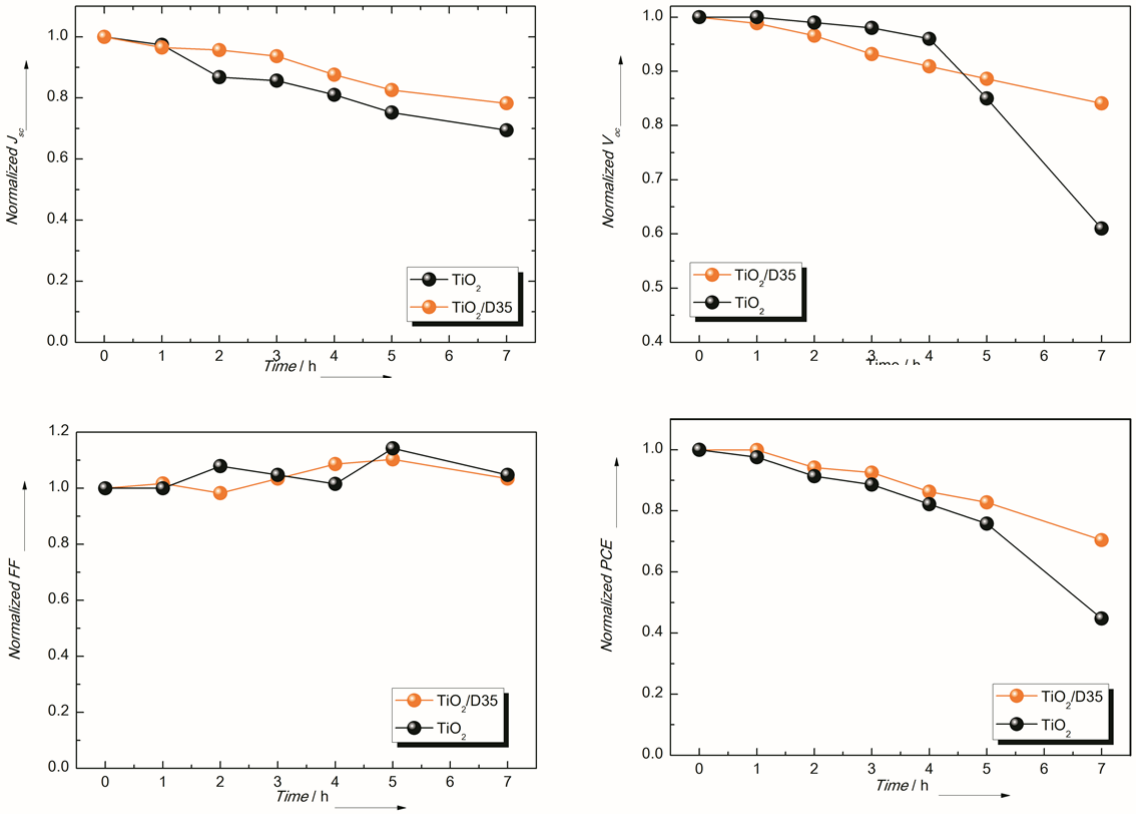

Figure 4.32 Evolution over time for the main PV parameters of light saturated PSCs with and without D35.

Subsequently we fabricated PSCs with the aforementioned photoanodes. It can be seen (Figure 4.32) that the devices employing D35 exhibited relatively better stability than the neat

TiO_2-based devices. The PCE value of the control devices (non-sealed cells left under ambient conditions at room temperature under dark) decreased by 56% after 7 hours irradiation, whereas the cells with D35 only lost~18% of their initial PCE. Moreover, FF presents the same trend for both cases, while the J_{sc} value of the control devices degraded by 35% after 7 hours of continuous illumination, whereas the cells with D35 only degraded by 17%. Finally, the V_{oc} value for the control PSCs declined by 37% after 7 hours, whereas the cells with D35 only lost 15% of their initial V_{oc}. In general, the degradation phenomena are closely related to the activation energy of ion migration in perovskite. In our case, the large crystals with high crystalline quality realized by the D35 sensitization interface engineering strategy, is strongly associated with the observed high PSC light stability. Moreover, upon exposure of the TiO_2 to light, the holes in the valence band recombine with adsorbed molecular oxygen, causing desorption and leaving positively charged deep trap sites in the TiO_2 surface. These traps then act as sinks for electrons, and this effect is followed by recombination of the trapped electrons occurring directly with the holes in the perovskite or HTM. On the contrary, D35 molecules may act as a protective shield over the compact TiO_2 ETL, thus suppressing the recombination process.as shield layer over the TiO_2 layer and this may be suppressed this recombination process.

4.4 Summary

Interface engineering is central to the development of highly performing and stable perovskite solar cells (PSCs). Here, for the first time, we proposed the concept of dye sensitization for optimizing the compact layer/perovskite interface. The introduction of the solution processable D35 organic dye modifier sensitizing the titania compact layer, leaded to planar PSCs delivering enhanced stabilized power conversion efficiency of up to ~13% which is accompanied by significantly increased stability. Our results indicate that this performance enhancement is attributed to enhanced recombination resistance, increased

electron transfer, better crystallization of the deposited perovskite and humidity sealing character of the hydrophobic dye monolayer.

In this chapter we presented the beneficial role of D35 interface engineering in the stability of a planar PSC devices based on lead acetate as the metal cation precursor, titania compact layer as the ETL and $MAPbI_3$ as the sunlight absorber. The results obtained by investigating this specific configuration suggest that the observed significant simultaneous thermal and light stability originates from the versatile contribution of D35 at the interface between the titania ETL and the perovskite absorber. The hydrophobicity of D35 is pivotal in the behavior of the devices since it contributes in the formation of well crystallized perovskite layers which, besides enhanced protection against humidity attack, offer extra stability against heat and light saturation. The sensitized PSCs preserved 75% of their initial PCE after 2h of thermal stress at 100^oC, a significant improvement considering that reference PSCs almost collapsed at the same time. The D35-based devices was also very stable after 7h under light stress, establishing the overall beneficial role of this organic dye in the development of high-quality planar perovskite solar cells presenting increased efficiency and enhanced stability.

References

[1] Kojima, A.; Teshima, K.; Shirai, Y.; Miyasaka, T. Organometal Halide Perovskites as Visible-Light Sensitizers for Photovoltaic Cells. J. Am. Chem. Soc. 2009, 131, 6050−6051.

[2] Im, J. H.; Lee, C. R.; Lee, J. W.; Park, S. W.; Park, N. G. 6.5% Efficient Perovskite Quantum-Dot-Sensitized Solar Cell. Nanoscale 2011, 3, 4088-4093.

[3] Kim, H. S.; Lee, C. R.; Im, J. H. ; Lee, K. B.; Marchioro, T. A.; Moon, S. J.; HumphryBaker, R. ; Yum, J. H.; Grätzel, J. E. M.; Park, N. G. Lead Iodide Perovskite Sensitized AllSolid-State Submicron Thin Film Mesoscopic Solar Cell with Efficiency Exceeding 9%. Sci. Rep. 2012, 2, 591.

[4] Chung, I.; Lee, B.; He, J.; Chang, R.P.H.; Kanatzidis, M.G. All-Solid-State Dye-Sensitized Solar Cells with High Efficiency. Nature 2012, 485, 486-489.

[5] Teshima A. K.; Shirai, Y.; Miyasaka, T. Organometal Halide Perovskites as Visible-Light Sensitizers for Photovoltaic Cells. J. Am. Chem. Soc. 2009, 131, 6050-6051.

[6] Yang,W. S.; Park , B. W.; Jung, E. H. ; Jeon, N. J. ; Kim, Y. C.; Lee, D. U.; Shin, S. S.; Seo, J.; Kim, E. K.; Noh, J. H.; Seok, S. I. High-Performance Photovoltaic Perovskite Layers Fabricated Through Intramolecular Exchange. Science 2015, 348, 1234-1237.

[7] Chen, W.; Wu, Y.; Yue, Y.; Liu, J.; Zhang, W.; Yang, X.; Chen, H.; Bi, E.; Ashraful, I.; Grätzel, M.; Han, L. Efficient and Stable Large-Area Perovskite Solar Cells with Inorganic Charge Extraction Layers. Science 2015, 350, 944-948.

[8] Di Giacomo, F.; Fakharuddin, A.; Jose, R.; Brown, T. M.; Progress, Challenges and Perspectives in Flexible Perovskite Solar Cells. Energy Environ. Sci. 2016, 9, 3007-3035.

[9] Bailie, C. D.; Christoforo, M. G.; Mailoa, J. P.; Bowring, A. R.; Unger, E. L.; Nguyen, W. H.; Burschka,J.; Pellet, N.; Lee, J. Z.; Grätzel, M.; Nouf, R.; Buonassisi, T.; Salleo, A.; McGehee, M. D. Semi-Transparent Perovskite Solar Cells for Tandems with Silicon and CIGS. Energy Environ. Sci. 2015, 8, 956-963.

[10] Guo, D.; Yu, J.; Fan, K.; Zou, H.; He, B. Nanosheet-Based Printable Perovskite Solar Cells. Sol. Energy Mater. Sol. Cells. 2017, 159, 518–525.

[11] Snaith, H. J.; Abate, A.; Ball, J. M.; Eperon, G. E.; Leijtens, T.; Noel, N. K.; Stranks, S. D.; Wang, J. T.W.; Wojciechowski, K.; Zhang, W. Anomalous Hysteresis in Perovskite Solar Cells. J. Phys. Chem. Lett., 2014, 5, 1511–1515.

[12] Sanchez, R. S.; Gonzalez-Pedro, V.; Lee, J. W.; Park, N. G.; Kang, Y. S.; Mora-Sero, I.; Bisquert, J. Slow Dynamic Processes in Lead Halide Perovskite Solar Cells. Characteristic Times and Hysteresis. J. Phys. Chem. Lett. 2014, 13, 2357–2363.

[13] Levine, I.; Nayak, P. K.; Wang, J. T. W.; Sakai, N.; Reenen, S. V.; Brenner, T. M.; Mukhopadhyay, S.; Snaith, H. J.; Hodes, G.; Cahen, D. Interface-Dependent Ion Migration/Accumulation Controls Hysteresis in MAPbI3 Solar Cells. J. Phys. Chem. C. 2016, 30, 16399-16411.

[14] Conings, Bert.; Drijkoningen , J.; Gauquelin , N.; Babayigit , A.; D'Haen , J.; D'Olieslaeger , L.; Ethirajan , A.; Verbeeck , J.; Manca , J.; , E. F.; Boyen, H.G. Intrinsic Thermal Instability of Methylammonium Lead Trihalide Perovskite. Adv. Energy Mater. 2015, 5, 1500477.

[15] Christians, J. A. ; Miranda Herrera, P. A.; Kamat, P. V. Transformation of the Excited State and Photovoltaic Efficiency of CH3NH3PbI3 Perovskite upon Controlled Exposure to Humidified Air. J. Am. Chem. Soc. 2015, 137,1530–1538.

[16] Roose, B.; Gödel, K.C.; Pathak, S.; Sadhanala, A.; Baena, J.P.C.; Wilts, B.D.; Snaith, H.J.; Wiesner, U.; Grätzel, M.; Steiner, U.; Abate. A. Enhanced Efficiency and Stability of Perovskite Solar Cells through Nd-Doping of Mesostructured TiO2. Adv. Energy Mater. 2016, 6, 1501868.

[17] Cho, K.T.; Grancini, G.; Lee, Y.; Konios, D.; Paek, S.; Kymakis, E.; Nazeeruddin, M.K. Beneficial Role of Reduced Graphene Oxide for Electron Extraction in Highly Efficient Perovskite Solar Cells. ChemSusChem. 2016, 9, 1 – 6.

[18] Kim, D.H.; Han,G.S.; Seong, W.M.; Lee, J.W.; Kim, B.J.;Park,N.G.; Hong,K.S.; Lee,S.L. Jung, S. Niobium Doping Effects on TiO2 Mesoscopic Electron Transport Layer-Based Perovskite Solar Cells. ChemSusChem. 2015, 8, 2392-2398.

[19] Leijtens, T.; Eperon, G.E.; Pathak, S.; Abate, A.; Lee, M.M.; Snaith, H.J.; Overcoming Ultraviolet Light Instability of Sensitized TiO2 with Meso-Superstructured Organometal Trihalide Perovskite Solar Cells. Nat. Commun. 2013, 4, 2885.

[20] Liua, D.; Lia, Sh.; Zhanga, P.; Wanga, Y.; Zhanga, R.; Sarvarib, H.; Wanga, F.; Wuc, J.; Wangd, Z.; Chen, Z. D. Efficient Planar Heterojunction Perovskite Solar Cells with Li-Doped Compact TiO2 Layer. Nano Energy 2017, 31, 462–468.

[21] Kim, D. H.; Han, G. S.; Seong, W. M.; Lee, J.-W.; Kim, B. J.; Park, N.-G.; Hong, K. S.; Lee, S.; Jung, H. S. Niobium Doping Effects on TiO2 Mesoscopic Electron Transport LayerBased Perovskite Solar Cells. ChemSusChem. 2015,14,2392-2398.

[22] Zhou, H.; Chen, Q.; Li, G.; Luo, S.; Song, T.-B.; Duan, H.-Sh.; Hong, Z.; You, J.; Liu, Y.; Yang, Y. Interface Engineering of Highly Efficient Perovskite Solar Cells. Science 2014, 345, 542-546.

[23] Tan, H.; Jain, A.; Voznyy, O.; Lan, X.; de Arquer,F.P.G.; Fan, J.Z.; Quintero-Bermudez, R.; Yuan,M.; Zhang,B.; Zhao, Y.; Fan, F.; Li, P.; Quan, L.N.; Zhao, Y.; Lu,Z.-H.; Yang,Z.; Hoogland, S.; Sargent, E.H. Efficient and Stable Solution-Processed Planar Perovskite Solar Cells via Contact Passivation. Science 2017, 355, 722–726.

[24] Mali, S. S.; Shim, Ch. S.; Park, H. K.; Heo, J.; Patil, P. S.; Hong, Ch. K. Ultrathin Atomic Layer Deposited TiO_2 for Surface Passivation of Hydrothermally Grown 1D TiO2 Nanorod Arrays for Efficient Solid-State Perovskite Solar Cells. Chem. Mater. 2015, 27, 1541–1551.

[25] Lee, Y. H.; Luo, J.; Son, M.-K.; Gao, P.; Cho, K. T.; Seo, J.; Zakeeruddin, S. M.; Grätzel M.; Nazeeruddin, M. K. Enhanced Charge Collection with Passivation Layers in Perovskite Solar Cells. Adv. Mater. 2016, 28, 3966–3972.

[26] Mahmood, K.; Swain, B. S.; Kirmani, A. R.; Amassian, A. Highly Efficient Perovskite Solar Cells Based on a Nanostructured WO_3-TiO_2 Core-Shell Electron Transporting Material. J. Mater. Chem. A. 2015, 3, 9051-9057.

[27] Ma, Y.; Deng, K.; Gu, B.; Cao, F.; Lu, H.; Zhang, Y.; Li, L. Boosting Efficiency and Stability of Perovskite Solar Cells with CdS Inserted at TiO_2/Perovskite Interface. Adv. Mater. Interfaces 2016, 3, 1600729.

[28] Chen, R.; Cao, J.; Wu, Y,;Jing, X.; Wu, B.; Zheng, N. Improving Effciency and Stability of Perovskite Solar Cells by Modifying Mesoporous TiO_2–Perovskite Interfaces with both Aminocaproic and Caproic Acids. Adv. Mater. Interfaces 2017, 1700897.

[29] Ogomi, Y.; Morita, A.; Tsukamoto, S.; Saitho, T.; Shen, Q.; Toyoda, T.; Yoshino, K.; Pandey, S. S.; Ma, T.; Hayase, S.; All-Solid Perovskite Solar Cells with HOCO-R-NH^{3+} I^- Anchor-Group Inserted between Porous Titania and Perovskite. J. Phys. Chem. C. 2014, 118, 16651.

[30] Zuo, L.; Gu, Z.; Ye, T.; Fu, W.; Wu, G.; Li, H.; Chen, H. Enhanced Photovoltaic Performance of $CH_3NH_3PbI_3$ Perovskite Solar Cells through Interfacial Engineering Using SelfAssembling Monolayer. J. Am. Chem. Soc. 2015, 137, 2674-2679.

[31] Liu, L.; Mei, A.; Liu, T.; Jiang P.; Sheng, Y.; Zhang, L.; Han, H. Fully Printable Mesoscopic Perovskite Solar Cells with Organic Silane Self-Assembled Monolayer. J. Am. Chem. Soc. 2015, 137, 1790–1793.

[32] Balis, N.; Verykios, A.; Soultati, A.; Constantoudis, V.; Papadakis, M.; Kournoutas, F.; Drivas, C.; Skoulikidou, M.-C.; Gardelis, S.; Fakis, M.; Kennou, S.; Kontos, A.G.; Coutsolelos, A.G.; Falaras, P.; Vasilopoulou, M. Triazine-Substituted Zinc Porphyrin as an Electron Transport Interfacial Material for Efficiency Enhancement and Degradation Retardation in Planar Perovskite Solar Cells. ACS Appl. Energy Mater. 2018, 1, 3216–3229.

[33] Li, X.; Zhao, X.; Hao, F.; Yin, X.; Yao, Z.; Zhou, Y.; Shen, H.; Lin, H. Bifacial Modified Charge Transport Materials for Highly Efficient and Stable Inverted Perovskite Solar Cells. ACS Appl. Mater. Interfaces 2018, 10, 17861–17870.

[34] Feldt, S.M.; Gibson, E.A.; Gabrielsson, E.; Sun, L.; Boschloo, G.; Hagfeldt, A. Design of Organic Dyes and Cobalt Polypyridine Redox Mediators for High-Efficiency Dye-Sensitized Solar Cells. J. Am. Chem. Soc. 2010, 132,16714–16724.

[35] Hagberg, D.-P.; Jiang, X.; Gabrielsson, E.; Linder, M.; Marinado, T.; Brinck, T.; Hagfeldt, A.; Sun, L. Symmetric and Unsymmetric Donor Functionalization. Comparing Structural and Spectral Benefits of Chromophores for Dye-Sensitized Solar Cells. J.Mater.Chem. 2009, 19, 7232–7238.

[36] Stergiopoulos,T.; Konstantakou, M.; Falaras, P.; Dye Solar Cells Combining a TiO_2 Surface-Blocking Organic Sensitizer and Solvent-Free Ionic Liquid-based Redox Electrolyte. RSC Advances 2013, 3, 15014-15021.

[37] Pazoki, M.; Lohse, P.W.; Taghavinia,N.; Hagfeldt, A.; Boschloo, G. The Effect of Dye Coverage on the Performance of Dye-Sensitized Solar Cells with a Cobalt-based Electrolyte. Phys. Chem. Chem. Phys. 2014, 16, 8503-8508.

[38] Dryza, V.; Bieske, E.J. Does the Triphenylamine-based D35 Dye Sensitizer Form Aggregates on Metal-Oxide Surfaces? J.Photoch. Photobio. A, 2015, 302, 35–41.

[39] Zhang, W.; Pathak, S.; Sakai, N.; Stergiopoulos, T.; Nayak, P. K.; Noel, N. K.; Haghighirad, A. A.; Burlakov, V. M.; de Quilettes, D. W.; Sadhanala, A.; Li, W.; Wang, L.; Ginger, D.S.; Friend, R.H.; Snaith, H.J. Enhanced Optoelectronic Quality of Perovskite Thin Films With Hypophosphorous Acid for Planar Heterojunction Solar Cells. Nat. Commun. 2015, 6, 10030.

[40] Tian, H.; Yang, X.; Chen, R.; Zhang, R.; Hagfeldt; A.; Sun, L. Effect of Different Dye Baths and Dye-Structures on the Performance of Dye-Sensitized Solar Cells based on Triphenylamine Dyes. J. Phys. Chem. C 2008, 112 , 11023-11033.

[41] Sygellou, L.; Paterakis, G.; Galiotis, C.; Tasis, D. Work Function Tuning of Reduced Graphene Oxide Thin Films J. Phys. Chem. C 2016, 120, 281−290.

[42] Biesinger, M. C.; Laua, L. W.M.; Gersonb, A. R.; Smart, R. St.C. Resolving Surface Chemical States in XPS Analysis of First Row Transition Metals, Oxides and Hydroxides: Sc, Ti, V, Cu and Zn. Appl. Surf. Sci. 2010, 257, 887–898.

[43] Choukourov, A.; Biederman, H.; Kholodkov,I.; Slavinska, D.; Trchova, M.; Hollander,A. Properties of Amine-Containing Coatings Prepared by Plasma Polymerization. J. Appl. Polym. Sci., 2004, 92, 979 –990.

[44] Eriksson, S. K.; Josefsson, I.; Ellis, H.; Amat, A.; Pastore, M.;Oscarsson, J.; Lindblad, R.; Eriksson, A. I. K.; Johansson, E. M. J.; Boschloo, G.; Hagfeldt , A.; Fantacci, S.; Odelius, M.; Rensmo, H. Geometrical and Energetical Structural Changes in Organic Dyes for Dye-Sensitized Solar Cells Probed Using Photoelectron Spectroscopy and DFT. Phys. Chem. Chem. Phys. 2016, 18, 252-260.

[45] Li, W.; Zhang, W.; Reenen, S.V.; Sutton, R.J.; Fan. J.; Haghighirad, A.A.; Johnston, M.B.; Wang, L.; Snaith, H.J. Enhanced UV-light stability of planar heterojunction perovskite solar cells with caesium bromide interface modification. Energy Environ. Sci. 2016, 9, 490-498.

[46] Ward, C.L.; DiMarco, B.N.; O'Donnell, R.M.; Meyer, G.L. Dye Excited States Oriented Relative to TiO2 Surface Electric Fields. J. Phys. Chem. C, 2018, 122, 13863–13871.

[47] Cappel, U.B.; Plogmaker, S.; Johansson, E.M.J.; Hagfeldt, A.; Boschloo, G.; Rensmo, H.; Energy Alignment and Surface Dipoles of Rylene Dyes Adsorbed to TiO2 Nanoparticles. Phys. Chem. Chem. Phys. 2011, 13, 14767–14774.

[48] Yip, H.-L.; Hau, S. K. ; Baek, N. S.; Alex, H. M.; Jen, K.-Y. Polymer Solar Cells that Use Self Assembled-Monolayer-Modified ZnO/Metals as Cathodes. Adv. Mater. 2008, 20, 2376– 2382.

[49] Falaras, P., Hugot- Le Goff, A., Bernard, M.C., Xagas, A. Characterization by Resonance Raman Spectroscopy of Sol-Gel TiO_2 Films Sensitized by the Ru(PPh3)2(dcbipy)Cl2 Complex for Solar Cells Application. Sol. Energy Mater. Sol. Cells, 2000, 64, 167-184.

[50] Littleforda, R.E.; Tackleyb, D.R.; Cherrymanb, J.C.; Dent, G.; Smith, W.E. A Raman and DFT Study of Substituted Triphenylamines for Use as Charge Transfer Materials in Light Emitting Polymers. J. Mol. Struct., 2004, 692, 81–90.

[51] Abate, S. Y.; Wu, W. T.; Pola, S.; Tao, Y. T. Compact TiO2 Films with Sandwiched Ag Nanoparticles as Electron-Collecting Layer in Planar Type Perovskite Solar Cells: Improvement in Efficiency and Stability. RSC Adv. 2018, 8, 7847-7854.

[52] Zuo, L.; Chen, Q.; De Marco, N.; Hsieh, Y-T.; Chen, H.; Sun, P.; Chang, Sh-Y.; Zhao, H.; Dong, Sh.; Yang, Y. Tailoring The Interfacial Chemical Interaction for High Efficiency Perovskite Solar Cells. Nano Lett. 2017, 17, 269–275.

[53] Likodimos, V.; Stergiopoulos, T.; Falaras, P.; Kunze, J.; Schmuki,P.; Phase Composition, Size, Orientation, and Antenna Effects of Self-Assembled Anodized Titania Nanotube Arrays: A Polarized Micro-Raman Investigation. J. Phys. Chem. C, 2008, 112, 12687-12696.

[54] Vaenas, N.; Stergiopoulos, T.; Kontos, A.G.; Likodimos,V.; Falaras P. Influence of Controlled-Charge Anodization Processes on the Morphology of TiO2 Nanotubes and their Efficiency in Dye-Sensitized Solar Cells. Electrochim. Acta. 2013, 113, 490 – 496.

[55] Agresti, A.; Pescetelli, S.; Cinà, L.; Konios, D.; Kakavelakis, G.; Kymakis, E.; Di Carlo, A. Efficiency and Stability Enhancement in Perovskite Solar Cells by Inserting Lithium-Neutralized Graphene Oxide as Electron Transporting Layer. Adv. Funct.Mater. 2016, 26, 2686–2694.

[56] Kim, H.-S.; Park, N.G.; Parameters Affecting I−V Hysteresis of $CH_3NH_3PbI_3$ Perovskite Solar Cells: Effects of Perovskite Crystal Size and Mesoporous TiO_2 Layer. J. Phys. Chem. Lett., 2014, 5, 2927–2934.

[57] Liu, D.; Li, S.; Zhang, P.; Wang, Y.; Zhang ,R.; Sarvari, H.; Wang, F.; Wu, J.; Wang, Z.; Chen,Z.D. Efficient Planar Heterojunction Perovskite Solar Cells with Li-Doped Compact TiO_2 Layer. Nano Energy 2017, 31,462–468.

[58] Bisquert, J.; Bertoluzzi, L.; Mora-Sero, I.; Garcia-Belmonte, G. Theory of Impedance and Capacitance Spectroscopy of Solar Cells with Dielectric Relaxation, Drift-Diffusion Transport, and Recombination. J. Phys. Chem. C. 2014, 118, 18983–18991.

[59] Tountas, M.; Verykios, A.; Polydorou, E., Soultati, A.; Kaltzoglou, A.; Balis, N.; Angaridis, P.A.; Papadakis, M.; Nikolaou, V.; Auras, F.; Palilis, L.; Tsikritzis, D.; Evangelou, E.; Gardelis, S.; Koutsoureli, M.; Papaioannou, G.; Petsalakis, I.; Kennou, S.; Davazoglou, D.; Argitis, P.; Falaras, P.; Coutsolelos, A.G.; Vasilopoulou, M. Engineering of Porphyrin Molecules for use as Effective Cathode Interfacial Modifiers in Organic Solar Cells of Enhanced Performance and Stability. ACS Appl. Mater. Interfaces 2018, 10, 20728-20739.

[60] Jiang, X.;Marinado, T.;Gabrielsson, E.; Hagberg, D.-P.; Sun, L.; Hagfeldt, A.; Structural Modification of Organic Dyes for Efficient Coadsorbent-Free Dye-Sensitized Solar Cells. J. Phys. Chem. C 2010, 114, 2799–2805.

[61] Jiang, X.; Karlsson, K.M.; Gabrielsson, E.; Johansson, E.M.J.; Quintana, M.;Karlsson, M.; Sun, L.; Boschloo, G.; Hagfeldt, A.; Highly Efficient Solid-State Dye-Sensitized Solar Cells Based on Triphenylamine Dyes. Adv. Funct. Mater. 2011, 21, 2944–2952.

[62] Fakharuddin, A.; Schmidt-Mende, L.; Garcia-Belmonte, G; Jose, R.; Mora-Sero, I. Interfaces in Perovskite Solar Cells. Adv. Energy Mater. 2017, 7, 1700623.

[63] Asghar, M. I.; Zhang, J.; Wang, H.; Lund, P. D. Device Stability of Perovskite Solar Cells – A Review. Renew. Sust. Energ.Rev. 2017, 77, 131-146.

[64] Pastrana-Martínez, L.M.; Morales-Torres, S.; Kontos , A.G.; Moustakas, N.G.; Faria, J.L.; Doña-Rodríguez, J.M.; Falaras, P.; Silva, A.M.T. TiO_2, Surface Modified TiO_2 and Graphene Oxide-TiO_2 Photocatalysts for Degradation of Water Pollutants under Near-UV/Vis and Visible Light. Chem. Eng. J. 2013, 224,17–23.

[65] R. G. Niemann, A.G. Kontos, D. Palles, E.I. Kamitsos, A. Kaltzoglou, F. Brivio, P. Falaras, P.J. Cameron Halogen Effects on Ordering and Bonding of CH_3NH^{3+} in $CH_3NH_3PbX_3$ (X = Cl, Br, I) Hybrid Perovskites: A Vibrational Spectroscopic Study. J. Phys. Chem. C. 2016, 120, 2509–2519.

[66] M. Antoniadou, M.; Siranidi, E.; Vaenas, N.; Kontos, A.G.; Stathatos, E.; Falaras, P. Photovoltaic Performance and Stability of $CH_3NH_3PbI_{3-x}Cl_x$ Perovskite. J. Surf. Interf. Mat. 2014, 2, 1–5.

[67] Barbé, J.; Kumar, V.; Newman, M.J.; Lee, H.K.H; Jain, S.M.; Hu Chen, H.; Charbonneau, C.; Cornelia Rodenburg, C.; Tsoi, W.C. Dark Electrical Bias Effect on Moisture-Induced Degradation in Inverted Lead Halide Perovskite Solar Cells Measured by Advanced Chemical Probes. Sust. Energy Fuels 2018, 2, 905-914.

[68] Gomez, A.; Sanchez, S.; Campoy-Quiles, M.; Abate,A. Topological Distribution of Reversible and Non-Reversible Degradation in Perovskite Solar Cells. Nanoenergy, 2018, 45, 94-100.

[69] Wen, X.; Sheng, R. Ho-Baillie, A. W. Y.; Aleš Benda, A.; Woo, S.; Ma, Q.; Huang, S.; Green, M.A. J Morphology and Carrier Extraction Study of Organic–Inorganic Metal Halide Perovskite by One- and Two-Photon Fluorescence Microscopy. Phys. Chem. Lett., 2014, 5, 3849–3853.

5 Chapter 5

5 Enhancing the Performance of Perovskite Solar Cells via Doping

5.1 Preface

The field of hybrid halide perovskites has been witnessing a surge of interest over the past few years across the breadth of nanoscience and nanotechnology. Of particular interest, controlling the nanomorphology of the hybrid perovskite absorber can modify intrinsically different properties (crystallinity, defects, grain boundaries) and optimize charge transport in the bulk structures and at the corresponding interfaces, thus leading to highly performing devices. Perovskite solar cells (PSCs), were recently developed and rapidly optimized due to the intriguing optoelectronic characteristics (long diffusion lengths, long charge carrier lifetime and high dielectric constant) of the perovskite polycrystals [1-6]. The latter, employed in the solar cells primarily as sunlight absorbers, are described by the general formula ABX_3, where A is organic and/or inorganic cations, B is a metal cation, and X refer to halide anions. PSCs are characterized by low cost and facile fabrication techniques along with high power conversion efficiency (PCE), which after thorough research has raised within a few years to 25.2% [7-9]. However, there are still unsettled issues restraining their further commercialization, such as further improvement of efficiency and long-term stability [10-16]. The structure of PSCs consists of a perovskite absorber sandwiched between two charge extraction/transport layers, which lead the photogenerated charge carriers (electrons and holes) to the corresponding electrodes. In this context, the electron transport layer (ETL) plays a vital role in obtaining efficient and stable PSCs [17-20], thus various materials

have been used as ETLs including ZnO [21-25], TiO_2 [26], SnO_2 [27-29], WO_x, [30] and $PbTiO_3$ [31]. Among transition metal oxides, titanium dioxide is the most popular one due to the large band gap, long electron lifetimes, low-cost and facile fabrication methods and its suitably located energy bands against the most common sunlight absorbers [32-35]. However, the TiO_2 conductivity and electron mobility is much lower compared to the corresponding value of the perovskite layer, provoking a significant imbalance in the electron flow towards the anode [36]. In addition, the TiO_2 layer may act as a photocatalyst of chemical reactions leading to degradation of the perovskites and to a permanent polarization of the film. Ito *et al*. also found that $CH_3NH_3PbI_3$ degraded on TiO_2 rapidly under visible and UV–vis light for 24 h in air but on the contrary, Al_2O_3 successfully protected the perovskite, which was verified by UV–vis and XRD measurements [37]. Therefore, ETLs with improved conductivity and increased electron mobility are required [38] in order to reduce the charge carriers accumulation and favor the electron passage to the ETL/perovskite interface. The latter can be achieved, among other ways, through ETL's dye sensitization approach [39,40] or by ETL doping/modification with metal ions such as Y^{3+}, Zn^{2+}, Fe^{3+}, Mg^{2+}, Nb^{5+}, Ta^{5+} and Li^{+}[41-47].

Recently, Soultati et al. confirmed that appropriate lithium doping of the ETL layer is an effective approach to suppress the photocatalytic activity of the titania underlayer, mitigate the interfacial degradation and increase the stability of fullerene and non-fullerene organic solar cells [48]. In the literature of perovskite solar cells, there are a few papers adopting copper materials as additives in charge transport or perovskite layers with positive effects in the performance of the corresponding PSC devices however, these works are focusing on their role as hole transporting materials [49]. On the other hand, copper has been extensively used to modify the photocatalytic properties of TiO_2 [50-53] however, as far as we know, the corresponding effects as additive in the ETL of PSCs have not been studied. Herein, a novel

interface engineering approach was adopted and Cu-modified TiO_2 was incorporated in planar perovskite solar cells in order to improve ETL/perovskite interface. The Cu-TiO_2 solution was obtained by blending Cu $(NO_3)_2.3H_2O$ with the TiO_2 precursor solution. The presence of copper significantly advanced the quality of the TiO_2 compact ETL by mitigating its photocatalytic action, increasing its conductivity and improving the adjacent interface with the perovskite layer. XPS analysis revealed the presence of copper in the form of oxide Cu_2O, J-V measurements for modified electron-only devices indicated improved electron mobility and conductivity, PL spectroscopy evidenced the advanced electron transport at the Cu-ETL/perovskite interface, while trap density measurements implied the suppression of surface perovskite trap states.

5.2 Copper Doping

5.2.1 Experimental

FTO conductive glasses (Aldrich, sheet resistance 7 $Ohm \cdot sq^{-1}$) were used as the anode substrates. They were etched with a 2M HCl solution combined with Zn powder. This was followed by thorough cleansing with Hellmanex, acetone and 2-propanol for 15 min. Then then samples were treated with UV ozone for 20 min. The titania ETL was prepared by dissolving titanium (IV) isopropoxide (Aldrich, 97%) in ethanol containing an aliquot of HCl. The final concentration of the 5 ml solution is 0.23M. The Cu-TiO_2 precursor solution was obtained by mixing an amount of a 0.5M Cu $(NO_3)_2.3H_2O$ ethanolic solution with the TiO_2 precursor solution (0.23M) in a doping range, from 0 % to 20% (Figure 5.1). The optimum concentration is 5%, thus mixing 5μl of copper solution with the titania solution. Both modified and pristine ETLs were spin coated at 2000r.p.m. for 60 s. The films were calcinated for 45 min at 500^oC ($5^oC \cdot min^{-1}$ temperature ramp rate) and subsequently were transferred into an Ar-filled glove box for the perovskite deposition. The perovskite layer was deposited by spin coating in a one-step procedure using a solution of anhydrous DMF,

containing 40 wt% Methylammonium iodide (Dyesol) along with Lead acetate trihydrate ($PbAc_2.3H_2O$, 99.999% trace metals basis, Aldrich) in a 3:1molar ratio. A tiny amount of hypophosphorous acid (50% w/w, aquatic solution, Alfa Aesar) was also added into the perovskite solution so as the final molar ratio of HPA:$PbAc_2$ to be 1:4. The deposition was realized at 2000 r.p.m. for 45s. The films were left to dry at room temperature for 5min and were annealed at 100^{o}C for 10min. Finally, a 7wt% Spiro-MeOTAD (Solaronix) solution in chlorobenzene was deposited as the hole transport layer, containing additives of lithium bis(trifluoromethanesulfonyl)imide lithium salt (≥99%, Aldrich) in acetonitrile and 4-tert-butylpyridine (96%, Aldrich). The deposition was done at 3000 r.p.m for 30s. Finally, the devices were transferred outside the glovebox and six 100 nm silver electrodes were thermally evaporated under vacuum of 10^{-6} Torr, at a rate of ~1Å·s^{-1}.

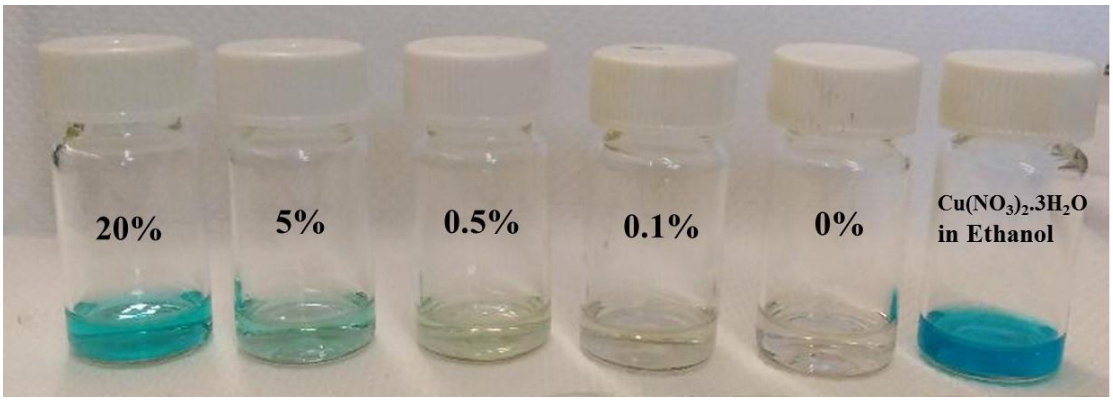

Figure 5.1 Vials containing various amounts of $Cu(NO_3)_2.3H_2O$ dissolved in ethanol

5.2.2 Results and Discussion

As described in the experimental section, copper was added in the titania precursor solution in the form of dissolved $Cu(NO_3)_2.3H_2O$ in ethanol. In general, the following characterizations pertain to the optimum copper concentration (0.5%) as derived from the preliminary tests conducted in PV devices (Figure 5.2).

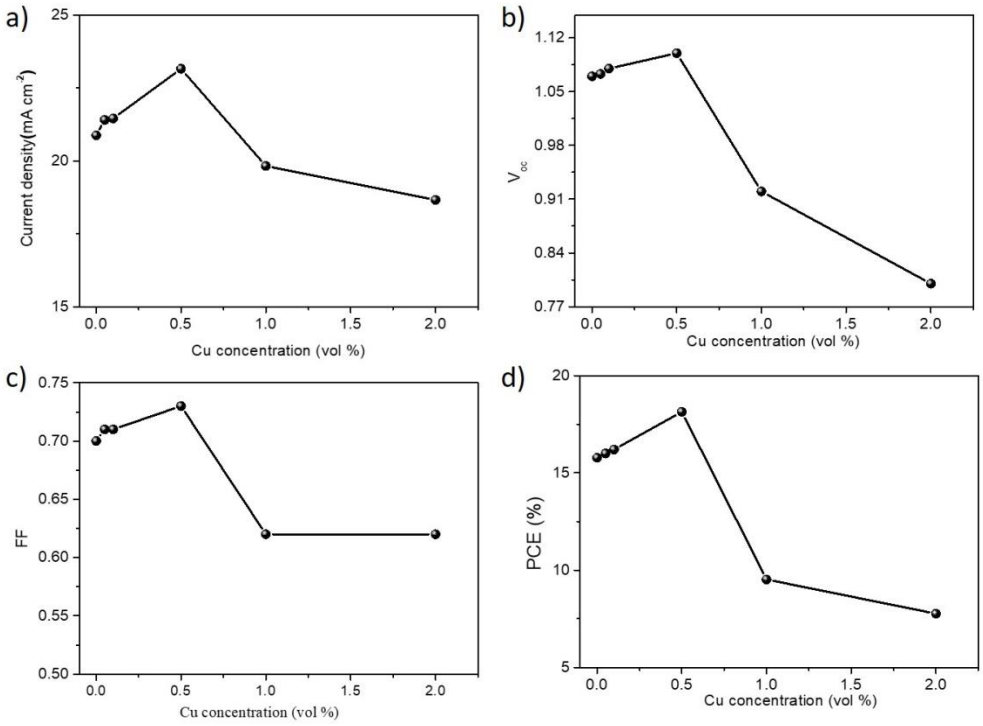

Figure 5.2 PV characteristics for PSCs containing various amounts of $Cu(NO_3)_2.3H_2O$

5.2.3 ETL Characterization

At first, UV-Vis spectroscopy was performed to evaluate the optical properties of titania films with and without copper addition. The presence of the metal did not alter the transmittance of the films (**Figure 5.3a**) and their absorption spectra were not practically affected. This is also the case of the optical band gap values calculated by Tauc equation [$(ahv)^{1/2}$ versus Energy graph, **Figure 5.4**], which relates the optical band gap (Eg) and absorption coefficient (α):

$$ahv = (hvE_g)^{1/2} \qquad (1)$$

where h is Planck's constant, and ν is the frequency of the incident photons.

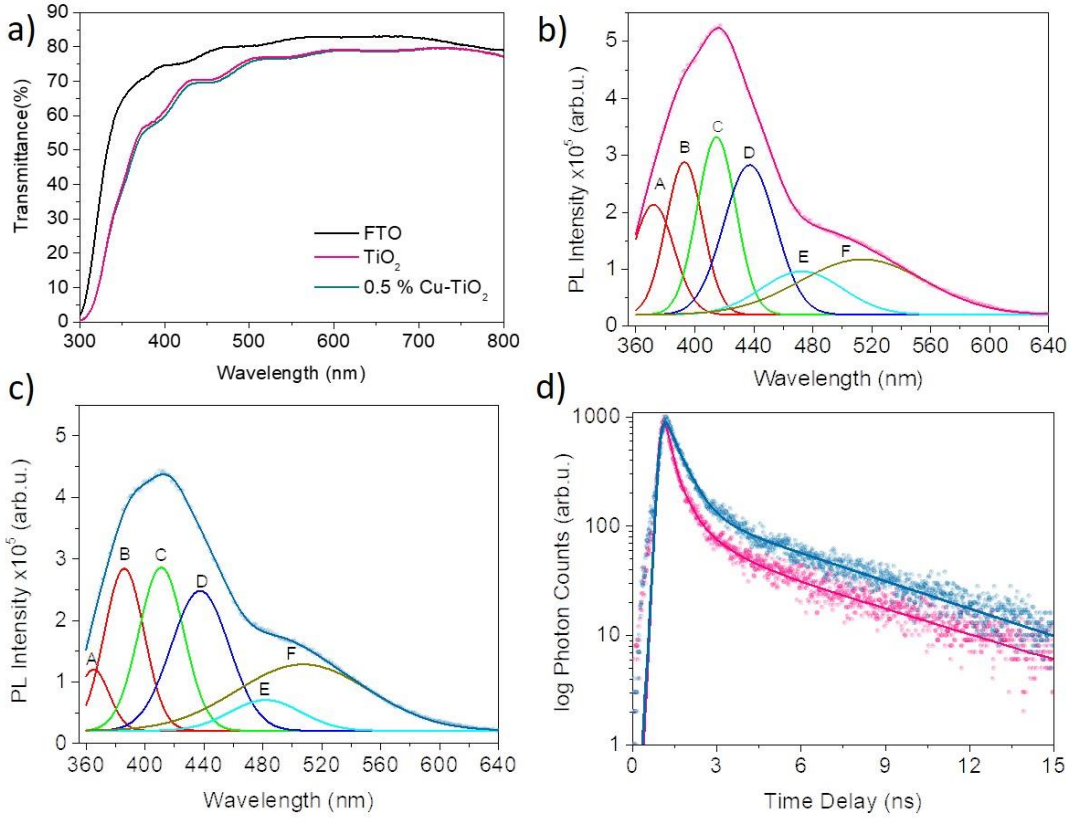

Figure 5.3 Transmittance spectra of FTO and titania films with and without copper (a); Fluorescence emission spectra (l_{exc}= 340nm) recorded for glass/TiO_2 (b) and glass/Cu-TiO_2 (c) samples at room temperature. Gaussian fitting of the PL spectra is also presented; Time-resolved fluorescence spectra (l_{exc}= 376nm) of glass/TiO_2 (pink) and glass/Cu-TiO_2 (blue) samples recorded at room temperature and probed at 400nm (d).

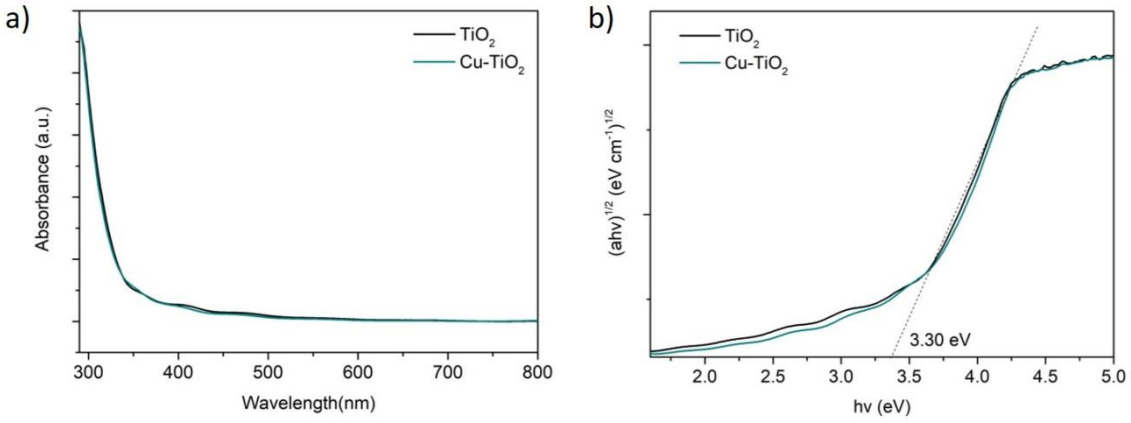

Figure 5.4 Absorption spectra (a) and Tauc plots (b) of the TiO_2 and Cu-TiO_2 film electrodes.

Insertion of copper cations within the TiO_2 lattice might induce crystal imperfections and color centers (*F*-centers) related to oxygen vacancies are emerging. Accordingly, the light harvesting ability of the TiO_2 layer is extended to the visible region of the spectra due to local states below the conduction band, namely transitions with lower energy [55]. The generation of oxygen vacancies is also related to the formation of Ti^{3+} species via interactions with the Ti^{4+} centres neighbouring the vacancies.

Those structural differences between the Cu-treated and pristine TiO_2 layers were further probed with the aid of photoluminescence spectroscopy. TiO_2 and Cu-TiO_2 coated glass substrates were illuminated by a 340nm laser and the recorded spectra are shown in **Figure 5.3 b-c**. In both samples a broad PL emission spectrum with a maximum around 410nm was observed, while in the Cu-modified samples it is quenched by 17%. Gaussian curve fitting of the emission spectra has been proposed as an analytic method for unravelling the structural characteristics of the TiO_2 semiconductors [56]. The emission spectra may be deconvoluted in various Gaussian derivatives related to the electronic properties of the materials. In general, the deconvoluted peaks below 400nm are attributed to the band-to-band emission while most of the visible light PL emission peaks are directly or indirectly related to oxygen vacancy defects and energy states below the energy level of the conduction band. In our samples, the PL emission curves were best fitted with six Gaussians.

The first peak, peak A, is located at ~370nm and possibly represents the phonon-assisted indirect bandgap emission, while the second one, peak B located at ~390nm is assigned to the direct band-to-band transition. Radiative recombination of trapped electrons by titanium (III) (Ti^{3+}) or oxygen vacancies lying below the level of the conduction band are contributing a strong emission feature located at ~410nm, peak C [57]. Moreover, the deconvoluted peaks with maxima at ~ 435nm (peak D), ~ 475 (peak E) and ~ 510nm (peak F) are attributed to trapped electrons localized on TiO_6^{8-} anions at the surface [58], deep surface traps arise from

Ti^{3+} [53,59,60,61]and charge transfer from Ti^{3+} to the nearby oxygen atoms of TiO_6^{8-} surface domains [62,63], respectively. Although the exact nature of those derivative peaks in the PL spectrum of TiO_2-based materials lying in the visible spectrum are under continuous investigation, it is established that could provide valuable information for the structural and electronic characteristics. As it can be seen in the fitted spectra presented in Figures 1b-c, the intensity of the A-F peaks is different for the Cu-TiO_2 samples. Peak B, which usually appears to be weaker than the defect-related emission peaks, is more intense in the Cu-TiO_2 indicating enhanced direct band to band emission [55]. Actually, the time-resolved fluorescence spectra recorded for Cu-TiO_2 revealed an increased fluorescence lifetime for the band-to-band transition (τ= 2.9ns), as compared to pristine TiO_2 (τ= 2.4ns). (**Figure 5.3d**) Concerning the defect-associated features in the two samples the differences are not so profound, however the incorporation of copper cations seems to reserve the defect density rather than disturb the crystal lattice structure.

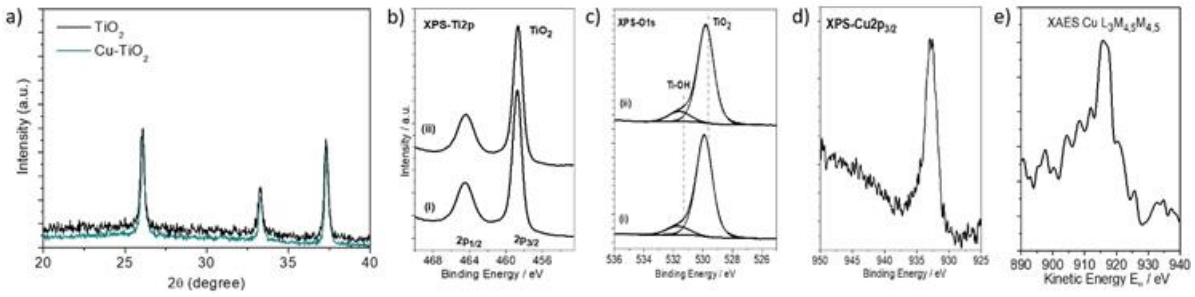

Figure 5.5 XRD patterns of pristine and modified titania films coated upon FTO substrates (a); Ti2p (b) and O1s (deconvoluted) (c) XPS spectra of ITO/TiO_2 (i) and ITO/Cu-TiO_2 (ii); the $Cu2p_{3/2}$ XPS (d) and Cu $L_3M_{4,5}M_{4,5}$ Auger (e) spectra of ITO/Cu-TiO_2 sample.

In order to understand how copper contributes to this absorption enhancement, structural and morphological characterization was performed. The crystallinity of FTO/TiO_2 and FTO/Cu-TiO_2 films were studied by XRD. **Figure 5.5a** shows the 20^o-40^o region of the obtained XRD patterns in magnification, where it is obvious that both pristine and modified TiO_2 films share the same diffraction pattern with equal peak intensities that corresponds to the anatase phase

[2θ=26.3° and 37.3°] of TiO_2. Incorporating copper in the TiO_2 layer did not affect the crystal structure and no new peaks were detected, probably due to the small concentration of Cu in TiO_2, meaning that the Cu was uniformly distributed without affecting the TiO_2 crystal lattice. Consequently, X-ray Photoelectron Spectroscopy (XPS) measurements recorded in order to take information about the copper chemical state and atomic percentage (**Figure 5.5b-e**). In general, the XPS spectra present significant differences, characteristic of the Cu presence at Cu-TiO_2/ITO. This sample did not show a charge due to radiation, which means it was more conductive. Figure 5.5b depicts the Ti2p Spectra for both ITO/TiO_2 and ITO/Cu-TiO_2 samples. The Ti2p3/2 binding energy is at 458.8±0.1eV assigned to Ti^{4+} in TiO_2. The deconvoluted O1s peak (Figure 5.5c) consists of two components assigned to lattice oxygen (at binding energy 529.8eV) and to Ti-OH groups which are present on the surface (at binding energy 531.6±0.1eV) [64]. The comparative analysis on the deconvoluted O1s peak in both materials shows a slightly smaller percentage of Ti-OH in the sample with Cu (**Table 5.1**), which can result in differences in both wetting properties and photocatalytic action.

Table 5-1. Lattice oxygen components (Ti-O and Ti-OH groups) concentration (% percentage.)

		TiO_2/ITO	**Cu-TiO_2/ITO**
Peak	**Eb [eV]**	**% comp. concentration**	**% comp. concentration**
Ti-O	529.9±0.1eV	87.83 ± 0.08	88.50 ± 0.08
Ti-OH	531.6±0.1eV	12.17 ± 0.08	11.50 ± 0.08

Additionally, the $Cu2p_{3/2}$ XP spectrum and the Cu $L_3M_{4,5}M_{4,5}$ Auger spectrum from the ITO/Cu-TiO_2 sample's surface are presented in Figure 5.5d-e. The kinetic energy of the Auger electrons induced under X-ray radiation (XAES), is useful to identify the signature of a specific oxidation state when the chemical shift of an element presents only few meV

variations. The binding energy of $Cu2p_{3/2}$ is at 932.8±0.1eV and the kinetic energy of Cu $L_3M_{4,5}M_{4,5}$ centered at 916.3eV (corresponding to a binding energy of 570.3eV) are assigned to Cu_2O [65]. Moreover, the modified Auger parameter derived from the sum of the binding energy of $Cu2p_{3/2}$ and the kinetic energy of Cu $L_3M_{4,5}M_{4,5}$ is 1849.1eV and is also assigned to Cu^{1+}, as previously reported in low copper concentrations mainly Cu_2O (Cu^{1+}) is present contrary to Cu^{2+} that dominates in higher concentrations [62]. From the total peak area of Ti2p, O1s, Cu2p and C1s, the experimentally calculated % atomic concentration for Ti, O and Cu are in good agreement with the theoretically expected values (**Table 5.2)**. Thus, the XPS measurements indicate that Cu^{+} dominates at such low copper concentration level in titania.–Taking into account the XRD patterns it seems that copper has been uniformly distributed in the interstitials sites without affecting the lattice, mainly in the form of monovalent cations which interact with the absorbed oxygen leading to the formation of Cu_2O [66,67].

Table 5-2 % Elements atomic concentration (% percentage) as calculated by XPS measurements.

Sample	**Ti**	**O**	**C**	**Cu**
ITO/TiO_2	23.96±0.03	58.58±0.06	17.45±0.06	-
ITO/Cu-TiO_2	23.67±0.03	57.60±0.06	18.26±0.07	0.47±0.007

In order to examine the surface topology of TiO_2-based films, microscopy techniques were used, including scanning electron microscopy (SEM) and atomic force microscopy (AFM). SEM images in **Figure 5.6** shows that the titania films morphology is not affected by the presence of copper, albeit Energy Dispersive Spectroscopy (EDS) confirmed the presence of elemental Cu within TiO_2 films in the respective images of Figure 5.6. The same conclusion

also stems from the corresponding AFM images of TiO_2 and Cu-TiO_2 films presented in **Figure 5.7**. The morphology of the films is not dramatically altered in the presence of copper; however, roughness is slightly decreased from 20.03nm to 19.65nm. Notably, the smoother surface of the ETL film is beneficial for depositing the perovskite film leading to facilitation of the charge transport, Moreover, the addition of Cu may affected the surface chemistry of TiO_2, as demonstrated from contact angle measurements (**Figure 5.8)**. Particularly, the TiO_2 compact layer becomes more hydrophobic in the presence of Cu since the contact angle of TiO_2 and Cu-TiO_2 were 43.45° and 63.6° respectively. Hydrophobicity may facilitate the growth of larger perovskite grains, attributed to the existence of less perovskite grains nucleation centers [68].

Enhanced hydrophobicity in modified films can be ascribed to an alteration in surface chemistry because of a lower number of surface defects, such as oxygen vacancies, acting as binding sites for water molecules [69]. This facilitates the growth of larger perovskite grains, attributed to the existence of less perovskite grains nucleation centers. Such enhanced hydrophobicity is explained by the increased recombination of photoexcited electrons and holes in the TiO_2 films containing the Cu dopants [70]. In addition, increased hydrophobicity may also result in lower photocatalytic activity of the ETL substrate. In fact, the presence of such a hydrophobic substrate decreases the possibility of interface wetting and hence the production of reactive oxygen species (mainly hydroxyl radicals-$OH^{\cdot}$) via reaction of the photogenerated hole carriers with adsorbed water molecules can be mitigated and/or suppressed. The effects of such a hydrophobic substrate might become more significant in PSCs under real operational conditions (e.g. 1 sun illumination), where pristine titania presents enhanced photoinduced superhydrophilicity [71].

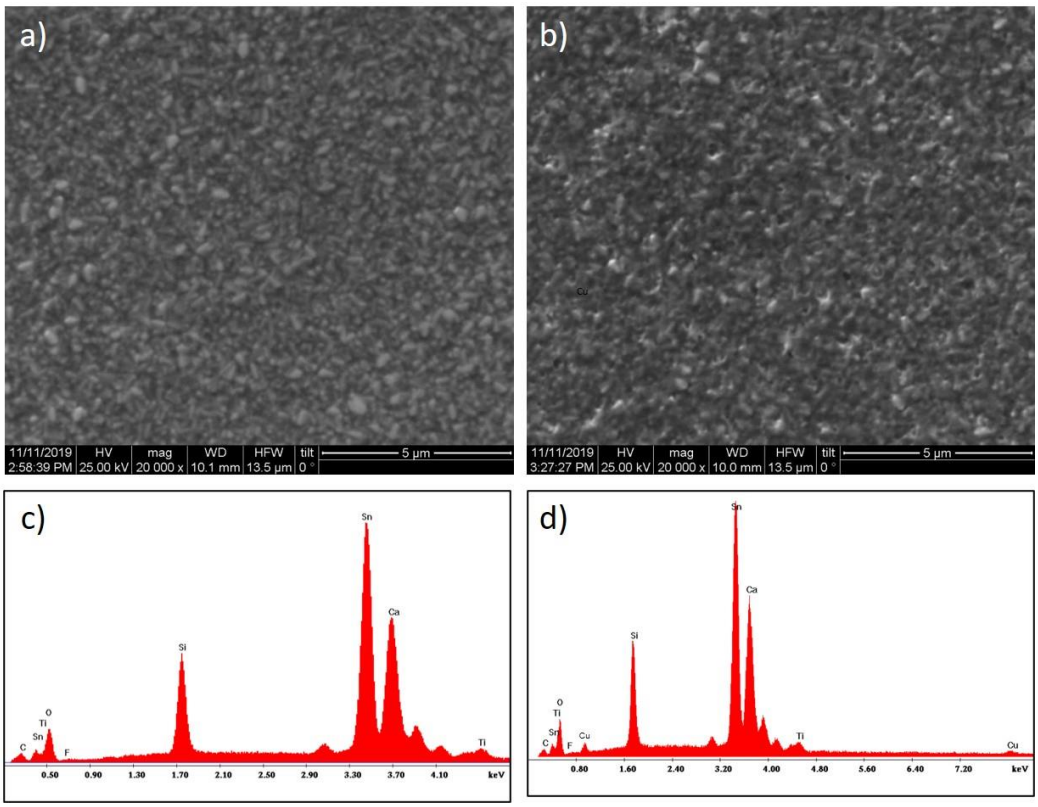

Figure 5.6 SEM images(a,b) and the corresponding EDS patterns (c,d) of titania films without (a,c) and with copper (b,d).

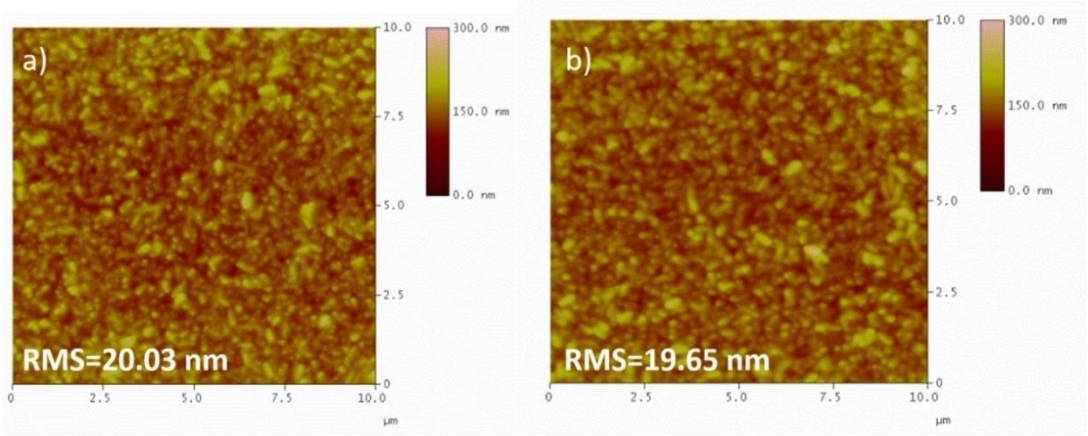

Figure 5.7 AFM images of titania films without (a) and with copper (b).

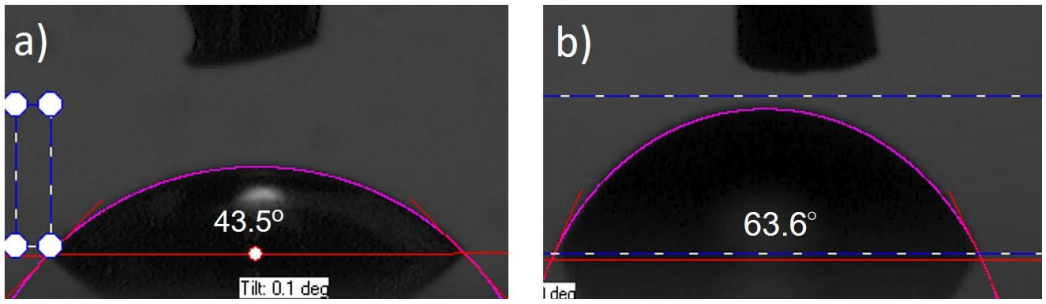

Figure 5.8 Contact angle measurements of neat (a) and copper-modified titania (b) films.

5.2.4 Perovskite film Characterization

Furthermore, the quality of perovskite films coated upon pristine and modified titania substrates was thoroughly investigated by structural, microscopic, and spectroscopic techniques. At first, the topology of the perovskite films was investigated by SEM and AFM techniques. Thus, the morphology of the perovskite films was examined by AFM analysis, as shown in **Figures 5.9a-b**.

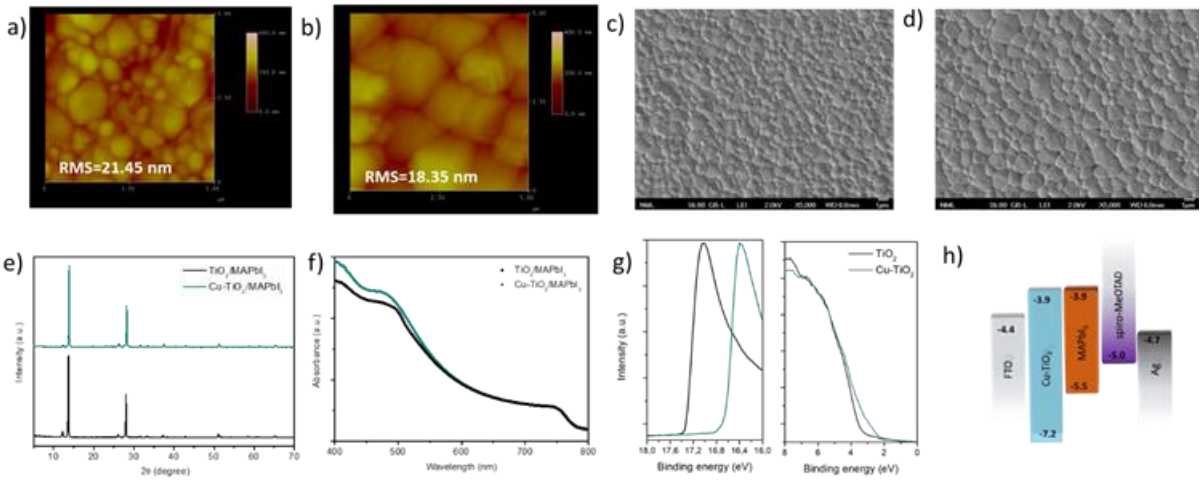

Figure 5.9 AFM (a,b); and SEM (c,d)) images of perovskite films grown upon pristine (a,c) and modified (b,d) titania substratesXRD patterns (e) of perovskite layers coated upon pristine and modified titania films and absorption spectra (f); UPS spectra of pristine and Cu-TiO_2 samples (g); Schematic diagram of the energy levels as derived from UPS and absorbance measurements(h).

In the case of perovskite layers grown upon copper containing TiO_2, larger and more uniform perovskite crystals are grown, while the roughness of the films is decreased. Smoother films are beneficial for the improved performance of the cells since they highlight reduced resistance parameters, hence improved fill factor. **Figures 5.9c** and **4.9d** show the SEM images of perovskite film grown upon TiO_2 and Cu-TiO_2 substrates, respectively. The obtained images indicate that the film grown atop of the modified ETL consist of larger perovskite grains while the morphology seems smoother. The former was confirmed by the statistical analysis conducted over a sample of 100 grains from each sample. The results are summarized in **Figure 5.10.** The mean size of the grains of the reference sample is 0.95μm, contrary to the modified one, where the mean size is higher, 1.30μm. Larger crystals mean less grain boundaries, something highly desirable towards improvement of PSCs, since grain boundaries are prone to oxygen or humidity penetration leading to rapid destabilization of the devices. Moreover, larger crystals entail improved light absorption (a hypothesis in good agreement with UV-Vis measurements), thus increased photocurrent collection. The thickness of the absorbing layers was estimated by 55^o tilted cross section images (**Figure 5.11**). As derived from the calculation, the mean thickness of the reference film is 350nm while the modified on is slightly thicker (370nm).

The perovskite's crystallinity was analyzed by XRD measurements of FTO/TiO_2/$MAPbI_3$ and FTO/Cu-TiO_2/$MAPbI_3$ films (**Figure 5.9e**). The planes [(110), (220) and (310) at $2\theta=14°$, $2\theta=28°$ and $2\theta=31.9°$, respectively], prove the 3D perovskite crystalline formation in the tetragonal $CH_3NH_3PbI_3$ phase. The peaks in both pristine and modified films indicate a well-crystallized perovskite film. The perovskite layer grown upon the Cu-modified TiO_2 substrate present higher diffraction peaks intensity, a fact associated with improved crystallinity and larger crystals, avoiding the recombination of the photogenerated carriers at the grain boundaries.The latter was also corroborated by UV-Vis measurements (**Figure 5.9f**)

which indicated the increased absorption of the modified perovskite layer below the 550nm region.

Furthermore, UPS measurements were performed in order to estimate the impact of Cu on the TiO_2 electronic structure. **Figure 5.9g** illustrates the UPS spectra, taken from ITO/TiO_2 and ITO/Cu-TiO_2 samples. The work function (W_F) can be calculated from the difference between the incident light energy ($h\nu$ = 21.22 eV) and the energy of the secondary cutoff: $W_F = h\nu - E_{cut\text{-}off}$. The corresponding W_F of the pristine TiO_2 and Cu-TiO_2 were estimated as 3.9 and 4.6 eV (vs vacuum). The Ionization Potential or the High Occupied Molecular Orbital (HOMO) is derived from the sum of the W_F and the Valence band Maximum (VBM) cut-off. The VBM cut-off is determined by linear extrapolation towards background in the low binding energy region which is shown in Figure 3g (right). The distance between the VBM and Fermi level (E_F) are about 3.4 and 2.6 eV for the pristine TiO_2 and Cu-TiO_2 (Figure 2f), with the corresponding VBM position to be 7.3 and 7.2 eV, respectively. The Fermi energy of TiO_2 is shifted downward after modification with Cu, possibly due to the decrease in the amount of oxygen vacancies on the surface of TiO_2. Oxygen vacancies are the active sites for water dissociation, as well as an origin of photoactivity under light illumination. Moreover, the optical band gaps obtained from the Tauc plots are 3.3eV for both films. The corresponding energy-level diagram of the fabricated device is shown in **Figure 5.9h**. The up-shifted Conduction Band Maximum (CBM) in the case of the modified TiO_2 film is more compatible with the perovskite layer leading to the minimization of the energy loss of electrons in the transportation.

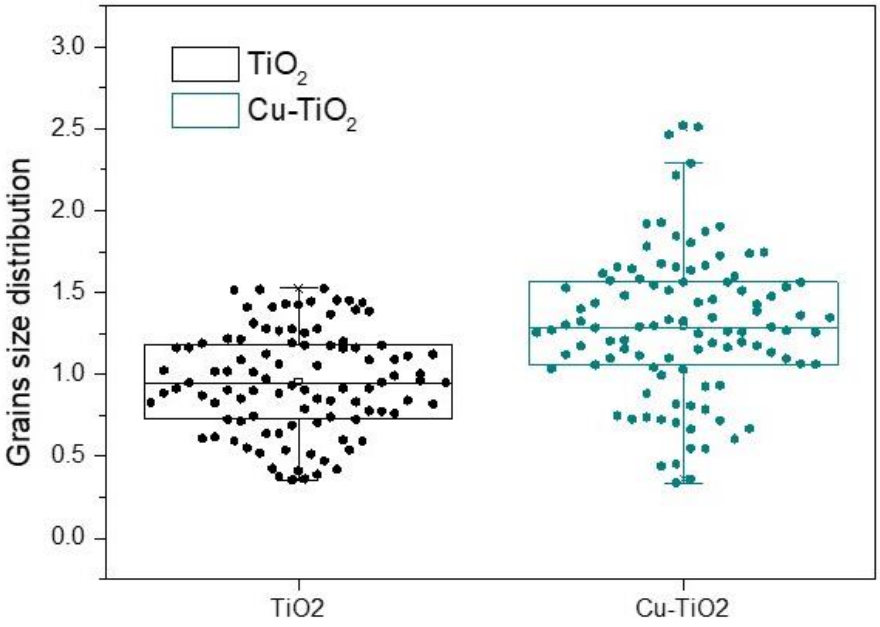

Figure 5.10 Size distribution of perovskite grains as derived from the SEM images.

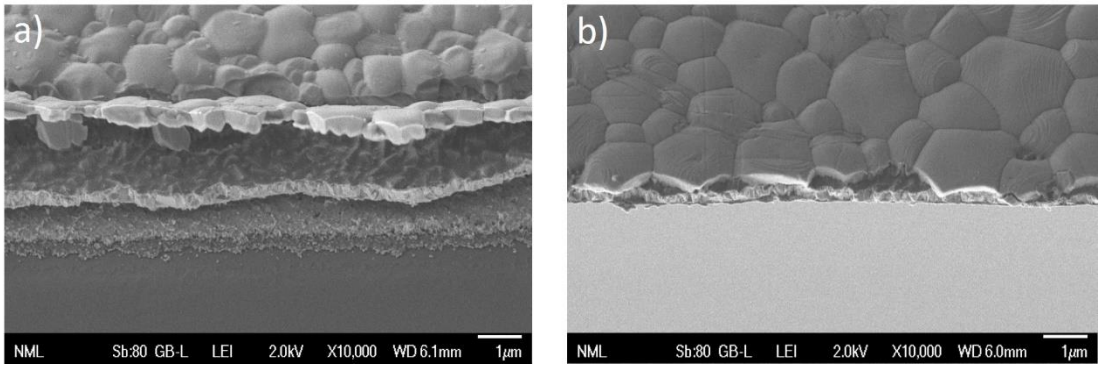

Figure 5.11 Cross section SEM images of perovskite layers grown upon neat (a) and modified (b) TiO2 substrates

5.2.5 Photocatalytic action of ETL against hybrid MAPbI3

In order to evaluate the $MAPbI_3$ perovskite photodegradation from the photoactive ETLs, the titania and copper-modified titania compact layers deposited on FTO conductive glass substrates and coated with the hybrid $MAPbI_3$ perovskite absorber (FTO/Cu-TiO_2/$MAPbI_3$ and reference FTO/TiO_2/$MAPbI_3$, respectively) were placed into a home-made photocatalytic

reactor. The photoreactor was equipped with four UV-A lamps (Sylvania GTE F15W/T8), emitting at 350–390 nm with power density 0.5 mW cm^{-2} (at a distance of 15 cm from the lamps, where the electrodes were placed) and a heat dissipation system, in order to avoid temperature increment in the inner chamber. Every one hour the irradiation was turned off, optical photos of the samples were taken and the Raman spectra of the electrodes were collected with a Renishaw inVia Reflex micro-Raman using a laser beam at 514.4 nm which was focused onto the samples surface via a 50x objectives to a sizeable spot, with power density below 0.1 mW μm^{-2}.

The robustness of the $MAPbI_3$ films deposited on the copper-modified titania ETL is easily corroborated by the optical images (**Figure 5.12**), depicting the evolution of the photocalytic degradation of the $MAPbI_3$ perovskite under UVA irradiation during 8h. The images show that the corresponding film grown on the reference (titania) substrate has progressively turned yellow due to the presence of PbI_2 and their comparison indicates that the $MAPbI_3$ perovskite grown over FTO/Cu-TiO_2 substrate is far less affected.

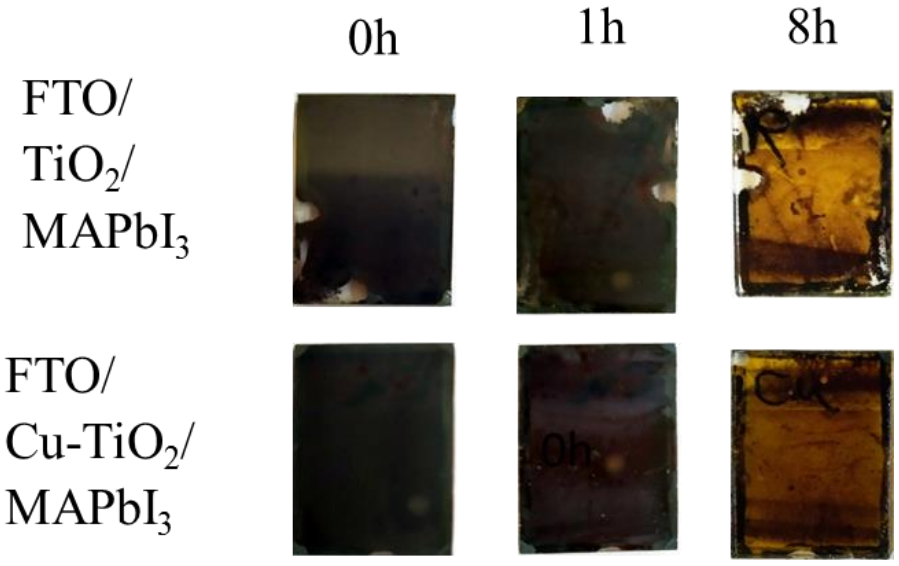

Figure 5.12 Optical images evolution (at 0, 1 and 8 h, respectively) of perovskite layers under UVA photocatalytic stress.

The above results were further confirmed by Raman spectroscopy. It is important to mention that no Raman signal of the pristine perovskite can be obtained under on-resonance Raman excitation due to laser induced degradation and phase transformations [72]. Thus, in principle, only the degradation PbI_2 products formed on the samples can be detected by Raman. Indeed, the Raman spectra recorded (**Figure 5.13**) on pristine titania present a vibration peak at 215 cm^{-1} indicating the formation of PbI_2 degradation product across the sample [73-74]. This peak is already present after 1h of UVA irradiation. In fact, as shown in Figure 5-12, the PbI_2 Raman signal exceeds the noise level after 1 h under UVA irradiation and becomes very strong for the 8h stressed films. On the contrary, the perovskite samples developed on the copper-modified substrate did not present any Raman vibration peak after 1h under UVA. In addition, the PbI_2 signal for the perovskite films grown on the Cu-TiO_2 substrates is systematically lower that of the reference films, verifying the higher robustness of these samples against photocatalytic degradation.

The PbI_2 formation of the UVA irradiated films was further tested by performing Raman mapping on relatively large areas of the films. The optical images from the Raman spots and the Raman data clearly show that the PbI_2 Raman signal is correlated with the areas observed yellowish under the optical microscope. Furthermore, in the copper-based film both large areas which are almost intact from degradation products and big isolated PbI_2 islands are observed.

On the other side, the reference film is almost fully covered by PbI_2 after 8h under UVA light. The photocatalytic activity of TiO_2 nanoparticles is due to the production of reactive oxygen species (ROS), including hydroxyl radical ($OH^{\bullet}$) and hydrogen peroxide (H_2O_2) under UV light irradiation [75].

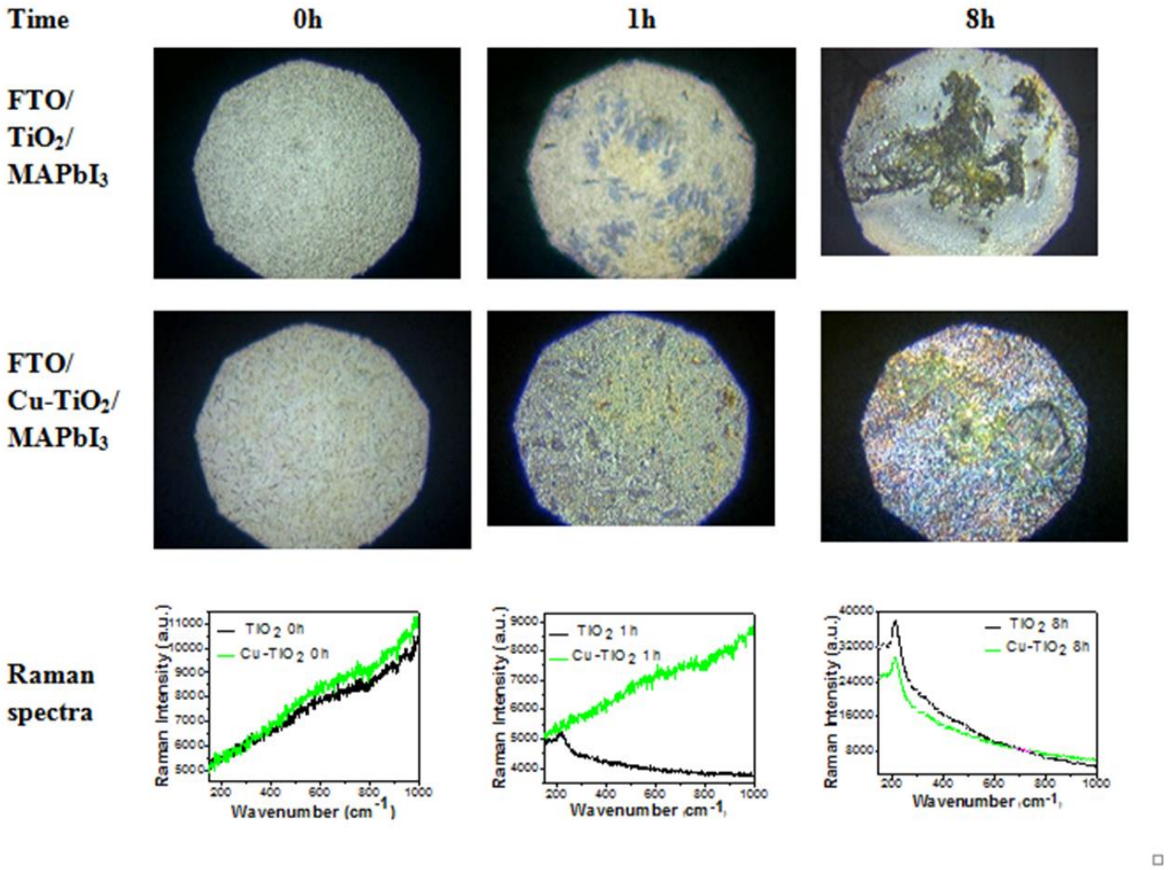

Figure 5.13 Evolution of Raman characteristics of perovskite layers under UVA stress. Characteristic laser spot images and corresponding Raman spectra comparison as a function of the irradiation time. The inset in the Raman spectra shows the main PbI_2 vibration band resulting from the $MAPbI_3$ perovskite photocatalytic degradation.

Cu modification translates into defects being detrimental to the photocatalytic action. In fact, in the case of Cu modified TiO_2, atomic rearrangements and surface reconstruction triggered by the incorporation Cu^{1+} into anatase structure resulted in recombination centers for charge carriers. These recombination centers were ascribed both to Cu^{+1} entities themselves and probably to the adverse trap states attributable to the excessive charge unbalance within the Cu-TiO_2 lattice [76].

5.2.6 Photovoltaic Performance

To verify the role of Cu modification within the compact layer, e-only devices were fabricated and were characterized in the space-charge-limited-current (SCLC) regime. The I-V response was measured for cells fabricated with the following structure: FTO/TiO_2/$MAPbI_3$/PCBM/Ag corresponding to the reference device and FTO/Cu-TiO_2/$MAPbI_3$/PCBM/Ag corresponding to the modified one [77]. As presented in **Figure 5.14a**, at low voltage values, the I-V plot is ohmic (linear), but at mid-voltages, the current shows a rapid nonlinear rise characterized by the transition within the trap filled limit (TFL) regime where all the available trap states are filled by the injected carriers. Finally, at high voltage values, the current has quadratic voltage dependence in the Child's regime. The ohmic to TFL transition point (V_{TFL}) is related to the trap density (Nt) according to the following equation (1):

$$V_{TFL} = \frac{eN_t d^2}{2\varepsilon\varepsilon_0} \qquad (1)$$

where e is the elementary charge, d is the thickness of the active layer (350 nm), ε (ε=28.8) is its dielectric constant, and ε_o is the dielectric constant in vacuum[78]. The calculated trap densities (N_t) are 2.10 x 10^{15} cm^{-3} for the reference device and 7.8 x 10^{14} cm^{-3} for the Cu-modified one, respectively.

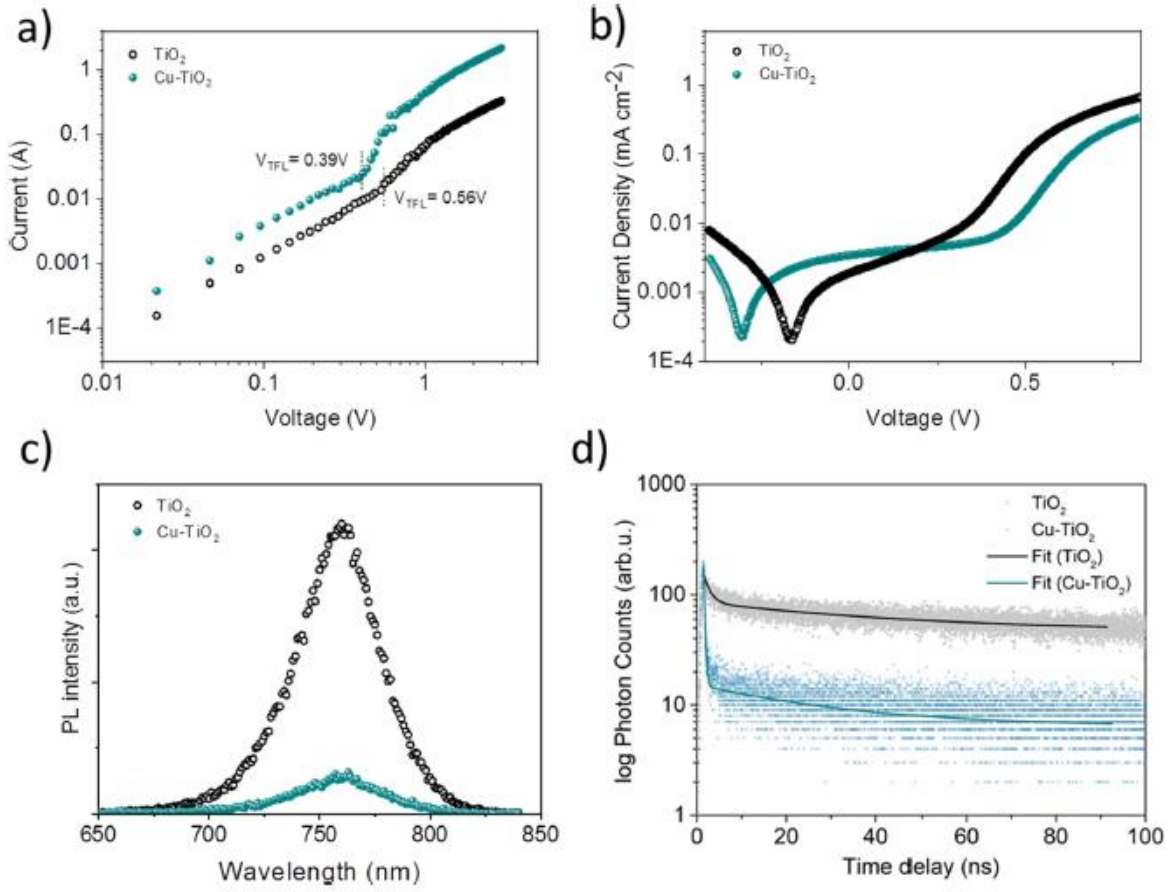

Figure 5.14 Dark I-V measurements of the electron-only devices (a); Dark J-V measurements for PSCs with and without modification (b); Steady-state PL spectra (c) and TRPL spectra (c) of perovskite films on pristine TiO_2 or Cu-doped substrates.

These results, indicating a significant reduction of perovskite's trap density in the case of Cu are associated with a possible V_{oc} enhancement and a significantly higher stabilized efficiency, something that will be further elucidated by photovoltaic measurements. From the dark J-V curves shown in Figure **5.14b,** it can be seen that the dark current of the Cu-modified device under forward bias is significantly lower than that of reference device, suggesting that the Cu-modified device shows lower leakage current. The latter is associated with lower shunt resistance and with a possible increase of the open circuit voltage.

Table 5-3 Parameters of the TRPL spectroscopy for the pristine TiO_2/perovskite and Cu-TiO_2/Perovskite samples deposited on FTO substrates. $t_1$and t_2 correspond to the long decay time and the fast decay time, respectively. The t_{mean} is estimated using the equation of $t_{mean} = \sum A_i t_i^2 / \sum A_i t_i$.

Sample	t_{mean}(ns)	t_1(ns)	A_1	t_2(ns)	A_2
TiO_2	183.31	187	0.98	2.69	0.02
Cu-TiO_2	86.29	96.9	0.89	0.45	0.11

In order to evaluate the contribution of copper in the conductivity of the titania ETLs, dark I-V characteristics for diodes with the following structure: FTO/TiO_2/Ag and FTO/Cu-TiO_2/Ag, were recorded. **Figure 5.15** shows the linear behavior of the ohmic region of the curves. According to expression $I = \sigma_0 \frac{A}{d} V$ (where A, d, and σ_0 are sample's area, thickness, and electrical conductivity, respectively), the electrical conductivity increased from 6.7×10^{-5} to 2.0×10^{-3} mS·cm^{-1} after copper modification.

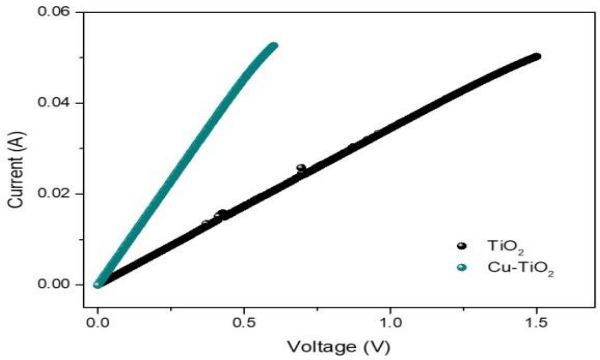

Figure 5.15 I-V curves of the ohmic region devices based on non-modified TiO_2 and Cu-TiO_2 as ETLs.

The dynamics of charge extraction at the ETL/perovskite interface was investigated by steady state photoluminescence (PL) and time resolved photoluminescence (TRPL) spectroscopy. Figure 5.3c shows the PL spectra of FTO/TiO_2/perovskite and FTO/Cu-TiO_2/perovskite samples, where emission peaks at 759 nm are observed for both films. However a significant quenching of the PL signal was obtained for the Cu-TiO_2 sample compare to the reference one, indicating less radiative recombinations that lead to improved charge extraction at the ETL/perovskite interface. This may be attributed to the increased conductivity of the Cu-TiO_2 film. Moreover, TRPL analysis was performed for each of the FTO/TiO_2/perovskite and FTO/Cu-TiO_2/perovskite films (Figure 5.14d). TRPL results show a higher carrier lifetime for the Cu-TiO_2/perovskite than for the reference one. Long decay time is essential for the long exciton diffusion length and low density of defects in the perovskite thin film.

The photovoltaic performance of perovskite PV devices was explored by measuring solar cells with the following structure: FTO/TiO_2/$MAPbI_3$/Spiro-MeOTAD denoted as 'TiO_2' and FTO/Cu-TiO_2/$MAPbI_3$/Spiro-MeOTAD denoted as 'Cu-TiO_2'. The J-V curves recorded at a reverse scan rate of 50mV·sec^{-1} are presented in **Figure 5.16a** and the detailed parameters are shown in Table 5.4. In the case of the PSC based on the Cu-modified compact layer, the short-circuit current density (J_{sc}) is increased from 20.87 for the reference PSC to 23.15 mA/cm^2 for the device with the optimum Cu concentration. This increase may be attributed to the enhanced light absorption of the corresponding perovskite layer. Moreover, it implies the improved charge transport to the anode and the reduced charge recombination at the perovskite/ETL interface.

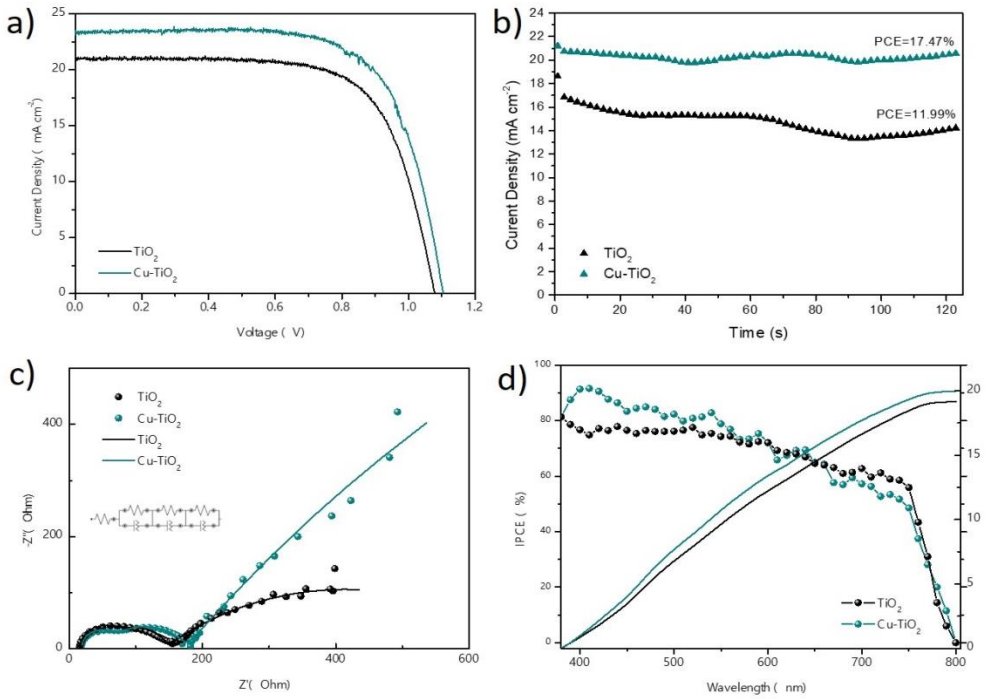

Figure 5.16 Photovoltaic characteristics of the best performing planar PSCs. *J-V* characteristics (a) and IPCE spectra of the best-performing cells based on prtistine and Cu-modified ETLs (b); PCE output of the cells based on the pristine and Cu-modified TiO_2 measured under one sun illumination conditions for 120s (c); Nyquist plots of the corresponding perovskite solar cells with the equivalent circuit depicted in the inset.

Additionally, open-circuit voltage (V_{oc}) was clearly enhanced in the case of the Cu-based PSC, reaching a maximum value of 1.12 V. This fact is probably associated to the decreased trap states density in the perovskite layer and a possibly better alignment of the corresponding energy bands. The champion Cu-containing PSC also presented a superior FF, clearly attributed to reduces resistance parameters and to the smoother interface between perovskite and ETL. Finally, a champion PCE equal to 18.15% was obtained for the PSC with the optimum Cu concentration. The modified cells outperformed the performance of the best reference device which showed a PCE equal to 15.78% (with a V_{oc} equal to 1.07 V, J_{sc} equal to 20.87 $mA \cdot cm^{-2}$ and FF equal to 70 %). The photovoltaic performance was further studied

by the statistical analysis of the obtained results and as depicted in **Figure 5.17** Cu modification of TiO_2 compact layer has a remarkable contribution in the improvement of the solar cells.

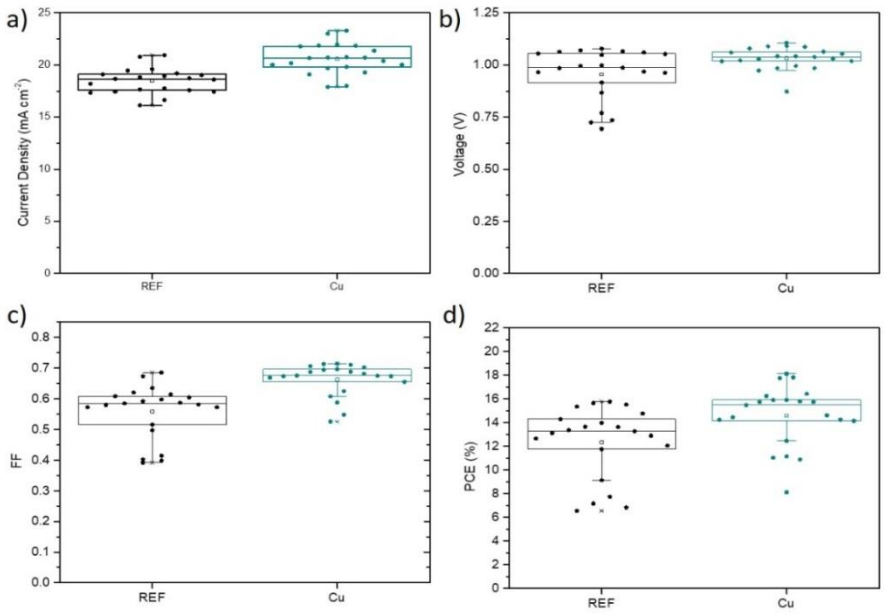

Figure 5.17 Statistical distribution of the main PV characteristics for 20 PSCs of each batch. "Ref" are denoted the PSCs based on pristine titania ETL while "Cu" refer to the modified PSCs.

Figure 5.16b shows the steady-state current density of PSCs with and without Cu under 1 sun illumination conditions. The cells were biased at the corresponding maximum power point voltage (V_{mp}), namely 0.86V for the modified and 0.84V for the reference one. The difference of their output is clear. The device with Cu-TiO_2 as the ETL preserves almost 100%of its efficiency under continuous irradiation, contrary to the reference device of which, PCE declines rapidly. Both forward and reverse-bias scans were recorded for both the Cu doped and non-doped PSCs where the hysteresis index was much lower than in the case of the Cu doped devices **(Figure 5.18).**

Table 5-4 Photovoltaic parameters of the champion PSCs based on pristine and Cu-modified titania substrates under AM 1.5D illumination. The mean values are included in the brackets as derived by the PV evaluation of 25 different devices from each batch.

Sample	**J_{sc}(mA·cm^{-2})**	**V_{oc} (V)**	**FF**	**PCE (%)**	**SPCE(%)**
TiO_2	20.87 (18.48±1.21)	1.07 (0.95±0.12)	0.70 (0.55±0.08)	15.78 (12.34±3.02)	11.99
Cu-TiO_2	23.15 (20.58±1.42)	1.12 (1.03±0.05)	0.73 (0.66±0.05)	18.15 (14.59±2.57)	17.47

The mean values are included in the brackets as derived by the PV evaluation of 25 different devices from each batch. All data were taken under reverse scan at 50 mV•s-1Voc: open-circuit voltage, Jsc: short-circuit current density, FF: fill factor, PCE: power conversion efficiency, SPCE: Stabilized PCE.

This is due to the electron transportation facilitation and reducing the charge accumulation at the Cu doped ETL/perovskite interface. **Figure 5.16c** shows the Incident Photon-to-Current Efficiency (IPCE) measurements of the as prepared PSCs. The response for the modified device is improved against the unmodified one, especially above the 600nm region, which is mainly due to the enhanced electron extraction capability and the improved light harvesting accompanying the Cu-TiO_2 ETL. The integrated J_{sc} values for the Cu-modified and unmodified devices are 20.03mA/cm^2 and 18.54mA/cm^2, respectively. The inconsistency between these values and the ones obtained from photovoltaic characterization is attributed to the omitted part of the spectra (below 480nm) in the case of the IPCE measurement. The improved performance of the Cu-modified solar cells was confirmed by Electrochemical Impedance Spectroscopy (EIS) measurements, which were conducted under light conditions

(100mW·cm^{-2}). **Figure 5.16d** shows the recorded Nyquist plots while illuminating the solar cells in the 0.1Hz-1MHz region under a 10mV AC perturbation. From the results we can compare series resistance (Rs) and the charge transfer (R_{ct}) and charge recombination (R_{rec}) resistances at the interfaces between the ETLs and the perovskite absorber. The EIS was measured for solar cells biased at the V_{mpp} voltage. The curves were simulated via the circuit model presented in the inset of the corresponding EIS figure. The results are summarized in Table 5.5. The Rs values of the devices based on pristine TiO_2 and Cu-TiO_2 compact layers are 18.3 Ω and 16.6Ω, respectively. R_{rec} is higher in the case of Cu-TiO_2 indicating a reduced charge carriers recombination rate at the corresponding device. In addition, the lower Rct value in the Cu-TiO_2 device indicates the superior charge transport from the perovskite layer to the Cu- modified ETL, in comparison with the unmodified one, confirming the higher conductivity of the corresponding layer, resulting in higher J_{sc} and FF values.

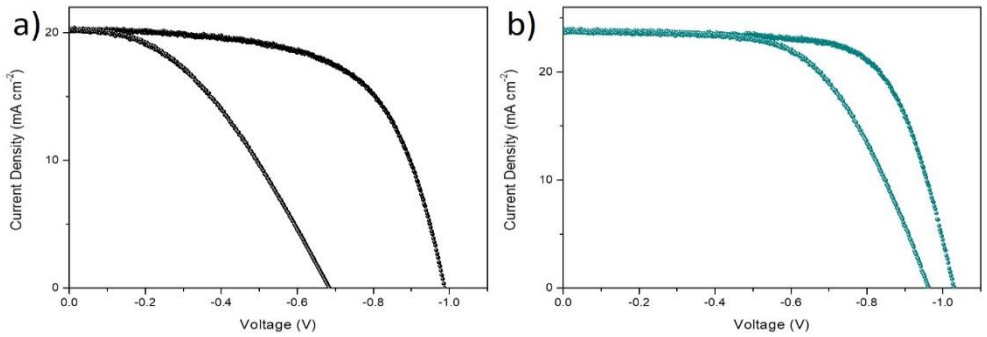

Figure 5.18 Hysteresis curves for reference (a) and modified devices (b). The J-V curves with the improved FF refer to the reverse scan in both cases while the other correspond to the forward scan

Table 5-5 Ohmic parameters for reference and modified PSC as derive by fitting the results from EIS measurements. The data were collected under 1 sun illumination.

Device	R_S (Ohm)	R_{rec} (Ohm)	$R_{ct\ (1)}$ (Ohm)	$R_{ct\ (2)}$ (Ohm)
TiO_2	18.3	40.8	4000	115
Cu-TiO_2	16.6	50.7	551	74.5

Stability tests were also carried out in order to investigate the role of Cu in the performance of the PSC after storing them in dark conditions, inside a desiccator, at open circuit conditions under relative humidity (RH) of ~25%. The devices were periodically taken out of the desiccator and their PV performance was evaluated. The results **(Figure 5.19),** show that the Cu-containing solar cells are more stable, namely retaining 53% of the initial PCE value after 51 days, contrary to the reference solar cell that retained only 37%. This behavior is attributed to the presence of Cu in the TiO_2 layer, permitting the formation of perovskite films of high quality and retarding the degradation mechanism triggered by the presence of trapped charges. The XRD and the optical images presented in **Figures 5.20 and 5.21**, prove the beneficial effect of Cu modification in the ETL whereas the reference PSC is seriously affected by the environmental exposure, resulting in large yellow areas of PbI_2 (or its byproducts following reaction with water) spread all over the surface of the cell, contrary to the Cu-based cells that remain visually intact.

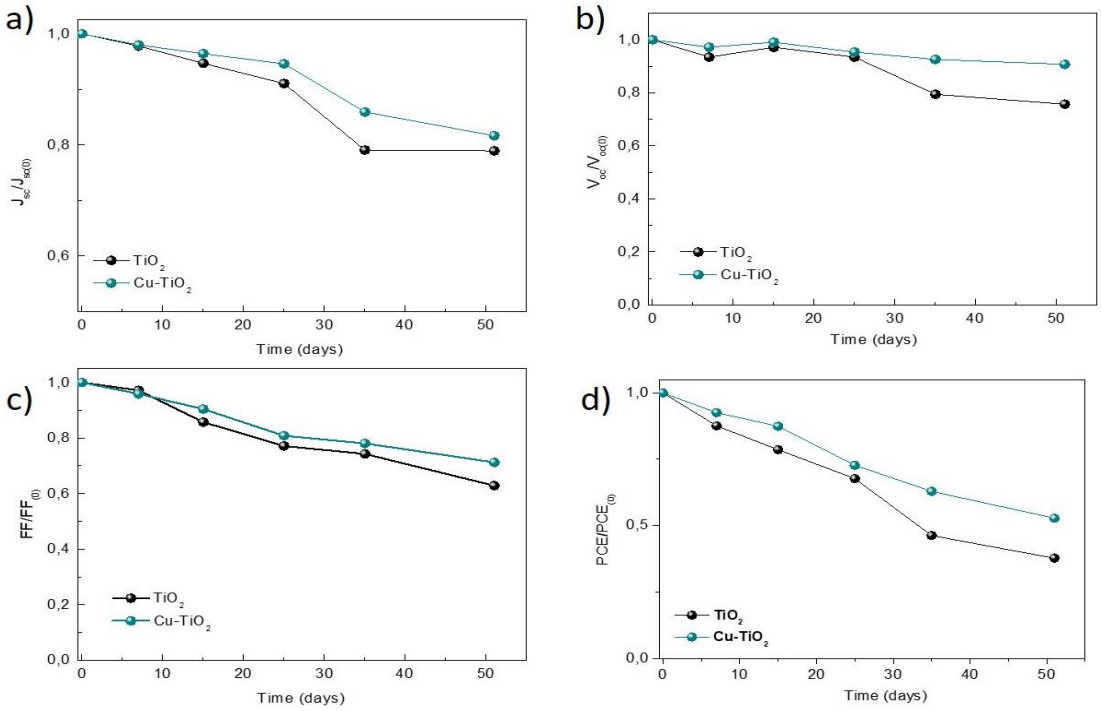

Figure 5.19 Effect of time aging on Device parameters

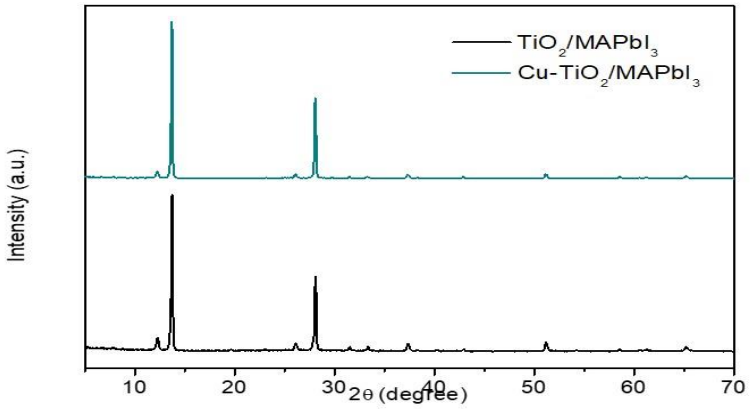

Figure 5.20 XRD patterns of aged perovskite layers coated upon pristine and modified titania films.

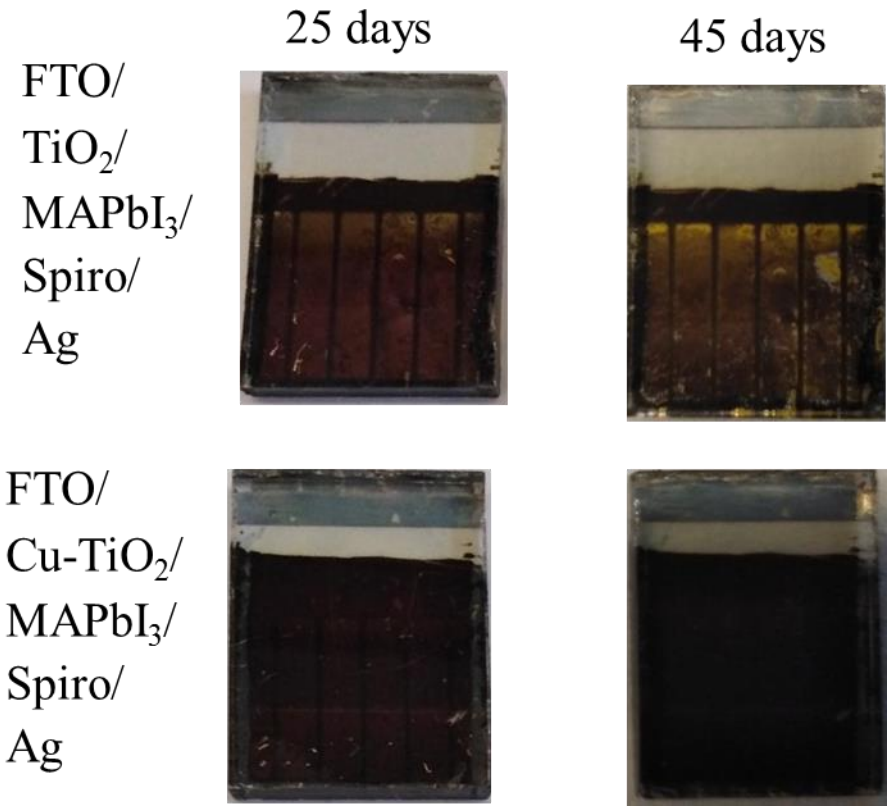

Figure 5.21 Photographs of perovskite solar cells (PSCs) after fabrication: 25 days (a); and 45 days (b).

Finally, in order to investigate the influence of copper in mesoporous PSCs, an optimum amount of copper solution was added within the mesoporous titania layer. The results, as presented in Table 5.6, show that all the relevant parameters were improved, including J_{sc}, V_{oc} and FF, expanding the beneficial role of copper in the specific structure.

To understand the enhanced photostability of TiO_2-Cu/$MAPbI_3$ based PSCs, one should take into account that the moisture (and/or oxygen) is not only a direct cause of the decomposition of the Pb-halide perovskite crystal and that the TiO_2 substrate is able to act as a photocatalyst for the decomposition of the perovskite at a local level, giving rise to the production of volatile species like I_2, H^+ ions and methylamine molecule CH_3NH_2 [37].

Table 5-6 Photovoltaic parameters of the champion mesoporous PSCs based on pristine and Cu-modified titania substrates under AM 1.5D illumination

Sample	J_{sc} (mA·cm^{-2})	V_{oc} (V)	FF	PCE(%)
TiO_2	20.4	1.08	0.73	16.22
Cu-TiO_2 (0%vol)	21.4	1.09	0.73	17.05
Cu-TiO_2 (0.00125% vol)	20.5	1.09	0.73	16.23
Cu-TiO_2 (0.025% vol)	23.3	1.06	0.75	17.8
Cu-TiO_2 (0.05%vol)	22.8	1.12	0.74	18.91
Cu-TiO_2 (0.1%vol)	20.4	1.07	0.7	15.3

Pietralunga *et al.* deemed that such a process is likely to occur in vacuum, since oxygen and moisture are not the unique ingredients to activate $MAPbI_3$ degradation [79]. Thus, under irradiation with light of energy higher than its energy gap, TiO_2 can generate electrons (e^-) in the conduction band and positively charged holes (h^+) in the valence band. On the surface of TiO_2 the photogenerated holes (h^+) will react with H_2O to form hydroxyl radicals ($OH^\bullet$) (Eq. (4). The photogenerated electrons (e^-) can be captured by O_2 to generate superoxide radicals ($O_2^{\bullet-}$) which further generates hydroxyl radicals ($OH^\bullet$) (Eq. (5,6). Hydroxyl radicals and superoxide radicals and are very powerful oxidants which can turn organic component (MA) of the hybrid perovskite absorber.

$$h^+ + H_2O \rightarrow OH^\bullet + H^+ \quad (4)$$

$$e^- + O_2 \rightarrow O_2^{\bullet-} \quad (5)$$

$$O_2^{\bullet-} + e^- + 2H^+ \rightarrow OH^\bullet + OH^- \quad (6)$$

The photodecomposition occurs at the interface between TiO_2 and perovskite in the presence of light and air (moisture and oxygen). In our approach, we modified the titania layer and the obtained results suggest that the highly hydrophobic modified ETL can delay the degradation of the perovskite absorber caused by the photocatalytic activity of the TiO_2. Increased hydrophobicity may result in lower photocatalytic activity of the ETL substrate. In fact, the presence of a hydrophobic substrate decreases the possibility of interface wetting and hence the production of reactive oxygen species (mainly hydroxyl radicals- $OH^{\bullet}$) via reaction of the photogenerated hole carriers with adsorbed water molecules can be mitigated and/or suppressed.

5.3 Reduced Graphene Oxide Doping

5.3.1 Experimental

5.3.1.1 Preparation of graphite oxide

Graphite oxide was prepared following a modified Hummers' method. At first 5 g of graphite powder were mixed with 240 ml of H_2SO_4 and 5 g of $NaNO_3$ under stirring in an ice bath. Then, 30 g of $KMnO_4$ was added slowly and the temperature was elevated to 35^{o}C. The mixture was stirred overnight and 1250 ml of water was added, followed by 35 ml of 30% H_2O_2. The obtained dispersion was centrifuged to remove the excess of acid and then it was washed with plenty of water until a pH of 5 was reached. The resulting paste was dried in an oven, overnight.

5.3.1.2 Preparation of reduced graphite oxide

Reduced graphite oxide was prepared via graphite oxide reduction following a well-established procedure using a mixture of hydriodic acid (Sigma Aldrich, ACS reagent**,** 55%) and acetic acid (ACS Reagent, Honeywell Fluka). More specifically, the as-prepared graphite oxide powder (0.1 g) was sonicated in acetic acid (37 mL) for 2 h and then 2 ml of hydroiodic acid (HI) was added followed by 40 h stirring at 40 ^{o}C. After isolating the product by

filtration, the powder was thoroughly rinsed by a three-step procedure including saturated sodium bicarbonate (3 x 2.5 mL), distilled water (3 x 2.5 mL), and acetone (2 x 2.5 mL). Finally, the obtained reduced graphite oxide was dried at 60 ^{o}C in a vacuum oven overnight.

5.3.1.3 Preparation of reduced graphene oxide (rGO) dispersions

The rGO dispersion in ethanol (EtOH) was prepared by liquid phase exfoliation (LPE) of rGO flakes in N-methyl-2-pyrrolidone (NMP) and exchange into EtOH. Initially, 125 mg of rGO were dispersed in 25 ml of NMP and ultrasonicated for 6 h. The obtained dispersion was then ultracentrifuged at 8000g for 60 min at 15 ^{o}C, in order to accelerate sedimentation of thick and unexfoliated rGO flakes. Then, we collected supernatant with a glass pipette and the sample was dried in a rotary evaporator at 70 ^{o}C, 5 mbar. Afterwards, the dried rGO powder was dispersed in 200 ml EtOH and sonicated for 10 min. Consecutively, the samples were centrifuged at 800g and after discarding the supernatant and dispersing the remaining sample in EtOH twice, as to wash out the NMP residuals, the sediments were finally redispersed in 100 mL EtOH to be used immediately. The rGO dispersion in N, N-dimethylformamide (DMF, Sigma–Aldrich**,** anhydrous, 99.8%) was prepared by mixing 1 mg of rGO with 1 mL DMF and by shaking for 2 min, sonicating for 2 h, and filtering with a 220 nm filter. The final concentration of the dispersion was 0.1 mg mL^{-1} and was further sonicated for 2 h before use.

5.3.1.4 Preparation of rGO-TiO2, rGO-perovskite and rGO-SpiroMeOTAD solutions

The rGO-doped TiO_2 (g-TiO_2) nonocomposite material consisted of titanium dioxide and reduced graphene oxide (rGO) nanoflakes. It was obtained by mixing an amount of the sonicated rGO (in EtOH) with the titania precursor solution and by further stirring the resulting dispersion overnight. According to preliminary experiments (Table 5.7), the optimum concentration was estimated to be 4 μg·mL^{-}(rGO in TiO_2 solution), where the obtained g-TiO_2 dispersion remained stable, even two months after its preparation (Figure

5.22). The rGO-$CH_3NH_3PbI_3$ material (g-$MAPbI_3$) was obtained by further mixing an aliquot of the well sonicated rGO/DMF dispersion with an amount of the $MAPbI_3$/DMF solution. According to preliminary experiments (Table 7.1), the optimum concentration was estimated to be 9 $\mu g \cdot mL^{-1}$ (rGO in $MAPbI_3$ solution). The final solution was further sonicated for 1 h prior to use. A similar route was followed for the dispersion of rGO in chlorobenzene and its addition in Spiro-MeOTAD solution. In general in this work, for films and devices containing rGO, the optimum concentrations were 2% vol (4 $\mu g\ mL^{-1}$) in EtOH for the TiO_2 ETL and 4% vol (9 $\mu g\ mL^{-1}$) in DMF for the $CH_3NH_3PbI_3$ absorber.

5.3.1.5 Device fabrication and characterization

The PSCs were prepared by coating the successive layers upon FTO conductive substrates (Dyesol, 7 Ω/□), patterned with a 2M aqueous HCl solution in combination with zinc powder (Alfa Aesar, 97.5%). The samples were then carefully cleaned with Triton-X, acetone and 2-propanol (Merck) into a sonicator for 15 min and then they were treated with UV-ozone for 15 min, prior to ETL deposition. The g-TiO_2 and TiO_2 ETL were spin coated at 2000 rpm for 60 s from an ethanolic, mildly acidic solution of titanium (IV) isopropoxide (Sigma–Aldrich, 97%) and the obtained films were annealed for 45 min at 500 ^oC (at a heating rate of 5 $^oC\ min^{-1}$). The $CH_3NH_3PbI_3$ layers, with and without rGO, were deposited by spin coating the perovskite precursor solution containing a 40 wt% Methylammonium iodide (Dyesol) along with Lead acetate trihydrate ($PbAc_2.3H_2O$, 99.999% trace metals basis, Sigma-Aldrich) in a 3:1molar ratio. Hypophosphorous acid (50% w/w, aquatic solution, Alfa Aesar) was also added to the perovskite solution resulting in a 1:4 HPA:$PbAc_2$ molar ratio. The deposition was carried out at 2000 rpm for 45 s, the films were left to dry at room temperature for 10 min and then were placed on a hotplate at 100 ^oC for 5 min. Finally, a 7 wt% Spiro-MeOTAD (Borun New Material) solution in chlorobenzene (Acros, 99.8%, Extra Dry), containing additives of lithium bis(trifluoromethanesulfonyl)imide lithium salt (≥99%, Sigma-Aldrich)

in acetonitrile, and 4-tert-butylpyridine (96%, Sigma-Aldrich) was deposited as the hole transport layer at 3000 rpm for 30 s. Finally, the devices were transferred outside the glove-box and 100 nm silver electrodes were thermally evaporated under vacuum of 10^{-6} Torr, at a rate of ~1 Å·s^{-1}.

5.3.2 Results and discussions

As a first step, the quality of the rGO material (including structural and morphological properties) used for modifying the PSC components was thoroughly analyzed. Transmission electron microscopy (TEM) images (Figure 5.23a) permit to have a deep insight into the lateral size and thickness of rGO. The examined samples are primarily composed of few-layered flakes, approximately between 2 and 6 stacked sheets. Their lateral dimension fluctuates in the 30nm-900nm range, with the average size being around 200nm.

Subsequently, we examined the graphene materials by UV-vis spectroscopy. Figure 5.23b depicts the absorption spectra of GO and rGO materials. The GO presents an absorption band at 230nm due to the p-p* transition of aromatic C–C bonds and another one at 300nm attributed to the n-p* transition of C=O bonds. After reduction, the C–C bonds absorption peak redshifted to 280 nm, indicating the restoration of the carbon aromatic structure.

Moreover, we further investigated the reduction of graphene oxide by Raman spectroscopy, as depicted in Figure 5.23c which zooms in the 1000-1800 cm^{-1} frequency range of interest. The corresponding extended Raman spectra (100-3500 cm^{-1}), including the region of the second orders Raman bands (2500-3500 cm^{-1}), are shown in the (Figure 5.24). At first misleading glance, the GO spectra present two broad Raman bands in between 1000-1800 cm^{-1}. Instead, a detailed analysis of the data in accordance to previous studies shows that a good fitting can only be achieved with four Raman bands: defect-activated D band at ~1354 cm^{-1} due to the vibrations of sp^3 C atoms with dangling or covalent (e.g. C–H, C–O) bonds,

the graphitic G band at ~1588 cm^{-1}, due to the bond stretching of sp^2 carbon atoms in a two-dimensional hexagonal lattice as well as two extra defect activated bands often termed as D' and D'' at 1620 cm^{-1} and ~1538 cm^{-1}, correspondingly.

Figure 5.22 Optical images of rGO dispersions in ethanol (left) and DMF (right), two weeks after their preparation. The vial with DMF is half-full.

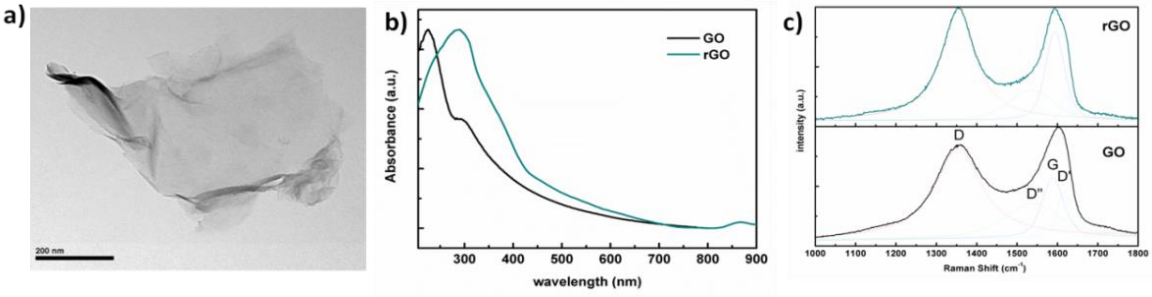

Figure 5.23 (a) TEM image of rGO flake dispersed in ethanol. (b) Absorption spectra of rGO and GO dispersions in EtOH and water respectively. (c) Raman spectra of rGO and GO dispersions in EtOH and water respectively. Measurements were taken from the corresponding powders dried on Al substrates.

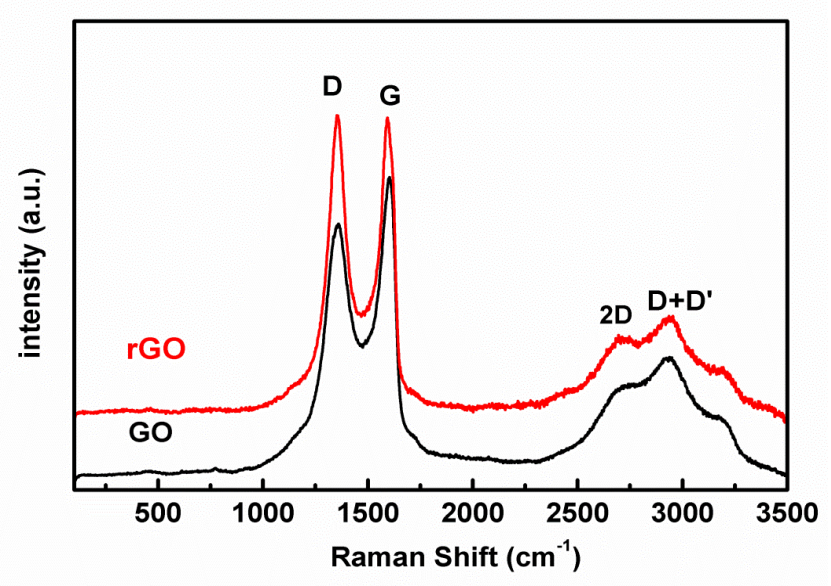

Figure 5.24 Extended Raman spectra of GO and rGO obtained with 514.4 nm excitation

Fitting components are shown superimposed on the spectra in Figure 5.23c and result in excellent simulated spectra. Accordingly, the intensity ratio of the D to the G band (I_D/I_G) was estimated to be 1.5. The corresponding Raman spectrum of rGO shows that the linewidth of the D band considerably narrows from 140 to 100 cm^{-1} and that its intensity (as well as those of the D' and S bands) is reduced, with I_D/I_G becoming equal to 1.2. These are clear indications of the restoration of sp^2 rings, very similar to what was observed in the literature.

Figure 5.25a shows the UV-vis absorption spectra of $CH_3NH_3PbI_3$ films spin-coated on g-TiO_2 and pristine TiO_2 substrates. More specifically, we compare the absorbance of $CH_3NH_3PbI_3$ grown on pristine TiO_2, against $CH_3NH_3PbI_3$ film spin coated on g-TiO_2 and g-$CH_3NH_3PbI_3$ grown on g-TiO_2. The absorption onset at about 790 nm as well as the plateau after 500 nm are characteristic of the $CH_3NH_3PbI_3$ spectrum. The presence of rGO within the titania compact layer seems to increase the light harvesting, a fact maybe associated with the improved crystallization of the perovskite. In addition, further absorption increase, although slight, is observed in the case of g-$CH_3NH_3PbI_3$ grown on g-TiO_2, implying an even better

quality for the perovskite films, in terms of improved crystallinity and larger $MAPbI_3$ polycrystals contributing to higher amount of photo-generated electrons and holes.

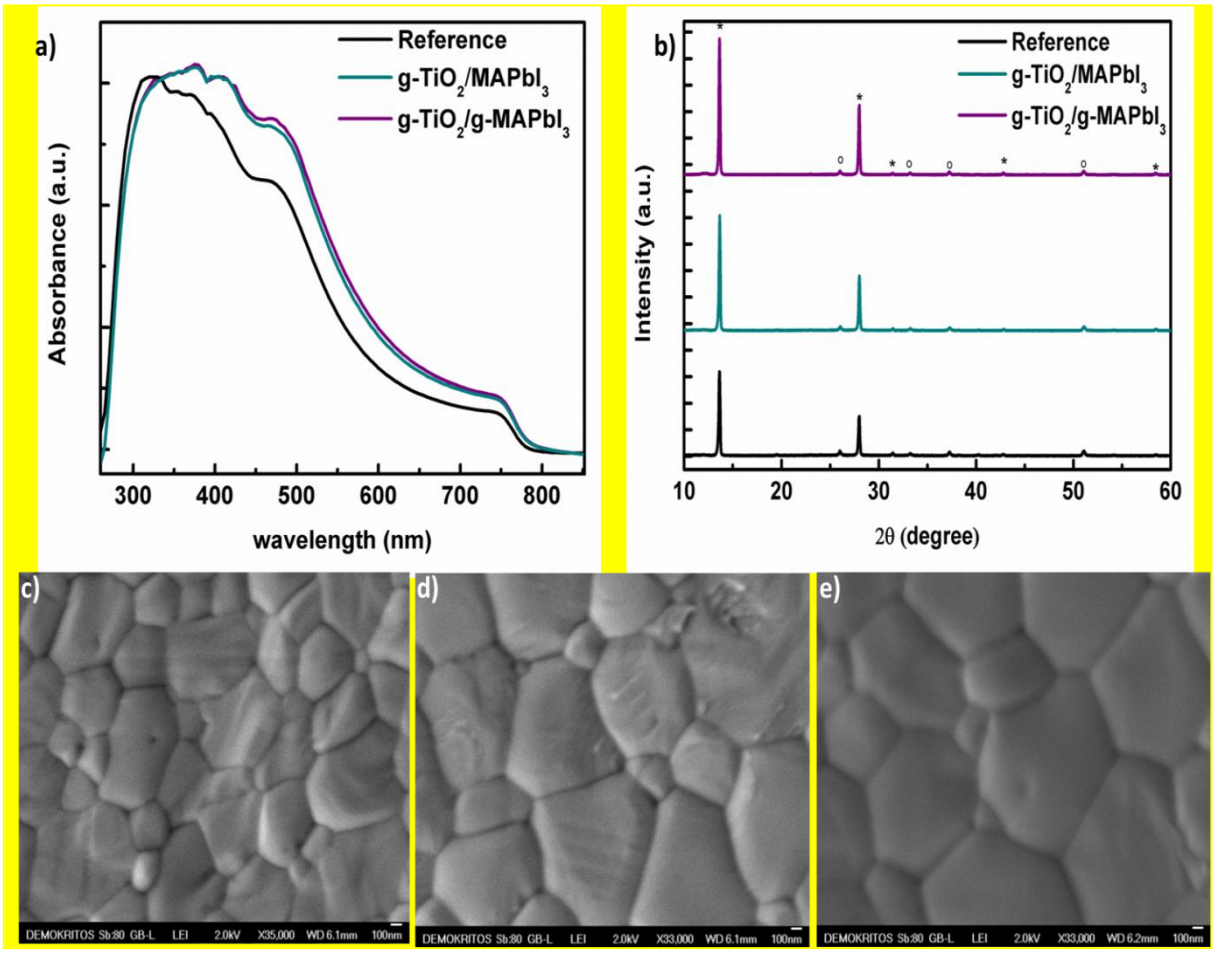

Figure 5.25 (a) Absorption spectra and (b) XRD patterns of the as prepared $CH_3NH_3PbI_3$ perovskite films (stars and circles denote to $CH_3NH_3PbI_3$ and SnO_2 peaks respectively). SEM images of (c) $CH_3NH_3PbI_3$ grown on TiO_2 and (d) on g-TiO_2, (e) SEM image of g-$MAPbI_3$ grown on g-TiO2 (scale bars are at 100nm).

Contact angle measurements (Figure 5.26) were performed on pristine TiO_2 and rGO-containing substrates, to evaluate the effect of rGO on the titania substrate properties. The analysis confirmed a slight but clear increase in hydrophobicity in the presence of rGO, fact which favors the formation of larger perovskite polycrystals since less-wetting surfaces are associated with fewer nucleation sites leading to the formation of larger perovskite crystallites. The XRD patterns (Figure 5.25b) match well the theoretical peaks [14.0°,

28.5°and 31.9° at 2θ values that correspond to the (110), (220) and (310) crystal facets, respectively], demonstrating that all perovskite films crystallize in the tetragonal $CH_3NH_3PbI_3$ phase, while the peak intensities are stronger and the crystallinity along the 001 direction is enhanced in the presence of rGO. In addition, a clear difference in the full-width at half maximum (FWHM) values for the perovskite was observed between them [e.g. for the reflection at 2θ = 28° FHWM($MAPbI_3/TiO_2$)=0.142(2)°, FHWM($MAPbI_3$/g-TiO_2)=0.135(2)° and FHWM(g-$MAPbI_3$/g-TiO_2)=0.126(2)°], confirming larger grains for the rGO-modified perovskite film grown on the g-TiO_2 substrate.

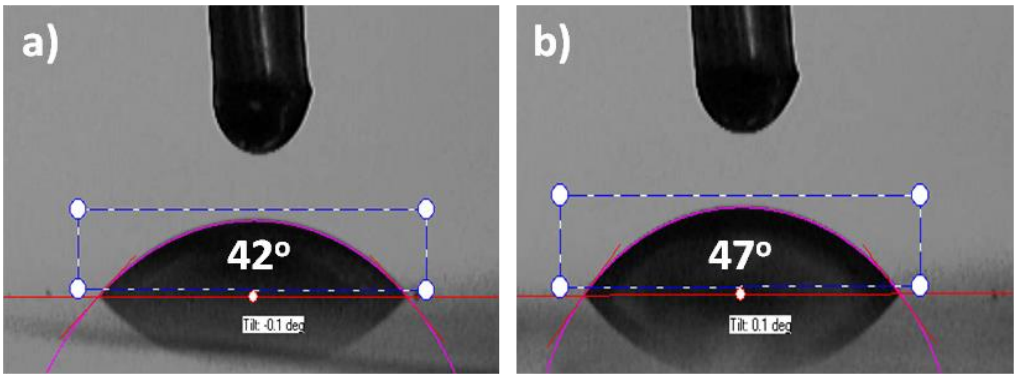

Figure 5.26 Optical images of contact-angle measurements with H_2O on TiO_2 substrates (a) without and (b) with rGO.

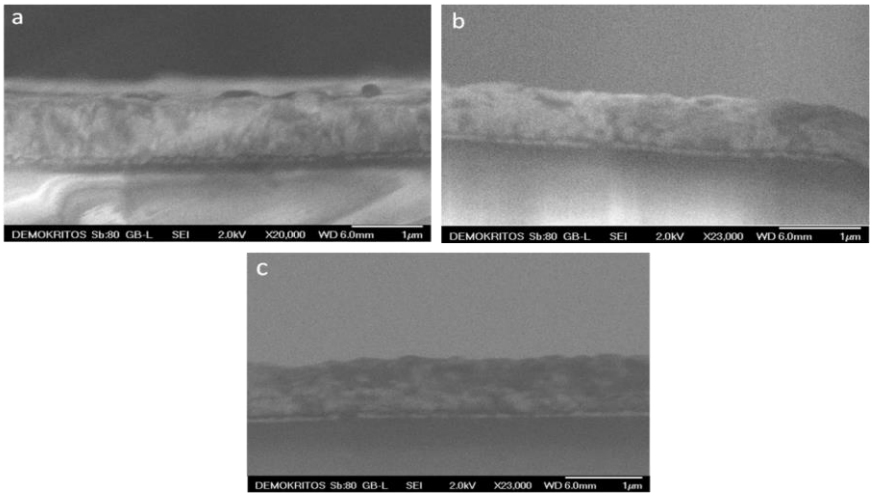

Figure 5.27 Cross-section images of (a) pristine $MAPbI_3$ grown on TiO_2, (b) g-TiO_2 on $MAPbI_3$ and (c)g-$MAPbI_3$ grown on g-TiO_2 .

Subsequently, AFM and SEM analysis was used to characterize the quality of the titania and the perovskite films. The SEM analysis (Figure 5.27) showed that the thickness of the perovskite films is around 600 nm, similar for both the reference and the rGO-containing samples. As depicted in the Figure 5.28, the root-mean-square (RMS) roughness for the ETL films increases in the presence of rGO (RMS=17.22 nm against 13.51 nm for the pristine TiO_2), in agreement with the literature. An analogous trend was observed for the $CH_3NH_3PbI_3$ films (Figure 5.29), since the roughness was increased by spin-coating the perovskite solution on g-TiO_2 (RMS=29.15 nm compared to 21.88 nm for the pristine TiO_2). Moreover, as depicted in SEM images at Figures 5.25c, 5.25d, 5.25e, and corroborated by the statistical analysis presented in the supporting information (Figure 5.30), the presence of rGO in the TiO_2 ETL results in a net increase of the $CH_3NH_3PbI_3$ grains size, from 1024nm (Figure 5.25c) to 1086nm (Figure 5.25d). On the other side, when depositing the g-$MAPbI_3$ layer on the g-TiO_2, the roughness significantly decreases (RMS = 13.01 nm), indicating that the presence of a specific amount of rGO in the perovskite layer positively affects the surface morphology and increases the films smoothness, a fact that can lead to a possible improved fill factor (FF) for the corresponding solar cells. Also, in the latter case the perovskite grain size was further increased reaching a mean value of 1146nm (Figure 5.25e). These grains form a smooth and thick film that apart from large crystals is characterized by a lower number of grain boundaries, a fact associated with lower surface trap density and improved V_{oc} in PSC devices. Furthermore, in the presence of rGO within the perovskite layer, the size distribution of the crystallites is significantly narrowed. In fact, the vast majority of the grains scales between 950nm and 1250nm, forming a characteristically homogenous and robust film (Figure 5.30).

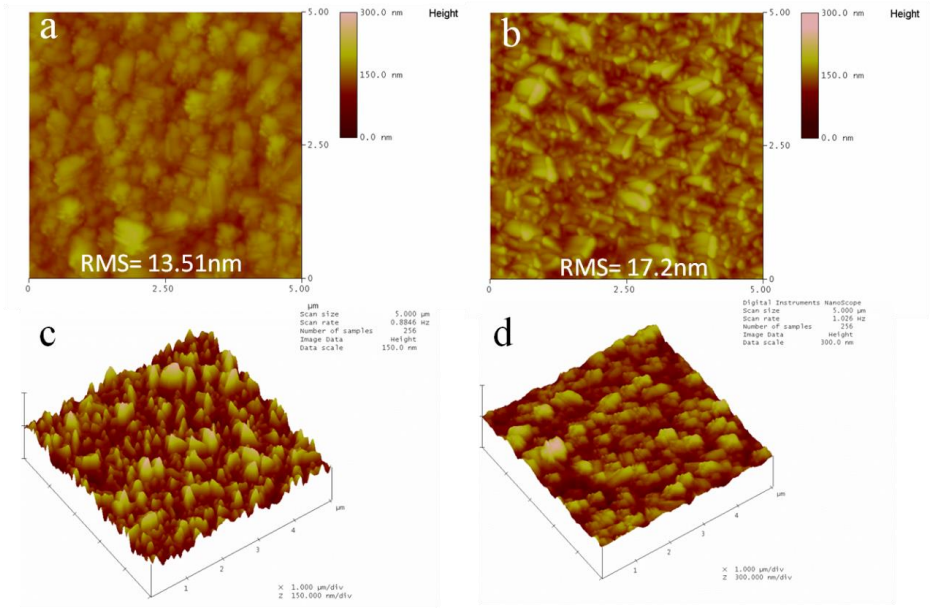

Figure 5.28 Top-view(a,b) and 3-dimensional (c,d) AFM images of pristine TiO_2 (a,c) and g-TiO_2 (b,d) films.

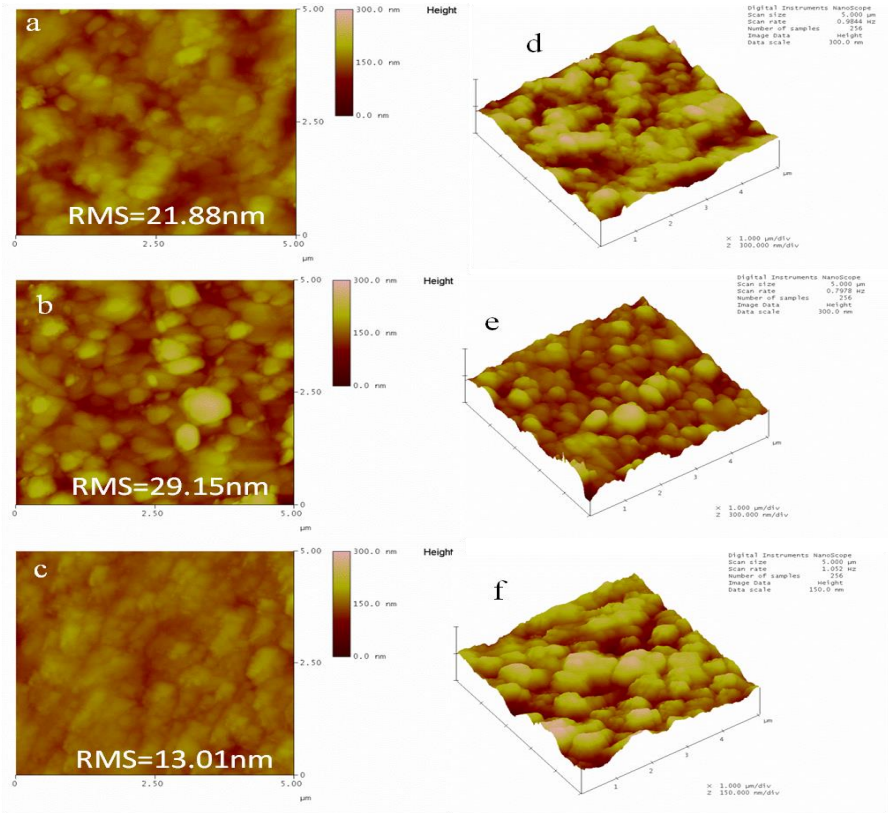

Figure 5.29 Top-view (a,b,c) and 3-dimensional (d,e,f) AFM images of pristine $MAPbI_3$ grown on TiO_2 (a,d) and g-TiO_2 (b,e) and g-$MAPbI_3$ grown on g-TiO_2 (c,f).

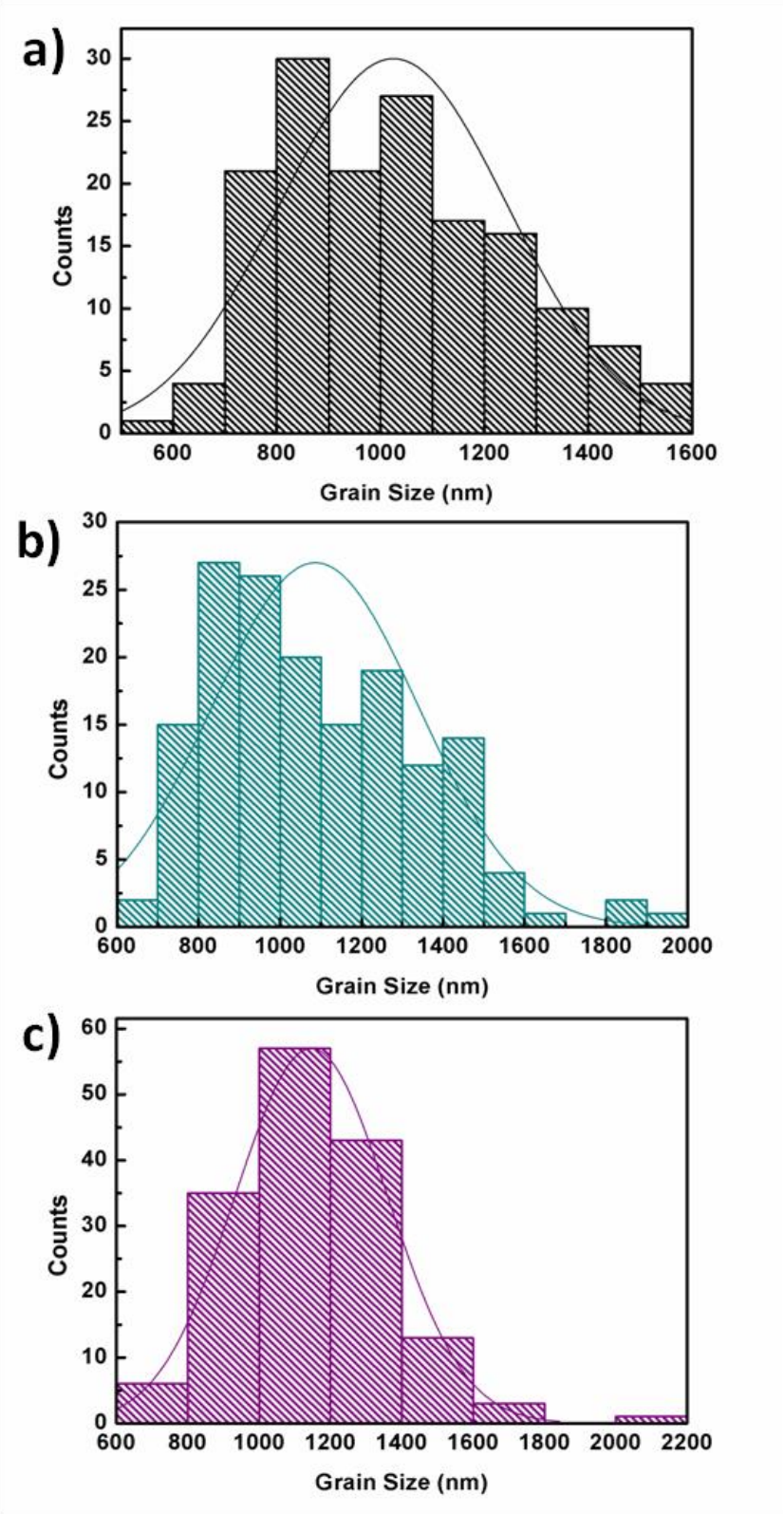

Figure 5.30 Size distribution of $MAPbI_3$ grains grown upon (a) TiO_2 and (b) g-TiO_2 substrates and (c) g-$MAPbI_3$ grown on g-TiO_2.

The beneficial presence of graphene materials within the perovskite absorber was also reported in the case of GO and N-doped rGO. This was attributed to graphene derivatives' excellent electronic properties serving as efficient chemical reaction (hydrophilic groups embracing -OH, -COOH and C=O form strong bonds with the perovskite) and crystallization nucleation centers during the perovskite film growth. Actually, rGO determines the nucleation procedure leading to almost defect-free perovskite films of enhanced crystallinity along with larger and evenly distributed grains. Thus, high quality films are obtained with enhanced light harvesting potential, hence increasing the photocurrent density and the resulting power conversion efficiency in the corresponding PSCs.

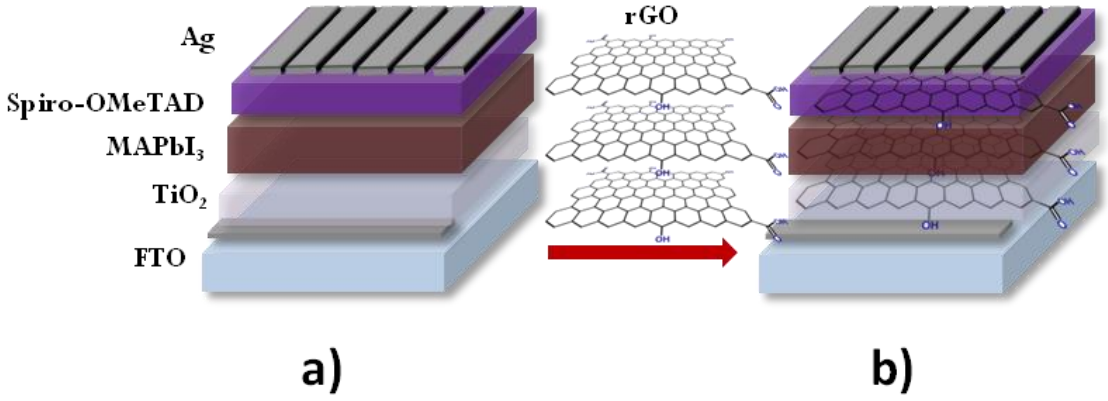

Figure 5.31 The structure of the PSC fabricated (a) without rGO, (b) by adding rGO in the compact TiO_2 layer, the $CH_3NH_3PbI_3$ absorber and the hole transporter.

Figure 5.31 presents the structure of the as-prepared solar cells, illustrating the incorporation of rGO flakes in the corresponding PSC layers. The influence of rGO in the performance of PSCs was investigated by adding different amounts of rGO in the TiO_2, the $CH_3NH_3PbI_3$ perovskite and the Spiro-MeOTAD layers (Table5.7).

Table 5-7 Photovoltaic parameters values for solar cells prepared with and without rGO addition. V_{OC}: open-circuit voltage, J_{SC}: short-circuit current density, FF: fill factor, PCE: power conversion efficiency

Solar Cell	Concentration	J_{sc} (mA cm^{-2})	V_{oc} (V)	FF	PCE (%)
Reference	0	20.60	1.00	0.67	13.80
rGO in $MAPbI_3$	5 μg mL^{-1}	20.32	0.98	0.68	13.58
	9 μg mL^{-1}	22.62	0.99	0.72	16.08
	20 μg mL^{-1}	19.34	0.97	0.62	11.70
rGO in TiO_2	2 μg mL^{-1}	21.23	0.97	0.69	14.29
	4 μg mL^{-1}	21.44	1.00	0.70	14.98
	6 μg mL^{-1}	20.72	0.95	0.59	11.58
	8 μg mL^{-1}	18.41	0.97	0.48	8.62
rGO in spiro-OMeTAD	0.2 mg mL^{-1}	20.52	0.86	0.60	10.58
	0.1 mg mL^{-1}	21.02	0.95	0.59	11.73
	0.05 mg mL^{-1}	20.80	0.97	0.65	13.05

As expected, the addition of rGO in the Spiro-MeOTAD did not lead to PSC performance enhancement, probably due to the creation of unwanted pathways between the perovskite and the silver electrodes that increase the probability of charge recombination. On the contrary, the PSC performance was improved in the presence of rGO within both the TiO_2 and the $CH_3NH_3PbI_3$ layers, a fact mainly associated with the increase of J_{SC} and FF values. In fact, the performance of the solar cells was intensively studied and the necessary characterization

measurements were performed, focusing on the following PSC configurations: a reference one: FTO/TiO_2/$MAPbI_3$/Spiro-MeOTAD/Ag (device A), one by adding an optimum quantity of rGO within the TiO_2: FTO/g-TiO_2/$MAPbI_3$/Spiro-MeOTAD/Ag (device B) and one by adding rGO in both the TiO_2 and perovskite layers: FTO/g-TiO_2/g-$MAPbI_3$/Spiro-MeOTAD/Ag (device C).

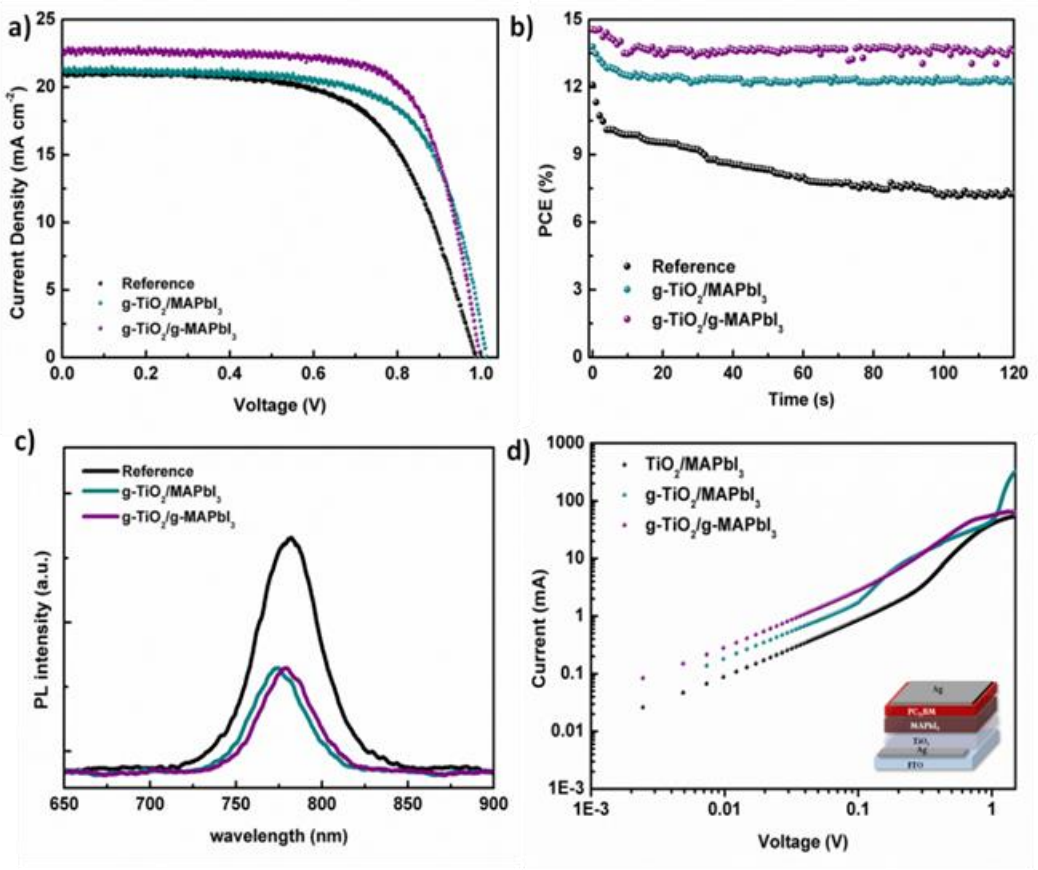

Figure 5.32 .(a) J-V plots obtained for planar PSC using the $CH_3NH_3PbI_3$ absorber grown on compact TiO_2 substrates. (b) The PCE at the maximum power point for devices with and without rGO. (c) Steady-state PL spectra of perovskite films with and without rGO on pristine and rGO-modified TiO_2 layers. (d) I-V curves for electron-only PSC with and without rGO.

The photovoltaic (PV) performance of the PSCs was tested by current density-voltage (J-V) measurements conducted under 1 sun (A.M. 1.5G) illumination conditions (Figure 5.32a) and the resulting parameters are summarized in Table 5.8. In the presence of the rGO within the ETL, the photocurrent density increases by ~2%. This fact is associated with various factors

including the possible increase of TiO_2 conductivity in the presence of rGO, along with the improved quality (enhanced crystallization, increased grain size, reduced grain boundaries, homogeneity and smoothness) of the perovskite film. In particular, the former is associated with increased electron injection rate to the anode, while the latter pertains to the growing photo generation and dissociation of charge carriers.

Table 5-8 Photovoltaic parameters for the champion devices prepared with and without rGO addition. Values inside brackets refer to the mean values and standard deviation. V_{OC}: open-circuit voltage, J_{SC}: short-circuit current density, FF: fill factor, PCE: power conversion efficiency.

Devices	J_{sc} (mA cm^{-2})	V_{oc} (V)	FF	PCE (%)
Device A	21.0 (20.06±0.41)	0.98 (0.97±0.01)	0.67(0.63±0.02)	13.8 (12.38±0.34)
Device B	21.4(21.05±0.2)	1.01(1.00±0.01)	0.71(0.67±0.02)	15.3 (13.95±0.23)
Device C	22.9(21.70±0.5)	1.00(1.00±0.07)	0.72(0.69±0.01)	16.5(14.97±0.43)

When adding rGO in the perovskite solution, a further improvement in J_{sc} is observed, resulting in a ~9% increase for the device C compared to device A, a fact attributed to the further improvement of the perovskite film quality, namely larger grains, improved crystallization and smoothness. The open circuit voltage (V_{oc}) is also affected by the presence of rGO within TiO_2, since devices B present a slightly increased V_{oc} probably due to suppressed charge recombination. This can be attributed to surface-passivation of the perovskite against charge trapping at the grain boundaries. Although V_{oc} is slightly decreased in the case of device C, it is worth mentioning that the fill factor (FF) is also improved as a result of the presence of rGO within the titania layer. This is mainly due to the role of rGO in promoting the formation of smooth perovskite films with larger grains (device C). Indeed,

smooth surfaces are associated with lower charge transfer resistance values at the corresponding interfaces, while larger grains reduce the total grain boundaries and facilitate the charge transport through encountering less boundaries. Moreover, PSC devices employing rGO present a slight decrease in the hysteresis (Figure 5.33), attributed to the increased conductivity of titania compact layer and the passivation of trap states in the perovskite absorber. The photovoltaic performance increase was confirmed by statistical analysis of the results corresponding to 30 solar cells of each configuration (Device A, B and C). As depicted in Figure 5.34, the statistical analysis of the photovoltaic parameters, clearly demonstrates that the rGO nanoflakes have remarkable contribution in the cell performance improvement.

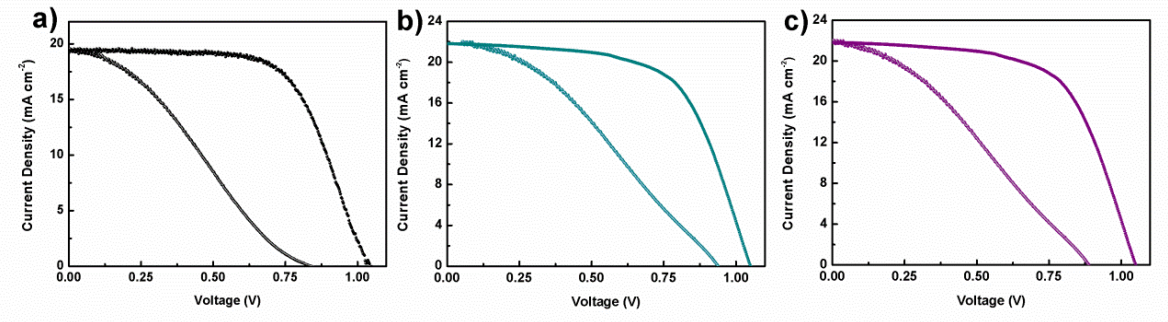

Figure 5.33 Forward (from short circuit to forward bias) and reverse scans (from forward bias to short circuit) for PSCs (a) without rGO; (b) with rGO in the titania layer; and (c) with rGO in both the titania and the perovskite layer

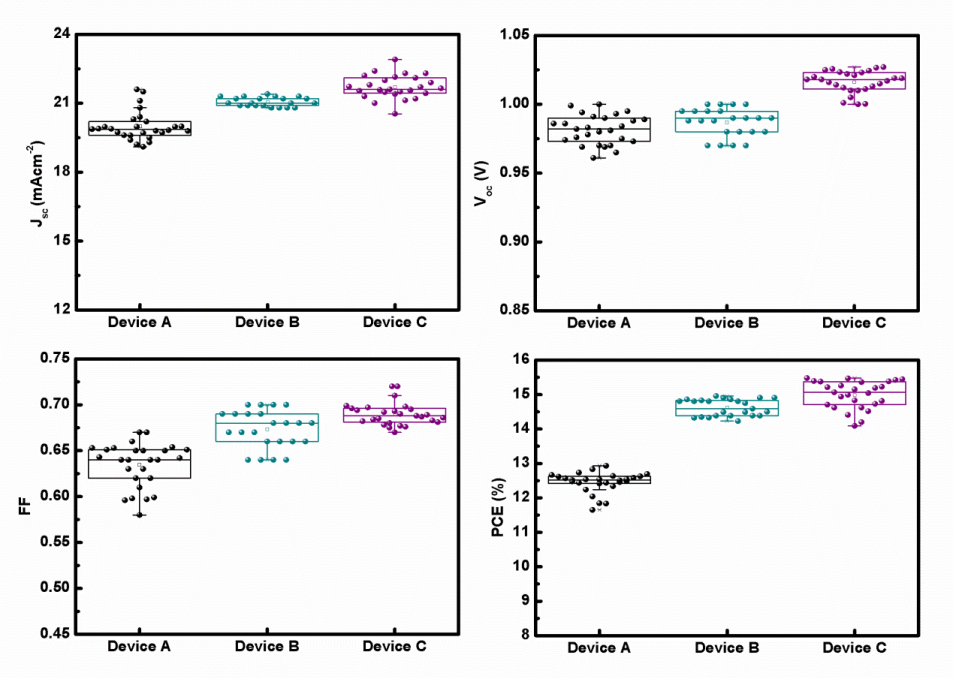

Figure 5.34 Statistic box chart comparison of PSC parameters

As a result, we obtained a final 16.48% PCE for the champion C device. The PCE increase for device C against that of device A is significant, approximately 20%, proving the determining role of rGO in the performance of PSCs. Moreover, stabilized output power values (corresponding to the maximum power point (MPP) in the J-V plots) were determined for the all types of prepared PSC. As depicted in Fig. 5.32b, an optimum stabilized PCE of 13.57% was obtained for the device C. In addition, it is evident that the devices containing rGO present an improved behavior, thus being more stable through time compared to the reference PSC that presents an exponential decay.

Steady-state PL measurements were also performed for perovskite films grown on TiO_2. As shown in Figure 5.32c, the rGO containing perovskites present a clear photoluminescence quenching. This confirms that the addition of rGO significantly facilitates the electron transport towards the anode. Moreover, the PL peak of g-TiO_2/$MAPbI_3$ samples presents a slight blue shift, a fact that can be associated with trap states passivation on the perovskite surface and subsequent increase of the $V_{oc.}$

To further verify the role of rGO, e^--only devices were fabricated and were characterized in the space-charge-limited-current (SCLC) regime. We followed the exact experimental procedure built by E.H. Sargent et al and the obtained I-V curves are very similar with those presented in the literature. The Figure 5.32d depicts the I-V response, measured for e^--only devices fabricated with the following structure: FTO/TiO_2/$MAPbI_3$/PCBM/Ag corresponding to device A', FTO/g-TiO_2/$MAPbI_3$/PCBM/Ag corresponding to device B' and FTO/g-TiO_2/g-$MAPbI_3$/PCBM/Ag corresponding to device C'. At low voltages, the J-V plot is ohmic (linear), but at mid-voltages, the current shows a rapid nonlinear rise characterized by the transition within the TFL regime where all the available trap states are filled by the injected carriers. Finally at high voltage values, the current has quadratic voltage dependence in the Child's regime. As reported in the literature, the ohmic to trap filled limit (TFL) transition point (V_{TFL}) is related to the trap density (N_t) according to the following equation (1):

$$V_{TFL} = \frac{eN_t d^2}{2\varepsilon\varepsilon_0} \qquad (1)$$

where e is the elementary charge, d is the thickness of the active layer (600 nm), ε (e=28.8) is its dielectric constant, and ε_0 is the dielectric constant in vacuum. The calculated trap density (N_t) are 3.99 x 10^{14} cm^{-3} for device B, 6.0 x 10^{14} cm^{-3} for device C and 1.53 x 10^{15} cm^{-3} for device A, respectively. These results, confirming the PL measurements, indicate that the presence of the rGO reduces the traps density of the perovskite layer especially in the case of device B, thus favoring increased V_{oc} and leading to significantly higher stabilized efficiency (Figure 5.32b).

Furthermore, to clarify the effect of rGO in the conductivity of the ETL, we recorded the J-V response in the SCLC regime for TiO_2 films with and without adding rGO in different concentrations, on electron-only diodes with the following configuration: FTO/TiO_2/Ag for

the reference and FTO/g-TiO_2/Ag (Figure 5.35) for the rGO-based PSC. As a result, a larger current density for the g-TiO_2 based-cell was clearly obtained in comparison with the pristine TiO_2 one, confirming its higher electrical conductivity. Following the report by Zhang et al. J-V curves were fitted using the following equation:

$$J = \frac{9}{8}\varepsilon_r\varepsilon_0\mu\frac{V^2}{L^3}$$

where J is the current density, μ is the zero-field mobility of electrons, ε_0 is the permittivity of the vacuum, is the relative permittivity of TiO_2 (ε_r =30), L is the thickness of the ETLs, which has a similar value for both layers (50 nm), and V is the applied voltage, respectively. The performed fitting confirmed that the electron mobility for the rGO containing device was increased (4.2 x 10^{-7} $cm^{2}\cdot V^{-1}\cdot s^{-1}$ for the device with the optimum rGO quantity and 2.5 x $10^{-7}cm^{2}\cdot V^{-1}\cdot s^{-1}$ for the reference PSC respectively), indicating that the presence of rGO significantly contributes to the enhancement of the electron transport rate towards the anode electrode, a fact associated with the improved J_{sc} value measured.

Stability tests were also carried out in order to investigate the role of rGO in the performance of the PSC after storing them in the dark in a dessicator, at open-circuit conditions under relative humidity (RH) of ~10%. We thus compared the reference PSC (device A) and the one containing rGO in both the ETL and the perovskite layer (device C). The results, depicted in Figure 5.36, show that the rGO-containing solar cells are more stable, namely retaining 40% of the initial PCE value after 50 days, contrary to the reference solar cell that retain only 20% of the initial value.

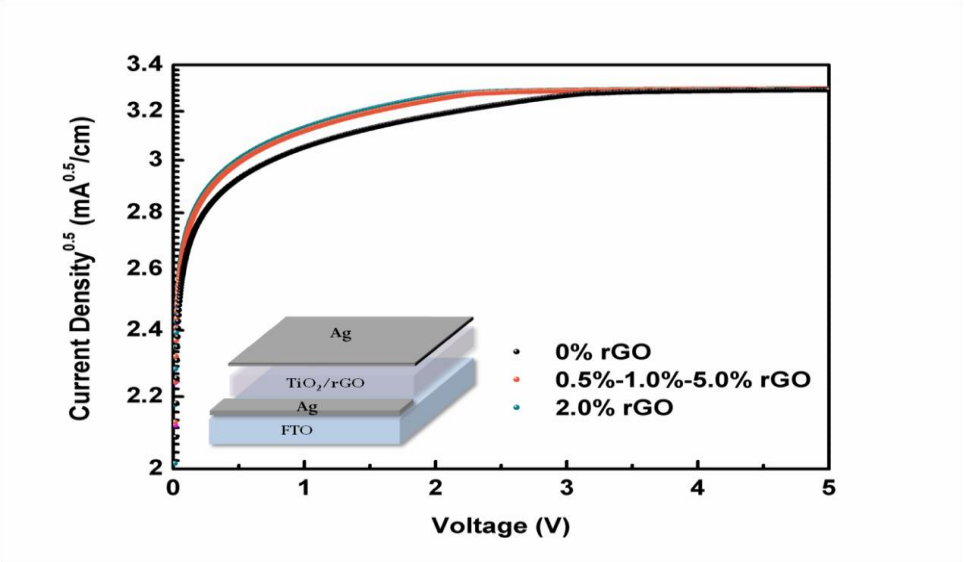

Figure 5.35 J-V curves under dark conditions for e⁻only devices (see inlay) for different concentrations of rGO within the TiO_2 ETL.

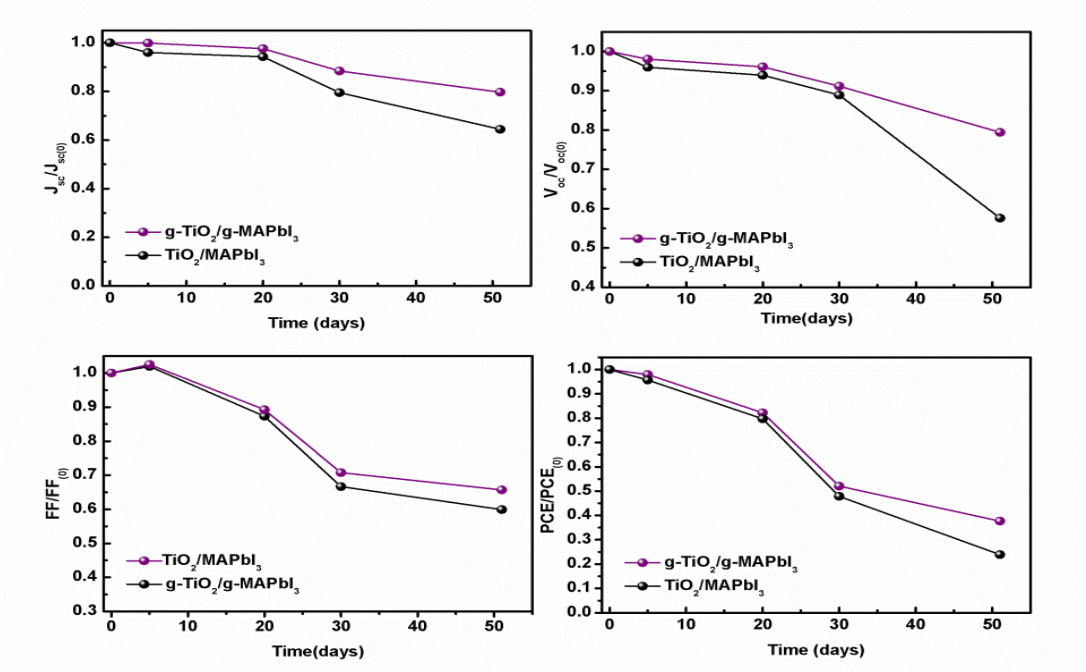

Figure 5.36 Variation of cell parameters as a function of the time under dark: (a) current density; (b) open circuit voltage; (c) fill factor; and (d) power conversion efficiency, for $CH_3NH_3PbI_3$ –based PSCs with and without rGO.

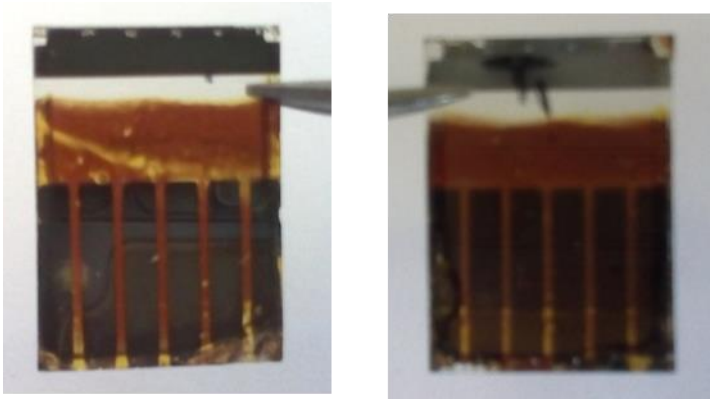

Figure 5.37 Optical images of PSC after 50 days of storage in dark (RH=10%); The reference PSC (left) and the corresponding device with rGO additives in both the TiO_2 and the $MAPbI_3$ layers (right).

This behavior is attributed to the presence of rGO in the TiO_2 and the perovskite layer, permitting the formation of perovskite films of improved quality, and retarding the degradation mechanism triggered by the presence of trapped charges. The superiority of the rGO-containing PSC is obvious in the optical images presented in Figure 5.37, where the reference PSC is seriously affected by the environmental exposure, resulting in large yellow areas of PbI_2 (or its byproducts following reaction with water) spread all over the surface of the cell, contrary to the rGO-based cells that remain visually intact.

5.4 Summary

Cu monovalent cations were used as a modifier in order to obtain a Cu-TiO2 ETL for efficient planar PSCs. The addition of Cu ions down shifted the Fermi level of TiO_2. This subsequently enhances the open circuit voltage of the PSCs, facilitate the electron passage at ETL/perovskite interface reducing the series resistance and increase the short circuit current density, open circuit voltage (V_{oc}) and fill factor. Contact angle measurements confirmed that the introduction of copper ions (Cu^{1+}) into the compact TiO_2 layer increased its

hydrophobicity, thus favoring improved perovskite crystallization, a fact corroborated by XRD analysis. As a result, PSCs with PCE higher than 18% owing to high open circuit voltage (V_{oc}) of 1.1 V, high current density (J_{sc}) of 23.15 $mA \cdot cm^{-2}$, and a high fill factor (FF) of 73% were obtained. Outperforming the performance of the reference device showing a PCE equal to 15.78% (with V_{oc} equal to 1.07 V, J_{sc} of 20.87 mA cm_{-2}, and FF equal to 70 %). Long term stability for 51 days was done for reference and Cu modified devices where, the Cu modified devices retained a J_{sc} of 0.82 from J_{sc0} , V_{oc} of 0.9 from V_{oc0} , FF of 0.71from FF_0 and PCE of 0.53 from PCE_0 while, the reference device retained 0.78,0.76,0.63 and 0.37 respectively.

The observed improved performance (in terms of enhanced PCE and high stability) of the PSCs is related to the hydrophobic character of the Cu-TiO_2 ETL which protects the perovskite against humidity. This is corroborated by the contact angle measurements, indicating enhanced hydrophobicity of the titania compact layer following copper addition. Lower surface wetting of the underneath compact layer increases its compatibility with the top hybrid perovskite absorber and leads to larger perovskite crystals with low number of structural defects. This is also at the origin of the observed higher resistance of the FTO/Cu-TiO_2/$MAPbI_3$ photoelectrodes to UV stress, as the copper-modified titania compact layer not only protects the top perovskite layer from self-decomposition (the instability in humid environments is the main drawback of the perovskite technology) but also severely mitigates the photocatalytic action of the ETL. Thus the direct photocatalytic decomposition of the perovskite absorber provoked by reactive oxygen species [ROS, e.g. highly reactive hydroxyl radicals ($OH^{\bullet}$) resulting of the reaction between the photogenerated holes and adsorbed water that act as potential perovskite killers] at the corresponding interface can be avoided, thus justifying an direct UV shield function.

In this chapter, we also fabricated efficient and relatively stable planar PSCs, by incorporating rGO nanoflakes within the TiO_2 ETL, the Spiro-MeOTAD HTL and the $CH_3NH_3PbI_3$ absorber. As a result, for the first time in similar devices, we ascertained its clear beneficial role when simultaneously employed in TiO_2 and $CH_3NH_3PbI_3$. Power conversion efficiencies as high as 16.48% were obtained, increased by almost 20% compared to the PCE of the reference device. This enhancement was attributed to the determining presence of rGO within the ETL which offers increased conductivity thus improved electron transport rate and charge mobility, it favors the growth of large perovskite crystals with improved crystallinity while it acts as a perovskite trap states passivator. In addition, the presence of rGO into the $CH_3NH_3PbI_3$ layer further increases the perovskite grains size and favors the growth of smooth and homogenous films. On the contrary the presence of the rGO in the Spiro-MeOTAD is detrimental, probably due to the creation of direct pathways between the perovskite and the top silver electrodes. As a result, the electrical parameters of the photovoltaic performance of the PSC were improved, displaying the determining role of graphene materials in the performance of PSC, in both terms of efficiency and stability.

References

[1] Y. Bai, X. Meng, S. Yang, Interface engineering for highly efficient and stable planar p-i-n perovskite solar cells, Adv. Energy Mater. 8 (2018) 1701883, https://doi.org/10.1002/aenm.201701883.

[2] X. Peng, J. Yuan, S. Shen, M. Gao, A.S.R. Chesman, H. Yin, J. Cheng, Q. Zhang, D. Angmo, Perovskite and organic solar cells fabricated by inkjet printing: progress and prospects, Adv. Funct. Mater. 27 (2017) 1703704, https://doi.org/10.1002/adfm.201703704.

[3] M. Vasilopoulou, A. Fakharuddin, A.G. Coutsolelos, P. Falaras, P. Argitis, A.R.M. Yusoff, M.K. Nazeeruddin, Molecular Materials as Interfacial Layers and Additives in Perovskite Solar Cells, Chem. Soc. Rev. 49 (2020) 4496-4526, https://doi.org/10.1039/C9CS00733D

[4] Z. Shi, J. Guo, Y. Chen, Q. Li, Y. Pan, H. Zhang, Y. Xia, W. Huang, Lead-free organic-inorganic hybrid perovskites for photovoltaic applications: recent advances and perspectives, Adv. Mater. 29 (2017) 1605005, https://doi.org/10.1002/adma.201605005.

[5] P. Wang, J. Zhao, J. Liu, L. Wei, Z. Liu, L. Guan, G. Cao, Stabilization of organometal halide perovskite films by SnO_2 coating with inactive surface hydroxyl groups on ZnO nanorods, J. Power Sources. 339 (2017) 51-60, https://doi.org/10.1016/j.jpowsour.2016.11.046.

[6] Y. Zhao, K. Zhu, Organic-inorganic hybrid lead halide perovskites for optoelectronic and electronic applications, Chem. Soc. Rev. 45 (2016) 655-689, https://doi.org/10.1039/C4CS00458B.

[7] National Renewable Energy Laboratory (NREL), https://www.nrel.gov/pv/cell efficiency.html (accessed September 2019).

[8] H.S. Kim, C.R. Lee, J.H. Im, K.B. Lee, T. Moehl, A. Marchioro, S.J. Moon , R. Humphry-Baker , J.H. Yum , J.E. Moser , M. Grätzel, N.G. Park , Lead iodide perovskite sensitized all-solid-state submicron thin film mesoscopic solar cell with efficiency exceeding 9%, Sci. Rep. 2 (2012) 591, https://doi.org/10.1038/srep00591.

[9] J. Burschka, N. Pellet, S.J. Moon, R. Humphry-Baker, P. Gao, M.K. Nazeeruddin, M. Gratzel, Sequential deposition as a route to high-performance perovskite-sensitized solar cells, Nature. 499 (2013) 316-319, https://doi.org/10.1038/nature12340.

[10] G.C. Xing, N. Mathews, S.Y. Sun, S.S. Lim, Y.M. Lam, M. Gratzel, S. Mhaisalkar, T.C. Sum, Long-range balanced electron- and hole-transport lengths in organic-inorganic $CH_3NH_3PbI_3$, Science. 342 (2013) 344-347, https://doi.org/10.1126/science.1243167.

[11] Q. Wang, Y.C. Shao, Q.F. Dong, Y.B. Yuan, Z.Xiao J.S. Huang, Large fill-factor bilayer iodine perovskite solar cells fabricated by a low-temperature solution-process, Energy Environ. Sci. 7 (2014) 2359-2365, https://doi.org/10.1039/C4EE00233D.

[12] Q. Chen, H.P. Zhou, Z.R. Hong, S. Luo, H.S. Duan, H.H. Wang, Y.S. Liu, G. Li, Y. Yang, Planar Heterojunction Perovskite Solar Cells via Vapor-Assisted Solution Process, J. Am. Chem. Soc. 136 (2014) 622-625, https://doi.org/10.1021/ja411509g.

[13] Y.H. Lou, M. Li, Z.K. Wang, Seed-mediated superior organometal halide films by GeO2 nano-particles for high performance perovskite solar cells,Appl. Phys. Lett. 108 (2016) 053301, https://doi.org/10.1063/1.4941416.

[14] J.H. Heo, S.H. Im, J.H. Noh, T.N. Mandal, C.-S. Lim, J.A. Chang, Y.H. Lee, H. Kim, A. Sarkar, M.K. Nazeeruddin, M. Grätzel, S.Il Seok, Efficient inorganic-organic hybrid heterojunction solar cells containing perovskite compound and polymeric hole conductors, Nat. Photonics. 7 (2013) 486-491, https://doi.org/10.1038/nphoton.2013.80.

[15] Z.K. Wang, X. Gong, M. Li, Y. Hu, J.M. Wang, H. Ma, L.S. Liao, Induced Crystallization of Perovskites by a Perylene Underlayer for High-Performance Solar Cells, ACS Nano. 10 (2016) 5479-5489, https://doi.org/10.1021/acsnano.6b01904 .

[16] M. Li, C. Zhao, Z.K. Wang, C.C. Zhang, H.K.H. Lee, A. Pockett, J. Barbe, T.C. Tsoi, Y.G. Yang, M.J. Carnie, X.Y. Gao, W.X. Yang, J.R. Durrant, L.S. Liao, S.J. Jain, Interface Modification by Ionic Liquid: A Promising Candidate for Indoor Light Harvesting and Stability Improvement of Planar Perovskite Solar Cells, Adv. Energy Mater. 8 (2018) 1801509, https://doi.org/10.1002/aenm.201801509.

[17] D.P. McMeekin, G. Sadoughi, W. Rehman, G.E. Eperon, M. Saliba, M.T. Hörantner, A. Haghighirad, N. Sakai, L. Korte, B. Rech, M.B. Johnston, L.M. Herz, H.J. Snaith, A mixed-cation lead mixed-halide perovskite absorber for tandem solar cells, Science. 351 (2016) 151-155, https://doi.org/10.1126/science.aad5845.

[18] H. Zhou, Q. Chen, G. Li, S. Luo, T. Song, H.-S. Duan, Z. Hong, J. You, Y. Liu, Y. Yang, Photovoltaics. Interface engineering of highly efficient perovskite solar cells, Science. 345(2014) 542-546, https://doi.org/10.1126/science.1254050.

[19] N.J. Jeon, J.H. Noh, W.S. Yang, Y.C. Kim, S. Ryu, J. Seo, S.I. Seok, Compositional engineering of perovskite materials for high-performance solar cells, Nature. 517 (2015) 476-480, https://doi.org/10.1038/nature14133.

[20] W. Chen, Y. Wu, Y. Yue, J. Liu, W. Zhang, X. Yang, H. Chen, E. Bi, I. Ashraful, M. Grätzel, L. Han, Efficient and stable large-area perovskite solar cells with inorganic charge extraction layers, Science. 350 (2015) 944-948, https://doi.org/10.1126/science.aad1015.

[21] M. Li, Z.K. Wang, Y.G. Yang, Y. Hu, S.L. Feng, J. M. Wang, X.Y. Gao, L.S. Liao, Copper Salts Doped Spiro-OMeTAD for High Performance Perovskite Solar Cells Adv. Energy Mater. 6 (2016) 1601156, https://doi.org/10.1002/aenm.201601156.

[22] J. Dong, Y. Zhao, J. Shi, H. Wei, J. Xiao, X. Xu, J. Luo, J. Xu, D. Li, Y. Luo, Q. Meng, Impressive enhancement in the cell performance of ZnO nanorod-based perovskite solar cells with Al-doped ZnO interfacial modification, Chem. Commun. 50 (2014) 13381-13384, https://doi.org/10.1039/C4CC04908J.

[23] M.A. Mahmud, N.K. Elumalai, M.B. Upama, D. Wang, V.G. Ales, Cesium compounds as interface modifiers for stable and efficient perovskite solar cells Sol. Energy Mater. Sol. Cells. 174 (2018) 172-186, https://doi.org/10.1016/j.solmat.2017.08.032.

[24] P. Ruankham, D. Wongratanaphisan, A. Gardchareon, S. Phadungdhitidhada, S. Choopun, T. Sagawa, Full coverage of perovskite layer onto ZnO nanorods via a modified sequential two-step deposition method for efficiency enhancement in perovskite solar cells, Appl. Surf. Sci. 410 (2017) 393-400, https://doi.org/10.1016/j.apsusc.2017.03.096.

[25] P. Zhang, J. Wu, T. Zhang, Y. Wang, D. Liu, H. Chen, L. Ji, C. Liu, W. Ahmad, Z.D. Chen, S. Li, Perovskite solar cells with ZnO electron-transporting materials, Adv. Mater. 30 (2018) 1703737, https://doi.org/10.1002/adma.201703737.

[26] A. Huang, L. Lei, J. Zhu, Y. Yu, Y. Liu, S. Yang, S. Bao, P. Jin, Controllable deposition of TiO_2 nanopillars at room temperature for high performance perovskite solar cells with suppressed hysteresis, Sol. Energy Mater. Sol. Cells. 168 (2017) 172-182, https://doi.org/10.1016/j.solmat.2017.04.035.

[27] X. Huang, Z. Hu, J. Xu, P. Wang, L. Wang, J. Zhang, Y. Zhu, Low-temperature processed SnO_2 compact layer by incorporating TiO_2 layer toward efficient planar heterojunction perovskite solar cells, Sol. Energy Mater. Sol. Cells. 164 (2017) 87-92, https://doi.org/10.1016/j.solmat.2017.02.010.

[28] X. Ren, D. Yang, Z. Yang, J. Feng, X. Zhu, Solution-processed Nb: SnO2 electron transport layer for efficient planar perovskite solar cells, ACS Appl. Mater. Interfaces. 9 (2017) 2421-2429, https://doi.org/10.1021/acsami.6b13362 .

[29] J. Song, E. Zheng, J. Bian, X. Wang, W. Tian, Y. Sanehira, T. Miyasaka, Low temperature SnO_2-based electron selective contact for efficient and stable perovskite solar cells, J. Mater. Chem. A. 3 (2015) 10837-10844, https://doi.org/10.1039/C5TA01207D.

[30] V.O. Eze, Y. Seike, T. Mori, Efficient planar perovskite solar cells using solution processed amorphous WOx/fullerene C60 as electron extraction layers, Org. Electron. 46 (2017) 253-262, https://doi.org/10.1016/j.orgel.2017.04.024.

[31] I. Pintilie, V. Stancu, A. Tomulescu, R. Radu, C. Besleaga Stan, L. Trinca, L. Pintilie, Properties of perovskite ferroelectrics deposited on F doped SnO_2 electrodes and the prospect of their integration into perovskite solar cells, Mater. Des. 135(2017) 112-121, https://doi.org/10.1016/j.matdes.2017.09.013.

[32] G.E. Eperon, V.M. Burlakov, P. Docampo, A. Goriely, H.J. Snaith, Morphological Control for High Performance, Solution Processed Planar Heterojunction Perovskite Solar Cells, Adv. Funct. Mater. 24 (2014) 151-157, https://doi.org/10.1002/adfm.201302090.

[33] S.Y. Sun, T. Salim, N. Mathews, M. Duchamp, C. Boothroyd, G.C. Xing, T.C. Sum, Y. M. Lam, The origin of high efficiency in low-temperature solution-processable bilayer organometal halide hybrid solar cells, Energy Environ. Sci. 7 (2014) 399-407, https://doi.org/10.1039/C3EE43161D.

[34] M.C. Wu, S.H. Chan, M.H. Jao, W.F. Su, Enhanced short-circuit current density of perovskite solar cells using Zn-doped TiO_2as electron transport layer Sol. Energy Mater. Sol. Cells. 157 (2016) 447-453, https://doi.org/10.1016/j.solmat.2016.07.003.

[35] K. Wojciechowski, S. D. Stranks, A. Abate, G. Sadoughi, A. Sadhanala, N. Kopidakis, G. Rumbles, C.Z. Li, R.H. Friend, A.K. Y. Jen, H.J. Snaith, Heterojunction Modification for Highly Efficient Organic-Inorganic Perovskite Solar Cells, ACS Nano. 8 (2014) 12701-12709, https://doi.org/10.1021/nn505723h.

[36] J.H. Heo, H.J. Han, D. Kim, T.K. Ahn, S.H. Im, Hysteresis-less inverted $CH_3NH_3PbI_3$ planar perovskite hybrid solar cells with 18.1% power conversion efficiency Energy Environ. Sci. 8 (2015) 1602-1608, https://doi.org/10.1039/C5EE00120J.

[37] G. Murugadoss, S. Tanaka, G. Mizuta, S. Kanaya, H. Nishino, T. Umeyama, H. Imahori, S. Ito, Light stability tests of methylammonium and formamidinium Pb-halide perovskite for solar cell applications, Jpn. J. Appl. Phys. 54 (2015) 08KF08, http://dx.doi.org/10.7567/JJAP.54.08KF08

[38] N. Balis, A.A. Zaky, C. Athanasekou, A.M.T. Silva, E. Sakellis, M. Vasilopoulou, T. Stergiopoulos, A.G. Kontos, P. Falaras, Investigating the role of reduced graphene oxide as a universal additive in planar perovskite solar cells, J. Photo.chem .Photo bio A: Chem. 386 (2020) 112141, https://doi.org/10.1016/j.jphotochem.2019.112141.

[39] N. Balis, A. Verykios, A. Soultati, V. Constantoudis, M. Papadakis, F. Kournoutas, C. Drivas, M.-C. Skoulikidou, S. Gardelis, M. Fakis, S. Kennou, A.G. Kontos, A.G. Coutsolelos, P. Falaras, M. Vasilopoulou, Triazine-Substituted Zinc Porphyrin as an Electron Transport Interfacial Material for Efficiency Enhancement and Degradation Retardation in Planar Perovskite Solar Cells, ACS Appl. Energy Mater. 1 (2018) 3216-3229, https://doi.org/10.1021/acsaem.8b00447.

[40] N. Balis, A.A. Zaky, D. Perganti, A. Kaltzoglou, L. Sygellou, F. Katsaros, T. Stergiopoulos, A.G. Kontos, P. Falaras, Dye Sensitization of Titania Compact Layer for

Efficient and Stable Perovskite Solar Cells, ACS Appl. Energy Mater. 1 (2018) 6161-6171, https://doi.org/10.1021/acsaem.8b01221.

[41] B. Chen, H. Rao, W. Li, Y. Xu, H. Chen, D. Kuang, C. Su, Achieving high performance planar perovskite solar cell with Nb-doped TiO_2 compact layer by enhanced electron injection and efficient charge extraction, J. Mater. Chem. A. 4 (2016) 5647-5653, https://doi.org/10.1039/C6TA00989A.

[42] X. Gu, Y. Wang, T. Zhang, D. Liu, R. Zhang, Enhanced electronic transport in Fe3+-doped TiO_2 for high efficiency perovskite solar cells, J. Mater. Chem. C. 5 (2017) 10754-10760, https://doi.org/10.1039/C7TC03845C.

[43] H. Zhou, Q. Chen, G. Li, S. Luo, T.b. Song, H.S. Duan, Z. Hong, J. You, Y.s. Liu,Y. Yang, Interface engineering of highly efficient perovskite solar cells, Science. 345 (2014) 542-546, https://doi.org/10.1126/science.1254050.

[44] D. Liu, S. Li, P. Zhang, Y. Wang, R. Zhang, H. Sarvari, F. Wang, J. Wu, Z. Wang, Z.D. Chen, Efficient planar heterojunction perovskite solar cells with Li-doped compact TiO_2 layer, Nano Energy. 31 (2017) 462-468, https://doi.org/10.1016/j.nanoen.2016.11.028.

[45] M. Lv, W. Lv, X. Fang, P. Sun, B. Lin, S. Zhang, X. Xu, J. Ding, N. Yuan, Performance enhancement of perovskite solar cells with a modified TiO_2 electron transport layer using Zn-based additives, RSC Adv. 6 (2016) 35044–35050, https://doi.org/10.1039/C6RA01149G.

[46] R. Ranjan, A. Prakash, A. Singh, A. Singh, A. Garg, Effect of tantalum doping in a TiO_2 compact layer on the performance of planar spiro-OMeTAD free perovskite solar cells, J. Mater. Chem. A. 6 (2018) 1037-1047, https://doi.org/10.1039/C7TA09193A.

[47] J. Wang, M. Qin, H. Tao, W. Ke, Z. Chen, Performance enhancement of perovskite solar cells with Mg-doped TiO_2 compact film as the hole-blocking layer, Appl. Phys. Lett. 106 (2015) 121104, https://doi.org/10.1063/1.4916345.

[48] A. Soultati, A. Fakharuddin, E. Polydorou, C. Drivas, A. Kaltzoglou, M.I. Haider, F. Kournoutas, M. Fakis, L.C. Palilis, S. Kennou, D. Davazoglou, P. Falaras, P. Argitis, S. Gardelis, A. Kordatos, A. Chroneos, L. Schmidt-Mende, M. Vasilopoulou, Lithium Doping of ZnO for High Efficiency and Stability Fullerene and Non-Fullerene Organic Solar Cells, ACS Appl. Energy Mater. 2 (2019) 1663-1675, https://doi.org/10.1021/acsaem.8b01658.

[49] N. Arora, M.I. Dar, A. Hinderhofer, N. Pellet, F. Schreiber, S.M. Zakeeruddin, M. Grätzel, Perovskite solar cells with CuSCN hole extraction layers yield stabilized efficiencies greater than 20%, Science. 358 (2017) 768-771, https://doi.org/10.1126/science.aam5655.

[50] R. Gusain, K. Gupta, P. Joshi, O.P. Khatri, Adsorptive removal and photocatalytic degradation of organic pollutants using metal oxides and their composites: A

comprehensive review, Adv. Colloid Interface Sci. 272 (2019), https://doi.org/10.1016/j.cis.2019.102009.

[51] L. Yoong, F.K. Chong, B.K. Dutta, Development of copper-doped TiO_2 photocatalyst for hydrogen production under visible light, Energy. 34 (2009) 1652-1661, https://doi.org/10.1016/j.energy.2009.07.024.

[52] L. Clarizia, D. Spasiano, I.D. Somma, R. Marotta, R. Andreozzi, D.D. Dionysiou, Copper modified-TiO_2 catalysts for hydrogen generation through photoreforming of organics, A short review, Int. J. Hydrogen Energy. 39 (2014) 16812-16831, https://doi.org/10.1016/j.ijhydene.2014.08.037.

[53] I.-H. Tseng, W.-C. Chang, J.C. Wu, Photoreduction of CO_2 using sol-gel derived titania and titania-supported copper catalysts, Appl. Catal. B. 37 (2002) 37-48, https://doi.org/10.1016/S0926-3373(01)00322-8.

[54] M.M. Elsenety, A. Stergiou, L. Sygellou, N. Tagmatarchis, N. Balis, P. Falaras, Boosting perovskite nanomorphology and charge transport properties via a functional D-π-A organic layer at the absorber/hole transporter interface, Nanoscale. 12 (2020) 15137-15149, https://doi.org/10.1039/D0NR02562C.

[55] X. Pan, M-Q. Yang, X. Fu, N. Zhang, Y-J. Xu, Defective TiO_2 with oxygen vacancies: synthesis, properties and photocatalytic applications, Nanoscale. 5 (2013) 3601-3614, https://doi.org/10.1039/C3NR00476G.

[56] A. Sarkar, G.G. Khan, The formation and detection techniques of oxygen vacancies in titanium oxide-based nanostructures, Nanoscale. 11 (2019) 3414-3444, https://doi.org/10.1039/C8NR09666J.

[57] M. Nasrollahzadeh, M. Bagherzadeh, H. Karimi, Preparation, characterization and catalytic activity of $CoFe_2O_4$ nanoparticles as a magnetically recoverable catalyst for selective oxidation of benzyl alcohol to benzaldehyde and reduction of organic dyes, J. Colloid Interface Sci. 465 (2016) 271-278, https://doi.org/10.1016/j.jcis.2015.11.074.

[58] P.A. Bharad, K. Sivaranjani, C.S. Gopinath, A rational approach towards enhancing solar water splitting: a case study of Au-RGO/N-RGO-TiO_2, Nanoscale. 7 (2015) 11206-11215, https://doi.org/10.1039/C5NR02613J.

[59] A. Sarkar, K. Karmakar, G.G. Khan, Designing Co-Pi Modified One-Dimensional n-p $TiO_2/ZnCo_2O_4$Nanoheterostructure Photoanode with Reduced Electron-Hole Pair Recombination and Excellent Photoconversion Efficiency (>3%), J. Phys. Chem. C. 121 (2017) 25705-25717, https://doi.org/10.1021/acs.jpcc.7b08213.

[60] H. Zhang M. Zhou, Q. Fu, B. Lei, W. Lin, H. Guo, M. Wu,Y. Lei, Observation of defect state in highly ordered titanium dioxide nanotube arrays, Nanotechnology. 25 (2014) 275603, https://doi.org/10.1088/0957-4484/25/27/275603.

[61] B. Choudhury, A. Choudhury, Luminescence characteristics of cobalt doped TiO_2 nanoparticles, J. Lumin. 132 (2012) 178-184, https://doi.org/10.1016/j.jlumin.2011.08.020.

[62] B. Santara, P.K. Giri, K. Imakita, M. Fujii, Evidence of oxygen vacancy induced room temperature ferromagnetism in solvothermally synthesized undoped TiO_2 nanoribbons, Nanoscale. 5 (2013) 5476-5488, https://doi.org/10.1039/C3NR00799E.

[63] C.P. Saini, A. Barman, D. Banerjee, O. Grynko, S. Prucnal, M. Gupta, D.M. Phase, A. K. Sinha, D. Kanjilal, W. Skorupa, A. Kanjilal, Impact of Self-Trapped Excitons on Blue Photoluminescence in TiO_2 Nanorods on Chemically Etched Si Pyramids, J. Phys. Chem. C. 121 (2017) 11448-11454, https://doi.org/10.1021/acs.jpcc.7b02218.

[64] M.K. Arfanis, C. P. Athanasekou, E. Sakellis, N. Boukos, N.Ioannidis, V. Likodimos, L. Sygellou, M. Bouroushian, A. G. Kontos, P. Falaras, Photocatalytic properties of copper-Modified core-shell titania nanocomposites, J. Photochem. Photobiol. A. 370 (2019) 145-155, https://doi.org/10.1016/j.jphotochem.2018.10.051.

[65] L. Martin, H. Martinez, D. Poinot, B. Pecquenard, F.L. Cras, Comprehensive X-ray Photoelectron Spectroscopy Study of the Conversion Reaction Mechanism of CuO in Lithiated Thin Film Electrodes, J. Phys. Chem. C. 117 (2013) 4421-4430, https://doi.org/10.1021/jp3119633.

[66] I. Ganesh, P.P. Kumar, I. Annapoorna, J.M. Sumliner, M. Ramakrishna, N.Y. Hebalkar, G. Padmanabham, G. Sundararajan, Preparation and characterization of Cu-doped TiO_2 materials for electrochemical, photoelectrochemical, and photocatalytic applications, Appl. Surf. Sci. 293 (2014) 229-247, https://doi.org/10.1016/j.apsusc.2013.12.140.

[67] H.S. Park, D.H. Kim, S.J. Kim, K.S. Lee, The photocatalytic activity of 2.5 wt% Cu-doped TiO_2 nano powders synthesized by mechanical alloying, J. All. Comp. 415 (2006) 51-55, https://doi.org/10.1016/j.jallcom.2005.07.055.

[68] P. Li, C. Liang, B. Bao, Y. Li, X. Hu, Y. Wang,Y. Zhang, F. Li, G. Shao, Y. Song, Inkjet manipulated homogeneous large size perovskite grains for efficient and large-area perovskite solar cells, Nano Energy. 46 (2018) 203-211, https://doi.org/10.1016/j.nanoen.2018.01.049.

[69] J. M. Polfus, B. Yildiz, H. L. Tuller, R. Bredesen, Adsorption of CO2 and Facile Carbonate Formation on $BaZrO_3$ Surfaces, J. Phys. Chem. 122 (2018) 307-314, https://doi.org/10.1021/acs.jpcc.7b08223

[70] Z. Liu, Y. Wang, X. Peng, Y. Li, Z. Liu, C. Liu, J. Ya, Y. Huang, Photoinduced superhydrophilicity of TiO_2 thin film with hierarchical Cu doping, Sci. Technol. Adv. Mater. 13 (2012) 025001, https://doi.org/10.1088/1468-6996/13/2/025001.

[71] A.I. Kontos, A.G. Kontos, D.S. Tsoukleris, G.D. Vlachos, P.m Falaras, Superhydrophilicity and photocatalytic property of nanocrystalline Titania sol-gel films, Thin Solid Films. 515 (2007) 7370-7375, https://doi.org/10.1016/j.tsf.2007.02.082.

[72] R. G. Niemann, A.G. Kontos, D. Palles, E.I. Kamitsos, A. Kaltzoglou, F. Brivio, P. Falaras, P.J. Cameron, Halogen Effects on Ordering and Bonding of $CH_3NH_3^+$ in $CH_3NH_3PbX_3$ (X = Cl, Br, I) Hybrid Perovskites: A vibrational spectroscopic study, J. Phys. Chem. C. 120 (2016) 2509–2519, https://doi.org/10.1021/acs.jpcc.5b11256.

[73] M. Antoniadou, M. E. Siranidi, N. Vaenas, A.G. Kontos, E. Stathatos, P. Falaras, Photovoltaic Performance and Stability of CH_3NH_3 PbI_{3-x} Cl_x Perovskites, J. Surf. Interf. Mat. 2 (2014) 1-5.

[74] J. Barbé, V. Kumar, M.J. Newman, H.K.H Lee, S.N. Jain, C.H. Chen, C. Charbonneau, C. Rodenburg, W.C. Tsoi, Dark Electrical Bias Effect on Moisture-Induced Degradation in Inverted Lead Halide Perovskite Solar Cells Measured by Advanced Chemical Probes, Sust. Energy Fuels. 2 (2018) 905-914, https://doi.org/10.1039/C7SE00545H.

[75] B. Moongraksathum, J.-Y. Shang, Y.-W. Chen, Photocatalytic Antibacterial Effectiveness of Cu-Doped TiO_2 Thin Film Prepared via the Peroxo Sol-Gel Method, Catalysts. 8 (2018) 352. https://doi.org/10.3390/catal8090352.

[76] C. Garlisi, C.-Y. Lai, L. George, M. Chiesa, G. Palmisano, Relating Photoelectrochemistry and Wettability of Sputtered Cu- and N-Doped TiO_2 Thin Films via an Integrated Approach, J. Phys. Chem. C. 122 (2018) 12369-12376, https://doi.org/10.1021/acs.jpcc.8b03650.

[77] S.S. Mali, J.V. Patil, H. Kim, C.K. Hong, Gallium Cationic Incorporated Compact TiO_2 as an Efficient Electron-Transporting Layer for Stable Perovskite Solar Cells, Matter.1 (2019) 452-464, https://doi.org/10.1016/j.matt.2019.04.001.

[78] J.H. Heo, M.S. You, M.H. Chang, W. Yin, T.K. Ahn, S.-J. Lee, S.-J. Sung, D.H. Kim, S.H. Im, Hysteresis-less mesoscopic $CH_3NH_3PbI_3$ perovskite hybrid solar cells by introduction of Li-treated TiO_2 electrode, Nanoenergy. 15 (2015) 530-539, https://doi.org/10.1016/j.nanoen.2015.05.014.

[79] S.M. Pietralunga, G. Irde, A.J. Barker, J.M. Ball, A. Petrozza, V. Sala, M. Zani, G. Lanzani, A. Tagliaferri, Dynamical Imaging of Surface Photopotentials in Hybrid Lead Iodide Perovskite Films under High Optical Irradiance and the Role of Selective Contacts, Adv. Mater. Interfaces. (2020), 2000297, https://doi.org/10.1002/admi.202000297.

6 Chapter 6

6 Elephant Herd Algorithm for Optimal Performance Emulation of PSCs Associated with Experimental Validation

6.1 Preface

There is no doubt that the global demand for energy is being increased and accelerating significantly in parallel with the depletion of the global reserves of fossil fuels. Therefore, there is a strong need to investigate advanced renewable energy technologies. Solar cells are the most promising renewable energy sources that convert solar energy to convenient electrical energy at least energy costs with the highest possibilities of producing large-scale solar cell manufacturing capabilities.[1] Indeed, the power striking from the sun into earth's surface is near to 1.8×10^{11} MW which is much more than all the present power demands. [2,3] Moreover it is a clean and environmentally friendly energy source, it has low running cost and occupies the highest rankings in terms of use and reliability, promising to expand its utilization more and more. In the recent years, increased contribution of solar cells is noticed to accomplish the growing demands of energy supplies. This contribution of solar energy and especially PV technologies has been encouraged due to many advantages such as safety, security and reliability, lack of maintenance need, effectiveness, and direct conversion of sunlight to electricity, economically feasibility into illumination of remote areas, flexibility and size tunability of the solar cell systems.

Due to very high absorption of light and carrier transportation, perovskite semiconductors with the general formula ABX_3 (where A is an organic/inorganic cation, B is a metal cation, and X is a halide anion) attracted the research interest towards high efficiency PSCs. [4] The

power conversion efficiency of PSCs is raised from 3.8 % in 2009 to 25.2% in 2019. [5-7] PSCs have high degree of nonlinearity and it is crucial to determine the cell characteristic parameters with high accuracy and well understand the device operation. Hence, it is very important to simulate the performance and analyze the working mechanism of PSCs by finding the accurate model to determine their optimal parameters as it has been done in the case of Si-based PVs. [8-9] To date, the planar architecture of PSCs has been rapidly developed because of its various advantages including simple structure, ease of fabrication, low cost and absence of high temperature procedures. [10-11]

To better understand the behavior and optimize the electrical properties of PVs, several simulation tools have been proposed in the literature. As single-diode, double diode and triple diode models are among the most suitable approaches, the aim of the present work is to check the suitability and validity of these electrical models for the simulation of PSCs, where the estimation of the electrical parameters of this third generation PV devices can be formulated as non-linear optimization problem. To solve this problem, there are two main solutions, deterministic and heuristic. Deterministic methods always suffer from getting into local optima that strongly depend on some approximations and initial assumptions such as linearization about certain operating point. On the other hand, heuristic optimization approaches are explored as efficient tools for solving the problem of PV parameters extraction. [12-16] Their prevailing advent lays on lower computational cost and their ability to address complex problems without any dependence on higher derivatives. In addition, their flexibility to find a global optimum makes them the right choice to estimate the PV parameters. [17, 18] Thus, based on the systematic exploration of metaheuristic principle; several approaches have been implemented to solve the problem of PV parameters extraction. Such methods include Mine Blast Algorithm (MBA), [19] Wind driven optimization algorithm, [20] Jaya Optimization Algorithm , [21, 22] Bird Mating Optimizer, [23] Firefly

Algorithm (FA), [24] Imperialist Competitive Algorithm (ICA), [25] Cuckoo Search (CS), [26] Sunflower Optimization algorithm, [27] Krill Herd Algorithm, [28] Sine Cosine Algorithm, [29] Hurricane Optimization Algorithm, [30] and Multi-Verse Optimizer. [31] However, modern and more competitive algorithms were developed. The Elephant Herd Optimization (EHO) algorithm, [32, 33] mimics the social life of elephants which in real world live in groups or clans ruled by a matriarch, usually the eldest female in the clan. Thanks to fewer numbers of control parameters and easier implementation, the EHO algorithm has been gaining research interest during the past decade. Recent modifications were applied for the original EHO to understand the impact of the control parameters, a parametric study of the EHO is carried out using a standard test bench, engineering problems, and real-world problems. [33, 34] Sample applications for EHO are also presented for optimizing the PID controller parameters, [35] and multiobjective allocation of distributed energy resources in distribution systems. [36] Another modified version of the EHO was used for solving the economic generation scheduling for distributed energy resources in grid based microgrid.[37]

Recently, the dye-sensitization approach was used to optimize the compact layer/perovskite interface in planar perovskite solar cells (PSCs). This modification leads to PSC devices presenting significantly improved performance and increased stability. [4] It is then important to see if and how the application of the EHO algorithm and the corresponding diode models gives new insights into how the molecular engineering via dye sensitization of the functional interfaces affects the cell parameters. Thus, in this contribution we assessed the performance of PSCs using the EHO algorithm to accurately estimate the parameters of PSCs, for single diode model (SDM), double diode model (DDM) and triple diode model (TDM). We thus proved the EHO capability to identify the best electrical model for PSCs simulation and accurately extract the corresponding PSCs' electrical parameters.

6.2 Experimental

6.2.1 Cell structure

The fabrication of planar Perovskite Solar Cells (PSCs) is described in detail in the previous chapters. The corresponding cell structure, including both reference cells and those modified with the triphenylamine-based metal-free organic dye, namely (E)-3-(5-(4-(bis(2',4'-dibutoxy-[1,1'-biphenyl]-4yl) amino) phenyl) thiophen-2-yl)-2-cyanoacrylic acid (D35) are given in Figure 6.1.

For easily setting-up the electrical models of PSCs (controlled and modified by D35 dye), it is necessary to know the difference between the studied devices. The addition of a dye monolayer over the TiO_2 compact layer was performed by immersing the titania electrodes overnight in an ethanolic solution of the D35 organic dye. The benefit of this layer is to transform the surface of the titania compact layer from hydrophilic to highly hydrophobic, which helps the perovskite crystallization and stability

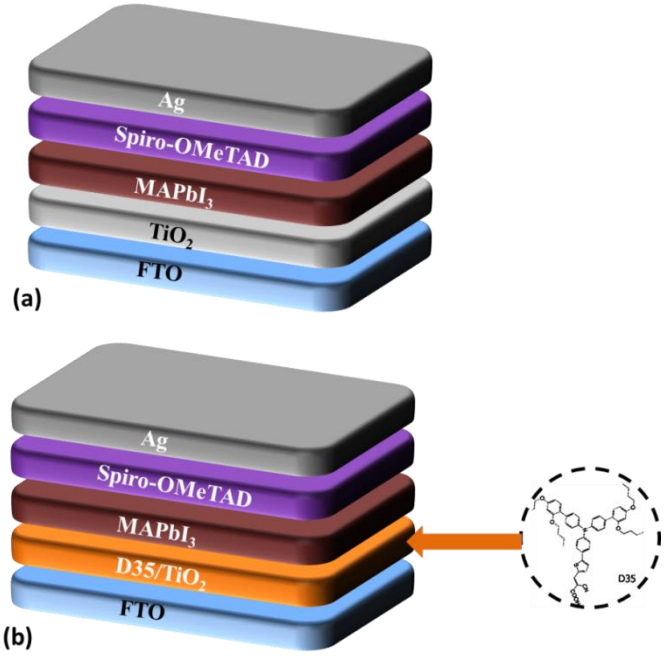

Figure 6.1 Schematic representation of perovskite solar cells: control (a); and modified (b).

6.3 Electrical Modeling (single, double and three diode models) of Perovskite Solar Cells

In this work, the performance of the PSCs was evaluated using three electrical models (single, double and three diode models). Generally, the rectification of characteristics of solar cells including heterojunctions and perovskites can be described by the Shockley diode equation as: [38, 39]

$$j_d = j_{d0}\left[\exp\left(\frac{qV}{(m \cdot k \cdot T}\right) - 1\right] \quad (1)$$

where, j_d is the dark current, V is the applied voltage, j_{d0} the reverse saturation current density, q is the elementary charge, m is the ideal factor of the cell, K is the Boltzmann constant, T is the absolute temperature.

The ideal model of PSCs is considered as a single PN junction (diode) in parallel with photo current j_{ph} . Eq. 2 presents the mathematical expression for the ideal model as: [40]

$$j = j_{ph} - j_{d0}\left[\exp\left(\frac{qV}{(m \cdot k \cdot T}\right) - 1\right] \quad (2)$$

where, j_{ph} is the photocurrent and j is the output current.

In practice, different electrical models were presented in the literature to model PV cells. In Figure 8.2.a, the PSCs are modeled by using single PN junction (diode model). In this model, the device is represented by a current source, two resistances and a diode. The current source represents the photocurrent (j_{ph}) which is sensitive to solar radiation change and ambient temperature. The series resistance represents all resistances (R_s) in the current path, electrode resistance, material bulk resistance and contact resistance. The shunt resistance (R_{sh}) represents the leakage current across the p-n junction.

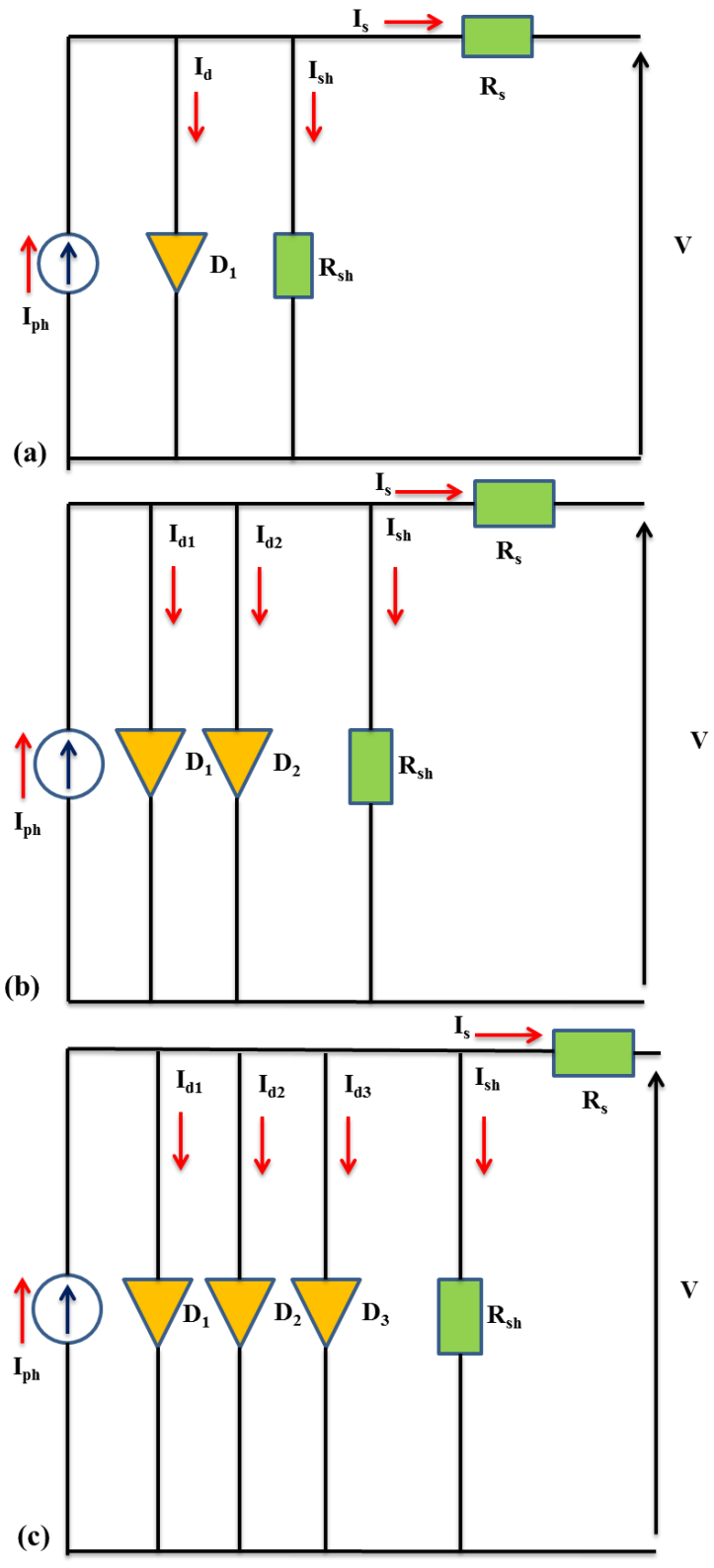

Figure 6.2 Perovskite solar cell model a) single diode model b) double diode model c) triple diode model

Applying Kirchhoff's current law, it is obvious that the output current j can be represented by Eq.3 as: [25]

$$j = j_{ph} - j_{d0}\left[\exp\left(\frac{q(V + R_s.j)}{m \cdot k \cdot T}\right) - 1\right] - \frac{V + R_s.j}{R_{sh}} \quad (3)$$

where, R_s and R_{sh} are the series and shunt resistance, respectively.

From Figure 6.2.b, it can be generalized the single diode model for PSCs to the two diode model as Eq.4 to consider the effect of recombination losses in the space charge region and expresses it an additional diode beside the first diode which represents the recombination and diffusion in the quasi neutral regions was added as: [41]

$$j = j_{ph} - j_{d1}\left[\exp\left(\frac{q(V + R_s.j)}{(m_1) \cdot k \cdot T}\right) - 1\right] - j_{d2}\left[\exp\left(\frac{q(V + R_s.j)}{(m_2) \cdot k \cdot T}\right) - 1\right] - \frac{V + R_s.j}{R_{sh}} \quad (4)$$

Also, the PSCs can be extended to triple diode model as shown in Figure 6.2.c and Eq.5 to include the effect of grain boundaries and leakage current which is considered by adding a third diode to the double diode PV model with the same physical meaning like the double diode model as: [27]

$$\begin{aligned} j = j_{ph} &- j_{d1}\left[\exp\left(\frac{q(V + R_s.j)}{(m_1) \cdot k \cdot T}\right) - 1\right] - j_{d2}\left[\exp\left(\frac{q(V + R_s.j)}{(m_2) \cdot k \cdot T}\right) - 1\right] \\ &- j_{d3}\left[\exp\left(\frac{q(V + R_s.j)}{(m_3) \cdot k \cdot T}\right) - 1\right] - \frac{V + R_s.j}{R_{sh}} \end{aligned} \quad (5)$$

6.4 Estimation Problem

The parameters estimation of PSCs can be expressed as a non-linear optimization problem with high degree of nonlinearity. To realize the optimal electrical models of PSCs in this work, the main target is to minimize the proposed objective function which is the sum of the variance and deviations between the estimated photoncurrents and those recorded by

experimental measurements. Non-linear functions can be implemented for each model to describe the error between each pair of photoncurrent values. Equations (6 - 8) present the non-linear functions for SDM, DDM and TDM, respectively:

$$f_1(V_t, j_t, y) = j_{ph} - j_{d1}\left[\exp\left(\frac{q(V_t + R_s.j_t)}{(m_1)\cdot k\cdot T}\right)-1\right] - \frac{V_t + R_s.j_t}{R_{sh}} - j_{measured} \quad (6)$$

$$f_2(V_t, j_t, y) = j_{ph} - j_{d1}\left[\exp\left(\frac{q(V_t + R_s.j_t)}{(m_1)\cdot k\cdot T}\right)-1\right] - j_{d2}\left[\exp\left(\frac{q(V_t + R_s.j_t)}{(m_2)\cdot k\cdot T}\right)-1\right] - \frac{V_t + R_s.j_t}{R_{sh}} - j_{measured} \quad (7)$$

$$f_3(V_t, j_t, y) = j_{ph} - j_{d1}\left[\exp\left(\frac{q(V_t + R_s.j_t)}{(m_1)\cdot k\cdot T}\right)-1\right] - j_{d2}\left[\exp\left(\frac{q(V_t + R_s.j_t)}{(m_2)\cdot k\cdot T}\right)-1\right] - j_{d3}\left[\exp\left(\frac{q(V_t + R_s.j_t)}{(m_3)\cdot k\cdot T}\right)-1\right] - \frac{V_t + R_s.j_t}{R_{sh}} - j_{measured} \quad (8)$$

For the previous functions, the control variables are organized as follows:

- For SDM, five decision variables that described in the vector y as: y = (j_{ph}, j_{d1}, R_s, R_{sh}, m_1) ,
- For DDM, seven decision variables that described in the vector y as: y = (j_{ph}, j_{d1}, j_{d2}, R_s, R_{sh}, m_1, m_2)
- For the third model (TDM), nine decision variables are described in the vector y as: y = (j_{ph}, j_{d1}, j_{d2}, j_{d3}, R_s, R_{sh}, m_1, m_2, m_3).

The root mean square error (RMSE) is developed to evaluate the suggested models as shown in Eq. (9).

$$\mathrm{RMSE\ F} = \sqrt{\frac{1}{N}\sum_{w=1}^{N} f_w(V_t, j_t, y)^2} \quad (9)$$

The optimization procedure minimizes the RMSE to tune the decision variables for the whole range of experimental data with size N.

6.5 Crow search optimization algorithm

Crows are very intelligent birds and live in groups. In comparing with their body their brain is big enough and according to brain-body ratio, their brain is very relative to humans. They have the ability to remember faces and warn each other if a strange one approaches. Moreover, they communicate in sophisticated ways and they can remember the places of their hidden food. They also watch other birds and see where they hide their catch and steal it after they leave. Crows use their experience as thief to predict the behavior of pilfered. Recently, Askarzadeh developed a new stochastic metaheuristic optimization algorithm based on the behavior of the crows and called it crow search optimization algorithm (CSOA).

The assumption is that is a d-dimensional space containing a number of crows (N) and the i^{th} crow place at time (the iteration) in the search area is represented by a vector $x^{i.iter}$ $x^{i.iter}$ =[$x_1^{i.iter}$, $x_2^{i.iter}$,..... $x_d^{i.iter}$]. Each crow has its hidden food place in its memory and this place appear in each iteration as $m^{i.iter}$. This position is the best position that the crow has obtained. Crows seek for the best food ways (the places of hidden food). Assuming at time iter, crow j wants to go to its food place where it hides its catch $m^{j.iter}$. In the same time another crow for example crow i decide to track crow j in order to know its hiding place. As a result of this tracking two situations may happen:

State 1: The crow j did not aware that another crow (crow i) following it. So, crow i will see the crow j food place (the hiding place) as a result, the crow i new position is given by:

$$\mathbf{X^{i.iter+1} = X^{i.iter} + r_i\, fl^{i.iter}\,(m^{j.iter} - x^{i.iter})}$$

Where, r_i is a random number between 0 and 1 and $fl^{i.iter}$ is the flight length of crow i at any iteration. Figure 6.3 shows the fl effect on the capability of search. When the fl values are small this leads to a very close searching (near to $x^{i.iter}$) in contrary the big values results in a far searching (far from $x^{i.iter}$).

State 2: Crow j knows that crow i following it. So, to avoid its food hiding place from discovery it will misleading crow i by going to fake place (another positon in the searching area).

Finally, states one and two can be represented as follow,

$$X^{i.iter+1} = X^{i.iter} + r_i \, fl^{i.iter} \left(m^{j.iter} - x^{i.iter}\right) \quad r_j \geq AP^{j.iter}$$

And random position otherwise

Where, $AP^{j.iter}$ represents the awareness probability of crow j at iteration iter.

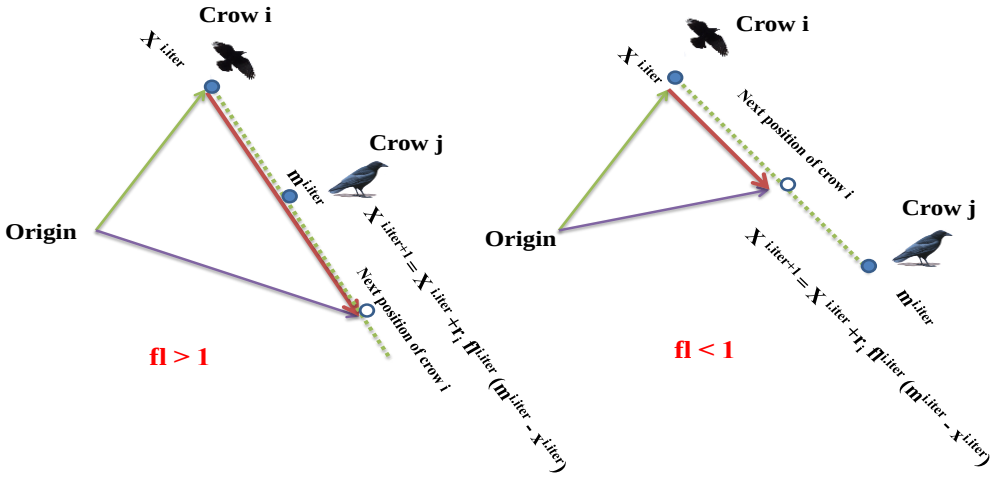

Figure 6.3 CSOA behaviour at fl > 1 (left) and fl < 1 (right) the dashed line shows the crow i path

6.6 Elephant Herd Optimization Algorithm

6.6.1 Clan updating

Elephants in real life live in clans. There is a female leader for each clan (matriarch) and a male elephant who leaves the clan when it reaches puberty.[32, 33] Based on that simple

rules each individual elephant inside the clan compares its position to the leader elephant's position so, for elephant j in clan c, its position can be updated according to Eq. (10)

$$x_{n,c,j} = x_{c,j} + \alpha \cdot r \cdot \left(x_{best,c} - x_{c,j} \right) \quad (10)$$

where, $x_{n,c,j}$ and $x_{c,j}$ are newly updated and old position for elephant j in clan c, respectively. α in the range of [0, 1] is a scale factor that determines the influence of matriarch c on $x_{c,j}$. $x_{best,c}$ represents matriarch c, which is the fittest elephant individual in the clan c, r in the range of [0, 1]. Here, the uniform distribution is used. The fittest elephant can be updated as

$$x_{n,c,j} = \beta \cdot x_{center,c} \quad (11)$$

where β in range of [0, 1] is a factor that determines the influence of the $x_{center,c}$ on $x_{n,c,j}$. We can see, the new individual $x_{n,c,j}$ in Eq. (11) is generated by the information obtained by all the elephants in clan c. $x_{center,c}$ is the center of clan ci, and for the d^{th} dimension it can be calculated as

$$X_{center,c,d} = \frac{1}{N_c} \sum_{j=1}^{N_c} x_{c,j,d} \quad (12)$$

where, $1 \leq d \leq D$ indicates the d^{th} dimension and D is its total dimension. N_c is the number of elephants in clan ci. $x_{c,j,d}$ is the d^{th} of the elephant individual $x_{c,j}$.

6.6.2 Separating operator

. The step where the male elephant leaves its clan (after reaching the puberty) can be modeled using a separating operator into the optimization problems.[33, 34] Assuming that the worst fitness is the leaving male elephant, the implementation of the separating operator for the current generation is shown in Eq. (13) as:

$$x_{worst,c} = x_{min} + r \cdot (x_{max} - x_{min} + 1) \quad (13)$$

where, x_{max} and x_{min} are respectively the upper and lower bound of the position of individual elephant. $x_{worst,c}$ is the worst position of individual elephant in clan ci. r is random number in the range of [0, 1] which is a kind of stochastic distribution and uniform distribution in the range [0,1].

It is worth mentioning that in the real life each elephant is a decision variable (proposed solution) in the problem domain while, the clan of elephants represents the samples population (recommended solutions).The clan's matriarch represents the clan's best solution in the problem domain also, and the male that departs from the clan (separation operator) represents the clan's worst solution. Finally, the elephant position corresponding to clan's matriarch position is the solution's fitness in the problem domain.

6.7 Results and Discussion

The cells incorporating the compact layer (modified or not), the perovskite absorber and the spiro hole transporter were illuminated using a Solar Light Co. 300W Air Mass Solar Simulator Model 16S-300 (1sun, 1000 W/m^2) and the current-voltage characteristic curves were recorded with an Autolab PG-STAT-30 potentiostat. Table 6.1 summarizes the experimental data (electrical specifications in terms of short circuit -J_{sc}, open circuit potential-V_{oc} and power conversion efficiency-PCE) recorded for the control and modified perovskite solar cells. The analysis of the experimental parameters shows that control cells present low open-circuit voltage and short-circuit photocurrent density compared with the modified ones. Also, the photovoltage and photocurrent values of the modified PSCs are higher than the control type and therefore the PCE was increased by approximately 14% in the case of modified PSCs.

Table 6-1 Experimental data for control and dye- modified perovskite solar cells

Parameter	Control device	Modified device
Open-circuit voltage (V_{oc}) (V)	1.02	1.05
Short-circuit current density (J_{sc}) (mA/cm^2)	20.54	22.53
Voltage at maximum power (V_{mp}) (V)	0.83	0.85
Current at maximum power (I_{mp}) (mA/cm^2)	17.9	19.9
Fill Factor	0.71	0.72
Efficiency (PCE %)	15.04%	17.04
Transfer resistance R_{ct} (ohm)	316	224
Recombination resistance R_{rec} (ohm)	321	573

6.7.1 Simulation results for controlled PSC devices

The mathematical description of EHO can be representatively implemented in two steps (the updating stage and the separation process). These two steps were adapted in order to extract the PSCs parameters and the whole procedure is shown in the flow chart in Figure 6.4. To operate the EHO procedure a pseudo code was developed (shown in Figure 6.5). Moreover, taking into consideration that each generation has fixed number of clans and each clan has fixed number of individual elephants.

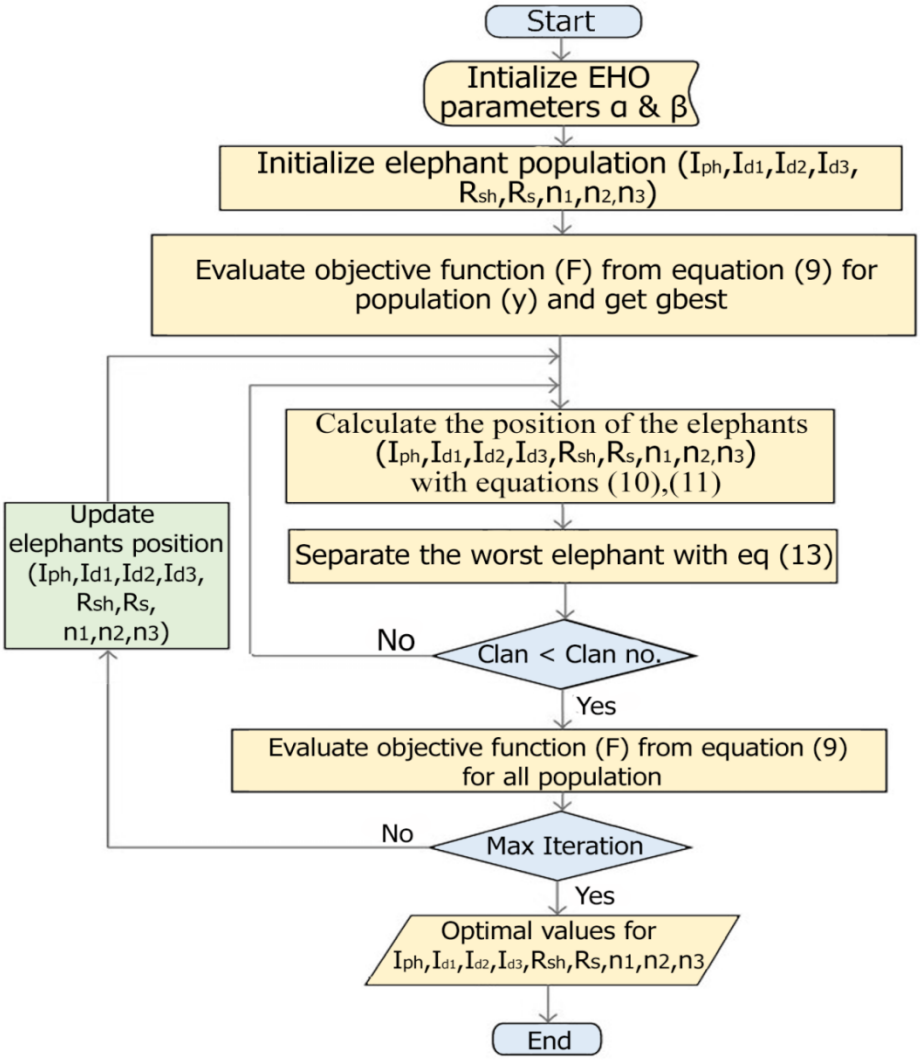

Figure 6.4 Flowchart of EHO for solving the PSCs parameters extraction problems

The experimental J-V curves of control devices and the corresponding estimated ones using the EHO approach for single, double and triple diode models are shown in Figure 6.6(a, b and c) respectively. From these figures it can be seen that the estimated J-V curves by the EHO algorithm are in total agreement with the experimental characteristics.

Initialization:
Initialize (Maximum generation, Population size, Boundaries).
Initialize the population.
Calculate elephant's fitness.
Repeat
Sort all the elephants according to their fitness.
Clan updating:
For c=1 to $nClan$ *(for all clans in elephant population) do*
For j=1 to nci *(for all elephants in clan c) do*
If $\boldsymbol{x_{c,j}}$ *=* $\boldsymbol{x_{best,ci}}$ *then*
Update $\boldsymbol{x_{c,j}}$ *(old elephant) and generate* $\boldsymbol{x_{n,c,j}}$ *(new elephant) by Eq. (11).*
Else
Update $\boldsymbol{x_{c,j}}$ *(old elephant) and generate* $\boldsymbol{x_{n,c,j}}$ *(new elephant) by Eq. (10).*
End if
End for j
End for c
Separating operator:
For c=1 to $nClan$ *(all the clans in elephant population) do*
Replace the worst elephant in clan c by Eq. (13).
End for c
Evaluate population by the newly updated positions.
Until *(Maximum number of generation)*

Figure 6.5 EHO pseudo code

Figure 6.7 (a, b and c) shows the convergence curves of the EHO algorithms (in comparison with the competitive DE,[41] and CSA, [42] ones) for single, double and triple diode models respectively. From this figure, it is clear that the EHO algorithm has the best convergence characteristics compared with the other competitive algorithms. The ranking of the competitive algorithms in terms of convergence is EHO followed by DE then CSA. Numerically, the EHO, DE and CSA reach to the steady state solutions after 35, 65 and 75 iterations, respectively for single diode model and after 43, 65 71 iterations in double diode model and 55, 70 and 75 iterations in triple diode model. Therefore, the EHO algorithm has the best performance compared to the other tools as it converges in the lowest time in the three models and also with the lowest error.

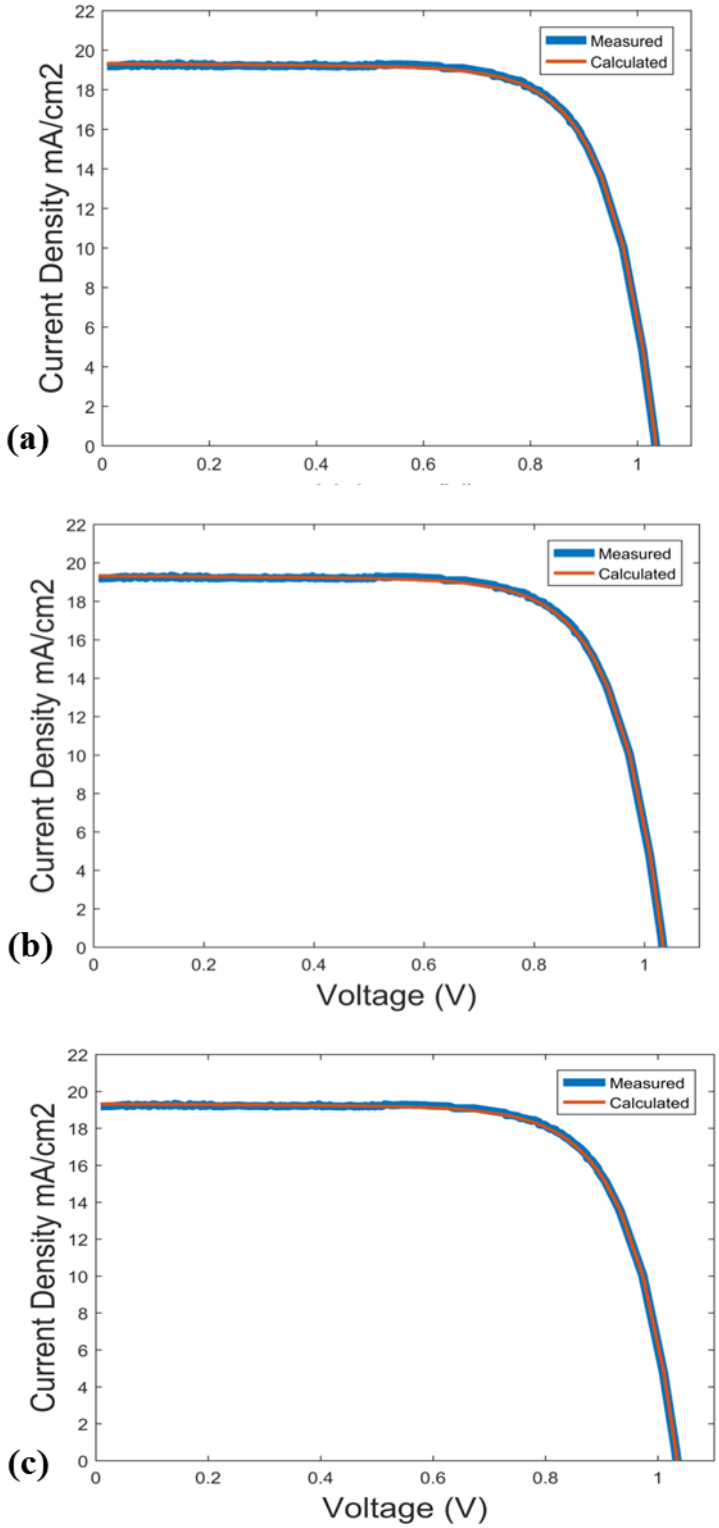

Figure 6.6 J-V curve for control device a) single diode model b) double diode model c) triple diode model

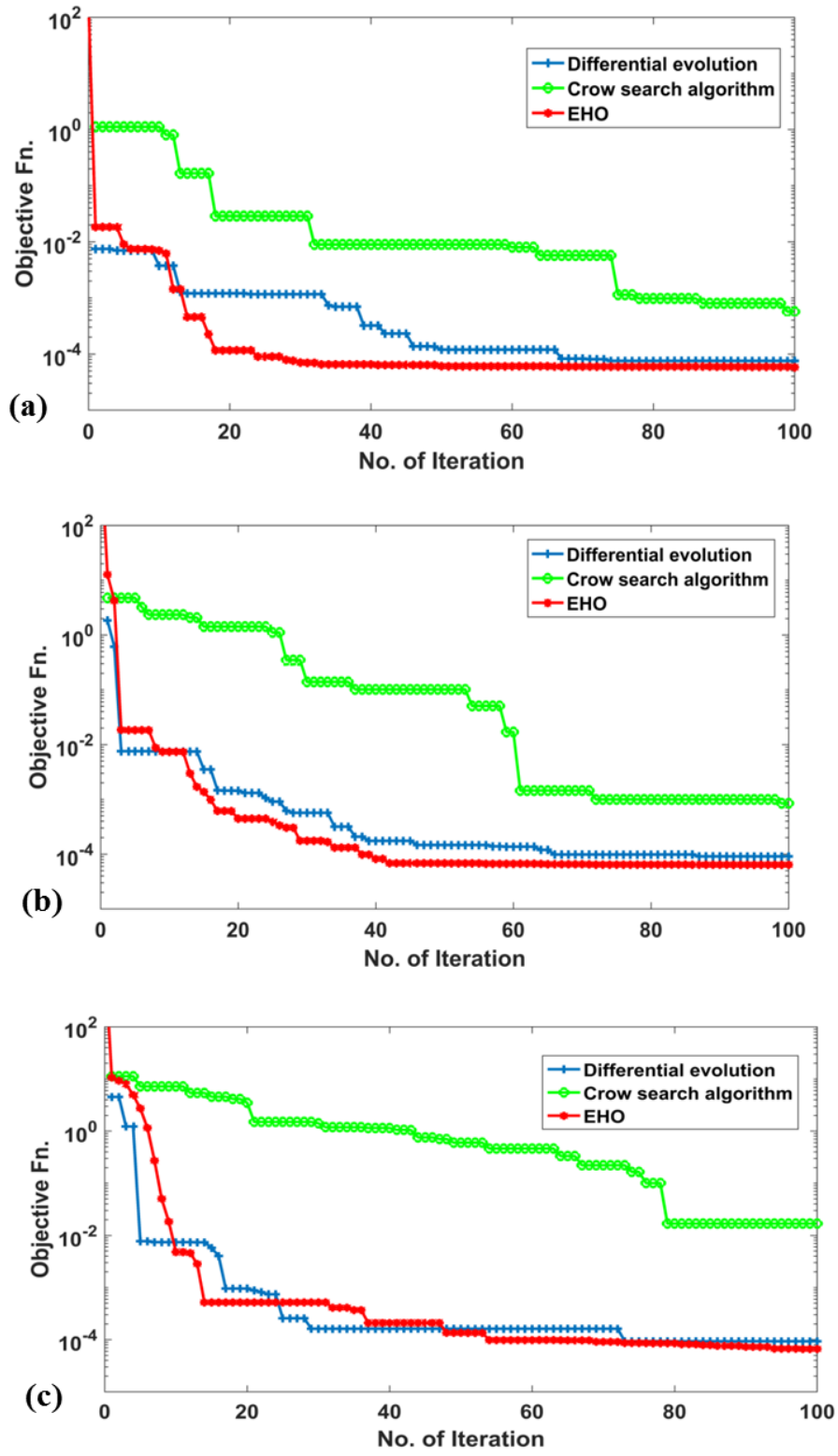

Figure 6.7 Comparison of convergence rates for DE, CSA and EHO for control device a) single diode model b) double diode model c) triple diode model

Table 6-2 PSCs control device Extracted data for SDM using competitive algorithms

Parameters	Lower limit	Upper limit	EHO	DE	CSA
$J_{ph}(mA/cm2)$	18	25	19.327	19.523	19.648
$J_{d1}(mA)$	$1e^{-9}$	0.1	5.8729e-5	1.4353e-4	5.9817e-5
R_s (ohm)	1	100	49.98	20.39	28.04
R_{sh} (ohm)	3000	5000	4995.2	5000	3647.59
m1	2	4	3.1724	3.4021	3.9147
RMSE	-	-	7.0974e-05	7.5495e-05	5.7109e-4

Table 6-3 Extracted data for perovskite solar cells control device for double diode model

Parameters	Lower limit	Upper limit	EHO	DE	CSA
$J_{ph}(mA/cm2)$	18	25	19.327	19.364	18.478
$J_{d1}(mA)$	$1e^{-9}$	0.1	1.4946e-7	1.9273e-7	9.5264e-4
$J_{d2}(mA)$	$1e^{-9}$	0.1	6.0846e-5	6.3858e-5	2.0523e-6
R_s (ohm)	1	100	49.9	20	23.52
R_{sh} (ohm)	3000	5000	5000	3000	3303.63
m1	2	4	3.9964	3.9027	3.8531
m2	2	4	3.1811	3.1991	3.9709
RMSE	-	-	7.1153e-05	9.1671e-05	8.496e-4

Table 6-4 Extracted data for perovskite solar cells control device for triple diode model

Parameters	Lower limit	Upper limit	EHO	DE	CSA
$J_{ph}(mA/cm2)$	18	25	19.336	19.295	19.626
$J_{d1}(mA)$	$1e^{-9}$	0.1	5.9278e-5	1.9273e-5	1.1533e-2
$J_{d2}(mA)$	$1e^{-9}$	0.1	7.3582e-6	1.7764e-4	1.2389e-4
$J_{d3}(mA)$	$1e^{-9}$	0.1	3.1438e-6	1e-9	4.4367e-3
R_s (ohm)	1	100	50	31.47	26.11
R_{sh} (ohm)	3000	5000	4948.5	5000	3444.88
m1	2.0000	4	3.8773	3	3.6547
m2	2	4	4	3.8494	3.9787
m3	2	4	4	4	3.9322
RMSE	-	-	7.2797e-05	9.3494e-05	0.016888

Tables 6.2, 6.3 and Table 6.4 show the extracted data of PSCs control device for single, double and triple diode models using the EHO algorithm. The corresponding data using the competitive DE and CSA algorithms are also included. From these tables it is obvious that in single diode model the EHO algorithm is the closest to the experimental data and its objective function ($7.0974e^{-05}$) is the best among all the examined algorithms (to be compared with $7.5495e^{-05}$ for DE and $5.7109e^{-4}$ for CSA). This is also the case in double diode model ($7.1153e^{-05}$ against $9.1671e^{-05}$ for DE and $8.496e^{-4}$ for CSA) and in triple diode model ($7.2797e^{-05}$ against $9.3494e^{-05}$ for DE and 0.016888 for CSA), respectively, confirming the high advantages of the EHO simulation.

6.7.2 Simulation results for modified device

The experimental and estimated J-V curves of modified devices are shown in Figure 6.8 (a, b and c) which also show a total agreement between the experimental and estimated data by EHO algorithm like the control device case.

Figure 6.9 (a, b and c) shows the convergence curves of the competitive algorithms EHO, DE and CSA for single, double and triple diode models respectively. As observed in the case of control devices, the EHO algorithm has the best performance compared to the other tools, reaching the final solution after 38 iterations in single diode model , 45 iterations in double diode model and 35 iterations in triple diode model. The EHO is followed by the DE with 50 iterations in single diode model, 48 iterations in double diode model and 60 iterations in triple diode model then the CSA with 80 iterations in single diode model, 90 iterations in both double and triple diode models.

Tables 6.5, 6.6 and Table 6.7 show data of the dye-modified PSCs devices extracted for single-, double- and triple-diode models using the EHO, DE and CSA algorithms, respectively. As in the case of the control devices, the EHO approach still has the lowest error among all the used algorithms. In fact, in single diode mode its objective function ($4.6662e^{-05}$) has the lowest value, in comparison with $4.7438e^{-05}$ for DE and $1.1242e^{-04}$ for CSA. The simulation quality for the EHO algorithm is also higher in the cases of double diode model (objective function value of $4.6692e^{-05}$ against $4.7456e^{-05}$ for DE and $1.7712e^{-4}$ for CSA) and triple diode model (objective function value of $4.6753e^{-05}$ against $4.8081e^{-05}$ for DE and $7.8303e^{-3}$ for CSA).

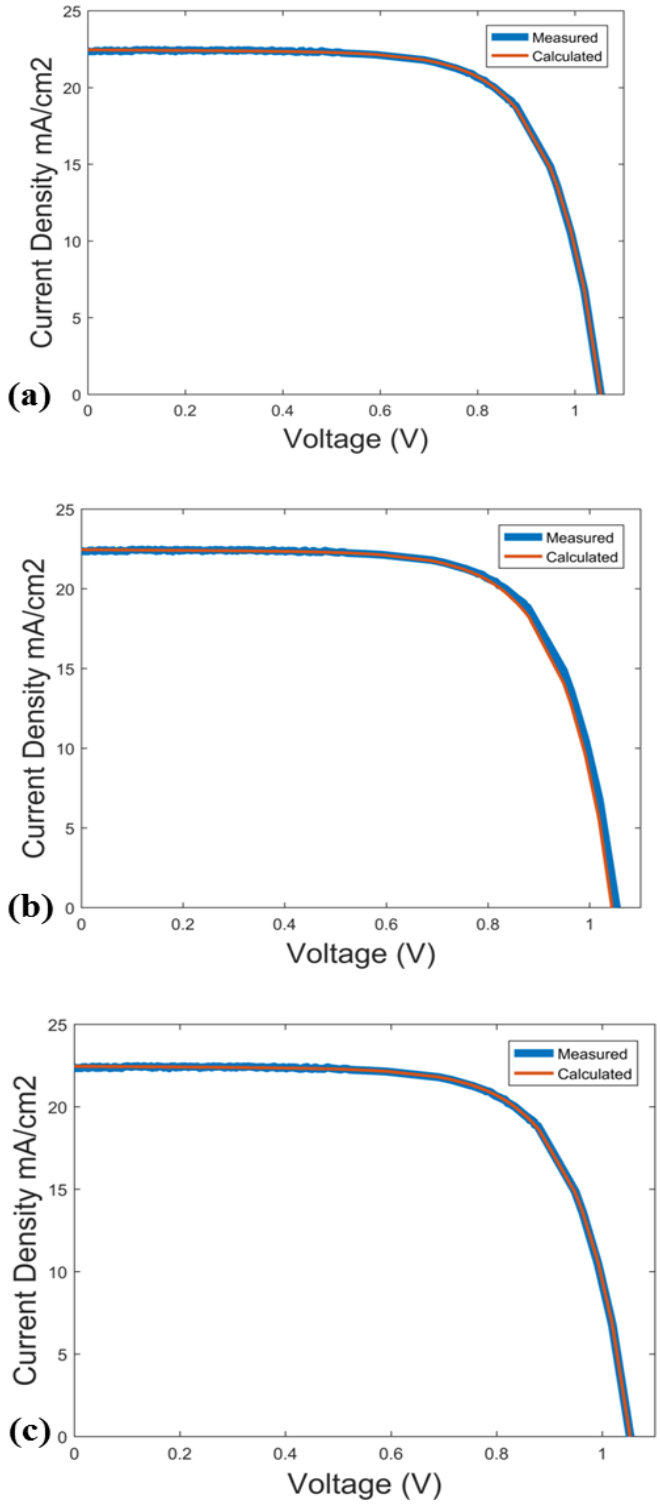

Figure 6.8 J-V curves for modified device a) single diode model b) double diode model c) triple diode

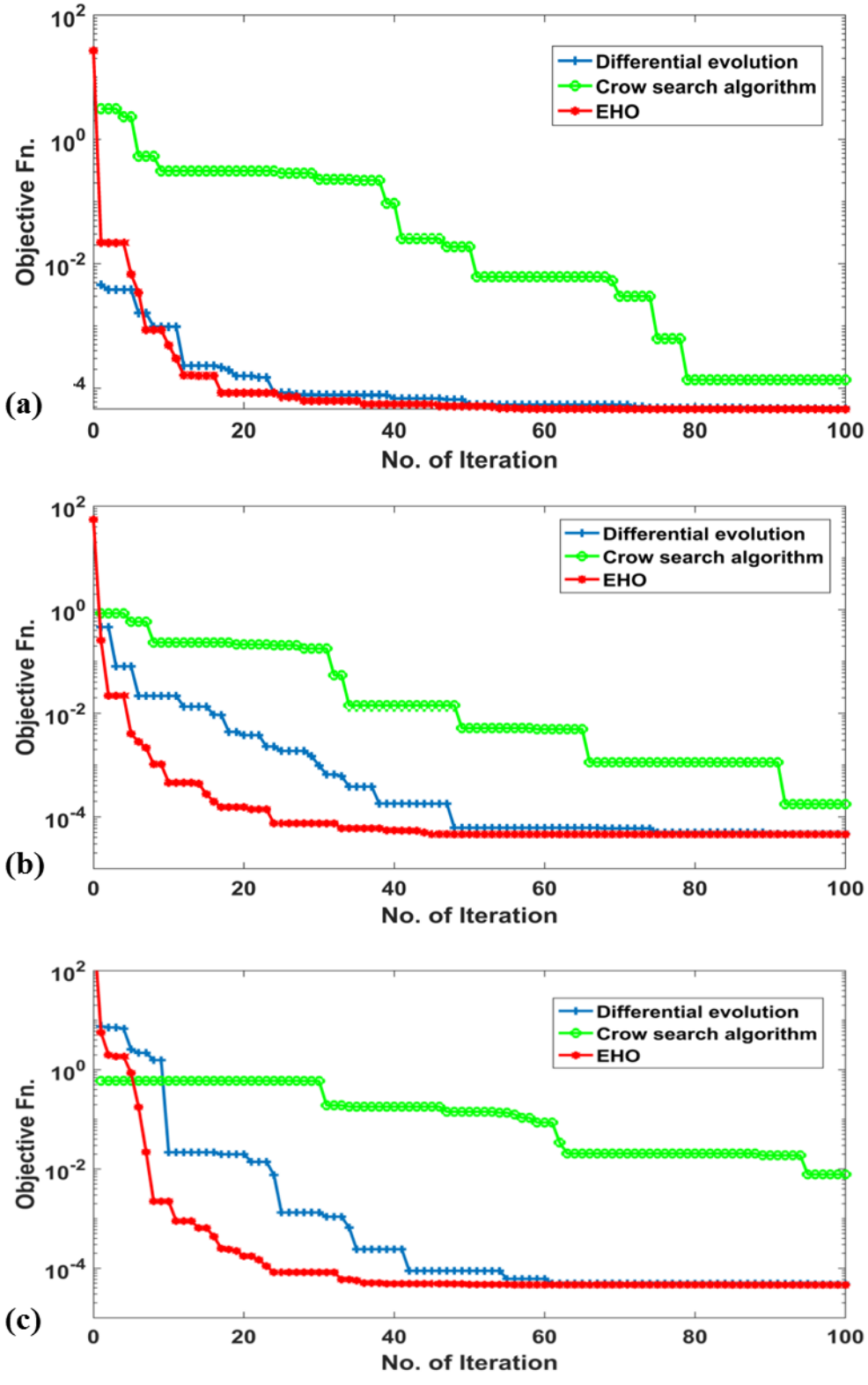

Figure 6.9 Comparison of convergence rates for DE, CSA and EHO for modified device a) single diode model b) double diode model c) triple diode model

Table 6-5 Extracted data for perovskite solar cells modified device for single diode model

Parameters	Lower limit	Upper limit	EHO	DE	CSA
$J_{ph}(mA/cm2)$	18	25	22.46	21.493	22.56
$J_{d1}(mA)$	$1e^{-9}$	0.1	3.9378e-6	1e-9	5.8114e-4
R_s (ohm)	1	100	49.8	20	29.07
R_{sh} (ohm)	3000	5000	5000	3000	4190.7
m1	2	4	3.7515	2	3.8871
RMSE	-	-	4.6662e-05	4.7438e-05	1.1242e-04

Table 6-6 Extracted data for perovskite solar cells modified device for double diode model

Parameters	Lower limit	Upper limit	EHO	DE	CSA
$J_{ph}(mA/cm2)$	18	25	22.463	22.453	22.033
$J_{d1}(mA)$	$1e^{-9}$	0.1	1e-6	1e-9	1.0393e-3
$J_{d2}(mA)$	$1e^{-9}$	0.1	3.6069e-6	3.5005e-4	2.5259e-5
R_s (ohm)	1	100	49.77	50	21.18
R_{sh} (ohm)	3000	5000	5000	3908.97	4379.24
m1	2	4	3.968	3.6318	3.9181
m2	2	4	3.73797	3.7143	3.4069
RMSE	-	-	4.6692e-05	4.7456e-05	1.7712e-4

Table 6-7 Extracted data with EHO algorithm for perovskite solar cells modified device for triple diode model

Parameters	Lower limit	Upper limit	EHO	DE	CSA
J_{ph}(mA /cm2)	18	25	22.463	22.48	21.341
J_{d1}(mA)	$1e^{-9}$	0.1	3.0162e-6	1e-9	1.7256e-3
J_{d2}(mA)	$1e^{-9}$	0.1	1.0556e -6	4.4955e-4	6.9518e-3
J_{d3}(mA)	$1e^{-9}$	0.1	2.9026e-8	1e-9	4.7337
R_s (ohm)	1	100	48.66	22.44	32.48
R_{sh} (ohm)	3000	5000	5000	4685.19	4607.85
m1	2	4	3.7109	2.9427	3.7405
m2	2	4	3.9975	3.7987	3.9721
m3	2	4	3.9378	3.7592	3.5693
RMSE	-	-	4.6753e-05	4.8081e-05	7.8303e-3

6.7.3 Performance evaluation of EHO and experimental verification

A comparison between the EHO, CSA and DE has been made. The comparison takes place under the same setting for the three algorithms. The population size is set to be 100 populations for all algorithms. The maximum number of generation is chosen to be 100. The search ranges are set to be as follow: Jsc $\in [18-25]$, mA/cm^2, $I_d \in [1e-9, 1e-1]$ mA,

$R_s \in [1-100]$ ohm, $R_{sh} \in [3000-5000]$ ohm, $m \in [2-4]$. The optimization process and the simulation results are executed using MATLAB software.

In the light of this comparison, optimal parameters of the proposed method are compared with optimal parameters that attained by CSA and DE as shown in Tables 6.2, 6.3, 6.4, 6.5 and Tables 6.6, 6.7. From these results, it can be realized that the optimal parameters of PSCs obtained by EHO is very close to the experimental ones. From the results tables in both control and modified devices it is obvious that the best model is the triple diode model.

Table 6.8 shows a comparison of estimated parameters values using EHO and triple diode model with their values from experimental data where the open-circuit voltage (V_{oc}), short-circuit current density (J_{sc}), fill factor and the efficiency (PCE %) extracted values were very close to the experimental ones with very low deviations, for instance in the case of control device the short-circuit current density (J_{sc}) determined by experimentally was 20.54 while the estimated value by EHO was 19.33 with a deviation of 0.05, the open-circuit voltage (V_{oc}) was the same by both experimentally and estimated method without any deviations while, the fill factor has only 0.007 deviation and the efficiency (PCE %) has 0.07 deviation. In other hand the modified device case has short-circuit current density (J_{sc}) deviation of 0.003, the open-circuit voltage (V_{oc}) and the fill factor were almost the same by both experimentally and estimated method with a small deviation of 0.009 and 0.006 respectively while, the efficiency (PCE %) has 0.01 deviation as it changed from 17.04 obtained experimentally to 16.86 obtained by the EHO algorithm.

For further verification, statistical analysis for EHO results has been done in terms of error and standard deviation and compared with other approaches which are CSA and DE as shown in Table 6.9. The comparison demonstrated that for the control device of PSCs, the EHO has error with 0.002 and standard deviation with 0.001 in SDM, the DE has error with 0.013 and standard deviation with 0.008 and the CSA has error with 0.033 and standard deviation with

0.023. In the DDM the EHO has error with 0.002 and standard deviation with 0.001, the DE has error with 0.003 and standard deviation with 0.002 and the CSA has error with 0.04 and standard deviation with 0.028. In the TDM the EHO has error with 0.002 and standard deviation with 0.002, the DE has error with 0.003 and standard deviation with 0.004 and the CSA has error with 0.014 and standard deviation with 0.01.Similarly for the modified PSCs device, in case of SDM the EHO has the lowest error and standard deviation, 0.002 and 0.001, respectively compared with DE (0.046, 0.627) and CSA (0.329 and 0.233).

Table 6-8 Comparison of estimated parameters values using EHO and triple diode model with their values from experimental data

Device	Control Device			Modified Device		
Parameters	Experimental	EHO	Deviation	Experimental	EHO	Deviation
$J_{sc}(mA/cm2)$	20.54	19.33	0.05	22.53	22.46	0.003
Voc(volt)	1.02	1.02	0.0	1.05	1.04	0.009
FF	0.71	0.705	0.007	0.72	0.725	0.006
PCE%	15.04	13.97	0.07	17.04	16.86	0.01

Table 6-9 Statistical analysis of error and standard deviation values obtained by EHO with their values obtained from CSA and DE

		Model type								
		SDM			DDM			TDM		
Optimization Algorithm		DE	CSA	EHO	DE	CSA	EHO	DE	CSA	EHO
Control device	Error	0.013	0.033	0.002	0.003	0.040	0.002	0.003	0.014	0.002
	St-dev	0.008	0.023	0.001	0.002	0.028	0.001	0.004	0.010	0.002
Modified device	Error	0.046	0.329	0.002	0.001	0.019	0.001	0.002	0.055	0.001
	St-dev	0.627	0.233	0.001	0.0014	0.013	0.001	0.002	0.038	0.001

For DDM EHO has error with 0.001 and standard deviation with 0.001, the DE has error with 0.001 and standard deviation with 0.0014 and the CSA has error with 0.019 and standard deviation with 0.013. Finally for TDM EHO has error with 0.001 and standard deviation with 0.001, the DE has error with 0.002 and standard deviation with 0.002 and the CSA has error with 0.055 and standard deviation with 0.038. From both control and modified devices case it is noticed that EHO has the lowest values of error and standard deviations in comparison with other competitive algorithms. Therefore, the superiority of EHO algorithm in extracting the parameters is proven.

Tables 6.4 and 6.7 summarize the electrical parameters extracted using the most accurate model (TDM). It is worth noticing that in this model, the series resistance value of the control

devices (50 ohm) is quite higher than that of the modified ones (48.6 ohm). This is probably due to the sensitization of the titania compact layer with D35 organic dye, facilitating the electron transport from the perovskite absorber to titania compact layer. Moreover, we observed that the shunt resistance in the modified devices (5000 ohm) is quite higher than the control devices (4948.5 ohm). This probably originates from lower leakage current that hence leads to higher net current and better efficiency. In addition, the modified devices present lower diode ideality factor values (than the control ones), clearly indicating a better PN junction quality.[43] The junction quality improvement is a result of the dye presence, which passivates the titania layer and increases the surface hydrophobicity of the titania compact layer, thus permitting the development of a more homogeneous perovskite layer able to crystalize under controlled conditions (humidity absence).

Furthemore, the above results are also reflected on the diode behavior and especially the diode saturation current (j_d), which is a characteristic factor corresponding to the excitation rate of electrons from the valence to the conduction band. This parameter is directly related to the recombination rate, which affects the open circuit voltage.[44] The simulation results in Tables 6.2 and 6.3 show that in the modified devices, the saturation diode currents values (j_{d1} = 3.0162e^{-6} mA, j_{d2} = 1.0556e $^{-6}$ mA and j_{d3} = 2.9026e^{-8} mA respectively) are significantly lower than the corresponding values in the control devices (j_{d1} = 5.9278e^{-5} mA, j_{d2} = 7.3582e^{-6} mA and j_{d3} = 3.1438e^{-6} mA). Therefore, the recombination rate in modified devices is lower than the recombination rate in control devices, which was also proved by the experimental data. In fact, the analysis performed by electrochemical impedance spectroscopy confirmed that the recombination resistance (R_{rec}) in modified devices (573 ohm) is higher than the R_{rec} in control devices (321 ohm) and the charge transfer resistance (R_{ct}) in the modified devices (224 ohm) is lower than the R_{ct} in the case of control devices (316 ohm). Lower j_d values mean not only lower recombination rates but also higher open circuit voltage (V_{oc}) values.

Indeed, the open circuit voltage in modified devices (1.05V) was fond slightly higher than the V_{oc} value in control devices (1.02V).

6.8 Summary

In this chapter, three electrical models of PSCs called single, double and triple diode models has been proposed for two PSCs devices. Estimation and extracting the PSC models parameters are carried out using the elephant herd optimization algorithm. To prove the capability of the proposed estimation procedure, a comparison study between the proposed EHO with crow search optimization and differential evolution algorithms has been employed. The simulation results have proved the EHO superiority compared with the competitive algorithms. In the view point of experimental verification, the simulation results assure the high closeness between the estimated parameters with experimental ones. It can be concluded that the proposed three diode model is the best one for modeling both modified and controlled devices. The modified devices present lower series resistance, higher shunt resistance, lower diode ideality factor, lower diode saturation current, and higher open circuit voltage values. This is due to the presence of the dye that permits the easier crystallization of the perovskite absorber and facilitates the electron transfer from the perovskite layer to titania compact layer and its effective collection on the fluorine-doped transparent oxide (FTO) conductive glass substrate. As a result, the EHO algorithm has been proved a very effective optimization paradigm to simulate the behavior of dye engineered perovskite solar cells. This work paves the way towards fabricating high stable PSCs with high power energy conversion as well, through titania layer passivation or doping and new perovskite materials to be used as a god absorber. Also new efficient optimization tools can be used in solving the parameter estimation problem like Cuckoo Search, Sunflower Optimization algorithm, Krill Herd Algorithm, Sine Cosine Algorithm, Hurricane Optimization Algorithm, and Multi-Verse Optimizer.

References

[1] D. Oliva, M. A. Elaziz, A. H. Elsheikh, and A. A. Ewees, J. Pow. Sources, 435, 126683 (2019).

[2] K. Yonghong, Z. Yongjun, Z. Bin, C. Yijia, L. Lijuan, and Z. Long, Rene. Sust. Ener. Reviews, 59, 504 (2016).

[3] R. Jordehi, Rene. Sust. Ener. Reviews, 61, 354 (2016).

[4] N. Balis, A A. Zaky, D. Perganti, A. Kaltzoglou, L. Sygellou, F. Katsaros, T. Stergiopoulos, A.G. Kontos, and P. Falaras, ACS Appl. Energy Mater., 1, 6161 (2018).

[5] National Renewable Energy Laboratory (NREL), https://www.nrel.gov/pv/cell efficiency.html (accessed September 2019).

[6] H. S. Kim, C. R. Lee, J. H. Im, K. B. Lee, T. Moehl, A. Marchioro, S. J. Moon , R. Humphry-Baker , J. H. Yum , J. E. Moser , M. Grätzel, and N. G. Park , Sci. Rep., 2, 591 (2012).

[7] J. Burschka, N. Pellet, S. J. Moon, R. Humphry-Baker, P. Gao, M. K. Nazeeruddin, and M. Gratzel, Nature, 499, 316 (2013).

[8] F. Khan, S. N. Singh, and M. Husain, Semicond. Sci. Tech., 25, 015002 (2010).

[9] S. S. Hegedus, and W. N. Shafarman, Prog. Photovoltaics, 12, 155 (2004).

[10] J. Kim, J. H. Yun, H. Kim, Y. Cho, H. H. Park, M. M. D. Kumar, J. Yi, W. A. Anderson, and D. W. Kim, , Sci. Rep., 5, 9256 (2015).

[11] L. Meng, J. B. You, T. F. Guo, and Y. Yang, Accounts Chem. Res., 49, 155 (2016).

[12] H. G. Beyer, and B. Sendhoff, Comp. Meth. Appl. Mech. Eng., 196, 3190 (2007).

[13] J. Cui, P. F. Li, Z. F. Chen, K. Cao, D. Li, J. Han, Y. Shen, M. Peng, Y. Q. Fu, and M. Wang, Appl. Phys. Lett., 109, 171103 (2016).

[14] M. R. Alrashidi, M. F. AlHajri, K. M. El-Naggar, and A. K. Al-Othman, Sol. Energy, 85, 1543 (2011).

[15] Askarzadeh, and A. Rezazadeh, Sol. Energy, 86, 3241 (2012).

[16] T. R. Ayodele, A.S. O. Ogunjuyigbe, and E. E. Ekoh, Sust. Ener. Tech. Assessments, 13, 51 (2016).

[17] Boussaïd, J. Lepagnot, and P. Siarry, Info. Sciences, 237, 82 (2013).

[18] Y. Jin, and J. Branke, IEEE. Trans. Evol. Computation, 9, 303(2005).

[19] El-Fergany, Electr. Power Compon. Syst., 43, 890 (2015).

[20] O. Abdalla, H. Rezk, and E. M. Ahmed, Sol. Energy, 180, 429 (2019).

[21] L. Wang, and C. Huang, Optik, 155, 351 (2018).

[22] S.A. El-Sattar, S. Kamel, R .A. El Sehiemy, F. Jurado, and J. Yu, Neural. Comput & Applic., 31, 8787 (2019).

[23] Askarzadeh, and L. dos Santos Coelho, Energy Convers. Manage. 89, 608 (2015).

[24] M. Louzazni, A. Craciunescu, E. H. Aroudam, and A. Dumitrache, In Proceedings of the 2015 Second International Conference on Mathematics and Computers in Sciences and in Industry (MCSI), Sliema, Malta, P. 7–12, 2015.

[25] Fathy, and H. Rezk, Renew. Energy, 111, 307 (2017).

[26] J. Ma, T. O. Ting, K. L. Man, N. Zhang, S. U. Guan, and P. W. H. Wong, J. Appl. Math., 2013, 362619 (2013).

[27] M. H. Qais, H. M. Hasanien, and S. Alghuwainem, Appl. Energy, 250, 109 (2019).

[28] Khelifi, B. Bentouati, S. Chettih, and R. A. El-Sehiemy, J. Elec. Systems, 15, 375 (2019).

[29] F. Attia, R. A. El Sehiemy, and H. M. Hasanien, Int. Jou. Elect. Pow. Ene. Systems, 99, 331 (2018).

[30] R. M. Rizk-Allah, R. A. El-Sehiemy, and G.G. Wang, Appl. So. Comput., 63, 206 (2018).

[31] M. Shaheen and R. A. El-Sehiemy, "Application of multi-verse optimizer for transmission network expansion planning in power systems," in Proceedings of the 2019 International Conference on Innovative Trends in Computer Engineering (ITCE), Aswan, Egypt, p. 371-376, 2019.

[32] G. G. Wang, S. Deb, X. Z. Gao, and L. Coelho, Int. J. Bio-Inspired Computation, 8,394 2016).

[33] M. A. Elhosseini, R. A. El Sehiemy, Y. I. Rashwan, and X. Z. Gao, Knowl. B. Systems, 166, 58(2019).

[34] H. Xu, Q. Cao, C. Fang, Y. Fu, J. Su, S. Wei, and P. Bykovyy, in Proceedings of the 2018 IEEE 4th International Symposium on Wireless Systems within the International Conferences on Intelligent Data Acquisition and Advanced Computing Systems, IDAACS-SWS 2018,p.16-20, IEEE 2018.

[35] S. Gupta, V. P. Singh, S. P. Singh, T. Prakash, and N. S. Rathore, Inter. J. Adv. Tech. and Eng. Exploration, 3, 2394(2016).

[36] N. K. Meena, S. Parshar, A. Swarnkar, N. Gupta, and K. R. Niazi, IEEE. Trans. Ind. Informatics, 14, 1029 (2017).

[37] S. Parashar, A. Swarankr, K.R. Niazi, and N. Gupta, J. Engineering, 2017, 1996 (2017).

[38] G. J. A. H. Wetzelaer, M. Scheepers, A. M. Sempere, C. Momblona, J. Avila, and H. J. Bolink, Adv. Mater, 27, 1837 (2015).

[39] P. Liao, X. Zhao, G. Li, Y. Shen, and M. Wang1, Nano-Micro Lett. 10, (2018).

[40] D. Allam, D. A. Yousri, and M. B. Eteiba, Energy Convers. Manage, 123,535 (2016).

[41] M. Shaheen, S. M. Farrag, and R. A. El-Sehiemy. IET. Gen. Trans. Distrib., 11, 570 (2017).

[42] A. Abou ElEla, R. A. El-Sehiemy, A. M. Shaheen, and A. S. Shalaby, in Proceedings of the 19th IEEE International Middle-East Power Systems Conference, Cairo, Egypt, IEEE 2017.

[43] J. Kim, J. H. Yun, H. Kim, Y. Cho, H. H. Park, M. M. D. Kumar, J. Yi, W. A. Anderson and D. W. Kim, , Sci. Rep., 5, 9256 (2015).

[44] J. B. You, Y. M. Yang, Z. R. Hong, T. B. Song and L. Meng, Appl. Phys. Lett., 105, 183902 (2014).

7 Chapter 7

7 Energy Efficiency Improvement of Water Pumping System Operated with Synchronous Reluctance Motor Using Perovskite Solar Cells

7.1 Preface

Perovskite solar cells (PSCs) have high power conversion efficiency (PCE) and are fabricated via low cost solution processed techniques, enabling them to gain high attention among other emerging photovoltaic (PV) technologies [1, 2]. This is resulting from the perovkites' outstanding optoelectronic properties such as tunable band gaps, [3] long diffusion lengths [4] and high absorbance coefficients in [5]. Therefore, in 2019 the PSCs efficiency reaches up to 25% in comparison with an almost 3% in 2009 [6]. Based on this high efficiency, a lot of research work is published every year towards enhancing their operation in both terms of efficiency and stability. [7-22]

Generally, third generation photovoltaics (PVs) are among the most promising types of renewable energy due to rapid efficiency increase and production cost reduction. These systems dispose almost zero running cost and can be considered as an environmental friendly clean energy source, able to be connected to grid or work as a standalone (off grid) structure. Recently, standalone PVs are receiving a great interest in rural regions where the main grid is absent or far and the grid connection is expensive. Their application can be extended to drive water pumping for irrigation, especially in the desert or in remote areas [23].

PV pumping system efficiency increment and total cost reduction are under investigation in many research groups [24-33]. DC motors were used in these systems due to their ability of direct connection to the PV electric power source or via DC-DC converter; however they

present significant problems such as continuous maintenance of brushes and commutators, low efficiency and high cost. To overcome these issues, pumping systems based on brushless DC Motors (BDCMs) [29, 33, and 34], induction motors (IMs) [28], permanent-magnet synchronous Motors (PMSMs) [32] and switched reluctance motors (SRMs) [31] has been investigated and presented in the literature. PV pumping systems based on BDCMs and PMSMs present several advantages such as high efficiency and power density, nevertheless the price of such motors remains high and depends on weather conditions. Besides, additional problems are raised including demagnetization and instability. In contrast, IMs have a low cost but their efficiency is not the optimum one, especially under partial loading conditions. [35]

On the contrary, synchronous reluctance motors (SynRMs) have several advantages compared to the other types of electric machines such as rugged construction, low cost and efficiency much higher than IMs [36]. PV pumping systems using SynRMs were discussed in a few studies [34], [37] and [38] however; all these publications use the conventional PV array modules of low efficiency and large area.

In this chapter, the design of a direct-coupled perovskite solar array feeding a SynRM for pumping applications is introduced. Besides investigation of the whole the system performance is presented. The perovskite solar cells are manufactured in the lab and their characteristics are measured. Then, SynRM geometry is optimized for obtaining the maximum output power at minimum torque ripple. Further, the perovskite solar array is designed to produce the maximum output power that corresponds to the maximum power per Ampère of the SynRM under standard irradiation and temperature conditions (1sun AM 1.5, 25 ^{o}C) through the proposed control method for the conventional inverter.

7.2 The proposed PV pumping system

Structure of the proposed PSCs -based pumping system

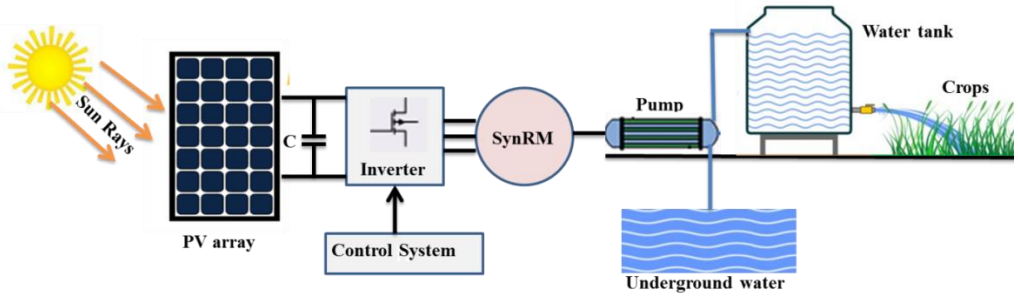

Figure 7.1 Schematic diagram of the proposed PV pumping system.

Figure 7.1 displays a schematic diagram of the proposed PV pumping system which consists of the following components: a perovskite solar array ; a conventional voltage source inverter (VSI) with control system ; a three phase synchronous reluctance motor (SynRM) ; and a centrifugal pump. It is obvious that the proposed system has operates without using DC-DC converters and storage batteries.

Table 7-1 Operational parameters of the proposed PV pumping system

Required amount of water	350 m3/day
Average number of the motor working hours	10 hours
Pump average flow rate	35 m^3/h
Height difference of the water	35m

The problem of water pumping for both irrigation system and human consumption, in a place situated far from the main electric grid or in case that there is no electric grid at all, can be solved by the proposed PV pumping system. In fact, the amount of needed water depends

on the population, the kind of plant and the corresponding area. Table 7.1 lists the required parameters to select the size of each component in the proposed system including the pump's average output power which is determined based on both the water flow rate and the height difference.

7.3 Modelling of the proposed PSCs based pumping system

7.3.1 PV array model

A PV array consist of several series and parallel connected PV modules was used in the proposed system each module has 36 series cells. The single diode model shown in Figure 7.2 used for representing the solar cell.

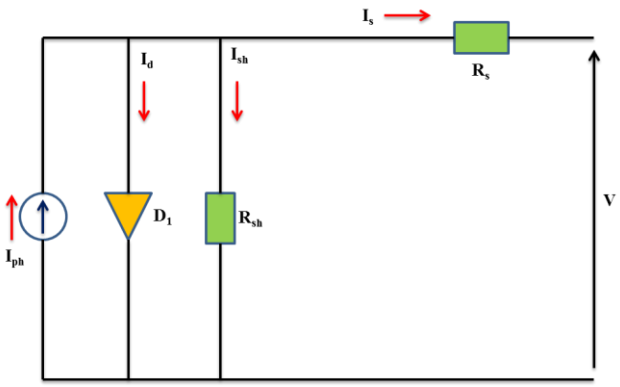

Figure 7.2 Single diode solar cell equivalent circuit.

The solar cell output current can be represented as fellows [39], [40]:

$$I_{PV} = I_{ph} - I_o\left[\exp\left(\frac{V_{PV}+R_s I_{PV}}{V_t a}\right)-1\right]-\frac{V_{PV}+R_s I_{PV}}{R_{sh}} \quad (1)$$

where I_{pv} and V_{pv} are the current and voltage of the solar module; I_o and I_{ph} are the saturation and photocurrents; V_t is the thermal voltage; a is the diode ideality factor; R_s and R_{sh} are the series and parallel resistances.

The schematic diagram of the perovskite solar cell (PSC) shown in Figure 7.3-a. The PSC layers were fabricated as follows:

TiO_2 compact layer (electron transport layer) The FTO conductive glasses (Aldrich, 7 Ohm·□-1) was cleaned with Hellmanex, 2-propanol and acetone in a sonication path after etching by a 2m HCl/H_2O solution in combination with Zn powder. The FTO conductive glasses treated with UV ozone for 15 min. The titania compact layer was deposited over the cleaned FTO conductive glasses by spin coating at 2000 r.p.m. for 60 s from an ethanolic solution of titanium (IV) isopropoxide (Aldrich, 97%) containing a small quantity of HCl. After the spin coating the films were exposed to 500°C (5°C·min^{-1} temperature ramp rate) in the oven for 45 min.

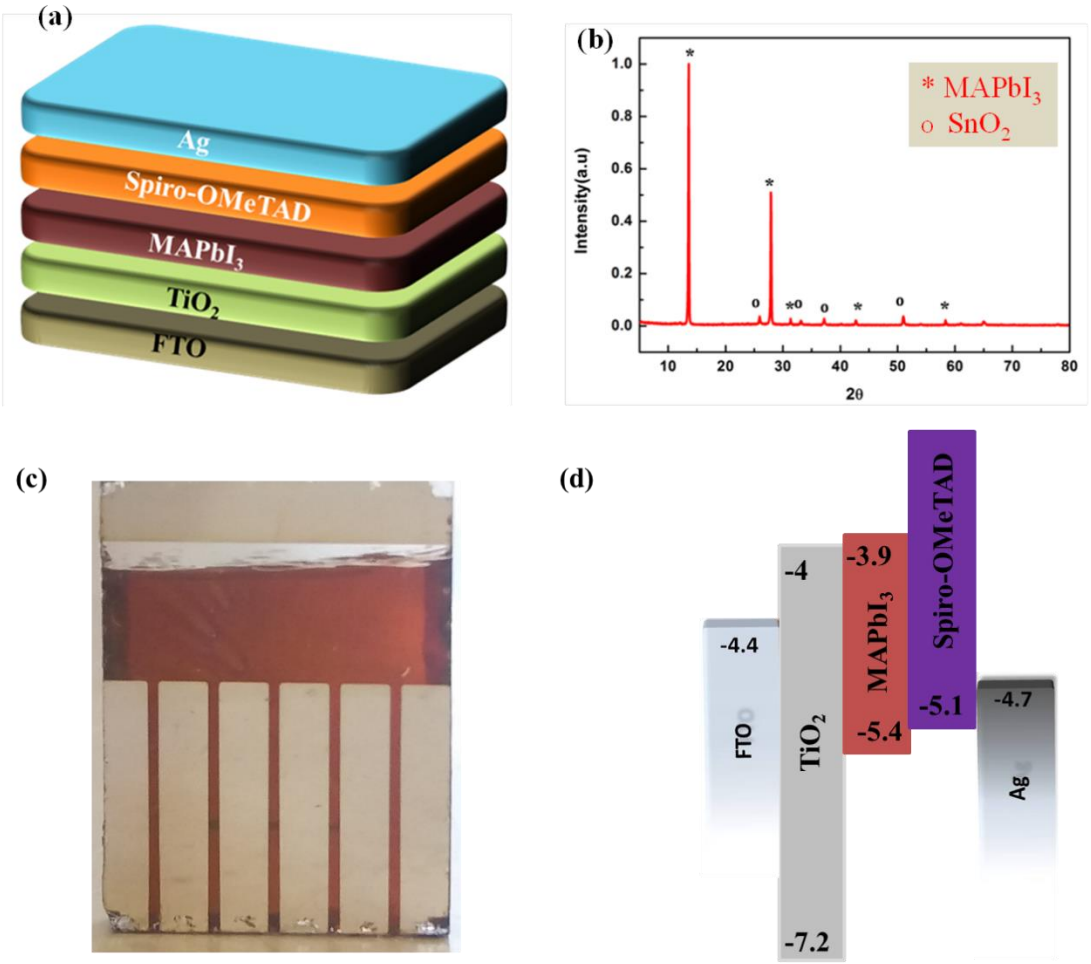

Figure 7.3 Schematic representation of the perovskite solar cell architecture (a); XRD patterns of $MAPbI_3$ perovskite films deposited on FTO glass substrates (b); The cells (a batch

of six similar cells) overview (c); The energy band diagram of the fabricated PSC devices (d).

Perovskite layer (absorber) After forming the titania compact layer the perovskite absorber layer ($MAPbI_3$) layer was deposited by spin coating at 2000 r.p.m. for 45 s in the glovebox using a perovskite solution containing a 40 wt% Methylammonium iodide (Dyesol) along with Lead acetate trihydrate ($PbAc_2.3H_2O$, 99.999% trace metals basis, Aldrich) in a 3:1molar ratio dissolved in anhydrous DMF. Finally a small amount of hypophosphorous acid (50% w/w, aquatic solution, Alfa Aesar) was also added to the solution and the final molar ratio of HPA:$PbAc_2$ to be 1:4. The films were annealed at 100^{o}C for 5 min after drying at room temperature for 10 min. The shape and size distribution of ($MAPbI_3$) grains grown upon TiO_2 substrate of this layer is shown in Figure 7.4.[17]

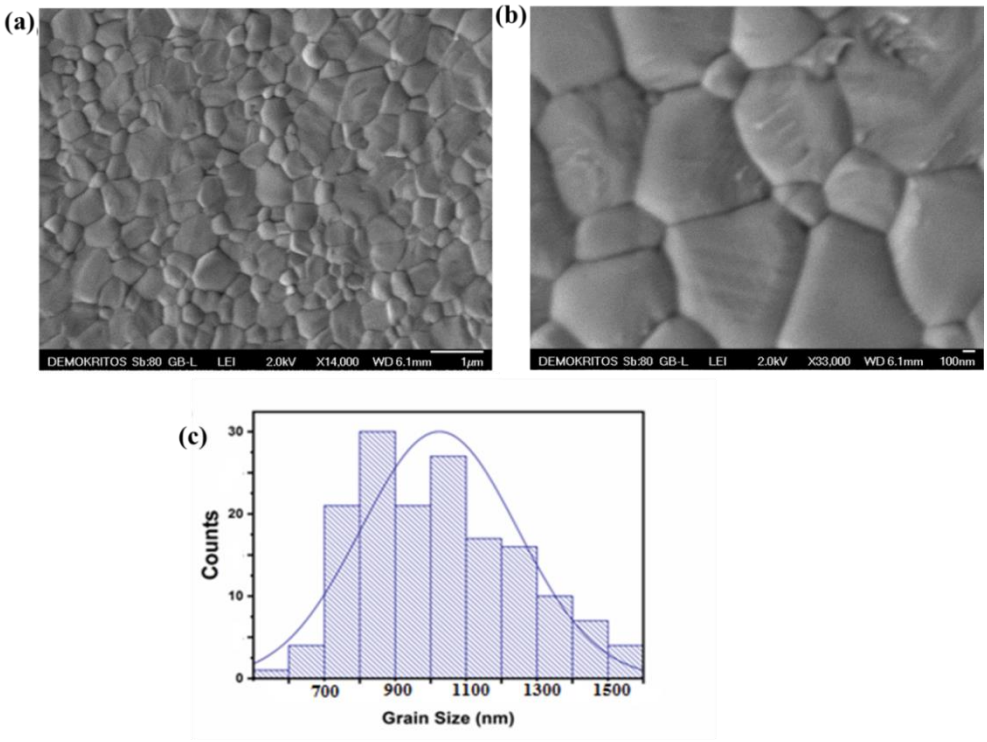

Figure 7.4 SEM images of a $MAPbI_3$ perovskite layer at different magnifications (a) and (b); Size distribution of $MAPbI_3$ grains grown upon TiO_2 substrate (c).

Spiro-MeOTAD layer (hole transporting layer): After the perovskite absorber, a hole transporting layer of Spiro-MeOTAD was deposited (by spin coating at 3000 r.p.m for 30s)

from chlorobenzene (7wt%), containing additives of bis(trifluoromethanesulfonyl)imide lithium salt (dissolved in acetonitrile) and 4-tert-butylpyridine.

Silver electrodes layer: Finally, 100 nm silver electrodes were deposited outside the glovebox, using a thermal evaporator (10^{-6} Torr and ~1Å·s^{-1} rate).

The perovskite layer formation quality and absorption characteristics were examined by X-Ray Diffraction, Scanning Electron Microscopy and a UV-Vis as shown in Figures 7.3-b, 7.4 a-b and 7.5 a where the perovskite was formed in a good manner.

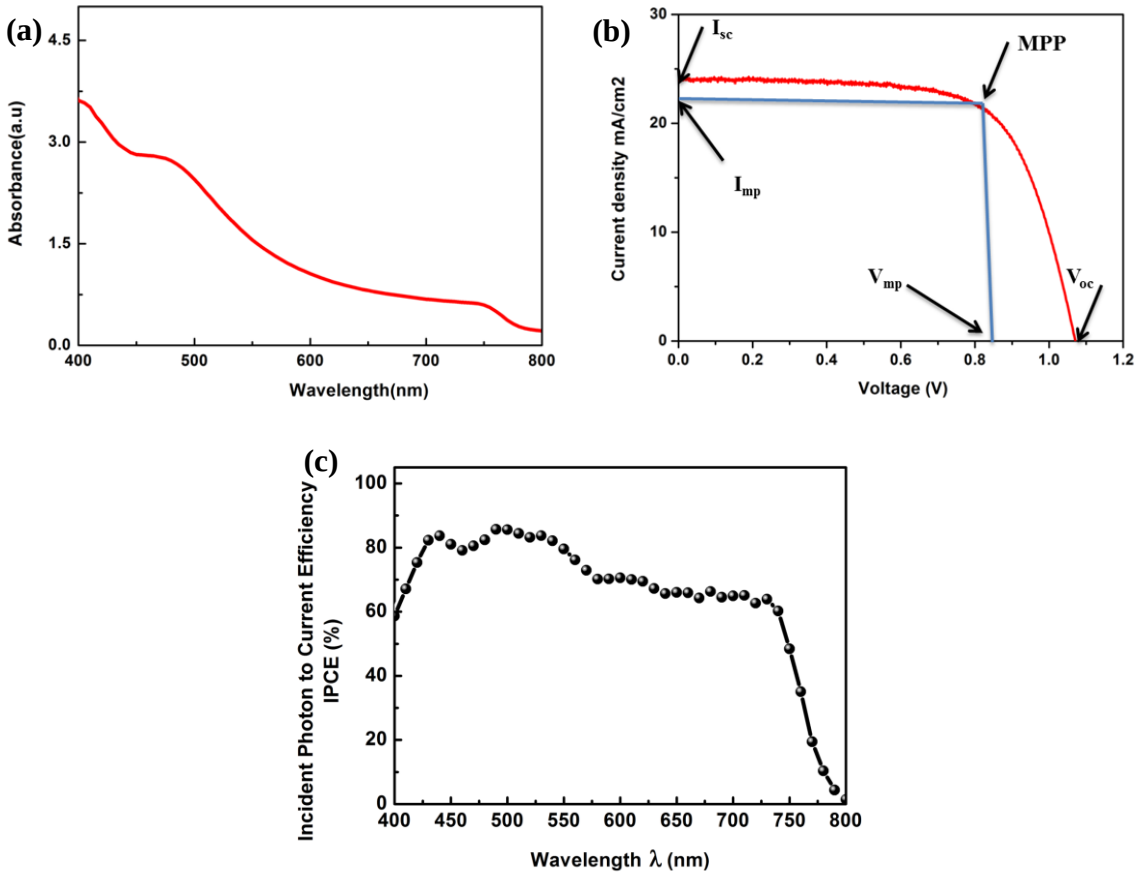

Figure 7.5 Uv-vis absorption spectrum of the FTO/TiO_2/$MAPbI_3$ electrode (a); J-V characteristic curve of the PSC device (b); Corresponding action spectrum -IPCE (c).

Both J-V curve and incident photon to current efficiency (IPCE) spectrum shown in Figures 7.5-b and 7.5-c respectively, were obtained by illuminating the solar cells using Solar Light Co. 300 W, Air Mass (AM) 1.5, Solar Simulator Model 16S-300 (1sun, 1000 W/m^2)

calibrated by Optopolymer Si reference cell. The electrochemical data were registered with an Autolab PG-STAT-30 potentiostat (at a scan rate of 150 mV·s^{-1}).

For a certain number of series (Ns) and parallel (Np) modules, the PV array output current can be represented as follows [37]:

$$I_{PV}= I_{ph}N_p - I_o N_p\left[\exp\left(\frac{V_{PV}+R_s I_{PV}\left(\frac{N_s}{N_p}\right)}{V_t a N_s}\right)-1\right]-\frac{V_{PV}+R_s I_{PV}\left(\frac{N_s}{N_p}\right)}{R_{sh}\left(\frac{N_s}{N_p}\right)} \quad (2)$$

The PV cell, module and array parameters are given in Table 7.2. The current-voltage characteristics of the PV array (with total area of 3.42 m^2) as a functionof irradiation levels (G=200 W/m^2, 500 W/m^2, 750 W/m^2 and 1000 W/m^2) and T=25°C are shown in Figure 7.6. It is evident that the parameters of the PV array strongly depends on the irradiation flux of the incident light.

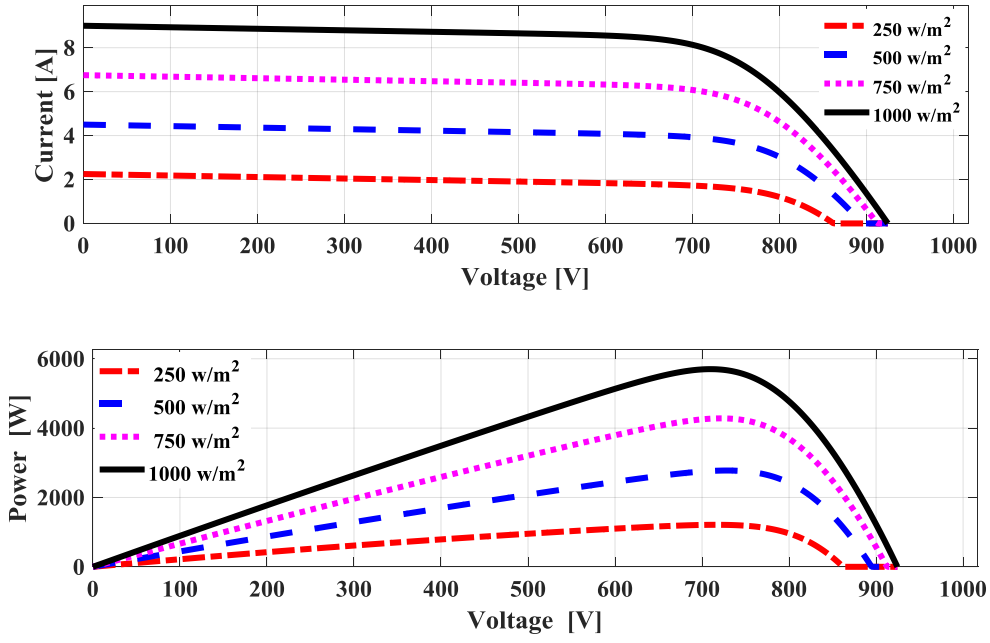

Figure 7.6 The PV array characteristics at different irradiation levels (G=250 W/m^2, 500 W/m^2, 750 W/m^2 and 1000 W/m^2) at uniform irradiation distribution and T=25°C.

Table 7-2 PSC cell, module and array specifications.

	V_{oc}	I_{sc}	I_{pm}	V_{pm}	P_{max}	A
Cell	1.07*(V)*	24.12 (mA/cm^2)	21.02 (mA/cm^2)	0.87*(V)*	0.0183 *(W)*	0.10 cm^2
Module	38.52*(V)*	0.0048A	0.0039 A	30.36*(V)*	0.1210*(W)*	18.00 cm^2
Array	924.48*(V)*	9 A	8.1 A	730.64*(V)*	5918*(W)*	3.42 m^2

V_{oc}: Open circuit voltage; I_{sc}: Short circuit photocurrent density; I_{pm}: Short circuit photocurrent density at maximum power; V_{pm}: Voltage at maximum power; A: Area

T_{ref}: Reference temperature=25 °C

The required PV array output power is selected 5.66 kW based on the corresponding parts of the system design. Accordingly, the number of PV modules is 1899 each one of 0.121 W (see Table 7.2). 24 modules are connected in series in order to supply the needed DC bus voltage and 1875 modules are coupled in parallel in order to deliver the required motor current, while each module has 18 cm^2 active surface. For a and total area of 3.42 m^2, the PV array based on this produces electrical energy having the following parameters: I_{sc} =9 A, V_{oc}=924.48 V, I_{max} =8.1 A, V_{max}=730.64 V, P_{out}= 5700 W.

7.3.2 Three phase inverter model

The output voltage of the inverter can be represented in terms of PV array voltage as follows [37]:

$$v_{an} = \frac{1}{3}(2K_1 - K_2 - K_3)V_{dc}$$
$$v_{bn} = \frac{1}{3}(-K_1 + 2K_2 - K_3)V_{dc} \qquad (3)$$
$$v_{cn} = \frac{1}{3}(-K_1 - K_2 + 2K_3)V_{dc}$$

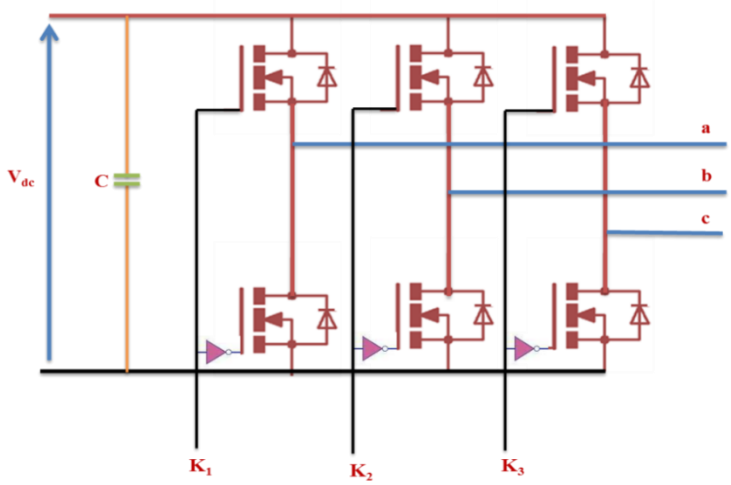

Figure 7.7 Schematic diagram of the voltage source inverter (VSI).

Using the switching states K_1, K_2 and K_3 of the 3 inverter legs, being either 1 or 0. When they equal 1, it means that the corresponding upper switch is ON while the lower one is OFF and vice versa as shown in Figure 7.7. The inverter conduction losses were neglected based on the assumption of ideal IGBTs.

7.3.3 SYNRM model

The dq-axis rotor reference frame was used for SynRM modeling. The detailed model given in [39-40] is used in this study. The main SynRM model equations are as follows [40]:

$$\left.\begin{aligned} v_d &= R_s i_d + p\lambda_d(i_d, i_q) - \omega_r P\lambda_q(i_d, i_q) \\ v_q &= R_s i_q + p\lambda_q(i_d, i_q) + \omega_r P\lambda_d(i_d, i_q) \\ T_e &= \frac{3}{2} P(\lambda_d(i_d, i_q) i_q - \lambda_q(i_d, i_q) i_d) \end{aligned}\right\} \quad (4)$$

where (v_d, v_q), (i_d, i_q) and (λ_d, λ_q) indicate the voltage, current and flux linkage of the direct and quadrature axis components of the motor respectively; R_s and T_e denote the winding resistance and the electromagnetic torque; P and p are the pole pairs number and the differential operator; ω_r is the rotor mechanical speed.

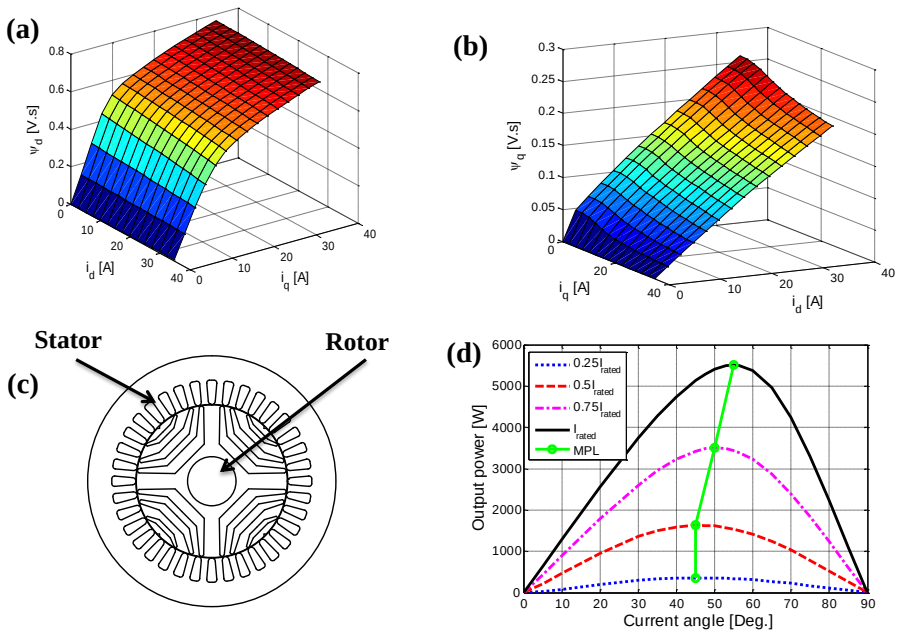

Figure 7.8 Direct (a) and quadrature (b) axis flux-linkages of the SynRM versus the current components c) Schematic diagram of the SynRM geometry d) SynRM output power versus current angle for several stator current amplitudes

Table 7-3 SynRM geometrical variables

Ratings	**Value**	**Geometrical parameters**			
Voltage	380 V	**slots/ poles**	36/4	**Phases number**	3
Current	12.23 A	**Stator diameter (outer /inner)**	180/110 mm	**Shaft diameter /**	35 mm
Power	5.5 kW	**Flux barriers /pole**	3	**Air gab length**	0.3 mm
Speed	3000 rpm	**Stack length**	140 mm	**Steel type (Rotor/stator)**	M330-50A/ M270-50A

Based on equation (4), we can conclude that the performance of SynRM depends mainly on the dq-axis flux-linkages which are influenced by the magnetic saturation behavior of the machine. Therefore, a model that includes the magnetic saturation behavior of the machine is essential. In this work, the magnetic saturation of dq-axis flux-linkages of the machine is considered as shown in Figure 7.8-a and 7.8-b via lookup tables (LUTs). These tables are obtained from FEM. In FEM, both i_d and i_q are modified in a given domain (not exceeding twice the value of the evaluated current), in order to achieve the requested analogy with the dq axis flux-linkages (ψ_d, ψ_q). This method is efficient for including the magnetic saturation behavior in the SynRM. The SynRM geometry is shown in Figure 7.8-c while, the motor geometrical variables are shown in Table 7.3. Finally, the motor output power versus current angle for several stator current amplitudes is shown in Figure 7.8-d. It is clear that it is essential to control the current angle correctly so that the motor delivers the maximum available power (the green line).

7.3.4 Modeling of the centrifugal pumb

The torque (T_{pump})-speed (ω_r) relation of the centrifugal pump is exemplified by [41]–[43]:

$$T_{pump} = k_p \omega_r^2 \tag{5}$$

where, k_p is the pump proportionality constant and ω_r is the rotor rotational speed in rad/s. The k_p value is determined according to the motor rated torque and speed.

7.4 The control system

The proposed system block diagram is outlined in Figure 7.9.

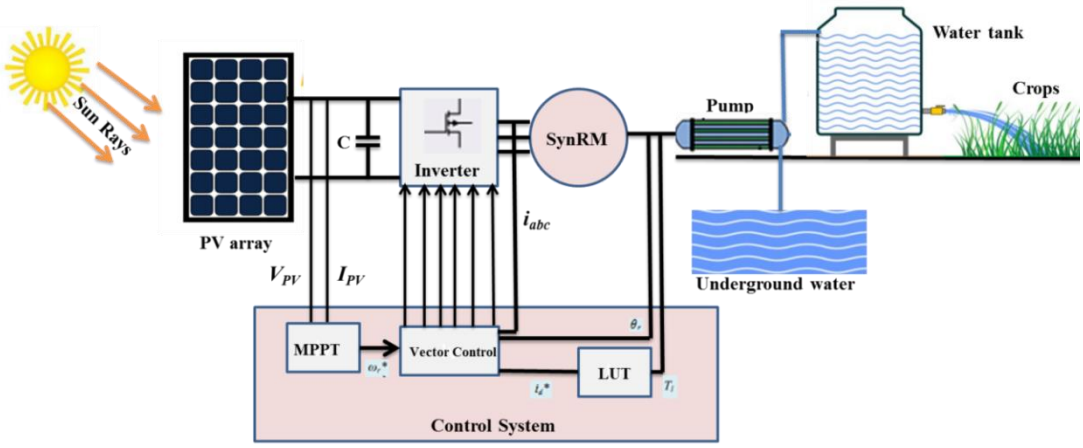

Figure 7.9 The complete block diagram of the proposed system.

SynRM requires a control system for working properly as it is not a self-starting motor. Concerning the PV array, it also requires a control system to work at, or at least near to, the maximum power point (MPP), in order to increase the output power of PV array. Working at MPP increases the PV system efficiency and optimizes the number of required PV modules which results in a reduction in the capital cost of the system [44]. In this proposed system, both driving the SynRM properly to work at the maximum power per Ampère and maximizing the PV output power are implemented using the motor inverter. The SynRM is controlled using the conventional field oriented control method and the PV output is maximized using the perturbation and observation (P&O) scheme as follows.

7.4.1 Field oriented control (FOC) technique

In this technique two reference signals are required as shown in Figure 7.10. The first reference signal is the speed signal (ω_r*) which controls the power flow of the system and the second reference signal is the d-axis current signal (i_d*) which controls the current angle of the SynRM so that the motor works at the maximum power per Ampère. The speed reference single (ω_r*) is obtained from the MPP tracking technique as described in Figure 7.11. The d-axis current single (i_d*) is obtained based on FEM in LUT which correlates the reference

current signal (i_d*) and the motor torque. The PI controller's parameters were determined based on trial and error method [39, 40].

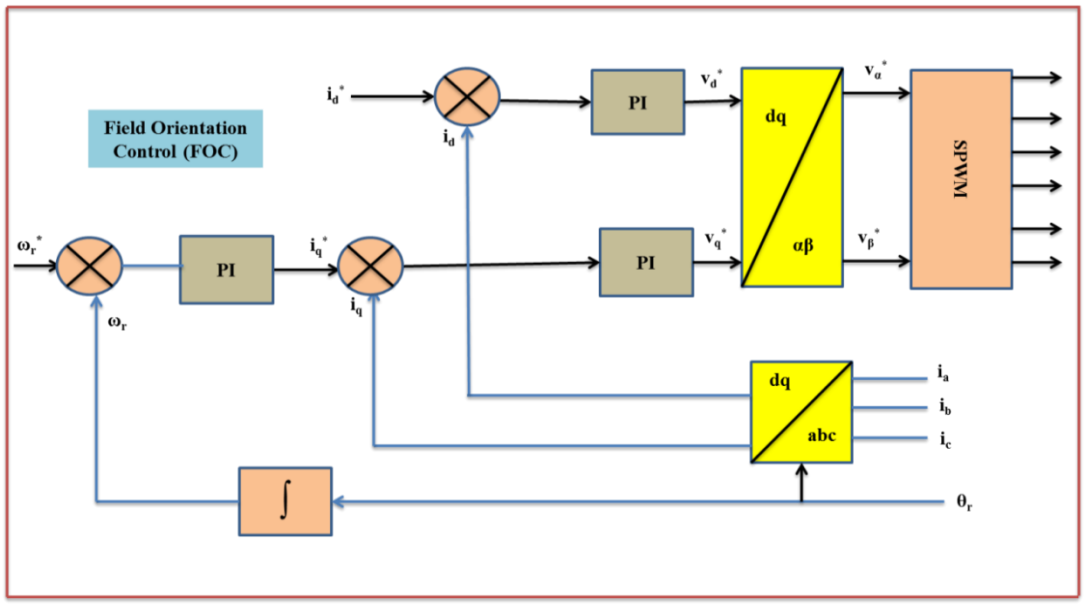

Figure 7.10 The block diagram of the vector control technique.

7.4.2 Maximum power point tracking technique (perturbation and observation (P&O) scheme)

The PV array has several modules and cells interconnected in series and/or in parallel to achieve the required rating. In order to keep the PV system always working at maximum power point a MPPT technique is highly needed.

Figure 7.11 shows the flow chart of the P&O MPPT technique. The proposed methodology uses the perturbation and observation strategy. In the beginning, both the voltage and the current of the PV system are measured. After that, the PV array output power is calculated. At each time instant *m* the present value of the PV power and voltage are compared with the previous values at time instant *m*-1. This process continues until the maximum power is reached. The output of this part is the motor reference speed.

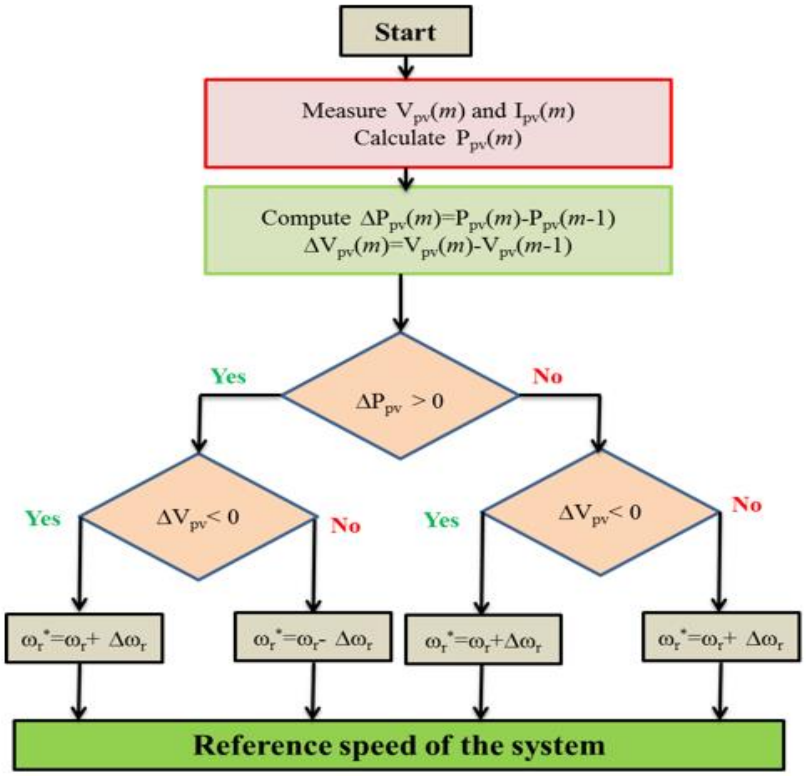

Figure 7.11 The methodology suggested for maximum power point tracking.

7.5 Performance of the proposed PV pumping system

The system under investigation was simulated in MATLAB environment for validation and performance assessment. The system performance was examined under two uniform irradiation cases (500 W/m^2 and 1000 W/m^2); the partial shading case was neglected due to the small area (3.42 m^2) of the perovskite solar array and this is an important merit for this type of new PV array in comparison to silicon analogues, which have a much bigger area (more than 36 m^2) for the same power output and can easily be exposed to partial shading conditions (due to their large size). A proposed control algorithm based on perturbation and observation (P&O) maximum power tracking scheme and vector control strategy is proposed to derive both the PV array and SynRM to work at the extreme output power using only the motor inverter, see Figure 7.11.

The proposed system performance is shown in Figures 7.12 and 7.13. Figures 7.12-a and 7.12-b show both the motor speed and torque response under the proposed control system. Obviously, the motor speed tracks precisely the reference speed obtained from the P&O scheme. Besides, the motor delivers the necessary load torque.

The motor current components (dq axis currents) are presented in Figures 7.12-c and 7.12-d respectively. Obviously the motor currents perfectly match the reference signals. Besides, the d-axis varies according to the required load torque to ensure a maximum torque per Ampère condition while the q-axis current varies based on the reference speed to increase the power of the motor and hence the system towards extracting the maximum available power from the PV array.

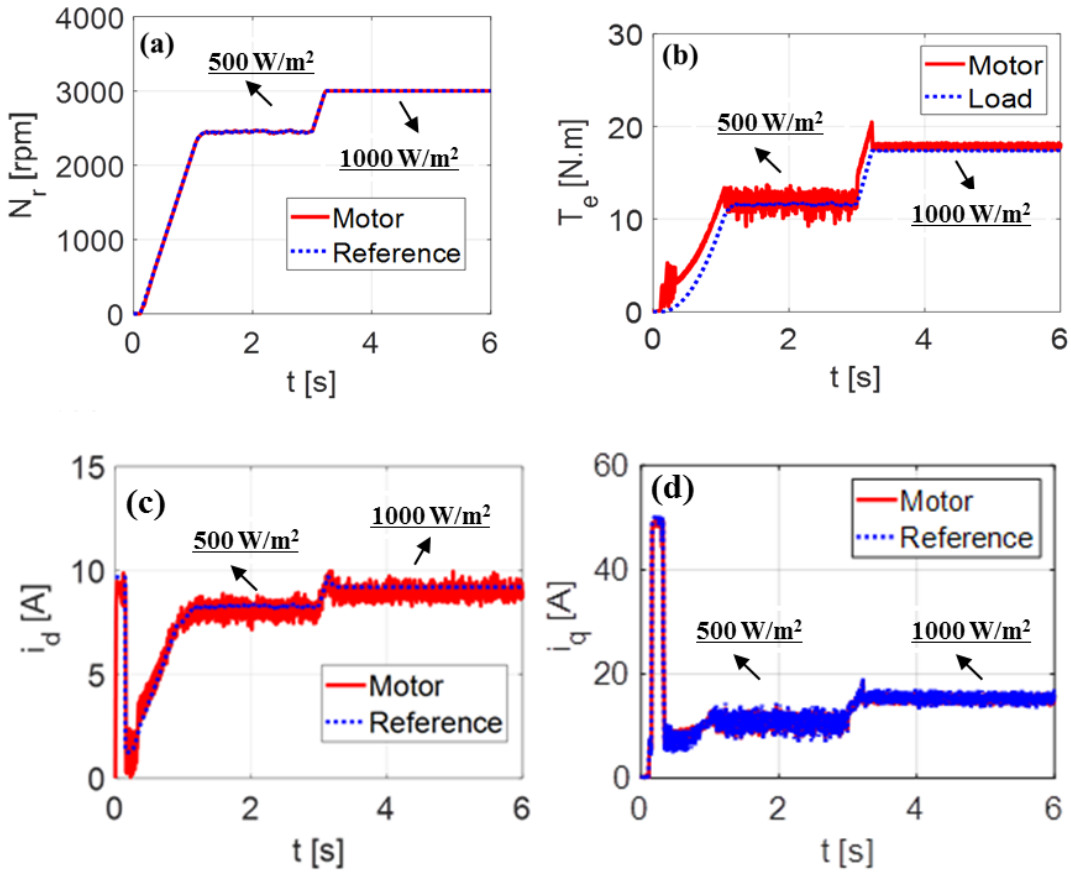

Figure 7.12 SynRM speed versus time a) SynRM torque versus time b) SynRM d axis current versus time c) SynRM q axis current versus time d)

The power produced by the PV array and the motor input power are shown in Figure 7.13-a. Obviously, the PV array output power is maximum based on P&O MPPT technique, see Figure 7.11. The motor power losses and efficiency are presented in Figures 7.13-b and 7.13-c respectively. Clearly, the motor efficiency is high for partial loading (at 500 W/m^2). Consequently, using the proposed motor and PV array, the whole system efficiency will be high. This results in a lower cost for the produced energy. Finally, the pump flow rate is shown in Figure 7.13-d.

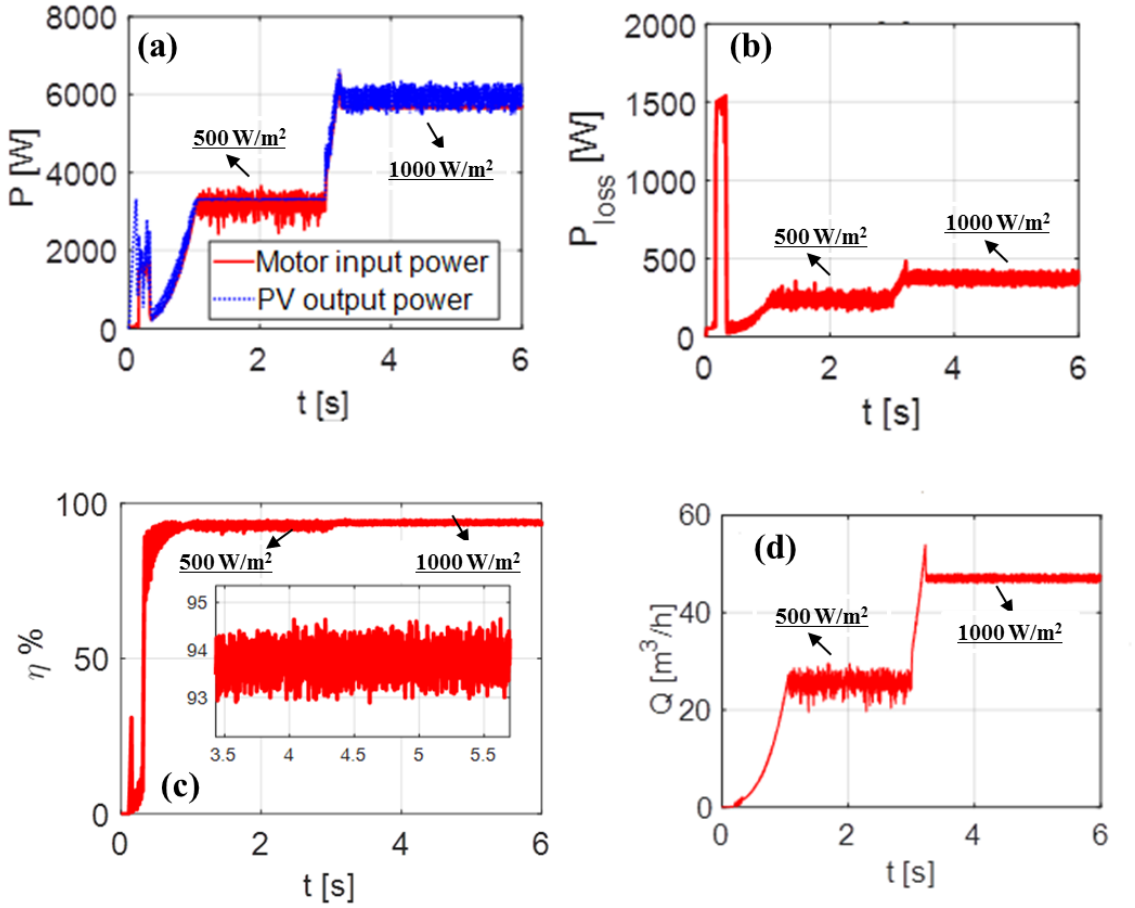

Figure 7.13 The PV array output power and the motor input power versus time SynRM q axis current versus time a) SynRM motor power losses versus time b) SynRM efficiency versus time c) The pump flow rate versus time d)

7.6 Experimental confirmation

In order to confirm the accuracy of the proposed system analysis, the experimental setup shown in Figure 7.14 has been constructed.

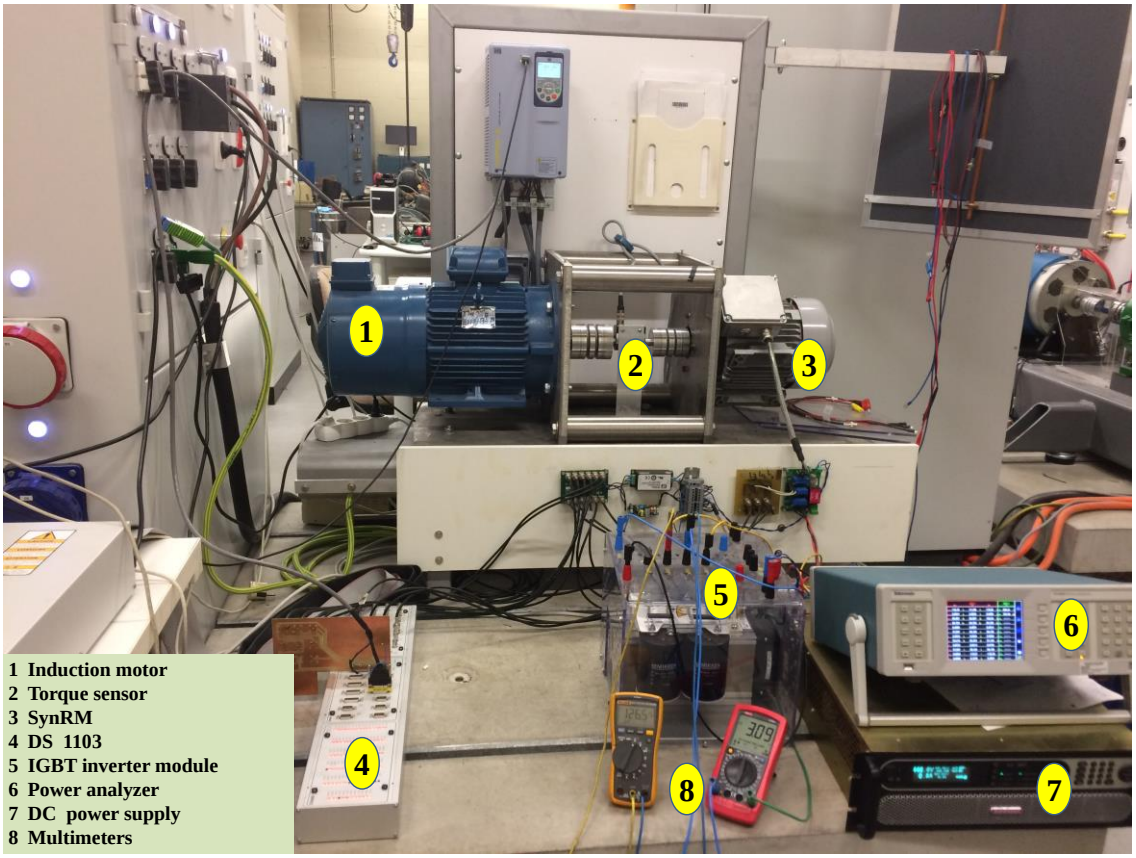

Figure 7.14 Laboratory experimental setup.

A 5.5 kW SynRM is connected with a 9.3 kW induction motor via a torque sensor unit. The SynRM is driven through a three-phase voltage source inverter. The control system explained above in Figures 7.9 and 7.10 is implemented in DS1103 unit and used for driving the SynRM. The motor speed is measured via an incremental encoder of 1024 sample/revolution. The SynRM currents are measured through three identical current sensors (LA25-P). A power analyzer is used for measuring the electrical components of the system i.e. voltage, current, power factor etc.

The PV array is emulated by a controlled DC supply while the pump loading conditions are emulated by an induction motor which is controlled by a commercial drive. The load torque is set at the rated value of the pump and the motor rated speed (3000 rpm) is given as a reference value for the control system of Figure 7.10. A lookup table (from FEM) used for determining the reference current i_d* in Figure 7.10 based on the load torque to achieve the maximum torque per ampere condition for the SynRM.

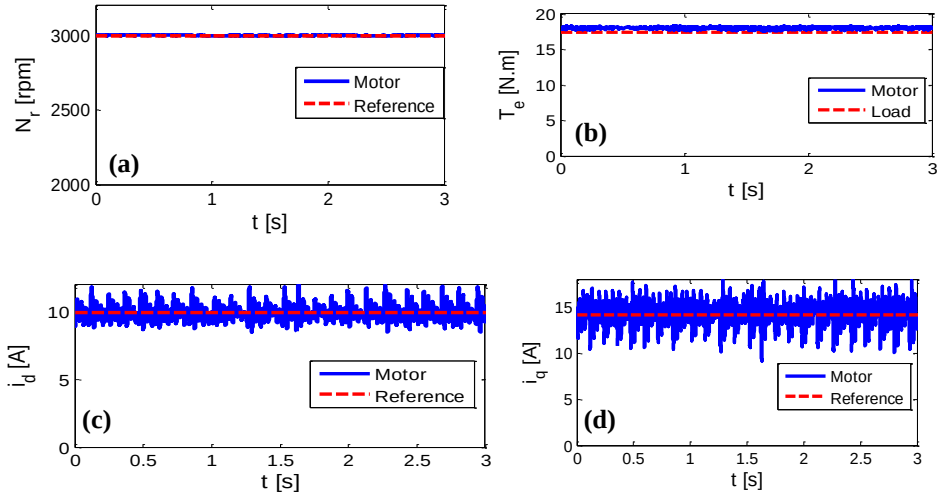

Figure 7.15 a)Measured SynRM speed against the time b) Measured torque against the time c) Measured *d*- axis currents versus the time d) Measured *q*- axis currents versus the time.

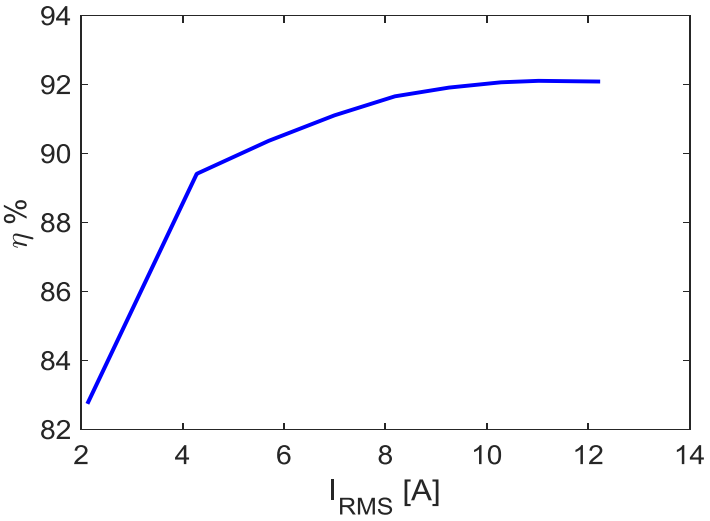

Figure 7.16 Measured efficiency of the whole drive (motor+ inverter) at different loading condition and rated speed.

The motor speed in comparison with the reference speed as a function of time is shown in Figure 7.15-a. In this Figure, obviously the motor speed follows successfully the reference speed. The motor torque and the pump torque time variations are shown in Figure 7.15-b. From Figure 7.15, it is obvious that the motor can supply the load with required torque successfully. Figure 7.15-c and 7.15-d show the *dq*-axis currents. At different load torque, the *d*-axis current is set to reach the maximum torque per ampere state. Firgure 7.16 reprots the measured efficiency of the drive system for different loading condition at the rated speed. It is evident that the SynRM efficiency is high enough even at low loading condition resulting in an increase in the whole PV system efficiency. Consequently, the experimental results validate the simulated results of the proposed system.

7.7 Summary

An efficient and low cost photovoltaic array based on perovskite solar cells (PSCs) feeding a synchronous reluctance motor for water pumping applications was proposed and experimentally validated. The whole system was modeled and analyzed, following an innovative strategy using a voltage source inverter regulated by a control system, without any conventional DC-DC converter or batteries and permitting both the PV array and SynRM to work at the maximum output energy.

The proposed pumping system has significant advantages over those reported in the recent literature. Its efficiency is high, thanks to using both the synchronous reluctance motor and the perovskite solar array, which also results in a lower cost of the produced energy. In addition, due to the high power density of the PSC array, the total area considered for installing the perovskite solar array was only 3.42 m^2, which is very small in comparison with the corresponding area of conventional silicon PVs that exceeds 36 m^2 for the same application. This helps to avoid, besides additional costs and space availability problems, the partial shading condition that usually reduces the efficiency of PV systems.

References

[1] Michael M. Lee, Joël Teuscher, Tsutomu Miyasaka, Takurou N. Murakami, Henry J. Snaith, "Efficient Hybrid Solar Cells Based on Meso-Superstructured Organometal Halide Perovskites ," Science , Vol. 338, no. 6107, pp. 643-647, Nov. 2012.

[2] Kim, H., Lee, C., Im, J. et al., "Lead Iodide Perovskite Sensitized All-Solid-State Submicron Thin Film Mesoscopic Solar Cell with Efficiency Exceeding 9%,". Sci Rep, vol.2, no.591, 2012.

[3] S. A. Kulkarni, T. Baikie, P. P. Boix, N. Yantara, N. Mathews, S. Mhaisalkar, "Band-gap tuning of lead halide perovskites using a sequential deposition process," J. Mater. Chem. A, Vol.2, no. 24, pp.9221-9225, 2014.

[4] H. Lu, H. Zhang, S. Yuan, J. Wang, Y. Zhan, L. Zheng, "An optical dynamic study of MAPbBr3single crystals passivated with MAPbCl3/I3-MAPbBr3 heterojunctions," Phys. Chem. Chem. Phys., Vol.19, pp.4516-4521, 2017.

[5] Xiao-dong Yang, Cheng Lu, Xin-xin Wang, Bao-lin Wang, Gui-xian Ge, Guang-hou Wang and Jian-guo Wan, "Tuning spontaneous polarization and optical absorption by intercalating Sr–Cl-layers in organic–inorganic halide perovskite CH3NH3PbI3 thin films," J. Mater. Chem. A, Vol.6, Art no. 17800, 2018.

[6] National Renewable Energy Laboratory (NREL), https://www.nrel.gov/pv/cell-efficiency.html.

[7] S. Rafizadeh et al., "The Role of Surface Passivation Layer Preparation on Crystallization and Optoelectronic Performance of Hybrid Evaporated-Spincoated Perovskite Solar Cells," IEEE Journal of Photovoltaics, vol. 9, no. 5, pp. 1428-1435, Sept. 2019.

[8] M. Yaghubinia, M. Ebnali, M. Zendehdel and M. Yaghoubinia, "Improvement of perovskite solar cells photovoltaic performance by localized surface plasmon effect of

silver-alumina core-shell nanoparticles," 2016 4th International Conference on Photonics, Optics and Laser Technology (PHOTOPTICS), Rome, 2016, pp. 1-3.

[9] M. F. Hossain, M. Faisal and H. Okada, "Device modeling and performance analysis of perovskite solar cells based on similarity with inorganic thin film solar cells structure," 2016 2nd International Conference on Electrical, Computer & Telecommunication Engineering (ICECTE), Rajshahi, 2016, pp. 1-4.

[10] G. Landi et al., "Evidence of Bipolar Resistive Switching Memory in Perovskite Solar Cell," IEEE Journal of the Electron Devices Society, vol. 6, pp. 454-463, 2018.

[11] M. Xu et al., "Surface Passivation of Perovskite Film by Small Molecule Infiltration for Improved Efficiency of Perovskite Solar Cells," IEEE Photonics Journal, vol. 8, no. 5, pp. 1-7, Oct. 2016, Art no. 6804807.

[12] D. Chen et al., "Simulation Study Toward High-Performance Transparent-Conductive-Oxide Free Perovskite Solar Cells Using Metal Microcavity and Optical Coupling Layer," IEEE Photonics Journal, vol. 10, no. 2, pp. 1-9, April 2018, Art no. 8400209.

[13] D. Wang et al., "Low-Cost and Flexible Anti-Reflection Films Constructed From Nano Multi-Layers of TiO2 and SiO2 for Perovskite Solar Cells," IEEE Access, vol. 7, pp. 176394-176403, 2019.

[14] M. Bliss et al., "Spectral Response Measurements of Perovskite Solar Cells," IEEE Journal of Photovoltaics, vol. 9, no. 1, pp. 220-226, Jan. 2019.

[15] N. Balis, A. A. Zaky, D. Perganti, A. Kaltzoglou, L. Sygellou, F. Katsaros, Stergiopoulos, A. G. Kontos, P. Falaras, "Dye Sensitization of Titania Compact Layer for Efficient and Stable Perovskite Solar Cells," ACS Appl. Energy Mater., Vol. 1, pp.6161-1671, 2018.

[16] N. Balis, A. Verykios, A. Soultati, V. Constantoudis, M. Papadakis, F. Kournoutas, C. Drivas, M.-C. Skoulikidou, S. Gardelis, M. Fakis, S. Kennou, A.G. Kontos, A. G.

Coutsolelos, P. Falaras, M. Vasilopoulou, "Triazine-Substituted Zinc Porphyrin as an Electron Transport Interfacial Material for Efficiency Enhancement and Degradation Retardation in Planar Perovskite Solar Cells," ACS Appl. Energy Mater., Vol.1,no.7, pp.3216-3229, 2018.

[17] Nikolaos Balis, Alaa A. Zaky, Chrysoula Athanasekou, Adrián MT Silva, Elias Sakellis, Maria Vasilopoulou, Thomas Stergiopoulos, Athanassios G. Kontos, Polycarpos Falaras, "Investigating the role of reduced graphene oxide as a universal additive in planar perovskite solar cells," J. of Photochem. and Photobio. A.,Vol. 386, Art no.112141,2020.

[18] Alaa A. Zaky, Ragab A. El Sehiemy,Yasser I. Rashwan, Mostafa A. Elhossieni, Konstantina Gkini, Antonios Kladas, Polycarpos Falaras, "Optimal Performance Emulation of PSCs using the Elephant Herd Algorithm Associated with Experimental Validation," The Electrochemical Society, vol. 8, no.12, pp. Q249-Q255, 2019.

[19] Singh, Arjun; Ranjan, Rahul; Ranjan, Sudhir; et al., "Effect of NiO Precursor Solution Ageing on the Perovskite Film Formation and Their Integration as Hole Transport Material for Perovskite Solar Cells," J. of Nanosc. and Nanotech., Vol. 20, no. 6, pp. 3710-3717, Jun. 2020.

[20] Kumar, Ashwani, Soleimanioun, Nazilla, Singh, Navjot, et al., "Effects of Thermal Annealing Duration on the Film Morphology of Methylamine Lead Triiodide (MAPbI3) Perovskite Thin Films in Ambient Air," J. of Nanosc. And Nanotech., Vol.20, no. 6, pp. 3795 -3801, Jun. 2020.

[21] Li, Juan; Gao, Rongrong; Gao, Fei; et al, "Fabrication of efficient CsPbBr3 perovskite solar cells by single-source thermal evaporation," J. of Allo. And Compo., Vol.818 , Art no., Mar. 2020.

[22] Wang, Cheng; Zhang, Junsen; Duan, Jipeng; et al, "All-inorganic, hole-transporting-layer-free, carbon-based CsPbIBr2 planar perovskite solar cells by a two-step

temperature-control annealing process," Mater. Sci. Semicon.Process, Vol.108, Art no. 104870, Mar. 2020.

[23] S. S. Chandel, M. N. Naik, and R. Chandel, "Review of solar photovoltaic water pumping system technology for irrigation and community drinking water supplies," Renew. Sustain. Energy Rev., vol. 49, pp. 1084-1099, Sep. 2015.

[24] M. Rezkallah, A. Chandra, M. Tremblay, H. Ibrahim, "Experimental implementation of an APC with enhanced MPPT for standalone solar photovoltaic based water pumping station", IEEE Trans Sustain. Energy, vol. 10, no. 1, pp. 181-191, Jan. 2019.

[25] M. Kolhe, J. C. Joshi, D. P. Kothari, "Performance analysis of a directly coupled photovoltaic water-pumping system", IEEE Trans. Energy Convers., vol. 19, no. 3, pp. 613-618, Sep. 2004.

[26] J. V. M. Caracas, G. d. C., Farias, L. F. M. Teixeira, L. A. d. S., Ribeiro, "Implementation of a high-efficiency high-lifetime and low-cost converter for an autonomous photovoltaic water pumping system", IEEE Trans. Ind. Appl., vol. 50, no. 1, pp. 631-641, Jan./Feb. 2014.

[27] M. A. Elgendy, B. Zahawi, D. J. Atkinson, "Comparison of directly connected and constant voltage controlled photovoltaic pumping systems", IEEE Trans. Sustain. Energy, vol. 1, no. 3, pp. 184-192, Oct. 2010.

[28] S. Jain, A. K. Thopukara, R. Karampuri, V. T. Somasekhar, "A single-stage photovoltaic system for a dual-inverter-fed open-end winding induction motor drive for pumping applications", IEEE Trans. Power Electron., vol. 30, no. 9, pp. 4809-4818, Sep. 2015

[29] M. Z. Youssef, "Design and performance of a cost-effective BLDC drive for water pump application",IEEE Trans. Ind. Electron., vol. 62, no. 5, pp. 3277-3284, May 2015.

[30] P. Sharma, J.-H. Lee, S. k. Sul, "New maximum power extraction algorithm for single stage solar water pump system working effectively for dynamically changing conditions", Proc. IEEE Int. Conf. Power Electron. Drives Energy Syst., pp. 1-6, 2016.

[31] V. Narayana, A. K. Mishra, B. Singh, "Design of SRM driven BESS based PV powered water pumping system", Proc. 7th Power India Int. Conf., pp. 1-6, 2016.

[32] S. Murshid, B. Singh, "A PV array fed BESS supported speed sensor-less PMSM driven water pumping system", Proc IEEE Transp. Electrific. Conf. Expo, pp. 63-68, 2018.

[33] R. Kumar, B. Singh, "Grid interfaced solar PV powered brushless DC motor driven water pumping system", Proc. 7th India Int. Conf. Power Electron., pp. 1-5, 2016.

[34] E. Mahmoud and H. el Nather, "Renewable energy and sustainable developments in Egypt: Photovoltaic water pumping in remote areas," Appl. Energy, vol. 74, nos. 1-2, pp. 141_147, Jan. 2003.

[35] Z.Yang, F. Shang, I. P. Brown, and M. Krishnamurthy, "Comparative study of interior permanent magnet, induction, and switched reluctance motor drives for EV and HEV applications," IEEE Trans. Transport. Electric. vol. 1, no. 3, pp. 245-254, Oct. 2015.

[36] R. Kumar and B. Singh, "BLDC motor-driven solar PV array-fed water pumping system employing zeta converter," IEEE Trans. Ind. Appl., vol. 52, no. 3, pp. 2315-2322, May 2016.

[37] M. Nabil, S. M. Allam, and E. M. Rashad, "Performance improvement of a photovoltaic pumping system using a synchronous reluctance motor," Electr. Power Compon. Syst., vol. 41, no. 4, pp. 447-464, Feb. 2013.

[38] M. N. Ibrahim, P. Sergeant, and E. M. Rashad, "Relevance of including saturation and position dependence in the inductances for accurate dynamic modeling and control of SynRMs," IEEE Trans. Ind. Appl., vol. 53, no. 1, pp. 151-160, Jan./Feb. 2017.

[39] V. C. Sontake and V. R. Kalamkar, "Solar photovoltaic water pumping system_A comprehensive review," Renew. Sustain. Energy Rev., vol. 59, pp. 1038-1067, Jun. 2016.

[40] M. Nabil, S. M. Allam, and E. M. Rashad, "Modeling and design considerations of a photovoltaic energy source feeding a synchronous reluctance motor suitable for pumping systems," Ain Shams Eng. J., vol. 3, no. 4, pp. 375-382, Dec. 2012.

[41] A. Hamza and A. Z. Taha, "Performance of submersible PV solar pumping systems under conditions in the Sudan," Renew. Energy, vol. 6, nos. 5-6, pp. 491-495, Jul./Sep. 1995.

[42] Hamidat, B. Benyoucef, and T. Hartani, "Small-scale irrigation with photovoltaic water pumping system in Sahara regions," Renew. Energy, vol. 28, no. 7, pp. 1081-1096, Jun. 2003.

[43] Chaurey, P. M. Sadaphal, and D. Tyaqi, "Experiences with SPV water pumping systems for rural applications in India," Renew. Energy, vol. 3, no. 8, pp. 961-964, Nov. 1993.

[44] H. Rezk and A. M. Eltamaly, "A comprehensive comparison of different MPPT techniques for photovoltaic systems," Solar Energy, vol. 112, pp. 1-11, Feb. 2015.

[45] M. N. Ibrahim, P. Sergeant, and E. M. Rashad, "Design of low cost and efficient photovoltaic pumping system utilizing synchronous reluctance motor," in Proc. IEEE Int. Electr. Mach. Drives Conf. (IEMDC), Miami, FL, USA, May 2017, pp. 1-7.

8 Chapter 8

8 Conclusions and future work

8.1 Conclusions

- For the first time, we proposed the concept of dye sensitization for optimizing the compact layer/perovskite interface. The introduction of the solution processable D35 organic dye modifier sensitizing the titania compact layer, leaded to planar PSCs delivering enhanced power conversion efficiency of up to ~17% which is accompanied by significantly increased stability. Our results indicate that this performance enhancement is attributed to enhanced recombination resistance, increased electron transfer, better crystallization of the deposited perovskite and humidity sealing character of the hydrophobic dye monolayer.The sensitized PSCs preserved 75% of their initial PCE after 2h of thermal stress at 100^{o}C, a significant improvement considering that reference PSCs almost collapsed at the same time. The D35-based devices was also very stable after 7h under light stress, establishing the overall beneficial role of this organic dye in the development of high-quality planar perovskite solar cells presenting increased efficiency and enhanced stability.
- We fabricated efficient and relatively stable planar PSCs, by incorporating rGO nanoflakes within the TiO_2 ETL, the Spiro-MeOTAD HTL and the $CH_3NH_3PbI_3$ absorber. As a result, for the first time in similar devices, we ascertained its clear beneficial role when simultaneously employed in TiO_2 and $CH_3NH_3PbI_3$. Power conversion efficiencies as high as 16.48% were obtained, increased by almost 20% compared to the PCE of the reference device. This enhancement was attributed to the determining presence of rGO within the ETL which offers increased conductivity thus improved electron transport rate and charge mobility, it favors the growth of large perovskite crystals with improved crystallinity while it acts as a perovskite trap states passivator. In addition, the presence of rGO into the

$CH_3NH_3PbI_3$ layer further increases the perovskite grains size and favors the growth of smooth and homogenous films. On the contrary the presence of the rGO in the Spiro-MeOTAD is detrimental, probably due to the creation of direct pathways between the perovskite and the top silver electrodes. As a result, the electrical parameters of the photovoltaic performance of the PSC were improved, displaying the determining role of graphene materials in the performance of PSC, in both terms of efficiency and stability.

- Cu ions were used as a modifier in order to obtain a Cu-TiO_2 ETL for efficient planar PSCs. The addition of Cu ions lifts the Fermi level of TiO_2. This subsequently enhances the open circuit voltage of the PSCs, facilitate the electron passage at ETL/perovskite interface reducing the series resistance and increase the short circuit current density, open circuit voltage (V_{oc}) and fill factor. The Cu-TiO_2 ETL based PSCs showed high electrical conductivity, low trap state density, low hysteresis index, and enhanced electron extraction. Contact angle measurements confirmed that the introduction of copper ions (Cu^{1+}) into the compact TiO_2 layer increased its hydrophobicity, thus favoring improved perovskite crystallization, a fact corroborated by XRD analysis. As a result, PSCs with PCE higher than 18% owing to high open circuit voltage (V_{oc}) of 1.1 V, high current density (J_{sc}) of 23.15 $mA \cdot cm^{-2}$, and a high fill factor (FF) of 73% were obtained. Outperforming the performance of the reference device showing a PCE equal to 15.78% (with V_{oc} equal to 1.07 V, J_{sc} of 20.87 mA cm_{-2}, and FF equal to 70 %). Long term stability for 51 days was done for reference and Cu modified devices where, the Cu modified devices retained a J_{sc} of 0.82 from J_{sc0} , V_{oc} of 0.9 from V_{oc0} , FF of 0.71from FF_0 and PCE of 0.53 from PCE_0 while, the reference device retained 0.78,0.76,0.63 and 0.37 respectively.
- Three electrical models of PSCs called single, double and triple diode models has been proposed for two PSCs devices. Estimation and extracting the PSC models parameters are carried out using the elephant herd optimization algorithm. To prove the capability of the

proposed estimation procedure, a comparison study between the proposed EHO with crow search optimization and differential evolution algorithms has been employed. The simulation results have proved the EHO superiority compared with the competitive algorithms. In the view point of experimental verification, the simulation results assure the high closeness between the estimated parameters with experimental ones. It can be concluded that the proposed three diode model is the best one for modeling both modified and controlled devices. The modified devices present lower series resistance, higher shunt resistance, lower diode ideality factor, lower diode saturation current, and higher open circuit voltage values. This is due to the presence of the dye that permits the easier crystallization of the perovskite absorber and facilitates the electron transfer from the perovskite layer to titania compact layer and its effective collection on the fluorine-doped transparent oxide (FTO) conductive glass substrate. As a result, the EHO algorithm has been proved a very effective optimization paradigm to simulate the behavior of dye engineered perovskite solar cells. This work paves the way towards fabricating high stable PSCs with high power energy conversion as well, through titania layer passivation or doping and new perovskite materials to be used as a god absorber. Also new efficient optimization tools can be used in solving the parameter estimation problem like Cuckoo Search, Sunflower Optimization algorithm, Krill Herd Algorithm, Sine Cosine Algorithm, Hurricane Optimization Algorithm, and Multi-Verse Optimizer.

- An efficient and low cost photovoltaic array based on perovskite solar cells (PSCs) feeding a synchronous reluctance motor for water pumping applications was proposed and experimentally validated. The whole system was modeled and analyzed, following an innovative strategy using a voltage source inverter regulated by a control system, without any conventional DC-DC converter or batteries and permitting both the PV array and SynRM to work at the maximum output energy. The proposed pumping system has significant

advantages over those reported in the recent literature. Its efficiency is high, thanks to using both the synchronous reluctance motor and the perovskite solar array, which also results in a lower cost of the produced energy. In addition, due to the high power density of the PSC array, the total area considered for installing the perovskite solar array was only 3.42 m^2, which is very small in comparison with the corresponding area of conventional silicon PVs that exceeds 36 m^2 for the same application. This helps to avoid, besides additional costs and space availability problems, the partial shading condition that usually reduces the efficiency of PV systems.

- The effect of incorporating PV generation units on the unit commitment problem in power system has been investigated and applied in two case studies namely 10 generation units and IEEE 30 Bus systems where, a power production cost reduction was obtained in comparison with the case of generation units without incorporating PV units, showing the economic benefits of using PV units as a generation units.
- A PV grid connected system performance under constant irradiation and variable irradiation levels was investigated via a matlab simulation model which, includes PV model, maximum poer point tracking model based on incremental conductance technique, Boost converter model, inverter model, inverter control model and utility grid model.

8.2 Future work

- Dynamic modelling of the cells and solving the dynamic model by efficient optimization algorithms.
- Using the interface engineering for increasing both efficiency and stability of the cells.
- Investigating the doping concept in order to increase the overall power conversion efficiency and stability of perovskite solar cells.

- Examine the third generation solar cells (perovskite solar cells) in more electrical applications.
- Hybride perovskite solar cells and thermoelectric generator (TEG) system for electricity production investigation.
- PV grid connected system investigation in the case of smart grid.

9 List of publications

9.1 Journal papers

[1] Enhancing the Performance of Planar Perovskite Solar Cells with Cu-modified Electron Transport Layer. Alaa A. Zaky, Konstantina Gkini, Michalis Arfanis, Labrini Sygellou,cAnastasios Stergiou, Nikos Tagmatarchis, Nikolaos Balis, Polycarpos Falaras. Applied Catalysis B. 284,2021,119714.

[2] " Energy Efficiency Improvement of Water Pumping System Using Synchronous Reluctance Motor Fed by Perovskite Solar Cells", Alaa A.Zaky, Mohamed N. Ibrahim, Hegazy Rezk, Eleftherios Christopoulos, Ragab A. El Sehiemy, Evangelos Hristophorou, Antonios Kladas, Peter Sergeant, Polycarpos Falaras. International Journal of Energy Research. 2020; 44: 11629-11642.

[3] "Investigating the Role of Reduced Graphene Oxide as a Universal Additive in Planar Perovskite Solar Cells", Nikolaos Balis, Alaa A.Zaky, Chrysoula Athanasekou, Adrián M T Silva, Elias Sakellis, Maria Vasilopoulou, Thomas Stergiopoulos, Athanassios G. Kontos, Polycarpos Falaras, Journal of Photochemistry & Photobiology A: Chemistry 386 (2020) 112141.

[4] "Dye Engineered Perovskite Solar Cells under Accelerated Thermal Stress and Prolonged Light Exposure", Alaa A.Zaky, Nikolaos Balis, Konstantina Gkini, Chrysoula Athanasekou, Andreas Kaltzoglou, Thomas Stergiopoulos, and Polycarpos Falaras, ChemistrySelect 5 (2020) 4454 –4462. DOI:10.1002/slct.202000771.

[5] "Optimal Performance Emulation of PSCs using the Elephant Herd Algorithm Associated with Experimental Validation", Alaa A.Zaky, Ragab A. El Sehiemy, Yasser I. Rashwan, Mostafa A. El Hossieni, Konstantina Gkini, Antonios Kladas,Polycarpos Falaras, Electronic and Photonic Devices and Systems section, ECS Journal of Solid State Science and Technology, 8 (2019) Q249-Q255. doi: 10.1149/2.0271912jss.

[6] "Dye Sensitization of Titania Compact Layer for Efficient and Stable Perovskite Solar Cells" Nikolaos Balis, Alaa A.Zaky, Dorothea Perganti, Andreas Kaltzoglou, Lamprini Sygellou, Fotios Katsaros, Thomas Stergiopoulos, Athanassios G. Kontos, and Polycarpos Falaras. ACS Appl. Energy Mater. 1 (2018) 6161−6171.DOI: 10.1021/acsaem.8b01221.

9.2 Conference papers

[1] Alaa A. Zaky, Nikolaos Balis, Athanassios G. Kontos, Chrysoula Athanasekou, Maria Antoniadou and Polycarpos Falaras, Thermal Stability Enhancement of Perovskite Solar Cells via Dye Sensitization of the Titania Compact Layer, the 2019 Spring Meeting of the European Materials Research Society (E-MRS),May 27 to 31, 2019, in Nice, France (Congress & Exhibition Centre Acropolis), (poster presentation).

[2] Alaa. A. Zaky, N.Balis, K.E. Gkini, A.G. Kontos, C. Athanassekou, P.Falaras. Thermal Stability Enhancement of Planar Perovskite solar cells via Dye Sensitization of Titania Compact Layer [12IPESM] 12th Pan-Hellenic Scientific Congress 29 - 31 May 2019, Athens, Greece (Oral presentation), Book of Abstracts.

[3] Alaa.A. Zaky, N. Balis, D. Perganti, A. Kaltzoglou, L. Sygellou, F. Katsaros, T. Stergiopoulos, A.G. Kontos, and P. Falaras. Dye sensitization of compact layer as a novel strategy for performance enhancing of Perovskite solar cells. Athens Conference on Advances in Chemistry (ACAC) 30 October-2 November 2018, Athens, Greece (poster presentation), Book of Abstracts.

[4] N. Balis, Alaa.A. Zaky, D. Perganti, A. Kaltzoglou, L. Sygellou, F. Katsaros, T. Stergiopoulos, A.G. Kontos, and P. Falaras. Efficient Planar Perovskite Solar Cells by Incorporating Reduced Graphene Oxide in Absorber and Electron Transport Layers. Athens Conference on Advances in Chemistry (ACAC) 30 October-2 November 2018, Athens, Greece (Oral presentation), Book of Abstracts.

10 List of courses taken in the frame of this thesis

No	Course Code	Course Name	Grade (-/10)
1	712	Magnetism and Magnetic Materials	10
2	103	Probabilistic Analysis of Energy Systems	10
3	113	Power Quality	10
4	106	Fast Electromagnetic Transients in Power Systems	10
5	204	Structure and Properties of Semiconductors	9
6	114	Multi Criteria Decision Support Systems	9

11 Appendix A

SUNPOWER

305 SOLAR PANEL

EXCEPTIONAL EFFICIENCY AND PERFORMANCE

BENEFITS

Highest Efficiency
SunPower™ Solar Panels are the most efficient photovoltaic panels on the market today.

More Power
Our panels produce more power in the same amount of space—up to 50% more than conventional designs and 100% more than thin film solar panels.

Reduced Installation Cost
More power per panel means fewer panels per install. This saves both time and money.

Reliable and Robust Design
Proven materials, tempered front glass, and a sturdy anodized frame allow panel to operate reliably in multiple mounting configurations.

SPR-305-WHT-D

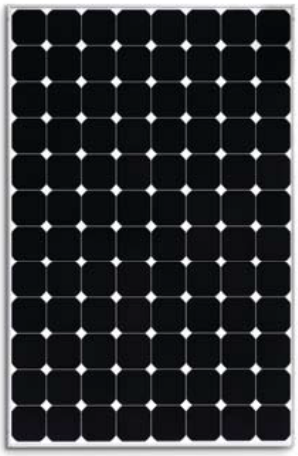

The SunPower™ 305 Solar Panel provides today's highest efficiency and performance. Utilizing 96 back-contact solar cells, the SunPower 305 delivers a total panel conversion efficiency of 18.7%. The panel's reduced voltage-temperature coefficient and exceptional low-light performance attributes provide outstanding energy delivery per peak power watt.

SunPower's High Efficiency Advantage - Up to Twice the Power

	Thin Film	Conventional	SunPower
Peak Watts / Panel	65	215	305
Efficiency	9.0%	12.8%	18.7%
Peak Watts / ft²(m²)	**8 (90)**	**12 (128)**	**17 (187)**

About SunPower

SunPower designs, manufactures and delivers high-performance solar electric technology worldwide. Our high-efficiency solar cells generate up to 50% more power than conventional solar cells. Our high-performance solar panels, roof tiles and trackers deliver significantly more energy than competing systems.

SUNPOWER

305 SOLAR PANEL

EXCEPTIONAL EFFICIENCY AND PERFORMANCE

Electrical Data

Measured at Standard Test Conditions (STC): irradiance of 1000W/m², AM 1.5, and cell temperature 25° C

Peak Power (+/-5%)	P_{max}	305 W
Rated Voltage	V_{mpp}	54.7 V
Rated Current	I_{mpp}	5.58 A
Open Circuit Voltage	V_{oc}	64.2 V
Short Circuit Current	I_{sc}	5.96 A
Maximum System Voltage	UL	600 V
Temperature Coefficients		
	Power	-0.38% / K
	Voltage (V_{oc})	-176.6mV / K
	Current (I_{sc})	3.5mA / K
NOCT		45° C +/-2° C
Series Fuse Rating		15 A

Mechanical Data

Solar Cells	96 SunPower all-back contact monocrystalline
Front Glass	high transmission tempered glass
Junction Box	IP-65 rated with 3 bypass diodes Dimensions: 32 x 155 x 128 (mm)
Output Cables	1000mm length cables / MultiContact (MC4) connectors
Frame	Anodized aluminum alloy type 6063 (silver); stacking pins
Weight	41 lbs. (18.6 kg)

I-V Curve

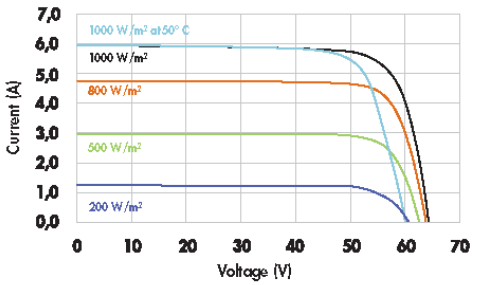

Current/voltage characteristics with dependence on irradiance and module temperature.

Tested Operating Conditions

Temperature	-40° F to +185° F (-40° C to + 85° C)
Max load	50 psf 245 kg/m² (2400 Pa) front and back – e.g. wind
Impact Resistance	Hail 1 in (25 mm) at 52mph (23 m/s)

Warranties and Certifications

Warranties	25 year limited power warranty
	10 year limited product warranty
Certifications	Tested to UL 1703. Class C Fire Rating

Dimensions

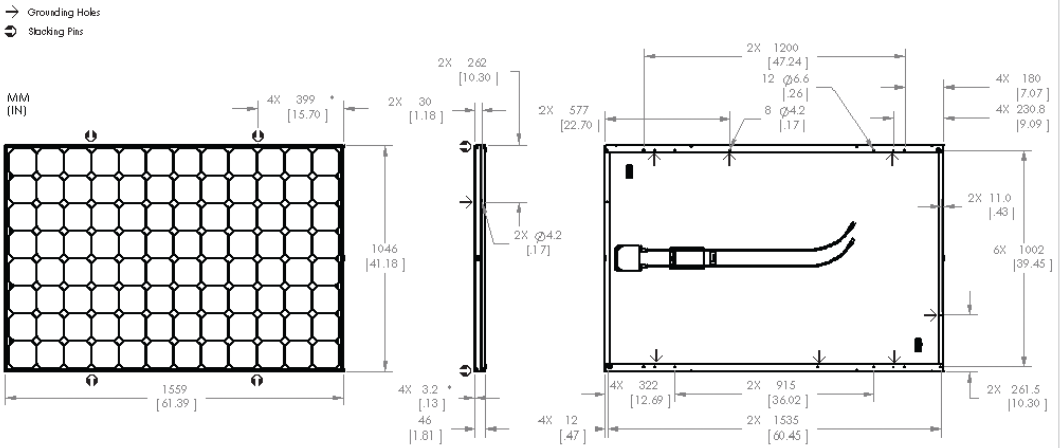

CAUTION: READ SAFETY AND INSTALLATION INSTRUCTIONS BEFORE USING THE PRODUCT.

Visit sunpowercorp.com for details

sunpowercorp.com

Document #001-52287 Rev** / LTR_EN

12 Appendix B

Types of Faults in Power System

Faults are classified into four types.

1. Single line-to-ground fault (L-G)
2. Line-to-line fault (L-L)
3. Double line-to-ground fault (L-L-G)
4. Balanced three-phase fault (L-L-L-G)

Single Line-to-Ground Fault

A single line-to-ground fault is shown in Figure 1 and this type is the most commonly occurring unsymmetrical fault. This type may be resulted from a vehicular accident causing one of the phase conductors to fall and come in contact with the earth, or it may be caused by tree branches, or it could be caused by flashovers across dusty insulators during rain-showers.

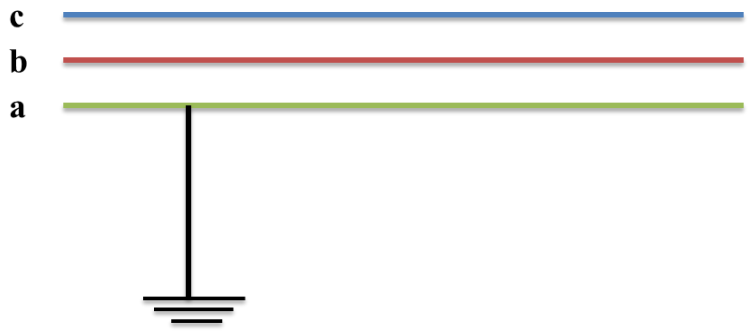

Figure B.1: A single line-to-ground fault

The fault conditions are

$$I_a = I_f$$
$$I_b = I_c = 0$$
$$V_a = V_f = I_f Z_f$$

The line currents symmetrical components are

$$\mathbf{I_{a1} = 1/3(I_a + aI_b + a^2I_C)}$$

$$\mathbf{I_{a2} = 1/3(I_a + a^2I_b + aI_C)}$$

$$\mathbf{I_{a0} = 1/3(I_a + I_b + I_C)}$$

From above equations

$$\mathbf{I_{a1} = I_{a2} = I_{a0} = 1/3(I_a + 0 + 0) = I_{a/3}}$$

$$\mathbf{I_a = I_{a1} + I_{a2} + I_{a0} = 3I_{a0}}$$

Voltages calculations

$$\mathbf{V_a = V_{a1} + V_{a2} + V_{a0}}$$

$$\mathbf{V_a = V_f = I_fZ_f}$$

$$\mathbf{V_a = I_aZ_f = 3I_{a0}Z_f = (3Z_f)I_{a0}}$$

$$\mathbf{(3Z_f)I_{a0} = V_{a1} + V_{a2} + V_{a0}}$$

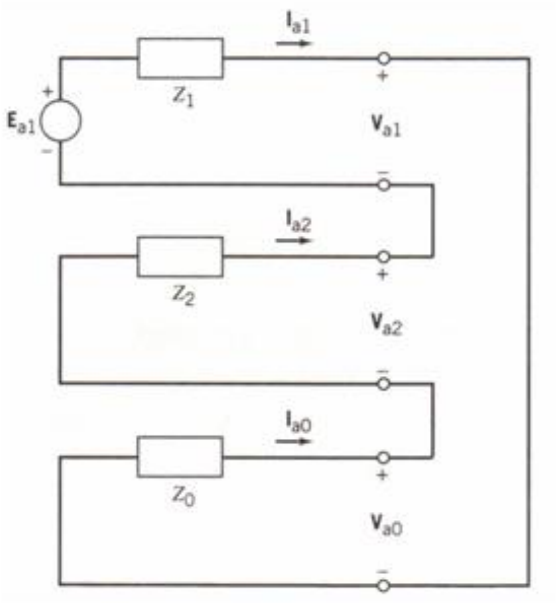

Figure B.2 equivalent circuit of line to ground fault

A line to line fault

A line to line fault or unsymmetrical fault occurs when two conductors are short circuited. In the figure shown below shows a three phase system with a line-to-line fault phases b and c. The fault impedance is assumed to be Z_f. The LL fault is placed between lines b and c so that the fault be symmetrical with respect to the reference phase a which is un-faulted.

Figure B.3: A line-to-line fault

The fault conditions are

$$I_a = -I_c = I_f$$

$$I_a = 0$$

$$V_b - V_c = V_f = I_b Z_f$$

$$a^2 I_{a1} + \quad a I_{a2} + I_{a0} = -a I_{a1} - a^2 I_{a2} - I_{a0})$$

$$2I_{a0} = -(a^2 + a) I_{a1} - (a^2 + a) I_{a2}$$

$$2I_{a0} = I_{a1} + I_{a2}$$

$$I_{a0} = -(I_{a1} + I_{a2})$$

$$I_{a2} = -I_{a1}$$

$$I_{a0} = 0$$

$$2I_{a0} = I_{a1} + I_{a2}$$

$$I_f = I_b = a^2 I_{a1} + a I_{a2} + I_{a0} = (a^2 - a) I_{a1}$$

Voltages calculations

$$V_b - V_c = V_f = I_f Z_f$$

$$(a^2 - a) V_{a1} + (a - a^2) V_{a2} = (a^2 - a)\, I_{a1} Z_f$$

$$I_{a1} Z_f = V_{a1} - V_{a2}$$

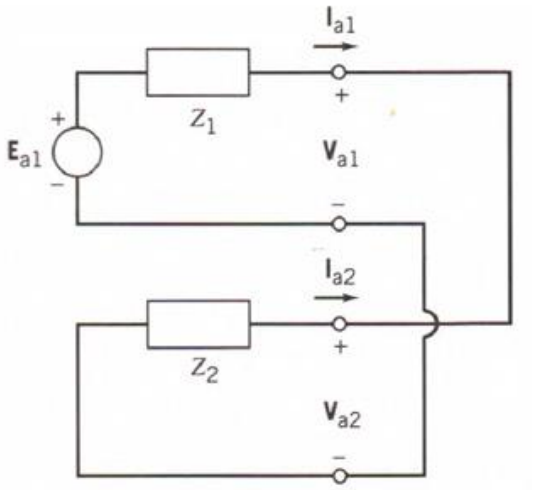

Figure B.4 equivalent circuit of line to line fault

A line-to-line to ground fault

Figure B.5: A line-to-line to ground fault

The fault conditions are

$$I_f = I_b + I_c$$

$$I_a = 0$$

$$V_b = V_c = V_f = I_f Z_f$$

$$I_{a0} = -(I_{a1} + I_{a2})$$

Voltages calculations

$$V_b = V_c$$

$$a^2V_{a1} + aV_{a2} + V_{a0} = aV_{a1} + a^2V_{a2} + V_{a0}$$

$$(a^2 - a)V_{a1} = (a^2 - a)V_{a2}$$

$$V_{a1} = V_{a2}$$

$$I_f = I_b + I_c = (a^2 + a)\, I_{a1} + (a^2 + a)\, I_{a2} + 2I_{a0}$$

$$I_f = -I_{a1} - I_{a2} + 2I_{a0}$$

$$I_f = 3I_{a0}$$

$$V_b = V_c = V_f = I_f Z_f = 3I_{a0}Z_f$$

$$a^2V_{a1} + aV_{a2} + V_{a0} = 3I_{a0}Z_f$$

$$V_{a1} - V_{a0} + V_{a0} = -3I_{a0}Z_f$$

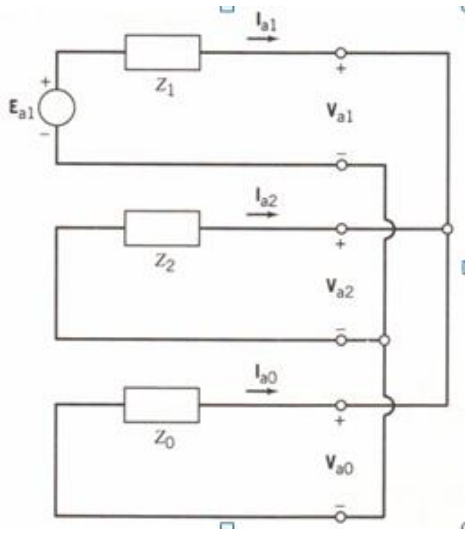

Figure B.6 equivalent circuit of line to line to ground fault